THE UNIVERSITY OF CALGARY

Novel Photocatalytic Reactor and Process for Wastewater Treatment

by

Amit Bhargava

A THESIS
SUBMITTED TO THE FACULTY OF GRADUATE STUDIES
IN PARTIAL FULFILLMENT OF THE REQUIREMENTS FOR THE
DEGREE OF MASTER OF SCIENCE IN CHEMICAL ENGINEERING

DEPARTMENT OF CHEMICAL AND PETROLEUM ENGINEERING

CALGARY, ALBERTA

MARCH, 2000

Abstract

Heterogeneous photocatalysis, as a technology for wastewater treatment, is a very attractive approach for treating low concentration, high volume fluids. For photocatalytic processes, the most suitable semiconductor is TiO_2 (anatase). It is characterized by chemical inertness, non-photocorrosivity, and non-toxic influence on microorganisms. These properties, coupled with its ability to create a highly reactive oxidant (hydroxyl radical) on excitation with UV radiation, make titanium compounds highly suitable for application in wastewater treatment. The hydroxyl radical ($OH^{\bullet}$), which is known to be one of the most powerful oxidizing species, mineralizes organic pollutants to carbon dioxide and inorganic ions. This technology is being developed and it is currently being evaluated for application at the pilot plant and semi-industrial scales of testing.

The design and development of the appropriate photocatalytic reactor requires a study of the hydrodynamics of the reactor coupled with the intrinsic rate kinetics to achieve higher quantum yields and optimum photocatalyst requirements. An annular fluidized bed photocatalytic reactor operating in absorption and regeneration modes has been constructed for the purpose of this study.

A technique using radioactive particle and two gamma cameras arranged perpendicularly to each other has been used successfully in order to study the fluidized bed behavior. This three dimensional Radioactive Particle Tracking (RPT) can enable to predict the amount of UV light a particle would receive during illumination, which decides the production rate of hydroxyl radicals and in turn the reaction rates. Also, CT Scanning of the bed at various superficial velocities provides a tool to predict the bed voidage reliably and accurately, in a particular region of interest when the conventional theory fails. A few reaction experiments conducted with a view to prove the technology in principle point towards more investigation as the reaction path proceeds towards polymerization instead of mineralization in the absence of hydrogen peroxide.

Acknowledgements

I wish to record my deepest sense of gratitude to Dr. Apostolos Kantzas, for his keen interest, constant supervision and sparing his immensely valuable time to guide me throughout the study.

My sincere gratitude to Dr. C.H. Langford who nourished my interest in the study and gave professional advice throughout the study.

Special thanks to Ms. Kelly Hamilton for her immense help in conducting the experiments, Mr. Dan Marentette for helping me get out of troubled waters, Mr. Ian Wright for his helpful suggestions in data analysis, Dr. Doug Philips and Dr. Jinwen Chen for their help with data analysis of radioactive particle tracking experiments and Dr. Madjid Mohseni and Trojan Technologies Inc. for providing an opportunity to work on a challenging problem.

My sincere thanks are due to Dr. Alex Starosud for providing the photocatalyst and Dr. Lela Eberlin for her help with chemical analysis and the astounding support from Dr. Langford's research group.

I have an immense pleasure in expressing my deep sense of gratitude to my great friends for staying along, through my thick and thin and providing a family atmosphere in an alien place miles away from home.

I am sincerely indebted to my beloved parents for all their sacrifice and the support of my better half, Surbhi. I would like to dedicate this piece of work to the fond memories of my mother whose soul always guards and guides me.

Last but not the least, I pay tribute to all my teachers, both past and present who provided me the knowledge I have and made me the person I am.

Dedicated to the fond memories of my beloved mother

Table of Contents

List of Tables

List of Figures

List of Symbols

$\mu_{\lambda,c}$	molar absorption coefficient
r	radial distance, m
ε_{mf}	voidage at minimum fluidization
2-CP	2-Chlorophenol
A	annular cross-sectional area, m^2
C_D	co-efficient of drag
C_i	pollutant concentration, mol/L
C_L	pollutant concentration in bulk liquid phase, mol/L
C_S	pollutant concentration on solid surface
d_p	particle diameter
g	acceleration due to gravity, m^2/s
Ga	Galileo number
H_{EX}	expanded bed height, m
H_{mf}	bed height at minimum fluidization, m
I_{abs}	absorbed light intensity, Einstein/L.s
I_{inc}	incident light intensity, Einstein/L.s
$K_{2\text{-}CP}$	adsorption constant for 2-CP
k_L	mass transfer coefficient
K_s	equilibrium adsorption constant of solvent
Mv	density number
n_P	number of particles in elemental volume
N_P	total number of particles in the reactor
N_{PD}	particle number density, particles/L
Q	flow rate, L/s
Q_{max}	maximal adsorbed concentration
q_λ	radiant power
r	radial distance
r_0	rate of reaction

Re_{mf}	Reynold's number at minimum fluidization velocity
Re_p	particle Reynold's number
R_i	inner radius of an annular photochemical reactor, m
R_o	outer radius of an annular photochemical reactor, m
r_P	mean particle radius, m
Sc	Schmidt number
Sh	Sherwood number
$S_{L,\lambda}$	photon rate of the light source per unit length, Einstein/m.s
u	velocity
U_G	superficial velocity of gas, m/s
U_L	superficial velocity of liquid, m/s
U_{mf}	minimum fluidization velocity, m/s
u_t	terminal velocity
z	axial distance
α	fraction of particles which are irradiated by the incident photons
β	fraction of incident light intensity absorbed
ϕ_s	sphericity
μ	viscosity
ρ_L	density of liquid, kg/m^3
ρ_P	density of particle, kg/m^3

List of Abbreviations

μ	Micron
°C	Degrees Centigrade
ADC	Analog to Digital Convertor
Amps	Amperes
AOP	Advanced Oxidation Processes
CAT	Computer Assisted Tomography
CB	Conduction Band
cm	centimeter
cp	Centipoise
CRT	Cathode Ray Tube
CT	Computed Tomography
DI	Diffuse Incident
ESDSE	Extense Source wirh Diffuse Superficial Emission
ESSE	Extense Source with Superficial Emission
ESVE	Extense Source with Volumetric Emission
ft	feet
g	Gram
g/ml	Gram per milliliter
hr	Hour
HU	Hounsfield Units
Hz	Hertz

kg	Kilogram
kg/cm^2	Kilograms per square centimeter
kJ/mole	Kilo Joule per mole
kmol	Kilo Mole
kV	KiloVolts
L	Liter
L/min	Liters per minute
l/s	Liters per second
LSPP	Line Source Parallel Plane
LSSE	Line Source with Spherical Emission
m^3	Cubic meter
m^3/hr	Cubic meter per hour
mA	milliAmperes
MAA	Macroaggregated Albumin
MAC	Macintosh
mg	Milligram
mg/L	Milligram per liter
min	Minute
ml	Milliliter
mm	millimeter
mol	Mole
nm	Nanometer
PDI	Partially Diffuse Incident

PFR	Plug Flow Reactor
PMT	Photomultiplier Tubes
ppm	Parts per million
RI	Radial Incident
RPT	Radioactive Particle Tracking
SPECT	Single Photon Emission Computed Tomography
UV	Ultraviolet
V	Volts
VB	Valence Band
W	Watts
wt	Weight

CHAPTER 1
Introduction

1.1 General Background

Environmental pollution and destruction on a global scale urgently calls for totally new environmentally friendly, inexpensive, clean chemical technologies and processes. The civilian, commercial and defence sectors of most advanced industrialised and developing nations are faced with tremendous environmental problems related to the remediation of hazardous wastes, contaminated groundwater and the control of toxic air contaminants.

Photocatalytic oxidation of organic compounds is of considerable interest for environmental applications and in particular for the control and eventual destruction of hazardous wastes. Several researchers have studied the photocatalytic reaction mechanisms and sufficient information is available in literature [Pelizzetti *et al.* (1993), Legrini *et al.* (1993)]. The primary driving force for the reaction is the photogeneration of electrons and holes within the photocatalyst due to the excitation of valence band electrons to conduction band by a photon of energy equivalent or more than the band gap energy of the semi-conductor photocatalyst. The majority of these recombine with the liberation of heat but in the presence of adsorbed oxygen or an electron acceptor species, chemical reactions occur forming peroxy and hydroxyl radicals. These hydroxyl radicals so generated are highly powerful oxidizing agents, which mineralize the pollutant to carbon dioxide and water by various multi-step radical reactions.

Photocatalysis is a very attractive method of treatment because, if carried to completion, it results in conversion of the organics to innocuous materials such as carbon dioxide and water. Advanced Oxidation Processes (AOPs) such as photocatalytic oxidation are often preferred over adsorption or biological processes, because in AOPs: (a) contaminants are destroyed rather than transferred to some other medium, (b) no residuals requiring further handling, such as sludge or spent carbon, are generated. The complete mineralization of a variety of aliphatic and aromatic chlorinated hydrocarbons via heterogeneous

photooxidation on immobilized TiO_2, aided with hydrogen peroxide or other electron trapping agent has been reported [Legrini *et al.* (1993)].

Heterogeneous photocatalytic processes are receiving great interest in the pollution control area owing to their ability to eliminate contaminant species present in aqueous and gaseous effluents. Heterogeneous photocatalysis offers an attractive alternative for wastewater treatment especially when treating low concentration. high volume fluids. The main advantages of this method are its non-specificity and the possibility of treating effluents with very low concentration of contaminants aided by a pre-concentration step, without which the reaction rate decreases to negligible values.

For photocatalytic processes, the most suitable semiconductor is TiO_2 (anatase). Chemical inertness, non-photocorrosivity, and non-toxic influence on microorganisms coupled with its ability to create a highly reactive oxidant (hydroxyl radical) on excitation with UV radiation makes titania highly suitable for application in wastewater treatment. The hydroxyl radical ($OH^{\bullet}$), which is known to be one of the most powerful oxidizing species, mineralizes organic pollutants to carbon dioxide and inorganic ions. This technology has been developed and it is currently being evaluated for application at pilot plant and semi-industrial scales of testing.

The efficiency of photocatalytic reactors with immobilized photocatalysts has been found to be lower than those using dispersed titania particles [Matthews and McEvoy (1992)]. However, for practical applications, immobilized catalyst is preferred, as it does not need an additional separation process to recover the photocatalyst. Application of finely powdered TiO_2 is technologically impracticable because powders could be easily washed out. To prevent this phenomenon, it is necessary to construct additional equipment [Haarstrick *et al.* (1996)], which causes a sharp rise in the cost of the process. The additional separation step to remove the catalyst from treated water is difficult from process engineering point of view as well, and is prohibitively expensive. Thus, there is a rigid practical necessity to immobilize titania [Haarstrick *et al.* (1996), Bellobono *et al.*

(1994)]. Many attempts have been made using glass beads, fiberglass, silicon, quartz, activated carbon and zeolites as supports [Haarstrick *et al.* (1996), Bellobono *et al.* (1994), Davis (1994)]. Zeolites as catalyst support offer the advantage of having high absorptivity for organics in wastewater aiding in the preconcentration step. The photocatalyst was synthesized based upon the "golf ball" concept where sintered glass beads (SIRAN) were used as the carrier and zeolites and titania were impregnated into the caverns. This provided a good mechanical structure to withstand the attrition encountered during fluidization. The photocatalyst is being evaluated for performance and mechanical stability during the course of this study.

The photocatalytic process has been widely tested for a large variety of chemical pollutants. However, it is surprising to note that only a very few experiments have been performed on a pilot scale. Rate kinetics of photocatalytic oxidation has been extensively studied but there is a lack of reliable intrinsic kinetic data in literature. Almost all of the researchers have used lumped kinetic constants, which hinders its use in a different reactor configuration. A very recent work by Rideh *et al.* (1997) does bridge some of the shortcomings, however a few issues like the effect of radial UV light intensity variation have been unaddressed. The Langmuir-Hinshelwood equation, which is based on pre-adsorption equilibrium and surface reaction, has been used in the evaluation of kinetic data and mechanisms in photocatalysis by several authors and is universally accepted.

For heterogeneous photocatalytic reactions the contact among reactants, photons and catalysts must be maximized. Mixing and flow characteristics of the photoreactor may greatly enhance these contacts. If a fixed bed reactor is used, the irradiated aliquot of catalyst is limited to a thin layer and a large reactor volume is required. For the liquid-solid and gas-solid systems, continuously stirred tank photo reactors and fluidized bed photo reactors, respectively, are the most suitable ones for enhancing contact efficiency even if their operation is quite expensive and troublesome. The rate of photocatalytic reaction is greatly affected by flow rates. The rate enhancement is not due to elimination

of mass transport resistances, as expected in classical catalytic systems, since such considerations do not apply for most heterogeneous photo-processes that are characterized by low reaction rate with respect to mass transport rate. The enhancement is determined by the fact that on increasing flow rates, the frequency of exposure of the catalyst particles to irradiation increases. The catalyst particles continuously receive diffuse radiation of reduced intensity due to absorption by other catalyst particles. They are directly irradiated intermittently due to the shielding effect of particles which randomly intercept direct irradiation. By increasing flow rates, the frequency with which the catalyst particles may be directly irradiated increases and eventually, the reaction rate is enhanced. With the above considerations, an annular liquid fluidized bed photocatalytic batch reactor operating in adsorption and regeneration modes was constructed.

In this kind of reactor, the extended light source is placed at the axis of a reactor composed of two coaxial cylindrical tubes. The emitted radiant power is absorbed by the reaction system contained in the annular reactor volume. Irradiance diminishes in a filled reactor with increasing radius. This geometry called the negative geometry of irradiation makes the most efficient use of the light emitted by an extended light source. In fact, this geometry is used in all immersion type photochemical reactors, and most industrial photochemical production units [Braun *et al.* (1993)].

1.2 Hypothesis

This study aims at developing a novel photocatalytic reactor and process capable of treating large quantities of wastewater or air contaminated with very low concentrations of toxic organic pollutants. New photocatalyst has been developed based on the golf ball concept where titania and zeolites are filled in the caverns of sintered glass beads. This unique concept provides a catalyst with good mechanical strength to withstand the attrition caused in a fluidised bed and at the same time aiding in the pre-concentration of contaminants. The process is a dual mode operation where all the pollutants from the contaminated stream are adsorbed in a fixed bed. Once the breakthrough is achieved, the

flow is reversed, the photocatalyst bed is fluidised and the UV lamp is turned on. The photocatalysis reactions occur and the photocatalyst particles are regenerated.

1.3 Objectives

This study focuses on the design, construction and hydrodynamic modeling of a liquid fluidised bed annular photocatalytic reactor for wastewater treatment by using zeolites and titania supported on sintered glass as the photocatalyst. The study will lead to the development of a novel photocatalytic reactor and process for obtaining better removal efficiency of toxic organics present in low concentration in contaminated wastewater.

The design and development of the photocatalytic reactor requires a study of the hydrodynamics of the reactor coupled with the intrinsic rate kinetics to achieve higher quantum yields and optimum photocatalyst requirements. Development of a hydrodynamic model requires determination of parameters such as residence time distribution, axial and radial dispersion, and voidage in discretized elements to be used in the hydrodynamic model, since conventional theory fails to predict satisfactorily. Various non-intrusive techniques such as Radioactive Particle Tracking (RPT), CAT-Scanning and pressure measurements are being employed to achieve this purpose. The originality of the research lies in the use of gamma cameras for particle tracking for the purpose of hydrodynamic modelling, a CT scanner for voidage distribution and in the development of a novel photocatalytic reactor system to achieve high removal efficiencies cost effectively.

The research objectives of this study are:

i) To design, develop and construct an annular liquid fluidized bed photocatalytic reactor operating in adsorption and regeneration modes.

ii) To use two gamma cameras arranged perpendicularly to each other to obtain three-dimensional trajectory images of photocatalyst particles.

iii) To obtain voidage density distribution maps and mean voidage profiles using a CT Scanner.

iv) To analyse the acquired images from the gamma cameras and the CT Scanner to develop a hydrodynamic model for the reactor.

v) To develop a simulator for modeling of the photocatalytic reactor for 2-Chlorophenol degradation using heterogeneous photocatalyst (TiO_2 in anatase form), based on kinetic studies carried out by Rideh *et al.* (1997).

vi) To study the effect of various operational parameters such as initial pollutant concentration, flow rate, oxygen partial pressure, absorbed UV light intensity using the developed simulator with a view to find out the range of operational parameters for optimum reactor performance.

vii) To conduct a few reaction experiments to prove the technology in principle.

CHAPTER 2

Literature Review

2.1 Background

In recent years, the focus of research on new methods for waste water treatment has moved from processes involving phase transfer of a contaminant (e.g., from liquid to solid such as activated carbon, or from liquid to gas in the case of air stripping of volatile contaminants) toward processes involving chemical destruction of the contaminant. The efforts have led to the development of advanced oxidation processes (AOPs) which includes photochemical processes such as H_2O_2/UV; O_3/UV; O_3/H_2O_2/UV process and photocatalytic process involving titania.

In photochemical AOPs, the use of hydrogen peroxide as oxidant brings a number of advantages: commercial availability of the oxidant, thermal stability and storage on–site, infinite solubility in water, no mass transfer problems associated with gases, minimal capital investment, very cost-effective source of hydroxyl radicals, and simple operation procedure. There are, however, also obstacles encountered, since the rate of chemical oxidation of the contaminant is limited by the rate of formation of hydroxyl radicals, and the rather small absorption cross section of H_2O_2 at 254 nm is a real disadvantage, in particular, in the cases where organic substrates will act as inner filters. The above problem is not encountered while using O_3 as the oxidant, however, the low ozone solubility in water and consequent mass transfer limitations represent one of the most serious and rather specific problems encountered in scale-up. The photocatalysis process has a number of advantages: a large number of organic compounds dissolved or dispersed in water can be completely mineralized; the rate of reaction is relatively high if large surface areas of the photocatalyst can be used; titania is available at a relatively modest price; UV lamps emitting in the spectral region required to initiate the photocatalytic oxidation are well known and are produced in various configurations.

The potential of heterogeneous photocatalysis for solving environmental problems, particularly in the field of trace organics and metals removal, has promoted much research activity in various groups around the world. The degradation of organic pollutants contained in wastewaters by irradiating dispersions of titania has become a fast growing field in basic and applied research. Partial or complete mineralization has been achieved for a large variety of chemicals [Legrini *et al.*, (1993)], since Carey *et al.* (1976) first reported the photocatalytic degradation of biphenyl and chlorophenyls in the presence of titanium dioxide. During the early 1980's Ollis and coworkers [Pruden and Ollis (1983a), Pruden and Ollis (1983b), Hsiao *et al.* (1983), Nguyen and Ollis (1984), Ahmed and Ollis (1984), Ollis *et al.* (1984)] also showed that in the presence of near-UV illuminated TiO_2 suspensions, common chlorinated aliphatic hydrocarbon contaminants in water were not only dechlorinated, but totally mineralized. It was later shown that under similar conditions [Matthews (1985), Matthews (1986)], not only chlorinated aliphatic compounds were converted to carbon dioxide, but complete mineralization of a whole range of contaminants, including some aromatic compounds that are resistant to oxidation was also realized. The oxidation rates observed were neither trivial, nor greatly different in the case of different compounds [Matthews (1993)]. Thus it became evident that near-UV illuminated TiO_2 suspensions provide a powerful wet oxidation method of general applicability.

2.2 Applications

Photocatalysis has been proposed as a viable alternative for controlling water pollution caused by organic contaminants [Pelizzetti *et al.* (1990)] and represents an economical and non-harmful method for the elimination of non-biodegradable organic pollutants [Tinucci *et al.* (1993)]. The highlights of the process are no by-products generation and no transfer of contaminants from one medium to another. Tinucci *et al.* (1993) have reported that the versatility of photocatalysis processes has found numerous applications such as the treatment of degreasing effluents [Pelizzetti *et al.* (1993)], of soils [Pelizzetti *et al.* (1992)] and sediments [Zhang *et al.* (1992)], of dyes [Matthews (1991), Mills and Davies (1992)], of pulp and paper effluents [Duran *et al.* (1991), Sierka and Bryant

(1992)], and of landfill leachate [Weichgrebe *et al.*(1993)]. Heterogeneous photocatalysis has the potential for removal of low concentration air pollutants such as a practical NO_x removal system for the treatment of exhaust air from closed spaces like a traffic tunnel [Ibusuki *et al.* (1993)]. Moreover, Matthews (1993) observed that the use of titania suspensions illuminated with sunlight have a striking effect on the destruction of fecal coliforms.

2.3 Reaction Mechanism

The primary photochemical events occurring upon the illumination of a photoactive semiconductor are now quite well understood and documented in several reviews [Legrini *et al.* (1993), Pelizzetti *et al.* (1993)]. The primary driving force for the reaction is the photogeneration of electrons and holes within the photocatalyst. The majority of these recombine with the liberation of heat but in the presence of adsorbed oxygen and an electron donor, chemical reactions occur forming peroxy and hydroxyl radicals. These hydroxyl radicals so generated are highly powerful oxidizing agents, which mineralize the pollutant to carbon dioxide and water by various multi-step reactions.

According to Legrini *et al.* (1993), the band-gap model has proven to be a very useful mechanistic explanation of the semiconductor - catalyzed oxidative degradation of organic material in aqueous systems. [Bard (1982), Childs and Ollis (1980)].

A photocatalyst is an insoluble inorganic semiconductor material (crystalline or amorphous) that upon the absorption of a photon(s), brings about chemical transformations of an adsorbed reactant(s) via intermediate interaction with reactive surface species which are regenerated after each reaction cycle. Consequently, the semiconductor photocatalyst may not be consumed during its catalytic activity. Such materials function as a pool of electrons and holes which are advantageous for multi-electron transfer reactions. A semiconductor, by solid state definition, has a band structure which is identified from its band-gap (E_g) separating the valence band (VB) and the conduction band (CB). The valence band is characterized as a series of energetically

closely spaced, populated energy levels associated with the bonding between atoms making up the crystallite. The conduction band on the other hand involves a series of spatially diffuse energetically similar but empty levels lying at higher energy. Solids with band-gap energies less that 3 eV are considered to be semiconductors.

The mechanistic pathway for the photocatalytic oxidation of organics in aqueous TiO_2 suspensions is believed to involve the photo-generated surface trapped holes. Some plausible pathways that may occur on photo-activated TiO_2 surface are listed in Figure 2.1 [Leopore (1995)]. Since the surface of TiO_2 is mainly hydrated, these holes can oxidize surface bound OH^- or water to produce $HO^\bullet$ (routes (T3) and (T4), respectively), that can then go on to attack adsorbed contaminants (T8) or diffuse into solution to react with nearby substrate(s) (T9). The hydroxyl radical is a powerful oxidant, having a standard redox potential of 2.7 V in acidic solution and 1.8 V in neutral solution where the free energy of neutralization of OH^- by H^+ is not available. In strong alkaline solution $OH^\bullet$ is rapidly converted to its conjugate base $O^{\bullet-}$, and in reactions with organic molecules the hydroxyl radical behaves as an electrophile whereas its conjugate base is a nucleophile.

The success of TiO_2 based systems is evident from the fact that a variety of contaminants ranging from chloro-aromatics such as polychlorinated biphenyls to herbicides (i.e. atrazine) have been broken down to less harmful by-products (in most cases complete mineralization).

A major limitation of such heterogeneous photocatalysts has been the relatively high recombination rate between the photo-excited electron-hole pairs and the consequent low quantum efficiency of surface redox processes. The quantum efficiency of redox reactions at the metal oxide-liquid interface will depend on how fast the carriers reach the surface of the solid and how rapidly they are captured through interfacial electron transfer by a thermodynamically appropriate electron donor or acceptor, in competition with the recombination rate within the particle.

Photo-activation (Carrier generation)

$TiO_2 + h\nu \rightarrow h^+_{(VB)} + e^-_{(CB)}$ (T1)

Recombination

$h^+_{(VB)} + e^-_{(CB)} \rightarrow heat$ (T2)

Carrier Trapping

$\square\text{–}Ti^{IV}\text{–}OH + h^+_{(VB)} \rightarrow \square\text{–}Ti^{IV}\cdots OH^\bullet$ (T3)

$\square\text{–}Ti^{IV}\text{–}H_2O + h^+_{(VB)} \rightarrow \square\text{–}Ti^{IV}\cdots OH^\bullet + H^+$ (T4)

$R_{1\ ads} + h^+_{(VB)} \rightarrow R_1^{+\bullet}$ (T5)

$\square\text{–}Ti^{IV} + e^-_{(CB)} = \square\text{–}Ti^{III}$ (T6)

$\square\text{–}Ti^{III} + O_2 = \square\text{–}Ti^{IV}\cdots O_2^{-\bullet}$ (T7)

Radical Reactions

$\square\text{–}Ti^{IV}\cdots OH^\bullet + R_{1\ ads} \rightarrow \square\text{–}Ti^{IV} + R_2{}^\bullet{}_{ads}$ (T8)

$HO^\bullet + R_1 \rightarrow HO\text{–}R_2{}^\bullet$ (T9)

$\square\text{–}Ti^{IV}\cdots O_2^{-\bullet} + [H^+] = \square\text{–}Ti^{IV}[HO_2{}^\bullet]$ (T10)

$\square\text{–}Ti^{IV}[HO_2{}^\bullet] + [H^+] + e^-_{(CB)} \rightarrow \square\text{–}Ti^{IV}[H_2O_2]$ (T11)

$\square\text{–}Ti^{IV}[H_2O_2] + e^-_{(CB)} \rightarrow \square\text{–}Ti^{IV}[HO^\bullet][HO^-]$ (T12)

Figure 2.1 Summary of Plausible Mechanistic Routes on Illuminated TiO_2
Source : Leopore (1995)

In water, the solvent itself is a potential electron acceptor, however, as water is not kinetically easy to reduce where O_2 is present it is the most likely electron acceptor. Adsorbed molecular oxygen can scavenge conduction bad electrons to give rise to superoxide radical anions, $O_2^{\bullet-}$. Superoxide is a very good nucleophile and has been shown to effectively degrade polyhalogenated aromatics in aprotic solvents, however it is unstable and can undergo disproportionation to yield H_2O_2. When TiO_2 is over-illuminated, hydrogen peroxide can undergo surface reactions (reduction) to yield surface hydroxyl radicals.

2.4 Titania as the Photocatalyst

Researchers have used other metal oxide semiconductors (ZrO_2, MoO_3, SnO_2 and WO_3) for heterogeneous photocatalysis but found them to be either poorly efficient (ZrO_2, MoO_3) [Al-Sayyed *et al.*(1991)] or quite inactive (SnO_2 & WO_3) [Barbeni *et al.* (1987)] as compared to TiO_2. This validates our choice of photocatalyst.

2.5 Advantages of Heterogeneous Photocatalysis

According to Herrmann *et al.* (1993), the advantages offered by heterogeneous photocatalysis are:

i) the chemical stability of TiO_2 in water under UV radiation
ii) the absence of chemical additives
iii) the absence of inhibition or the low inhibition by ions generally present in water (carbonates & bicarbonates)
iv) the low cost of TiO_2
v) the possibility to work with solutions containing very low concentrations of the pollutant
vi) the total mineralization achieved for many organic pollutants.

2.6 Immobilized vs. Dispersed Titania

According to Haarstrick *et al.* (1996), for photocatalytic degradation processes, two modes of TiO_2 application are favored: (a) TiO_2 suspended in aqueous media and (b) TiO_2 immobilized on support materials, e.g., quartz sand, glass, activated carbon, zeolites or noble metal. Possible alternative reactor configurations include either fluidized [Braun (1991)] or fixed-bed [Braun *et al.* (1993)] reactors. Matthews and McEvoy (1992), found that the efficiency of photocatalytic reactors with immobilized photocatalysts is lower than those using dispersed titania particles. Matthews (1993) proposed that the lower efficiencies achieved with immobilized photocatalyst can be attributed to:

i) The diminished number of activated sites in a given photoactivated volume that are available when the catalyst is immobilized versus the same weight of catalyst that is freely suspended.

ii) The mass transfer limitation that may become rate controlling at low flow rates [Turchi and Ollis (1988)]. The latter is particularly serious in high intensity illuminations since the mass transport may be unable to keep pace with the reaction at the photoactivated surface and the reaction could become entirely mass transfer limited. When this happens increasing photon intensity will make negligible difference to the reaction rate [Ollis (1991)].

An increase of photocatalytic degradation efficiency by at least a factor of 10 has been reported by Braun (1991) for dispersed titania when compared to TiO_2 applied in fixed bed configurations [Hofstadler *et al.* (1994), Brezova *et al.* (1994)]. However, for technical application, immobilized TiO_2 is preferable [Hoffman *et al.* (1994)] to dispersed fine TiO_2 because of simplicity of operation and elimination of a separation and resuspension step in the process, besides no need of additional equipment and energy for the recovery of catalyst particles. Haarstick *et al.* (1996) suggest that reactors using immobilized photocatalysts may be quite attractive for the combination with bioreactors where the expected easily biodegradable photooxidation products can be totally degraded.

2.7 Photocatalytic Reactors

The three main components of a photocatalytic process are indeed the photoreactor, the radiation source and the photocatalyst. According to Augugliaro *et al.* (1997), for thermal and catalytic processes the reactors are generally chosen on the basis of the following parameters: (i) the mode of operation; (ii) the phases present in the reactor; (iii) the flow characteristics; (iv) the needs of heat exchange; (v) the composition and the operative conditions of the reacting mixture, which affects the selection of materials of construction. However, for selection of the type of heterogeneous photocatalytic reactor additional parameters have to be considered owing to the fact that photons are needed for the occurrence of photoreaction. The selection of the construction material is done in order to allow the penetration of radiation into the reacting mixture. The choice of the radiation source is easier than that of the photoreactor since the radiation spectrum of the lamp should coincide with the absorption spectrum of the reacting system and the emitted

photons should have energy equal to or more than the band-gap of the semiconductor photocatalyst. Based upon these three components photocatalytic reactor systems can be classified under the following types:

2.7.1 Light Source

The light source is a very important factor to be considered since the performance of a photoreactor is strongly dependent upon the irradiation source. There can be two types of light sources, natural i.e. solar light and artificial. The artificial light sources can be of many types such as: (a) arc lamps; (b) fluorescent lamps; (c) incandescent lamps; (d) lasers. In general, arc lamps and fluorescent lamps are the most commonly used in photoreactor systems.

In fluorescent lamps the emission is obtained by exciting an emitting fluorescent substance, deposited in the inner side of a cylinder, by an electric discharge occurring in the gas filling the lamps. Generally, these lamps emit in the visible region, but the 'actinic' type have emissions in the near-UV region and the emission spectrum depends on the nature of the mixture of fluorescent substances used. Their power output is quite small (up to 180 W) and hence they find uses in laboratory scale units.

For arc lamps and in particular for mercury lamps, a classification based on the pressure of Hg is made by Augugliaro *et al.* (1997) and it is as follows:

i) Low-pressure Hg lamps: This type of lamp contains Hg vapor at a pressure of about 0.1 Pa , emitting mainly at 253.7 and 184.9 nm.

ii) Medium-pressure Hg lamps: this type of lamp has a radiation source containing mercury vapor at pressures ranging from 100 to several hundred kPa and the emission is mostly from 310 to 1000 nm with most intense lines at 313, 366, 436, 576,and 578 nm.

iii) High-pressure Hg lamps: This type of lamp contains mercury at a pressure of 10 MPa or higher, which emits broad lines and a background continuous between 200 and 1000 nm.

iv) Xenon and Hg-Xenon lamps: In this type of lamp an intense source of ultraviolet, visible and near-IR radiation in a mixture of Hg and Xe vapors under high pressure is obtained.

A fluorescent lamp (180 W) has been used in all the bench top laboratory studies conducted during the course of this project in the Department of Chemistry at the University of Calgary and a medium pressure Hg lamp provided by Trojan Technologies Inc., Ontario has been used in our laboratory for all the experiments conducted at pilot scale.

2.7.2 Reactor Configuration

The geometry and the spatial relation between the reaction chamber and light source are most important for photoreactors. The reason lies in the fact that geometry plays an important role in determining reaction yields as well as reactor operability. A particular reactor configuration is chosen to derive the maximum benefits from the pattern of irradiation taking into account shape and cooling requirements of available lamps useful for the desired wavelengths. In selecting the reactor configuration, it is very important to determine the optical path of the light that will be obtained within the reactor. Augugliaro *et al.* (1997) have summarized the various types of reactor configurations, their advantages and disadvantages as follows:

i) **Immersion Well Photoreactor:** This is the simplest type, mostly used on a laboratory scale as well as on a pilot or production scale. It is a stirred tank reactor in which photocatalyst is in suspension. One or more lamps are immersed in the suspension and it can operate in a batch or continuous mode. The advantage is simplicity and very high photonic efficiency but its efficiency may decrease over time due to deposition of a film of very fine particles on the lamp surface unless cleaning is performed at fixed intervals.

ii) **Multilamp Photoreactor:** This kind of photoreactor is cylindrical, externally surrounded by several lamps and the lamps in turn are surrounded by reflecting surfaces. It is generally adopted when fluorescent lamps are used which are

characterized by small power. The reflecting surfaces have parabolic shape and the lamps are positioned at the focus.

iii) **Elliptical Photoreactor:** In this configuration the reactor, of cylindrical shape, and the lamp are vertically positioned on the axes of the foci of a cylindrical reflecting surface of elliptical cross section. The radiant energy field at the outer wall of the photoreactor is not uniform and the intensity depends upon angular and axial coordinates.

iv) **Film Type Photoreactor:** In this type of reactor the reacting medium forms a thin film of flowing liquid on the reactor wall which is externally irradiated. If the reactor wall is cylindrical (as in falling film reactors) it may be designed for lamps which can provide external or internal irradiation.

v) **Flat Walls Photoreactor:** This type of configuration is used when the radiation field is a parallel beam as in the case of short arc lamps with concave mirror and optics, or solar irradiation. The transparent wall of the reactor is usually flat and it can have co-current, counter-current or cross-flow arrangements, when the radiation fields and reagent flow are in the same direction, opposite direction and transversal direction respectively.

vi) **Annular Photoreactor:** In this kind of reactor, two coaxial cylinders delimit the reaction zone and the lamp is placed on the symmetry axis. It can operate in batch or continuous mode. Practically all the photons emitted by the lamp reach the reaction medium if the outer walls of the reactor are reflective. This geometry has been selected for the photoreactor used in our study and offers a number of advantages viz. efficient photon capture, practical to fluidize the photocatalyst in a cylindrical geometry and an inner jacket can be used for meeting the cooling requirements of the medium-pressure Hg vapor lamp.

2.7.3 Means of Catalyst Immobilization

One of the disadvantages of using insoluble conductor powder (titania) for wastewater treatment is the need to separate titania from water following the treatment and to resuspend it in the next volume of water to be treated. Various techniques could be used

for separation but all of them would involve additional expense and more complex processes. The above complication can be avoided if titania can be attached to a stationary or mobile illuminated support and the water passes over through the immobilized catalyst bed. This immobilization can be achieved in many ways since some small particles of titania can be easily attached to stationary substrates such as glass. This adhesion is probably caused by the electrostatic charge on the TiO_2 particle surface being attracted to the negatively charged surface of the glass. According to Matthews (1993), a variety of transparent and translucent siliceous compounds can be coated quite readily with titanium oxide utilizing inexpensive techniques.

Once these catalyst coated support materials are prepared, various reactor concepts can be envisaged. Some of the concepts converted to reality (either on lab-scale or pilot-scale) are: glass beads [Serpone *et al.* (1986)], the inner wall of a glass spiral [Matthews (1987a)] or glass mesh in the annulus of a jacket around a tube lamp [Matthews (1987b)]. These arrangements have been powered by ultraviolet lamps or by sunlight. Some of the most recent novel photocatalytic reactor arrangements based on catalyst immobilization are: novel optical fiber cable reactor [Peill and Hoffmann (1996)], titania on pyrex glass plate roughened by sand blasting used in a swirl-flow reactor [Ray and Beenackers (1997)], titania impregnated on silica gel in a fixed bed photocatalytic reactor [Crittenden *et al.* (1997)], and a tubular reactor consisting of stainless steel cylindrical supports coated by a thin film of titania and a coaxial UV source [Mazzarino and Piccinini (1999)].

2.8 Modeling of a Photocatalytic Reactor

The problem of modeling and scale-up of heterogeneous photocatalytic reactors is considerably more complex than that of conventional chemical reactors or homogeneous photoreactors. A validated mathematical model of a multiphasic heterogeneous photoreactor would provide a versatile and reliable method for purposes of scale-up and design. The solution of a validated model will provide insight into effects of various reactor parameters on the process for new situations, without having to conduct extensive

and expensive experimentation. A reliable model may be used for optimization of existing or new processes and for the design of full-scale units.

The mathematical modeling of conventional chemical reactors is based on the coupled heat and mass balances and on the kinetics of the chemical reaction [Andre *et al.* (1990)]. Modeling of heterogeneous photoreactors presents an additional complication since the radiation energy balance has to be taken into account. According to Braun *et al.* (1993), this coupling between mass and light energy balances which depends upon the concentration of reactants and products, photocatalyst concentration, incident light distribution, and photon concentration, presents additional difficulties which are not yet resolved. Modeling taking into account this strong coupling between the radiant energy conservation equation and the momentum, mass and heat balances call for describing this interaction as a function of time and space. Such radiation models have been in development over the past 35 years, and the published results may be classified into two main categories: incidence models which assume the existence of a given radiant energy distribution in the vicinity of the reactor, and emission models in which lamp characteristics, reaction, and flow processes are taken into account.

2.8.1 Incidence Models

Pioneering attempts to describe the radiant power distribution in photoreactors can be summarized under the heading of RI model (radial incident model) [Braun *et al.* (1993)]. This model is based on the hypothesis of a radial radiation field, that is, all the light striking the reactor wall will be directed radially inward. Corresponding profiles of radiant power or of irradiance are a strong function of the radius of the cylindrical reactor.

The radial incident (RI) model was adapted by various researchers and has been tested in an ideal elliptical photoreactor, where the lamp was considered as a linear light source and the cylindrical reactor tube and lamp are located at the foci of an elliptical reflector. However, in actual practice, any tubular light source will have a finite diameter and will not behave as a true line source. Radiation from an extended light source will emanate

from points displaced from the lamp's axis, causing the lamp to appear rather like a diffuse light source [Braun *et al.* (1993)]. The DI model (diffuse incident model) was suggested and was thought to take into account the above mentioned inadequacies. In the RI model, all incident rays intersect at the center axis of the reactor tube and as $r \rightarrow 0$ irradiance approaches an infinite value. The DI model, on the other hand, proposes parallel layers of rays which are wider than the diameter of the tubular reactor and which traverse the reactor perpendicularly to its axis from all directions with equal probability. The calculated results of both models are far from reality, as found in industrial photoreactors. Matsuura and Smith (1970) proposed an intermediate model (PDI model, partially diffuse model) in which parallel layers of rays are assumed, and the width of each is smaller than the diameter of the tubular reactor. These two-dimensional bands form by themselves radial arrangements, the center ray of each band intersecting the axis of the reactor tube.

2.8.2 Emission Models

Incident models do not make use of all the operating variables, such as radiant power, diameter and length of the light source or other dimensions of the reactor. Models that describe the space of irradiation on the basis of geometry and process variables are known as emission models.

The simplest emission model is the line source with parallel plane (LSPP) emission model. In this model the lamp is considered to be a linear source in which each point emits radiation in parallel planes perpendicular to the lamp axis. Harris and Dranoff (1965) were the first to use the LSPP model to study the performance of a photoreactor for scale-up purposes. Experimentally, two different sizes of perfectly mixed photoreactors were used for the decomposition of hexachloroplatinic acid in dilute aqueous solution, and the result of the theoretical analysis was acceptable in comparison with the experimental data. Jacob and Dranoff (1970) developed a very important extension of the LSPP model by taking into account the three-dimensional nature of the light emission process. In the resulting line source with spherical emission (LSSE) model,

the lamp is still considered to be linear, but each of its points emits radiation isotropically and in all directions. Further development of the emission models was made by Irazoqui *et al.* (1973) who introduced the three-dimensional nature of the extended light source. Hence, the most significant feature of the extense source with volumetric emission (ESVE) model is the inclusion of a radiant energy source with finite spatial dimensions.

2.9 Influence of Operational Parameters on Photocatalytic Process

2.9.1 pH

Although the pH can be one of the most important parameters for photocatalytic processes, its influence on the photocatalytic degradation has been investigated in detail only by a few research groups. The pH generally influences a semiconductor in an electrochemical system by shifting the valence and the conduction band following the Nernst law. Also, the charge of the semiconductor surface and therefore the adsorption properties, depends upon the pH. Since in photocatalysis the adsorption of a pollutant is a prerequisite for its degradation, a change in pH can lead to a change of the degradation rate and of the amounts and concentrations of intermediates. Nonetheless, changes in rate of photocatalytic activity from one end of the pH range to the other are usually small, often less than 1 order of magnitude [Fox and Dulay (1993)]. The absence of marked effect of the pH represents an advantage of photocatalytic process over biological treatment. According to Herrmann *et al.* (1993), an elevation of pH above 10 caused an increase in the reaction rates, as is expected from an increase in the formation rate of $OH^{\bullet}$ radicals from the reaction:

$$OH^{-} + p^{+} \rightarrow OH^{\bullet}$$

In a more recent study, Rideh *et al.*(1997) found that the rate constant for 2-Chlorophenol degradation is lower in the acid medium than in the basic medium and it is more or less constant in the neutral pH range. They also suggest that pH has a higher direct effect on the conversion rate; it can affect either the surface properties of the photocatalyst or the chemical form of the substrate. Titania has an amphoteric character with a point of zero charge around pH equal to 6 [Pelizzetti *et al.* (1993)], and the substrate can undergo acid-

base equilibria. Consequently, the adsorption of the substrate may be affected, strongly influencing the degradation rate [Kormann *et al.*(1991)].

2.9.2 Temperature

Experiments have shown for 4-Chlorophenol [Al-Sayyed *et al.* (1991)] and 2-Chlorophenol [Rideh *et al.* (1997)], that the variations of the initial rate of reaction in the range 278-333 K follow the Arrhenius law. However, the apparent activation energy is very small (5.5 kJ/mole and 6.23 kJ/mole respectively), which indicates that the thermally activated steps are negligible. In the latter case, a temperature increase of 103 °C would be required to double the rate constant. Irradiation is the primary source of electron-hole pair generation at ambient temperature as the band gap energy is too high to be overcome by thermal activation. Therefore, the slight increase in rate constant can be attributed to the increasing collision frequency of molecules in solution that increases with increasing temperature [Chen and Ray (1998)]. An expected increase of the reaction rate constant with increasing temperature is possibly compensated by a decrease of the adsorption equilibrium constant [Koster *et al.* (1993)]. This clearly demonstrates that the photocatalytic treatment is well adapted for decontaminating liquid water at temperatures close to ambient.

2.9.3 Oxygen Partial Pressure

Literature results appear to provide a consensus regarding the influence of oxygen; it is necessary for the complete mineralization and it appears not to be competitive with the pollutant during adsorption. Most researchers agree that the adsorption of oxygen in a nondissociated form, on a site different from that for contaminant, would provide a Langmuir type function.

Most researchers attribute the limitation of the rate of photocatalytic degradation to the recombination of photogenerated electron-hole pairs. Oxygen adsorbed on the surface of titania prevents the recombination process by trapping electrons according to the reaction:

$$O_2 + e^- \rightarrow O_2^{\bullet -}$$

Barbeni *et al.* (1987) reported that the partial pressure of oxygen is a crucial factor in photocatalytic reactions. Experimental results of Rideh *et al.* (1997) show that 2-Chlorophenol degradation increases nonlinearly with oxygen partial pressure. Rideh *et al.* (1997) proposed that the reaction rate is a function of the fraction of adsorption sites occupied by oxygen; hence oxygen adsorption becomes a limiting factor at very low dissolved oxygen concentrations. Chen and Ray (1998) studied the effect of oxygen concentration on degradation rates and found that the degradation rate constant of 4-Nitrophenol increased with increasing oxygen partial pressure and reached about 70% of its maximum value when the partial pressure of oxygen was 0.2 atm. Similar observations were made by Rideh *et al.* (1997) for 2-Chlorophenol degradation. This indicates that in commercial applications it is possible to replace pure oxygen with air.

2.9.4 Hydrogen Peroxide

Photocatalyzed reactions have been reported to exhibit appreciable, even substantial rate increases when hydrogen peroxide is added to aqueous photocatalyst slurry. However, in various experimental studies researchers have obtained controversial results about the effect of hydrogen peroxide on the decomposition of many organic pollutants by the photocatalytic process. While the decomposition rates of phenol, salicylic acid, organochlorine insecticides have been reported to increase, the decomposition rates of methyl orange and benzamide have been reported to decrease by the addition of H_2O_2 [Akmehmet and Inel (1996)]. The photocatalytic oxidation of aqueous solutions of phenol, p-nitrophenol, 4-chlorophenol, aniline, hydroquinone and pyridine have been studied by Akmehmet and Inel (1996) in a gas recycling reactor utilizing TiO_2 as photocatalyst in the presence and absence of hydrogen peroxide. The results obtained indicate that the disappearance of each solute obeys pseudo first order kinetics with respect to organics whereas the rate of mineralization is zeroth order. They found that while addition of small amounts of hydrogen peroxide significantly enhanced the photomineralization rate of all organic compounds, at higher concentration it inhibited the reaction. The optimum concentration of H_2O_2 in their case ranges from $1x\ 10^{-2}$ to $0.5x10^{-2}$ M for 10^{-4} M organic solutions. The complete mineralization for each organic

component resulted in approximately 50-110 minutes whereas this period was shortened to 6-28 minutes by the addition of an optimum amount of hydrogen peroxide. The enhanced reaction rate may be attributed to a decrease in the electron-hole recombination process because of the reaction of hydrogen peroxide with conduction band electrons or superoxide ions. While, in the case of high concentrations of H_2O_2, the inhibitory effect is observed due to probable competition of organics with H_2O_2 for the hydroxyl radical.

2.9.5 Catalyst Concentration

Many researchers have investigated under different experimental conditions the evolution of the reaction rate as a function of catalyst concentration [Mengyne *et al.* (1995); Kawaguchi (1993)]. Rideh *et al.* (1997) conducted a series of experiments to find an optimum catalyst concentration and their results are in good agreement with other studies found in literature. The initial photodegradation rate increases linearly with catalyst concentration and approached a limiting value at higher concentrations. This plateau mainly results from the following two factors: (a) aggregation of photocatalyst particles at high concentrations, causing a decrease in the number of surface active sites, and (b) increase in turbidity and light scattering at high concentrations leading to a decrease in the passage of radiation.

2.9.6 Initial concentration of pollutant

As the effect of pollutant concentration is of utmost importance in any water treatment process, the dependence has been extensively investigated for various pollutants by researchers. In recent years, the Langmuir-Hinshelwood rate has been used successfully for heterogeneous photocatalytic degradation to describe the relationship between initial degradation rate and initial concentration [Al-Sayyed *et al.* (1991); Lu *et al.* (1993); D'Oliveira *et al.* (1990)]. The Langmuir-Hinshelwood model is represented by:

$$r_0 = k K C_0 / (1+KC_0)$$

where r_0 is the rate of reaction, k is the rate constant, which depends on the operating conditions (temperature, pH, wavelengths, radiant flux etc.), and K is the adsorption constant of the pollutant considered on TiO_2 in competition with water.

Rideh *et al.* (1997) studied the effect of initial concentration of 2-chlorophenol on its photodegradation rates and found that the photodegradation decreases with increasing initial concentration and the Langmuir-Hinshelwood model obtained good fits with experimental data. A plausible explanation of this behavior can be the following: as the initial concentration increases, more and more organic pollutants are adsorbed on the photocatalyst surface, but the intensity of light and illumination time were constant; consequently, the hydroxyl radicals formed on the surface of titanium dioxide are limited, the relative number of hydroxyl radicals attacking the pollutant molecules decreases, and thus the photodegradation efficiency decreases too [Mengyne *et al.* (1995)].

2.9.7 Light Intensity

Various studies [D'Oliveira *et al.* (1990); Ollis *et al.* (1991) and Al-Sayyed *et al.* (1991)] on photodegradation rate versus illumination intensity indicated that the reaction rate increases with the square root of intensity at high intensity levels when mass transfer is not limiting. At sufficiently low levels of illumination (catalyst dependant), on the other hand, degradation rate is of first-order with respect to intensity. Increased illumination results in an increase in volumetric reaction rate, until the mass transfer limit is encountered. The transition points between these regimes, however, will vary upon the photocatalytic system. More recent studies by Chen and Ray (1998) and Rideh *et al.* (1997) also confirmed the above findings, however in the latter study the experiments were conducted in the region of lower intensity and their reaction rate was first order with the light intensity. Several studies [D'Oliveira *et al.* (1990); Ollis *et al.* (1991) and Al-Sayyed *et al.* (1991)] attributed this rate transition from first-order to half-order to the recombination of photogenerated electron-hole pairs at high light intensity. This phenomenon is obviously detrimental to the photocatalytic process as the quantum efficiency decreases. The recombination process may be slowed down possibly by the addition of better electron acceptors such as H_2O_2, Cu^+ and Ag^+ [Ollis *et al.* (1991)].

CHAPTER 3

Photocatalytic Reactor Modeling

The purpose of this part of the study was to model and simulate a liquid fluidized bed photocatalytic reactor for 2-Chlorophenol degradation operating in once through and dual mode (adsorption followed by regeneration). Also, to analyze the effect of various operational parameters such as initial pollutant concentration, flow rate, oxygen partial pressure, absorbed UV light intensity, initial bed height using the developed simulator with a view to find out the range of operational parameters for optimum reactor performance.

3.1 Hydrodynamic Modeling

A hydrodynamic model was set up using the Wen and Yu Correlation [Wen and Yu (1966)] to predict the bed voidage as a function of superficial velocity. The number of particles in the elemental volume under consideration was calculated using geometry. We could arrive at the average light intensity reaching a photocatalyst particle surface using the line source with parallel plane (LSPP) emission model [Harris and Dranoff (1965)]. In this model, the lamp is considered to be a linear source in which each point emits radiation in parallel planes perpendicular to the lamp axis. Combining this hypothesis with the Beer-Lambert equation, the integration of the differential equation describing the radiant power or irradiance as a function of the optical path yields the profile of radiant power or irradiance.

3.1.1 Minimum Fluidization Velocity

When a fluid is passed through a packed bed of solids, initially at low velocity, the bed remains stationary. As the fluid velocity is increased, the drag on the solid particle increases and liquid merely percolates through the bed. Under these conditions the pressure drop is proportional to the superficial velocity of the fluid. As the superficial velocity is increased, the pressure drop across the bed counter balances the force of gravity on the particles or the weight of the bed. Any further increase in linear velocity causes the bed to expand. Initially the bed expands only slightly but with further increase

in fluid velocity, the particles become separated enough to move in the bed and true fluidization begins. This fluid velocity is called the minimum fluidization velocity, U_{mf}. At fluid velocities greater than minimum fluidization velocity, the whole bed exhibits many qualities of a fluid and hence is known as a fluidized bed.

Minimum fluidization velocity can be calculated by making a force balance across the bed. At the superficial velocity of the fluid when the bed is first fluidized, setting the pressure drop across the bed equal to the weight of the bed per unit area of cross-section and correcting for the buoyant force of the fluid gives the Ergun equation.

The Ergun equation provides a quadratic equation for minimum fluidization velocity, U_{mf} as,

$$\frac{1.75}{\varepsilon_{mf}^2 \phi_S}\left(\mathrm{Re}_{mf}^{\cdot}\right)^2 + \frac{150\left(1-\varepsilon_{mf}\right)}{\varepsilon_{mf}^3 \phi_S^2}\left(\mathrm{Re}_{mf}^{\cdot}\right) = Ga$$

where,

$$Ga = \frac{\rho_L\left(\rho_P - \rho_L\right) g d_P^3}{\mu^2}$$

$$\mathrm{Re}_{mf}^{\cdot} = \frac{d_P u_{mf} \rho_L}{\mu_L}$$

3.1.2 Terminal or Free Settling Velocity

The terminal velocity of a particle is given by the Stoke's equation:

$$u_t = \left[\frac{4 g d_P\left(\rho_P - \rho_L\right)}{3 \rho_L C_D}\right]^{1/2}$$

For spherical particles, the drag coefficient C_D is given by the following equations, depending upon the particle Reynolds number Re_p,

$C_D = 24 / Re_p$ for $Re_p < 0.4$

$C_D = 10 / (Re_p)^{1/2}$ for $0.4 < Re_p < 500$

$C_D = 0.43$ for $Re_p > 500$

where,

Particle Reynolds Number, $Re_P = \frac{d_P \mu \rho_L}{\mu_L}$

3.1.3 Bed Expansion

Wen and Yu (1966), based on their as well as other researchers data, proposed the following correlation for bed void fraction

$$\text{Voidage, } \varepsilon = \left[\frac{18Re_p + 2.7(Re_p)^{1.687}}{Ga} \right]^{1/4.7}$$

where,

Ga = Galileo number and Re_p = particle Reynolds number, as defined above.

The operational range of liquid flow rates can be determined from the minimum fluidization velocity and terminal velocity of the particles. The bed voidage within this operational range is found using Wen and Yu Correlation (1966) which has been used in the model to predict the light intensity reaching a photocatalyst particle surface.

3.2 Light Energy Balance

The mathematical modeling of chemical reactors is based on the coupled heat and mass system balances and on the kinetics of the chemical reaction. Modeling of photochemical reactors presents an additional complication, as the light energy balance has to be taken into account. This new coupling between mass and light energy balances, the latter

depending on the concentrations of reactants and products, incident light distribution, and photon concentration, presents additional difficulties, which are not yet resolved.

The technical development of photochemical reactions involves specific problems due to the necessity to activate by electronic excitation one of the substrates present in a reaction mixture. Thus in addition to the rather well mastered mass and energy balances in conventional process development, optimal light distribution must be achieved, a condition difficult to satisfy when taking into account synthetically meaningful substrate concentrations. Difficulties encountered in up-scaling photochemical reactions are then mainly due to the consequences of the inhomogeneity between irradiated and non-irradiated reaction volumes which are created by the reaction systems particular absorption characteristics and by the light distribution of the chosen light source. Even in a well-mixed reactor, where a thermal reaction would proceed in all parts of the reactor, a photochemical reaction will only take place within the volume where light is absorbed, and no means of mixing will be able to move electronically excited states within their lifetime into the non-irradiated volume.

3.2.1 Radiation Models

Calculations taking into account the strong coupling between the radiant energy conservation equation and the momentum, mass, and heat balances call for a model describing this interaction as function of space and time. According to Braun *et al.* (1993), such radiation models have been in development over the last 30 years, and the published results may be classified in two main categories: incidence models which may be characterized by mathematical models assuming the existence of a given radiant energy distribution in the vicinity of the reactor, and emission models in which lamp characteristics, reaction, and flow processes are taken into account.

Incident models do not make use of all the operating variables, such as radiant power or radiant exitance, diameter, and length of the light source. Models that describe the space of irradiation on the basis of geometry and process variables are known as emission models.

3.2.1.1 Line Source with Parallel Plane (LSPP) Emission Model

The simplest emission model is the line source with parallel plane (LSPP) emission model. In this model the lamp is considered to be a linear source in which each point emits radiation in parallel planes perpendicular to the lamp axis (Figure 3.1).

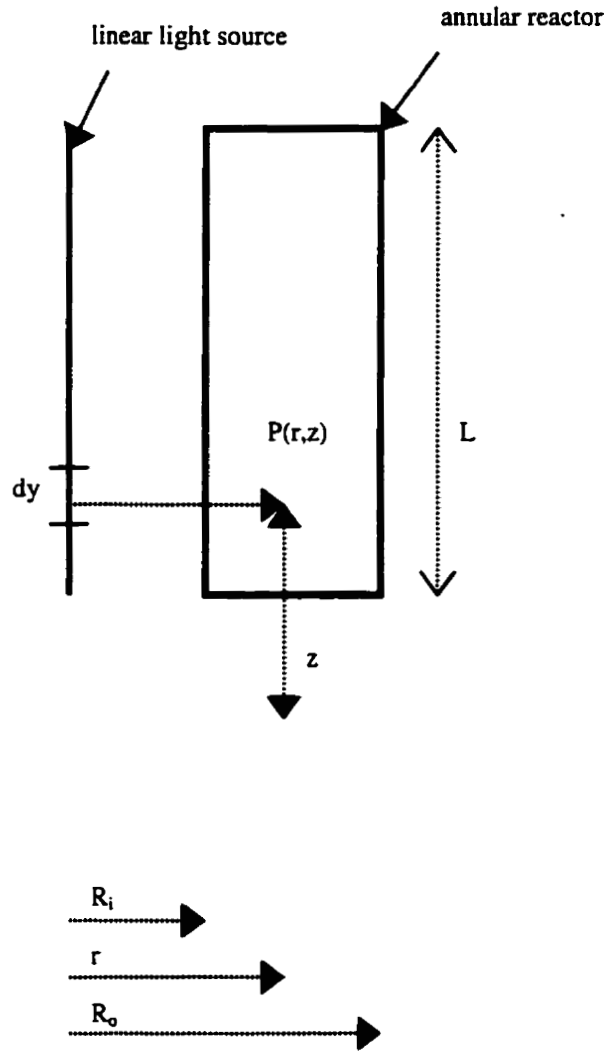

Figure 3.1 Scheme for Line Source with Parallel Plane (LSPP) model
Source: Harris and Dranoff (1965)

Combining this hypothesis with the Beer-Lambert equation, the integration of the differential equation describing the radiant power or irradiance as a function of the optical path yields the profile of radiant power or irradiance.

$$q_\lambda = \frac{S_{L,\lambda}}{2\pi}\frac{1}{r}\exp\left[-\mu_{\lambda,c}\left(r - R_i\right)\right]$$

where, $S_{L,\lambda}$ is the photon rate of the light source per unit length, and R_i is the inner radius of an annular photochemical reactor.

Harris and Dranoff (1965) appear to have been the first to use the LSPP model to study the performance of a photochemical reactor for scale-up purposes. Experimentally, two sizes of perfectly mixed photochemical reactor were used for the decomposition of hexachloroplatinic acid in dilute aqueous solution, and the result of the theoretical analysis was acceptable in comparison with the experimental data.

The highly sophisticated emission models for photochemical reactors include the extense source with superficial emission (ESSE) model in which the light source is assumed to be a surface [Stramigioli *et al.* (1977)], and the equivalent extense source with diffuse superficial emission (ESDSE) model which has been developed to calculate the radiant power profile generated by several superficial light sources. Radiation field modeling for photochemical reactors has been extensively reviewed by Alfano *et al.* (1986) and Cassano *et al.* (1989).

3.3 Kinetic Modeling

Kinetic modeling of the primary degradation steps is essential for any practical application of the process. Rideh *et al.* (1997) showed that 2 - Chlorophenol was degraded in an illuminated suspension of TiO_2 according to the following stoichiometry:

$$2C_6H_4OHCl + 13O_2 \xrightarrow{TiO_2/h\upsilon} 2HCl + 12CO_2 + 4H_2O$$

In order to obtain a greater precision on the kinetic parameters of photodegradation, Rideh *et al.* (1997) measured independently kinetic and isotherm adsorption of 2-CP and oxygen on TiO_2. 2-CP adsorption isotherm can be represented by a Langmuir adsorption

type. At 25 °C, the adsorption constant and maximal adsorbed concentration is respectively,

$K_{2\text{-}CP} = 3600\ m^3 . kmol^{-1}$ and $Q_{max} = 0.107\ kmol . kg^{-1}$

On the other hand, the oxygen adsorption was carried out using a dynamic method. In the studied range, oxygen adsorption obeys the Freundlich isotherm. The Freundlich parameters are respectively

$k' = 1.35 \times 10^{-5}\ mol^{0.62}.g^{-1}.L^{-0.38}$ and $n = 0.38$

A direct measurement of oxygen adsorption on TiO_2 in an aqueous suspension has not been realized so far.

Rideh *et al.* (1997) propose a simple kinetic model:

After electrons and holes were transferred to catalyst surface, they could react with adsorbed species to generate $OH^{\bullet}$ radicals. At stationary state, the rate of formation of holes is equal to the rate of their disappearance.

Results obtained by Rideh *et al.* (1997) show that the reaction rate is proportional to the intensity of light; this is proof that the range of the photonic flux is low. Under these conditions it can be assumed that the photogenerated electron- holes concentration is low.

Al-Ekabi and Serpone (1988) and Pelizzetti *et al.* (1993) have suggested that the rate must include competitive adsorption by solvent and pollutant. Under these reasonable conditions, the reaction rate can be expressed as follows:

$$rate = \frac{k_r^{*} I_{Abs} C_{O_2}^{n} C_{2-CP}}{1 + K_S C_S + K_{2-CP} C_{2-CP}}$$

where K_s and $K_{2\text{-}CP}$ are the equilibrium adsorption constants of solvents and 2-CP, respectively, $C_{2\text{-}CP}$ is the concentration of 2-CP, and C_s is the concentration of the solvent. Moreover, to the extent that $C_s > C_{2\text{-}CP}$ and C_s remains essentially constant, the part of surface covered by the solvent is approximately unchanged for all the reactant concentrations used. Under these conditions, the above equation can be further simplified to:

$$rate = \frac{k_r^{"} I_{Abs} C_{O_2}^n C_{2-CP}}{K + K_{2-CP} C_{2-CP}}$$

where K is equal to $1 + K_s C_s$.

Inserting into the Langmuir-Hinshelwood equation the value of $K_{2\text{-}CP}$ and n determined from dark adsorption measurements, the parameters K and k_r" were evaluated by Rideh *et al.* (1997) by fitting the results obtained at different initial concentrations of 2-CP, at different oxygen concentrations and at different absorbed light intensities. They were found to be $k_r" = 1197.6\ (L/mol)^{1.38}$ and K=2.25.

With these optimized values the representation of their results is less satisfactory than that obtained if they do not fix the order n of oxygen concentration. The optimal value of n found by Rideh *et al.* (1997) was 0.20 and the corresponding values of K and k_r" were:

$K = 2.25$ and $k_r" = 329.60\ (L/mol)^{1.2}$

According to Rideh *et al.* (1997), it should be noted however that the exponent given by kinetic law (n = 0.20) is less than the one measured in the absence of chemical transformation (n = 0.38); it is probable that oxygen adsorption sites are partially covered by intermediate products of the degradation reaction.

With these last values, the rate expression is able to represent very satisfactorily the observed decays of $C_{2\text{-}CP}$ versus time and the observed dependence of the measured

kinetic constant on initial 2-CP concentration, on the dissolved oxygen concentration, and on the absorbed light intensity.

3.4 Energy Balance

The apparent energy of activation obtained by Rideh *et al.* (1997) from the Arrhenius plot was 6.23 kJ/mole. On the basis of energy of activation of 6.23 kJ/mol, a temperatures increase of 103 °C would be required to double the rate constant. This fact showed that the oxidation rate of 2-CP did not change significantly in the range of 15-65 °C (the operational range used by Rideh *et al.* (1997)). They suggest that an expected increase of the reaction rate constant with increasing temperature is possibly compensated by a decrease of the adsorption equilibrium constant. Hence, energy balance has been neglected for the purpose of this study.

3.5 Model Assumptions

A pseudo-plug flow model has been used to simulate the process. A number of discrete plug flow reactors of an annular shape have been considered to represent the reactor. The assumptions used in the development of model are:

i) Complete radial mixing and no axial mixing in the elemental volume.
ii) No mixing between the adjacent annular PFR's.
iii) No reaction in the part of the reactor above the expanded bed (i.e., no direct photolysis).
iv) Even distribution of photocatalyst particles in the expanded bed region.
v) Same inlet concentration to all the annular PFR's.
vi) Complete mixing of the wastewater while effluent is recirculated.

3.6 Model Development

A simple LSPP (Linear Source Parallel Plane) Model has been used to quantify the amount of light intensity reaching the surface of the photocatalyst. This model assumes the lamp to be a linear source in which each point emits radiation in parallel planes perpendicular to lamp axis. Harris and Dranoff (1965) were the first to use the LSPP model and the results of the theoretical analysis were acceptable in comparison with the experimental data. The most sophisticated and extensive model available in literature is the Extense Source with Diffuse Superficial Emission (ESDSE) model, however to avoid in resulting complicated rate expressions, LSPP Model has been used in this study.

The latest study by Rideh *et al.* (1997) provided the data to arrive at intrinsic rate expressions. The Langmuir-Hinshelwood equation based on pre-adsorption equilibrium and surface reaction has been used in the evaluation of kinetic data and mechanisms in photocatalysis by several authors and is universally accepted. The L-H model has been adopted for the purpose of this study.

3.6.1 Elemental Volume

The elemental volume was chosen as a concentric annular ring situated at a distance 'r' from the axis and whose outer radius is 'r + dr' and whose height is 'dz' (Figure 4.2). Complete radial mixing within the small element but no mixing with the adjacent annulus and no axial dispersion has been assumed.

A pseudo-plug flow model has been used to develop the simulator. A number of discrete plug flow reactors of an annular shape have been considered to represent the reactor.

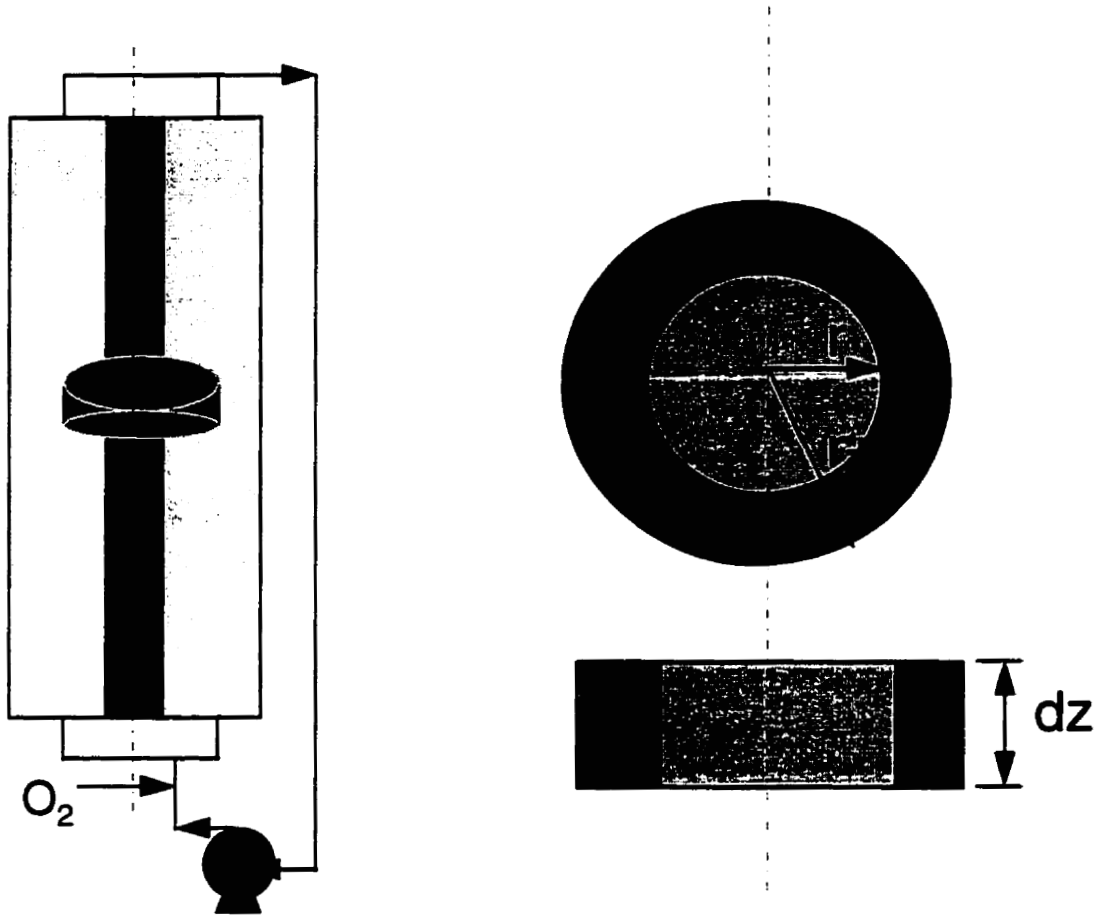

Figure 3.2 Schematic of Photocatalytic Reactor showing the elemental volume

3.6.2 Prediction of Absorbed Light Intensity

Total number of particles in the reactor can be calculated from the voidage and height of bed at minimum fluidization:

$$N_P = \frac{3}{4}\frac{\left(1-\varepsilon_{mf}\right)\left(R_O^2 - R_I^2\right)H_{mf}}{r_P^3}$$

Particle number density in the expanded bed region can be calculated from the total number of particles in the reactor, assuming equal distribution of particles in the expanded bed region.

$$N_{PD} = \frac{N_P}{\pi\left(R_O^2 - R_I^2\right)H_{EX}}$$

Where, the expanded bed height is calculated from the voidage predicted by Wen & Yu Correlation:

$$H_{EX} = \frac{\left(1-\varepsilon_{mf}\right)}{(1-\varepsilon)} H_{mf}$$

Thus, number of particles in the elemental volume can be calculated as:

$$n_P = N_{PD}\pi\left(R_O^2 - R_I^2\right)\Delta z$$

The light intensity incident to the elemental volume under consideration is given by the LSPP Emission Model:

$$I_{Inc} = \frac{S_{L:\lambda}\exp[-\mu(r-R_I)]}{\pi(R_o^2 - R_i^2)}$$

Hence, the net light intensity absorbed by the photocatalyst particles present in the elemental volume is given by:

$$I_{Abs} = \frac{I_{Inc} n_P \pi r_P^2}{2\pi r \Delta z}\alpha\beta$$

where,

α = fraction of particles which are irradiated by the incident photons.

β = fraction of incident light intensity absorbed.

3.6.3 Material Balance for Once Through Process

In the once through process, the photocatalyst undergoes adsorption and regeneration processes simultaneously during fluidized bed and irradiated conditions. Material balance based on the amount of pollutant (2-Chlorophenol) inside the elemental volume can be written at steady state as follows:

[Mass of 2-CP in] - [Mass of 2-CP out] - [Mass of 2-CP degraded by photocatalysis] = [Accumulation]

At steady state, [Accumulation] = 0.

Also,

[Mass transfer of 2-CP from bulk to photocatalyst surface] = [Mass of 2-CP degraded by photocatalysis]

$$Q.(C_i)_{r,z} - Q.(C_i)_{r,z+\Delta z} = A.\Delta z.(rate)$$

$$\frac{dC_i}{dz} = -\frac{(rate)}{U_L}$$

$$\int \frac{dC_i}{(rate)} = -\frac{1}{U_L}\int dz$$

where, the rate expression is evaluated in the same manner as Rideh *et al.* (1997).

3.6.4 Material Balance for Dual Mode Process

In the case of dual mode process, the photocatalyst undergoes dark adsorption followed by regeneration during fluidized bed and UV irradiated conditions. A similar material

balance conducted for 2-CP in the bulk liquid and solid catalyst phase results in a set of ordinary differential equations.

For bulk liquid phase:

$$\frac{dC_L}{dz} = \frac{1}{u} \int k_L a (C_S - C_L)$$

For solid catalyst phase:

$$\frac{dC_S}{dz} = -\int \frac{A}{W} \left[k_L a (C_S - C_L) + k_r k' I_{abs} C_{O_2}^n C_S \right]$$

The liquid-solid mass transfer coefficient was evaluated using the correlation proposed by Hassanien *et al.* (1984):

$$Sh = 0.33 (Ga.Mv.Sc)^{1/3} [1 + 0.22 Mv^{-0.57} (U_G / U_L)^{0.77}]$$

where, Sh is Sherwood number, Ga is Galileo number, Mv is density number, Sc is Schimidt number, U_G is superficial velocity of gas (m/s) and U_L is superficial velocity of liquid (m/s).

3.6.5 Solution of Model Equations

The material balance conducted for the pollutant in the liquid and solid phase in a plug flow reactor (PFR) over the elemental volume at a fixed radial distance resulted in a set of simultaneous first-order ordinary differential equations. The equations were solved numerically using the fourth order Runge-Kutta method to obtain 2-CP concentrations at various axial distances. The above steps were carried out for all the annular PFRs. The values of 2-CP concentrations obtained at the outlet of the reactor were then averaged and formed a new initial concentration to the inlet of the reactor for the next time step. The same procedure was repeated for a number of circulations to obtain 2-CP concentrations

at the outlet of the reactor corresponding to time. For the adsorption cycle, break-through of the photocatalyst bed was considered when more than 95 % of it was saturated. For the regeneration cycle, the bed was considered as regenerated when 99 % of the initial adsorbed concentration was removed from the solid phase due to reaction or transfer to the bulk liquid phase.

3.7 Simulation Results

The dimensions and process variables required as input for the simulations are presented in Table 3.1.

Table 3.1 Dimensions and process variables

Parameter	Value
Mean particle diameter	500 microns
Particle density	3000 kg/m^3
Sphericity of particles	0.67
Viscosity of water @ 25°C	0.001002 kg.m/s
Density of water @ 25°C	998.2 kg/m^3
Molar absorption coefficient	0.01
Reactor length	0.80 m
Inner radius of the reactor	0.06 m
Outer radius of the reactor	0.10 m
Initial bed height	0.45 m
Voidage at min. fluidization	0.49
Oxygen partial pressure	0.575 atm
Recirculation flow rate (regeneration cycle)	27 L/min
Superficial velocity	0.0224 m/s
Residence time	0.595 min
Power emitted by source	1.98×10^{-5} Einstein/m.sec
α (Fraction of particles incident to light)	0.50
β (Fraction of incident light absorbed)	0.75

The model for once through process was run using the above process variables and dimensions. The effect of initial concentration on 2-CP degradation was studied by maintaining the water recirculation rate at 27 L/min (when bed is fully expanded) and the initial 2-CP concentration was varied from 0.0003 to 0.004 mol/L. The effect of oxygen partial pressure on 2-CP degradation was studied by maintaining the water recirculation rate at 27 L/min and an initial 2-CP concentration of 0.0005 mol/L. The results of simulations for the once through process are presented in graphical form in Figures 3.3 and 3.4. The trends obtained with respect to the effect of initial concentration and oxygen partial pressure on 2-CP degradation satisfactorily match those obtained by Rideh *et al.* (1997). However, the values obtained do not match perfectly due to the following reasons: (a) our reactor was much larger than theirs (b) they used the power emitted by the radiation source measured by uranyloxalate actinometry whereas a LSPP model was used in our study to arrive at the light intensity in a particular volume element under consideration (c) difference in the photocatalyst properties such as particle size, particle density, etc.

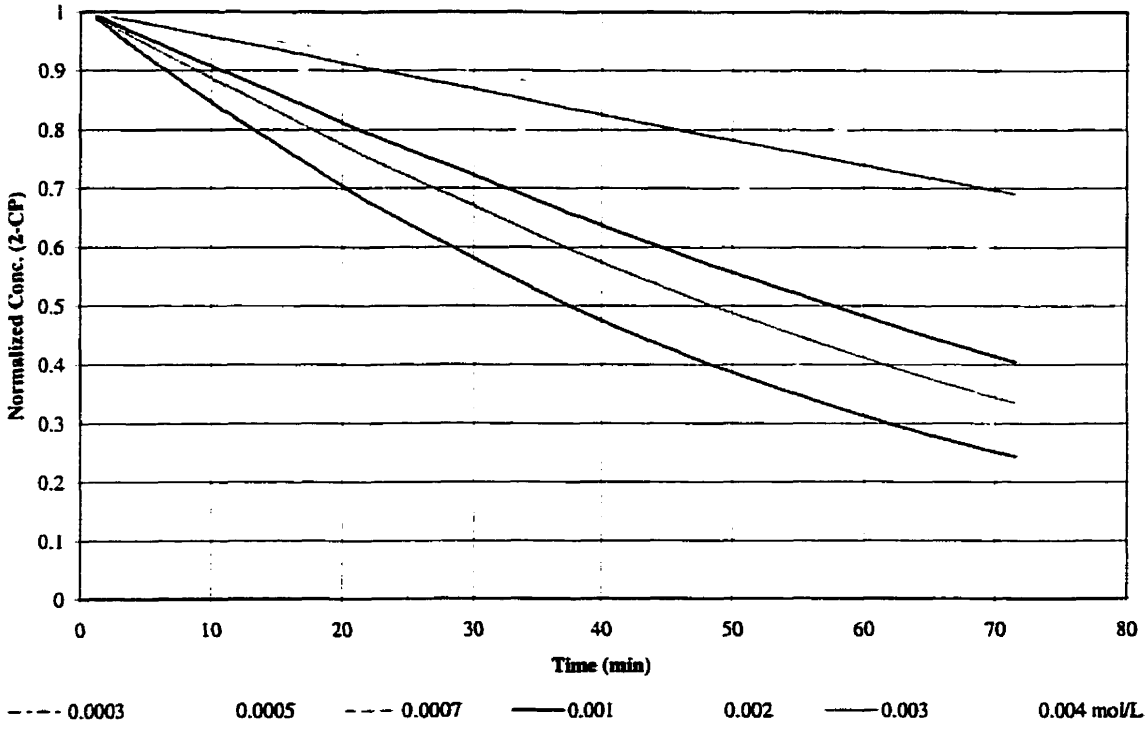

Figure 3.3. Effect of initial concentration on 2-CP degradation

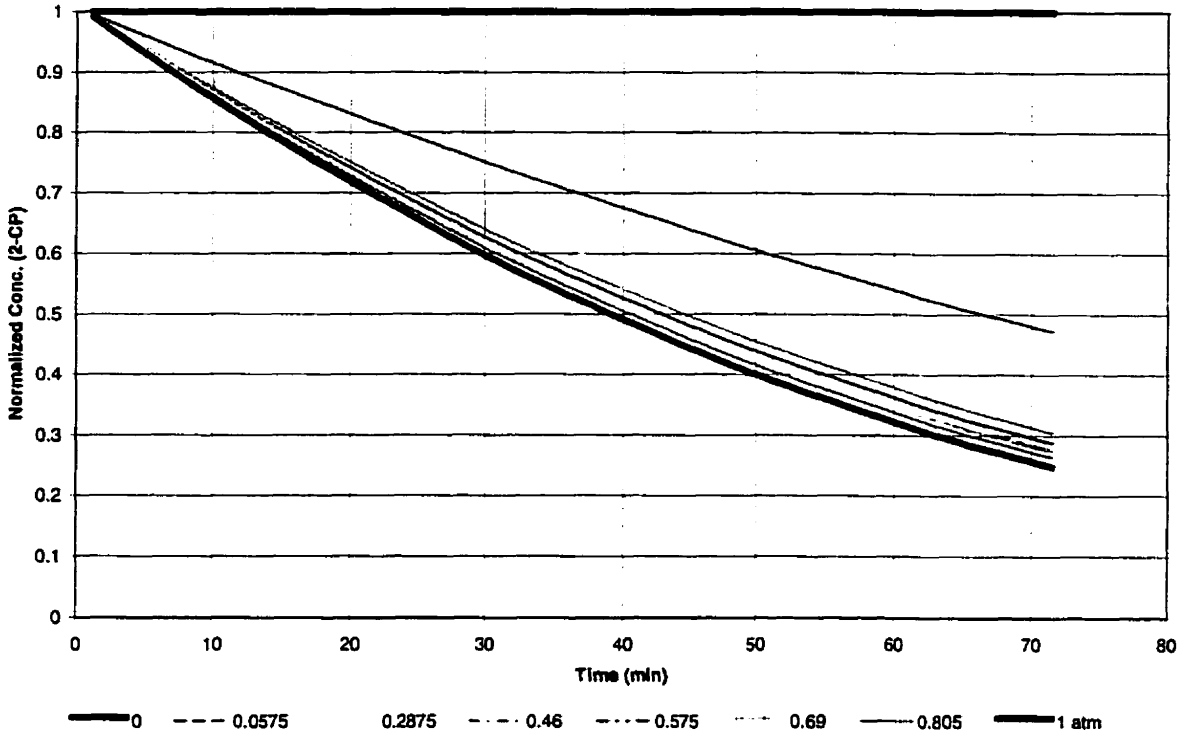

Figure 3.4. Effect of oxygen partial pressure on 2-CP degradation

For studying the effect of operational parameters in the dual mode process, the range of values of various operational parameters used in simulations are presented in Table 3.2.

Table 3.2 Range of values of operational parameters

Parameters	**Values**
Water recirculation rate	9 - 42 L/min
Oxygen partial pressure	0.0575 - 1.0 atm
Power emitted by source	(3.96×10^{-6}) - (9.9×10^{-5}) Einstein/m.sec
Initial bed height	0.1 - 0.65 m

The effect of varying water recirculation rate on regeneration time is depicted graphically in Figure 3.5. There is a pronounced drop in regeneration time required when the flow rate is increased to a value where the bed is fully fluidized, this is because of the fact that

on increasing flow rates, the frequency of exposure of particles to irradiation increases. Also, the height of the bed exposed to irradiation increases and the decrease in particle density facilitates more effective capture of the incident radiation. The decrease in regeneration time is not so pronounced once the bed is fully expanded at a flow rate of 27 L/min, as the only beneficiary factor is the increase in frequency of exposure.

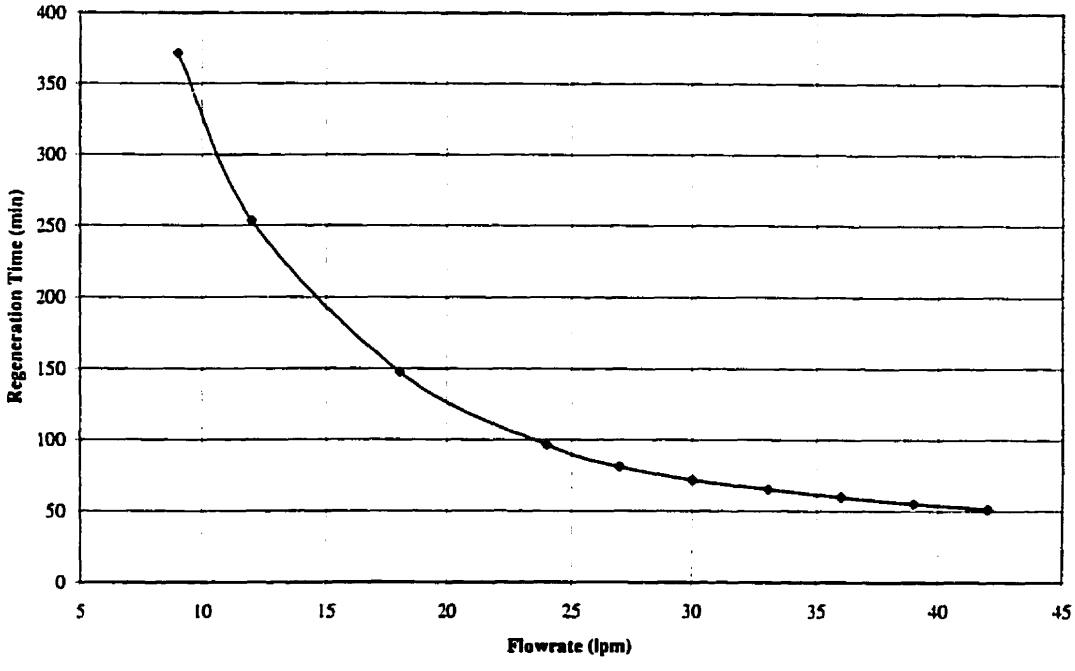

Figure 3.5 Effect of flow rate on regeneration time

According to Figure 3.6, there is a sharp nonlinear decrease in the regeneration time on increasing the oxygen partial pressure. It confirms the fact that the partial pressure of oxygen is a crucial factor in the photocatalytic reaction and the limitation of the rate of photocatalytic degradation is attributed by most researchers to the recombination of photogenerated electron-hole pairs. Since oxygen adsorbed on titanium dioxide surface prevents the recombination process by trapping electrons, it can be inferred that the reaction rate is a function of the fraction of adsorption sites occupied by oxygen. Hence, oxygen adsorption becomes a governing factor at very low dissolved oxygen concentrations.

Results reported in Figure 3.7 show an exponential decrease in the regeneration time required with an increase in the light intensity. The slope decreases after a certain value when it approaches saturation of the catalyst by the incident photons. Since the annular irradiated thickness is quite large in the reactor, it requires a very high intensity lamp to reach saturation. A trade-off depending on the lamp availability and its power requirement has to be investigated to optimize reactor performance.

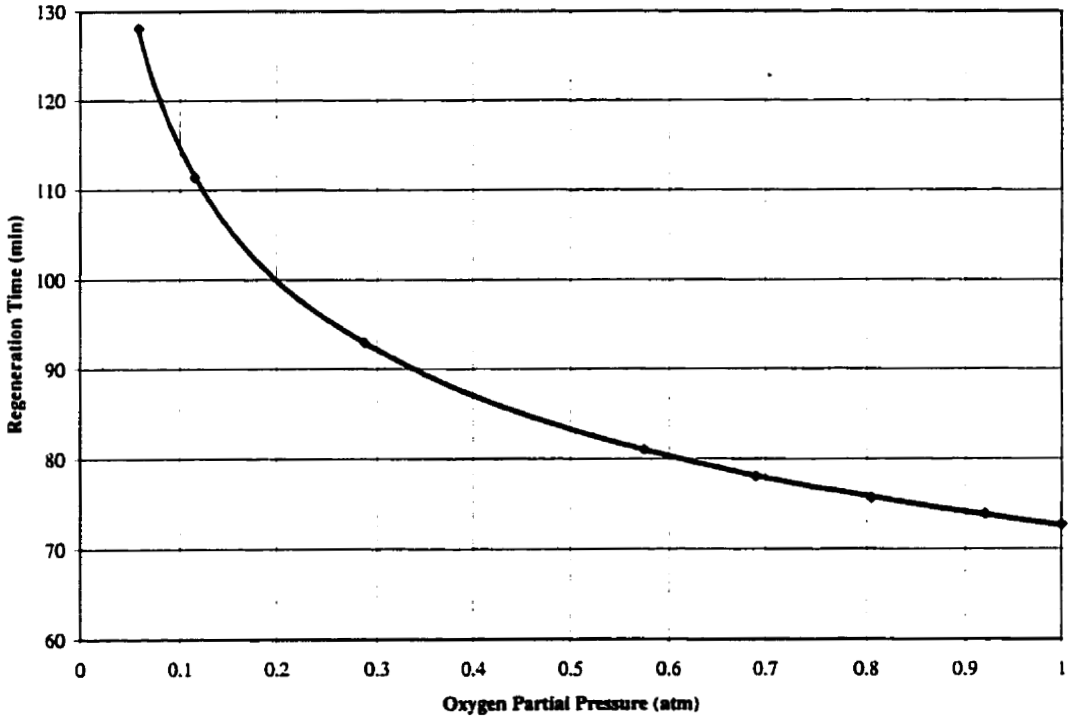

Figure 3.6 Effect of oxygen partial pressure on regeneration time

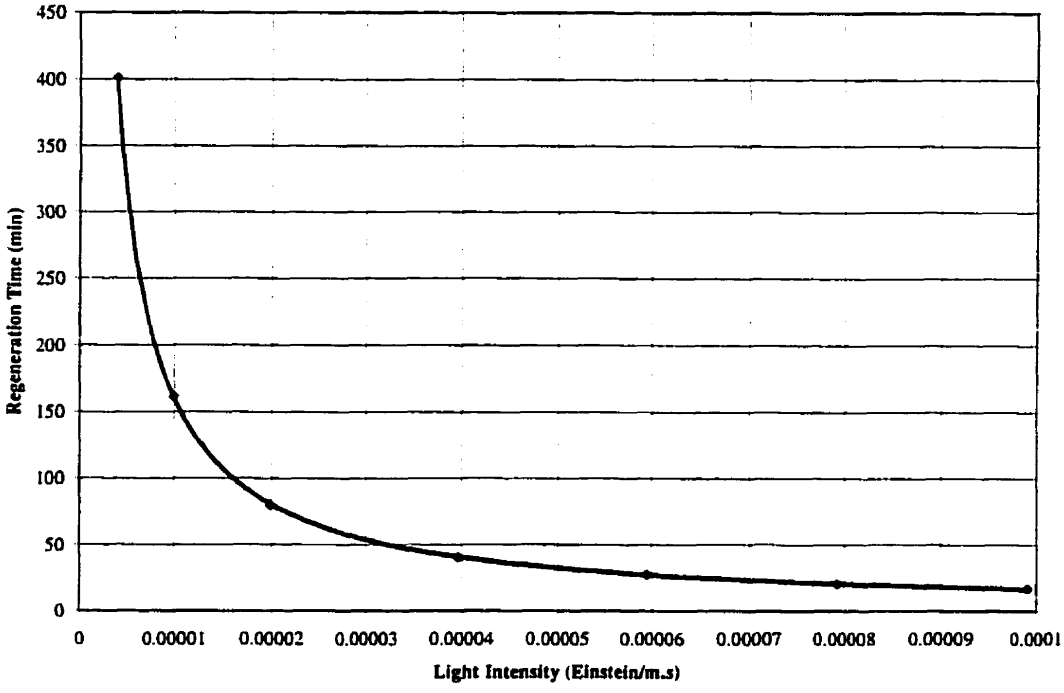

Figure 3.7 Effect of light intensity emitted by source on regeneration time

Simulations were carried out to study the effect of initial bed height on regeneration time and bed exhaust time, keeping the flow rates in both the modes constant at 27 L/min and a pollutant concentration of 0.0005 mol/L in the adsorption phase. The results shown in Figure 3.8 illustrate that there is a linear dependence of bed exhaust time with initial bed height and the slope will depend upon the flow rate and pollutant concentration in the adsorption cycle. The regeneration time is around 80 min and remains about the same for initial bed heights of up to 0.4 m and then increases linearly for higher initial bed heights. This increase in regeneration can be attributed to complete utilization of available photons, the increase in scattering of light and the shielding effect of photocatalyst particles which are closer to the lamp. The water recirculation rate of 27 L/min suffices to raise the initial bed height of 0.45 m to full expansion. The bed exhaust times are more than ten times higher than regeneration times: so, there is a possibility of increasing the flow rates in adsorption by a factor of ten. This can serve to equalize the bed exhaust and bed regeneration times which will facilitate continuous operation of two units in parallel,

one in adsorption and the other one in regeneration phase, switching over from one to another.

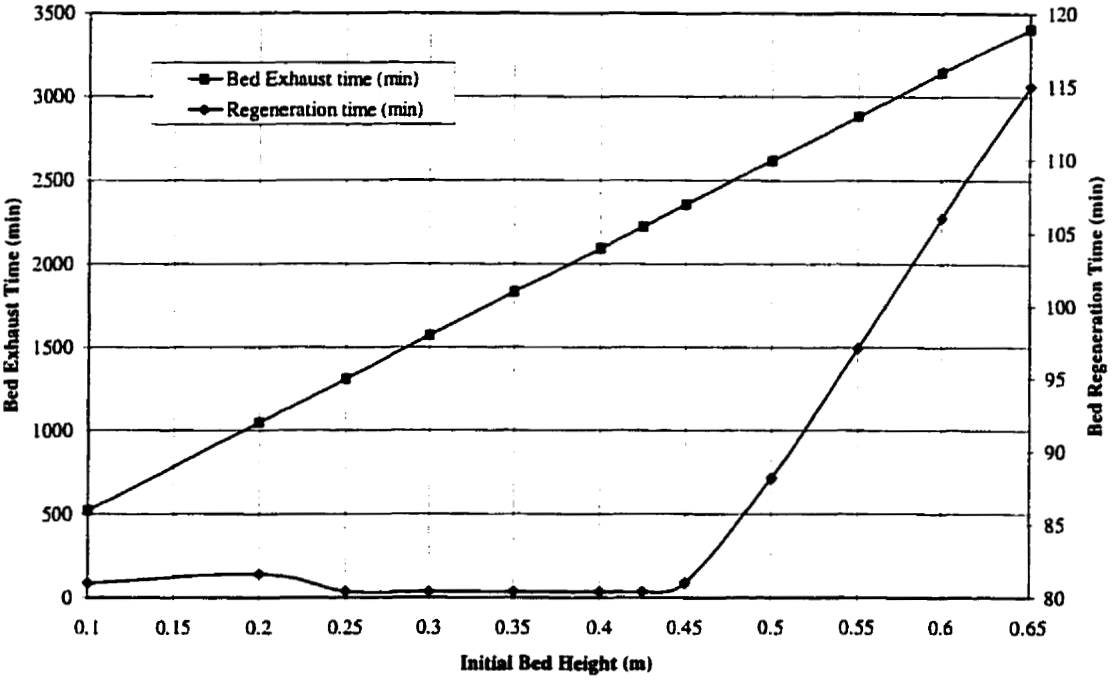

Figure 3.8 Effect of initial bed height on regeneration time and bed exhaust time

CHAPTER 4

Experimental Methods

4.1 Reactor Design and Construction

For heterogeneous photocatalytic reactions the contact among reactants, photons and catalysts must be maximized. Mixing and flow characteristics of the photoreactor may greatly enhance these contacts. If a fixed bed reactor is used, the irradiated aliquot of catalyst is limited to a thin layer and a large reactor volume is required. For the liquid-solid and gas-solid systems, continuously stirred tank photo.reactors and fluidized bed photo reactors, respectively, are the most suitable ones for enhancing contact efficiency even if their operation is quite expensive and troublesome. The rate of photocatalytic reaction is greatly affected by flow rates. The rate enhancement is not due to elimination of mass transport resistances, as expected in classical catalytic systems, since such considerations do not apply for most heterogeneous photo-processes that are characterized by low reaction rate with respect to mass transport rate. The enhancement is determined by the fact that on increasing flow rates, the frequency of exposure of the catalyst particles to irradiation increases. The catalyst particles continuously receive diffuse radiation of reduced intensity due to absorption by other catalyst particles. They are directly irradiated intermittently due to shielding effect of particles that randomly intercept direct irradiation. By increasing flow rates, the frequency with which the catalyst particles may be directly irradiated increases and eventually, the reaction rate is enhanced.

With the above considerations, an annular liquid fluidized bed photocatalytic batch reactor with full recirculation was constructed. In this kind of reactor, the extended light source is placed at the axis of a reactor composed of two coaxial cylindrical tubes. The emitted radiant power is absorbed by the reaction system contained in the annular reactor volume. Irradiance diminishes in a filled reactor with increasing radius. This geometry called the negative geometry of irradiation makes the most efficient use of the light emitted by an extended light source. In fact, this geometry is used in all immersion type photochemical reactors, and most industrial photochemical production units [Braun *et*

al.(1993)]. The detailed design of photoreactor along with its precise dimensions is illustrated in Figure 4.1.

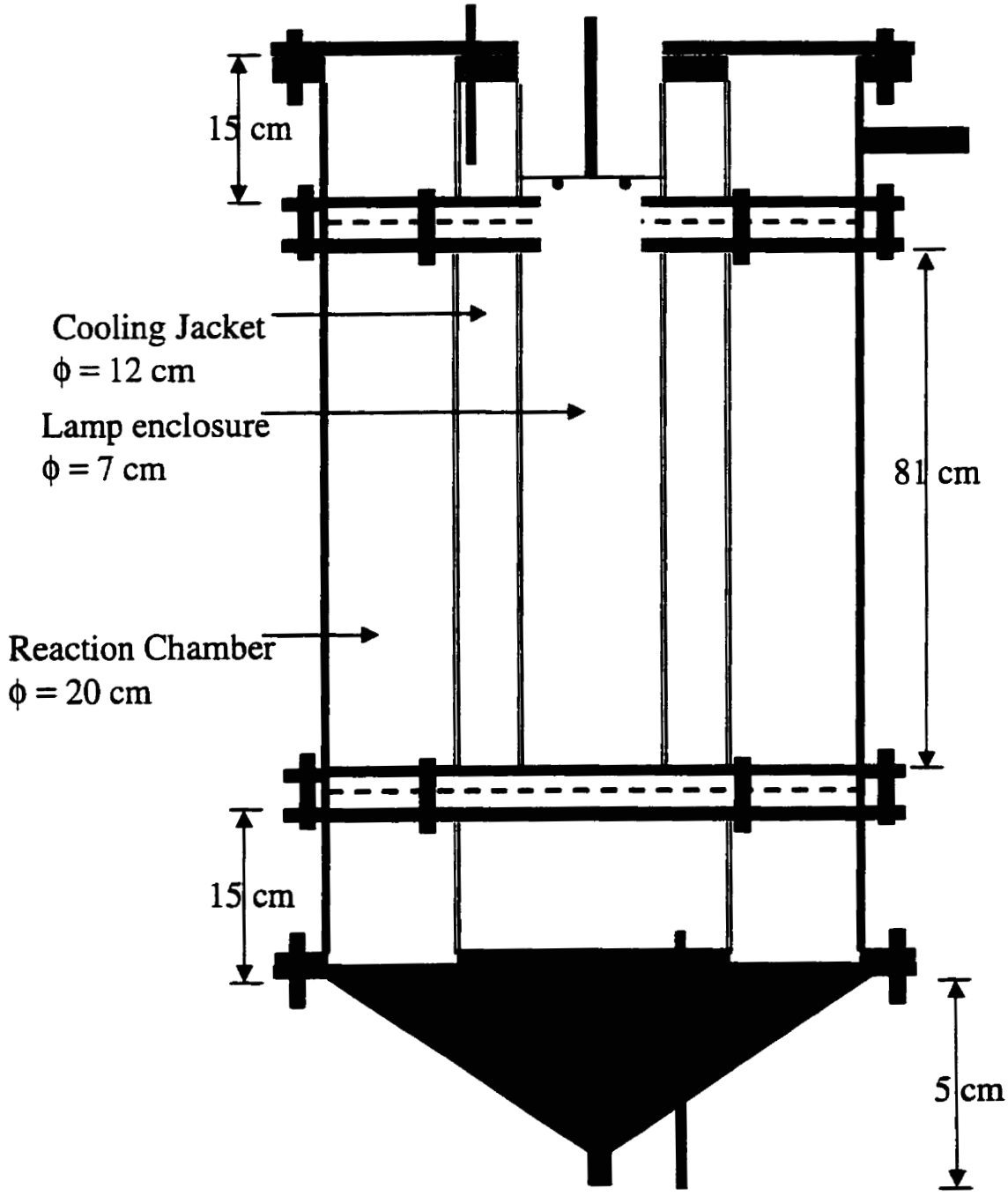

Figure 4.1 Detailed design of photoreactor

The photoreactor consists of an annular reaction chamber, an annular cooling jacket and a lamp enclosure. The innermost lamp enclosure houses the UV lamp, in order to prevent heat build-up, it is surrounded by a cooling water jacket. The UV lamp used is a medium pressure mercury vapor lamp manufactured by Trojan Technologies Inc. which uses a power supply from American Ultraviolet Company drawing 230 V and 40 Amps input. The power supply delivers three different light intensities viz. 100, 200 and 300 W/ inch. The cooling water enters at the bottom and exits at the top. The lamp enclosure and the inside of the annular reaction chamber is made of quartz glass since it practically transmits all UV radiation and offers the advantage of withstanding higher operating temperatures. However, for the purpose of Radioactive Particle Tracking, the quartz glass is replaced by a plexiglass tube of similar dimensions in order to prevent attenuation of gamma radiation. There is a calming section at the bottom of the reactor and a collection section at the top. The reactor has two access ports, one at the bottom center and another one at the top periphery which act as inlet and outlet for water depending upon the reactor's mode of operation. The access ports are equipped with sampling ports. The distributor plate is made up of two circular plexiglass plates with 58 holes of 5 mm diameter each arranged in a triangular pitch and has a Nylon screen of 425 microns size sandwiched between, in order to prevent the back-flushing of photocatalyst particles. A similar structure prevents the photocatalyst particles from entrainment at the top. Nylon bolts have been used in the reaction chamber region in order to eliminate artifacts generated during CT Scanning. The top of the reactor has a vent to expel air from the photoreactor while it is being filled with water. A pressure gauge has been installed at the bottom access port to keep a track of pressure build up in the reactor in an event of mesh clogging due to fines generation during the process. Another in-line mixing port has been provided for injection of hydrogen peroxide at the inlet.

4.2 Photocatalyst Particle Characteristics

The photocatalyst was synthesized based upon the "golf ball" concept where sintered glass beads (SIRAN) were used as the carrier and zeolites and titania were impregnated into the caverns. This provided a good mechanical structure to withstand the attrition encountered during fluidization. The photocatalyst was sieved to remove any fines, a

500μ mesh was used for this purpose. The particle size distribution of the photocatalyst is shown in Figure 4.2.

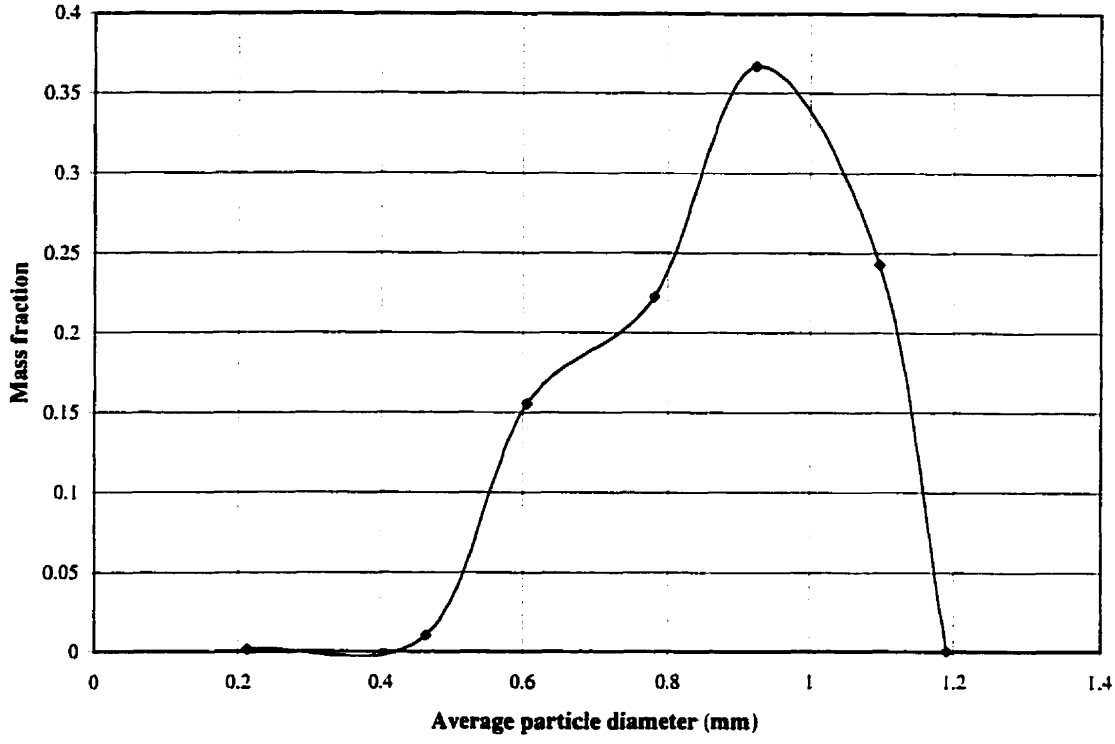

Figure 4.2 Particle size distribution for the photocatalyst

The dry bulk density and wet bulk density of the photocatalyst in water were 766 kg/m^3 and 1416 kg/m^3 respectively. The mean particle diameter was found to be 880 μ and the wet particle density was 2000 kg/m^3. Some of the other characteristics of SIRAN provided by the supplier were: pore volume of 55-60%, pore diameter < 120 μ and surface area of 27,450 ft^2/ft^3.

4.3 Ultra Violet Lamp

The UV Lamp used in the study was a Medium Pressure Mercury Vapor Lamp supplied by Trojan Technologies Inc., London, Ontario. The UV Output of the lamp corresponding to different wavelengths is depicted in Figure 4.3.

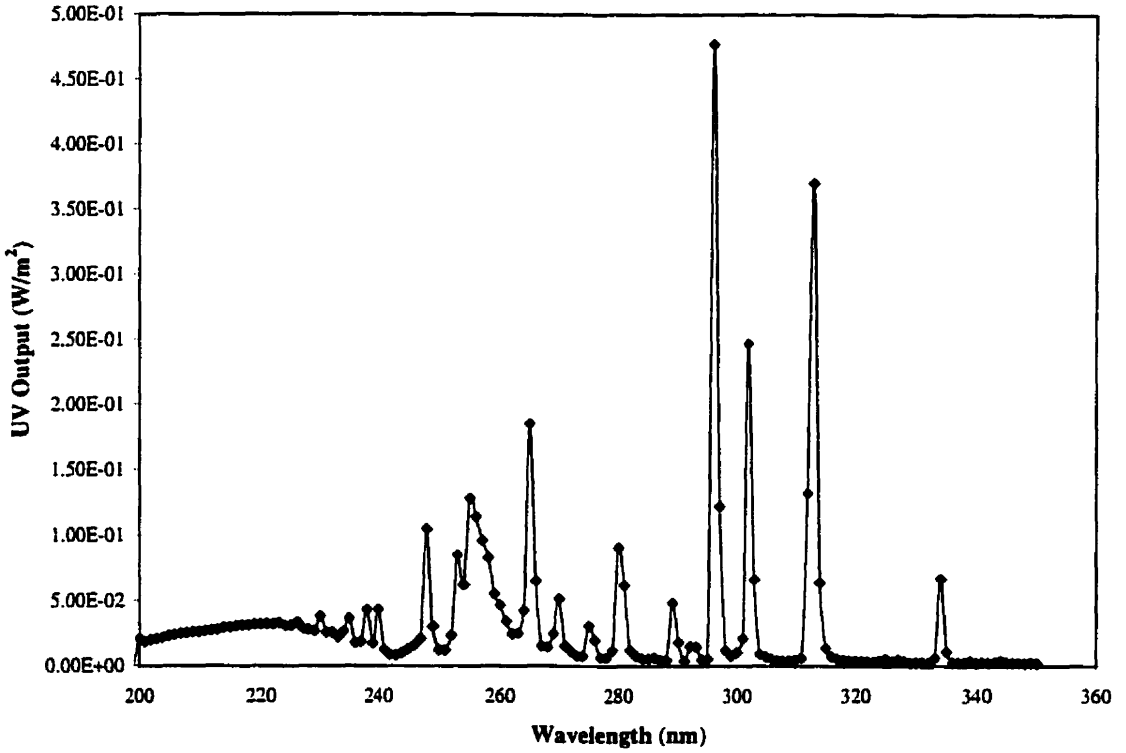

Figure 4.3 UV Output of the Medium Pressure Mercury Vapour lamp

Source : Trojan Technologies Inc., London, Ontario

4.4 Experimental Set-up

A schematic of the experimental set-up with flow patterns in the adsorption and regeneration cycles is depicted in Figure 4.4. The experimental set-up consists of a Goulds NPE close coupled, end suction, single stage centrifugal pump with a recirculation line for flow regulation and a tank to facilitate storage of water for use during regeneration and adsorption cycles. The tank is provided with a number of spargers in order to maintain dissolved oxygen concentration in water at desired levels. Air supply from a compressor is used to achieve this purpose. A flowmeter panel comprising of three in-line variable area flowmeters (Cole Palmer) of different ranges fitted with valves was used in order to measure the water flowrate for a wide range of flows with better accuracy. All the connections from the pump to the flowmeter panel, to the photoreactor and recirculation to the tank are of flexible rubber hoses.

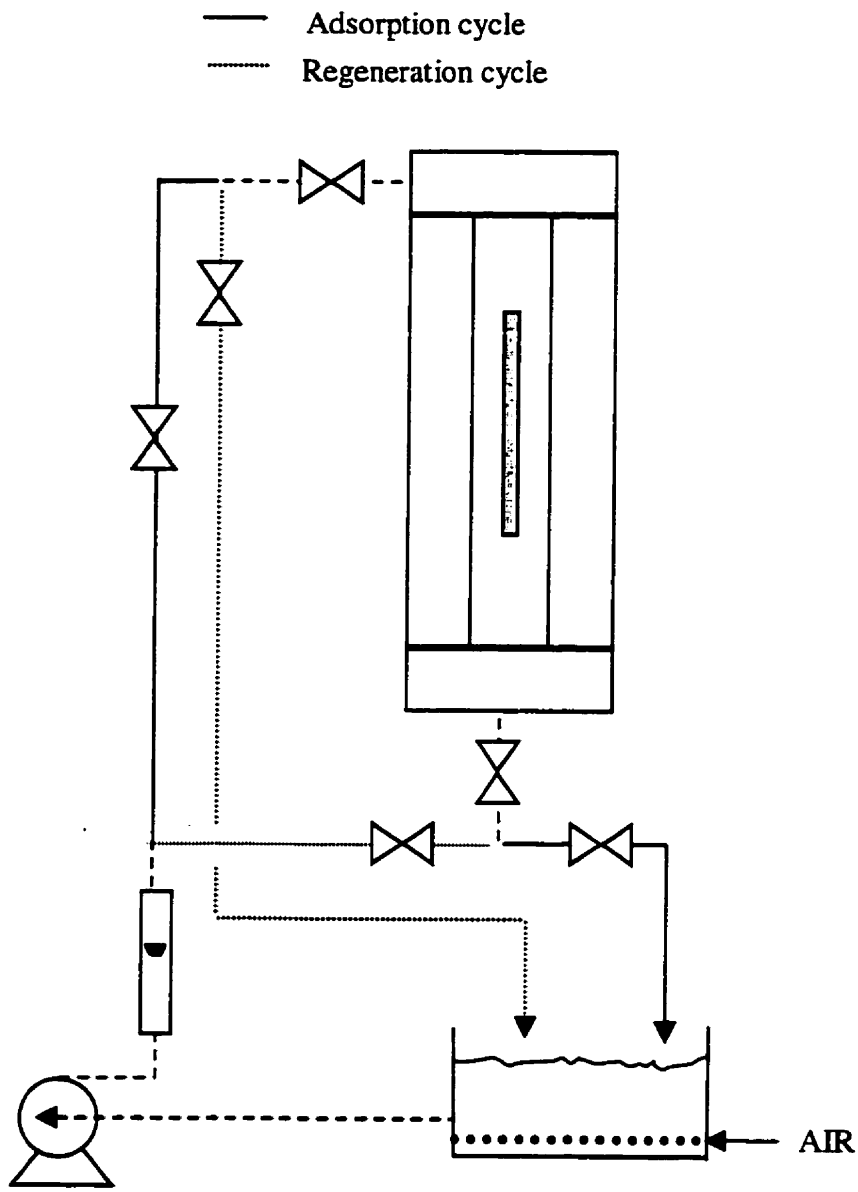

Figure 4.4 Schematic diagram of the experimental set-up

4.5 X-ray Computer Assisted Tomography

Computer Assisted Tomography (CAT or CT) is a tomographic imaging technique that generates cross-sectional images in the axial plane. The images produced are maps of the relative linear attenuation values of objects. For a fixed position of the x-ray tube, a fan beam is passed through the object and measurements of transmitted x-ray beam intensities are made by an array of detectors. Measured x-ray transmission values are

called projections. CT images are derived by mathematical analysis of multiple projections. The relative attenuation coefficient is normally expressed in Hounsfield units (HU) which are also known as CT numbers. The CT number for water is 0 and the value for air is –1000.

Generating an image from the data acquired requires determining the linear attenuation coefficients of the individual pixels. A mathematical algorithm takes the projection data and reconstructs the cross-sectional CT image. Most modern scanners use filtered back projection image reconstruction algorithms. Image reconstruction involving millions of data points may be performed in seconds using array processors. Different filters may be used in filtered back projection reconstruction, offering tradeoffs between spatial resolution and noise.

Reconstructed images can be viewed on CRT monitors. Window width and level are used to optimize the appearance of CT images by determining the contrast and brightness levels assigned to the CT image data. Window level, or center, is the CT number to be displayed as the medium intensity in the image. Window width is the range of CT numbers displayed around the selected center and, therefore, determines contrast. A narrow window width provides higher contrast than a wide window width.

Fourth generation scanners have a rotating tube and fixed ring of detectors in the gantry. They typically acquire a single section in 1 or 2 seconds. The x-ray beam is collimated as it exits the tube and again before it strikes the detectors. Collimating defines the section thickness and reduces scatter. Adjustable collimators allow section thickness to range between 1- 10 mm. The detectors used in fourth-generation scanners are solid-state detectors, the most common being cadmium tungstenate ($CdWO_4$).

CAT scanning experiments were run using a fourth generation x-ray CAT scanner (EMI 7070) that has been modified to perform scans on vertically placed objects. A schematic of the CT-Scanner set-up is presented in Figure 4.5. The spatial resolution can be as low as 0.2 mm by 0.2 mm in cross section and the temporal resolution as low as 2 seconds.

This scanner represents a notable improvement over previously reported equipment [Kantzas *et al.* (1997); Kantzas and Kalogerakis (1996)]. The algorithms and methods of analysis presented previously [Kantzas *et al.* (1997); Kantzas and Kalogerakis (1996)] were also used here with minor modifications. Data was acquired by scanning the bed using a slice thickness of 1 cm at various heights spaced 1 cm along the column and at various superficial velocities.

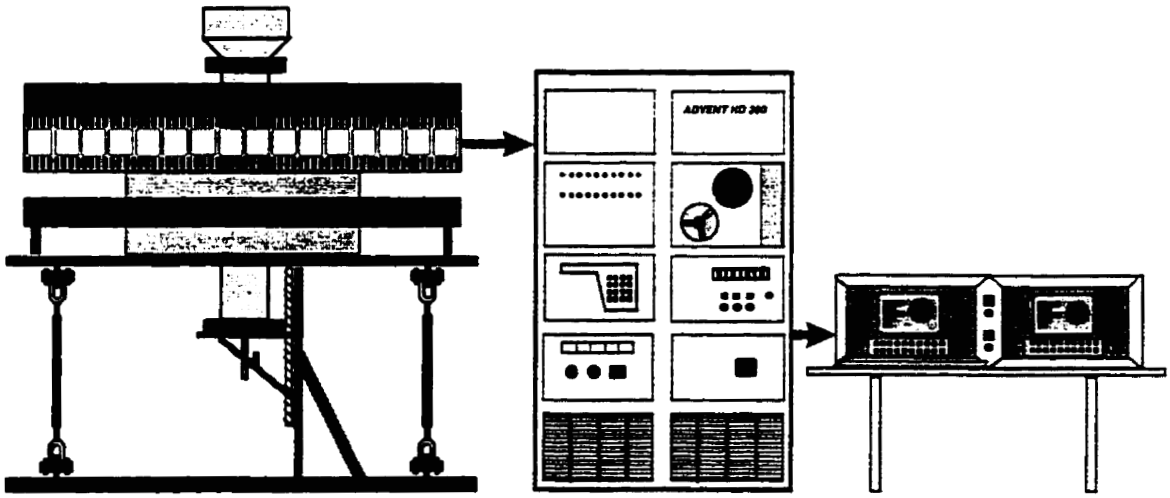

Figure 4.5 Schematic of CT-Scanner set-up

4.6 Radioactive Particle Tracking

Radioactive particle tracking experiments were performed using a gamma-camera system [Hamilton *et al.* (1997); Kantzas *et al.* (1999)] in a manner similar but with an improvement to the work reported earlier [Castellana and Duddley (1984)]. There are a number of different types of gamma cameras available on the market but the principle of operation remains the same. The two cameras available in our laboratory are Siemens Orbiter and ZLC, each one of them has 75 photomultiplier tubes (PMT) and a NaI crystal diameter of 41 cm. The gamma camera is designed to detect gamma radiation. The gamma rays originate from a radio-labeled particle. The camera has the ability to detect the distribution of radioactivity. This is accomplished by recording the emissions from the radioactivity with an array of detectors (PMT) placed inside the camera head.

The collimator projects a gamma ray image onto the NaI(Tl) detector crystal, creating a pattern of scintillation in the crystal that outlines the distribution of radioactivity in front of the collimator. An array of PMT viewing the back surface of the crystal, and a series of electronic position logic circuits, determine the location of each scintillation event as it occurs in the crystal. Individual events are also analyzed for energy by pulse-height analyzer circuits. When an event falls within the selected energy window, the electron beam in a cathode ray tube (CRT) display is deflected by X- and Z- position signals to a location on the CRT face corresponding to the location at which the scintillation event occurred in the crystal. The beam is turned on momentarily, causing a flash of light to appear at that point on the display. Therefore, the CRT display shows a pattern of light flashes corresponding to the pattern of scintillation events occurring in the detector crystal [Sorenson and Phelps (1987)].

The gamma camera is capable of producing different types of images - static, dynamic and single photon emission computed tomography (SPECT). In static imaging studies, an image of an unchanging distribution of radioactivity can be recorded over an extended imaging time. It can be used for dynamic imaging studies in which changes in the distribution of radiation can be observed. As soon as the acquisition of the first frame is complete, it immediately begins to collect a second image on the next frame and so on until the desired number of frames is reached. The images produced with these two methods of acquisition are two-dimensional and can either be recorded directly onto film or they can be acquired and stored by a computer. Some software packages also have the ability to generate 3D images from a dynamic series. True 3D images can be produced using SPECT imaging. With this type of acquisition, the head of the camera physically orbits the object of interest taking a series of static images at different angles. From these 2D images, a 3D image can be produced using computer software. With the advent of SPECT, computers have become indispensable in reconstructing the images obtained. Reconstruction algorithms are used to assimilate all the images and reconstruct them into 3D images from which tomographic slices can be made at any level and in any direction. There is a variety of medical imaging software packages on the market. The software available in our laboratory is Macintosh NucLear Power (NucLear MAC).

The NucLear MAC gamma camera computer is a high performance system for acquiring, displaying and processing nuclear medicine images. It provides the performance expected from modern nuclear computers, but with the ease-of-use associated with the Macintosh II family of computers. The software follows the standard Macintosh user interface guidelines. It operates through the familiar menus, windows, mouse controls, and dialog boxes. The NucLear MAC supports the standard image formats of the Macintosh (Interfile, PICT, TIFF) so images can be displayed using other standard programs.

The output from the gamma camera is analog and must therefore be converted to a digital form by an analog to digital converter (ADC). After the X- (horizontal) and Z- (vertical) position signals of the gamma camera are digitized, their position values are used to generate images. This is achieved by storing the X- and Z- values in a buffer (500 counts) on the interface board and are then placed in computer memory. After a certain number of these pairs of values are stored, they are read from memory and used to update the image. Each pair represents a location on the image, and when a particular pair is read, the brightness of the pixel at the corresponding position is increased by one. One thousand to 10,000 points are stored in memory between image updates. Because this amount of data buffering represents only a fraction of a second, the images appear to form in nearly real time. This process is performed until a desired number of counts or total acquisition time is reached.

The Siemens Orbiter gamma camera can provide images of the radioactive particle in two dimensions with resolution that can be as low as 2.6 mm at sampling frequency as high as 1000 Hz. Radiopharmaceuticals are used to tag particles that are subsequently used for the particle tracking experiments. Three-dimensional images can be acquired by using the two gamma cameras available in our lab, positioned perpendicularly to each other. The schematic of Radioactive Particle Tracking system set-up is illustrated in Figure 4.6.

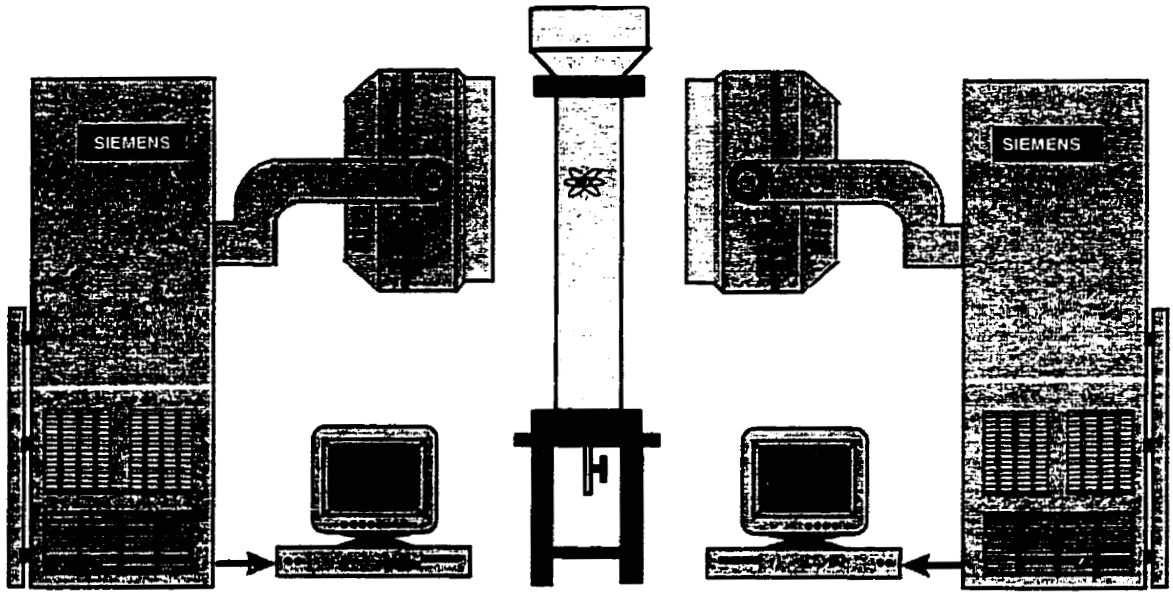

Figure 4.6 Schematic diagram of RPT set-up

Particle tracking experiments for the photocatalyst were performed by tagging a given particle with Technetium macroaggregated albumin (^{99m}Tc-MAA). The choice of radio-pharmaceuticals as opposed to other approaches in the literature was taken so that short half-life material could be used for the tests thus eliminating the need for sophisticated disposal methods. Furthermore, the use of commercially available imaging systems eliminates the need for custom-made software and hardware development.

Each experiment is performed with the placement of the column that includes the radioactive particle in front of the camera. The field of view is circular with a diameter of 41.0 cm. The camera acquires images of the field of view and stores them in arrays of specified sizes. The arrays used in this work are 128 by 128 elements. The resulting pixel size of 3.2 mm is the level of uncertainty for the location of the particle. Updated images with the location of the particle are obtained with a frequency of 20 Hz. The choice of frequency depends on the activity of the radioactive particle. Every time an update is done, the image is stored in the computer that is interfaced with the camera. The maximum size for the data file is 1000 frames. Thus, for every experiment, data is stored and saved in files with 1000 sequential frames. This is translated into time periods of 50 seconds per data set. At this point, the computer file must be closed and a new file

must be opened. By following this procedure, data was collected using both Gamma cameras simultaneously over several hours and at variable water velocities.

4.7 Reaction Experiments

Three reaction experiments were carried out to prove the technology in principle. The experiments were conducted to study the effect of the presence and absence of oxygen, hydrogen peroxide and acid on degradation of phenol in the photocatalytic reactor. Also, adsorption of phenol on the photocatalyst and the effect of using fresh water or contaminated water for regeneration were studied in the reactor. Phenol detection was conducted using a HPLC in Department of Chemistry. UV-Visible Spectrophotometer was also used to detect the presence of intermediates and confirm the degradation of phenol. Photocatalyst samples were collected and analyzed to determine the phenol residuals.

CHAPTER 5

Results and Discussion

5.1 CT Scanning Results

CT scanning experiments were conducted using a fourth generation x-ray CAT scanner (EMI 7070) that has been modified to perform scans on vertically placed objects. The specifications of the particular technique used for image acquisition were: 120kV, 50 mA, 3 seconds scan time and the field of view was circular with 250 mm diameter. The images were acquired back to back along the column height with a slice thickness of 10 mm. These scans were repeated for a fixed bed or settled bed i.e. no flow condition and five different superficial velocities. Acquired images were analyzed based upon the calibration generated for the particular technique, which is presented in Appendix A. All the analysis was carried out utilizing software developed in-house. Mean and standard deviation of voidage along column height, voidage maps, radial distribution and frequency distributions of voidage were obtained as a result of data analysis.

Results for voidage maps, frequency distribution, radial distributions of voidage for settled bed and superficial velocities of 1.0-2.3 cm/s in the distributor region (3 cm above the distributor) are presented graphically in Figure 5.1 through Figure 5.6 respectively. Settled bed shows a very uniform voidage except the wall effect, which is more predominant on the inside wall of the reactor. In general, as the superficial velocity increases, range of radial distribution of voidage broadens and the curve shifts higher i.e. towards greater voidage, as expected. In settled bed, the voidage varies from 0.2 to 0.6 with most part having a voidage in the range of 0.2 to 0.3. As the superficial velocity is increased, voidage is between 0.2-0.4 near minimum fluidization and goes on increasing to reach 0.5-0.7 range at higher superficial velocities. The voidage maps give a clear picture of the effect of superficial velocity on voidage and the distributor effect is quite noticeable in this region. The frequency distribution curves are bimodal in nature. All the frequency distributions show two noticeable peaks, one where most of the voidage lies and a smaller one depicts the wall region. As the superficial velocity increases, the frequency

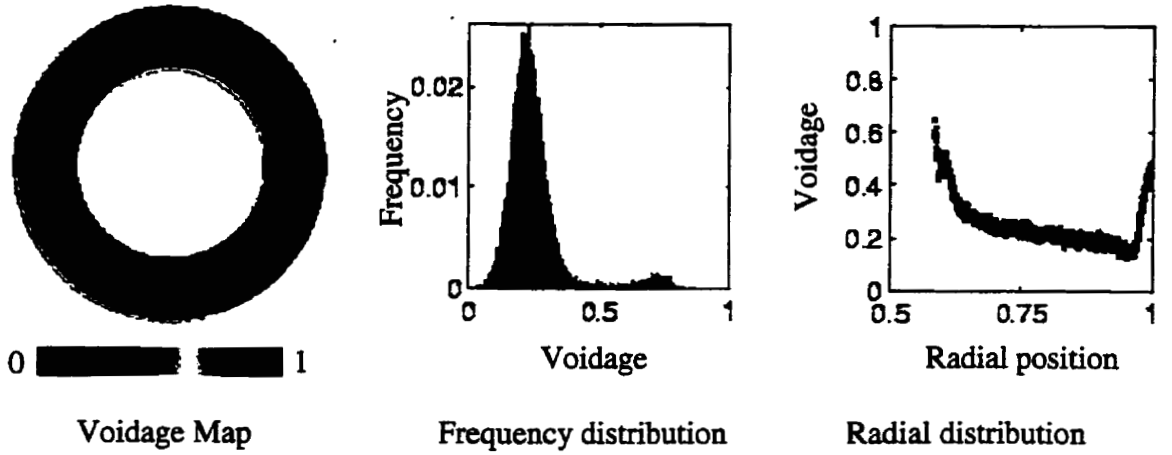

Voidage Map | Frequency distribution | Radial distribution

Figure 5.1 Settled bed in distributor region

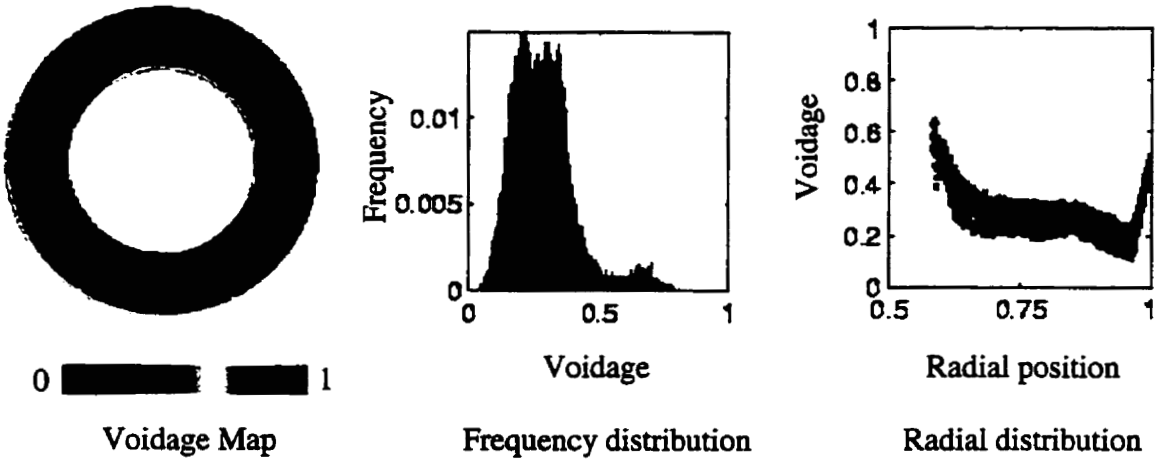

Voidage Map | Frequency distribution | Radial distribution

Figure 5.2 Near-Fluidized bed (U_s=1.00 cm/s) in distributor region

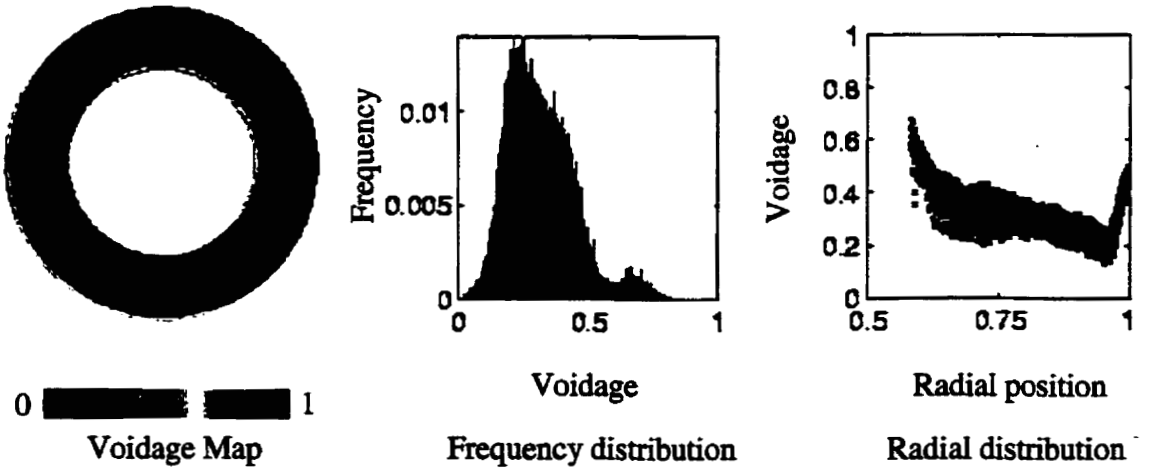

Voidage Map | Frequency distribution | Radial distribution

Figure 5.3 Fluidized bed (U_s=1.33 cm/s) in distributor region

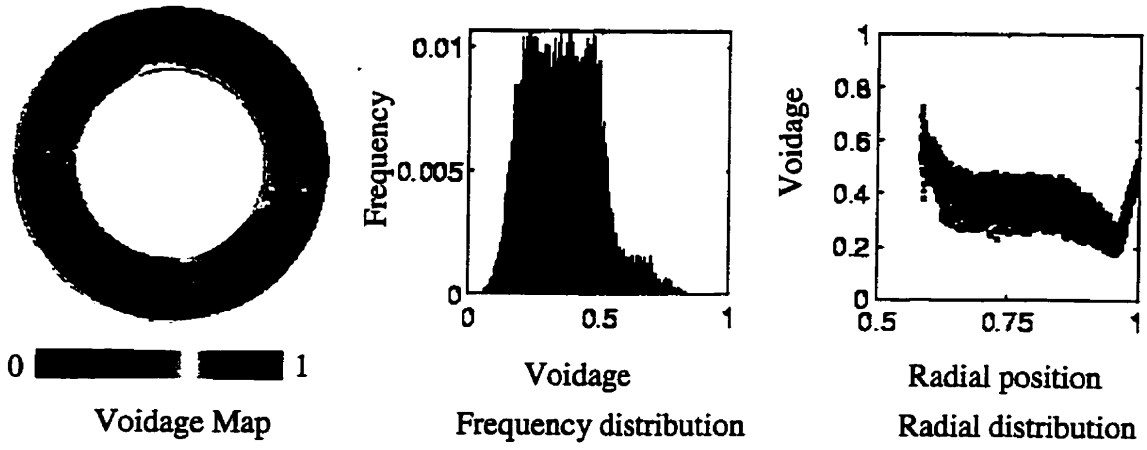

Figure 5.4 Fluidized bed (U_s=1.66 cm/s) in distributor region

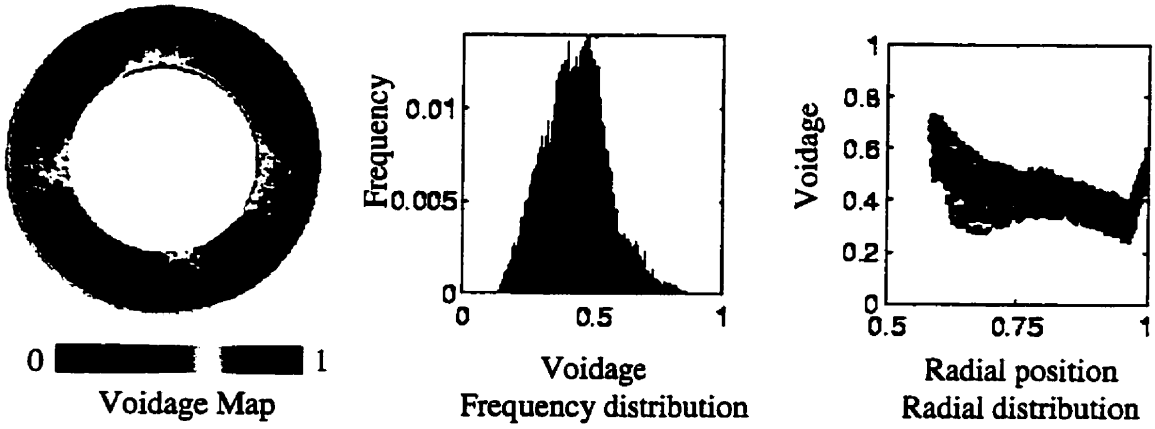

Figure 5.5 Fluidized bed (U_s=2.00 cm/s) in distributor region

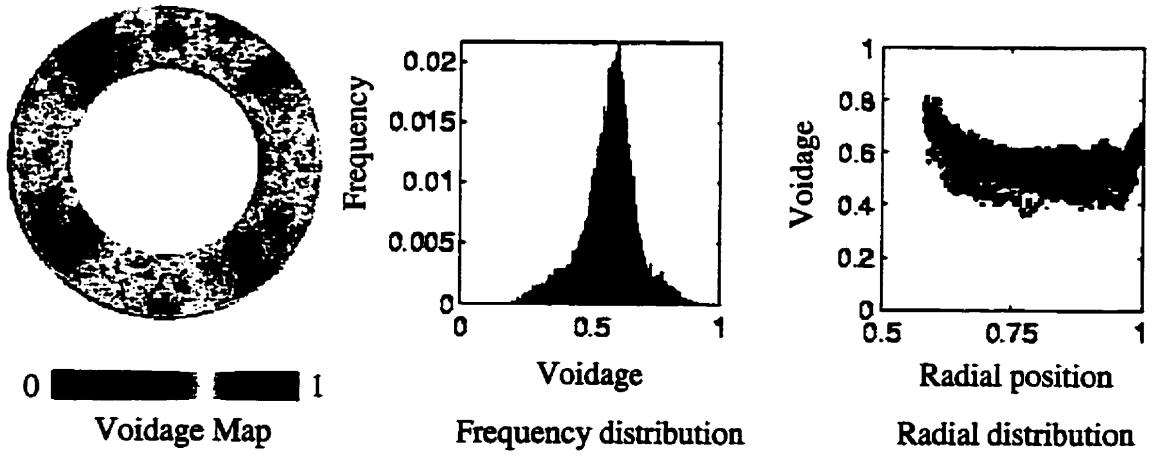

Figure 5.6 Fluidized bed (U_s=2.32 cm/s) in distributor region

distribution curve for voidage broadens and shifts towards higher voidage and then starts shrinking again at higher velocities. This observation may be attributed to better mixing at higher superficial velocities, which leads to an even voidage distribution. Also, the temporal resolution of the CT Scanner is 3 sec., which results in a time-averaged image of very fast moving particles within a pixel showing up as a smoother image.

The results for voidage maps, frequency distribution, radial distributions of voidage for settled bed and superficial velocities of 1.0-2.3 cm/s in the fully developed flow region (10 cm above the distributor) are presented graphically in Figure 5.7 through Figure 5.12 respectively. The settled bed shows a very uniform voidage similar to the one in the distributor region. As the superficial velocity was increased, the range of radial distribution of voidage broadened slightly, however it is not as pronounced as in the distributor region. The curve shifts higher i.e. towards greater voidage, starting from 0.2-0.3 in the settled bed, increases to a voidage of 0.3 near minimum fluidization and goes on increasing to reach 0.5-0.6 range at higher superficial velocities. The voidage maps give a clear picture of the effect of superficial velocity on voidage. These voidage maps show the disappearance of any distributor effect and we can safely conclude that the fluidization is smooth and uniform in this region. A study of other voidage maps obtained at various heights in the column and at various superficial velocities also supports this fact. Rest of the results obtained at other heights and superficial velocities are presented in Appendix B through Appendix G. The frequency distribution curve in all cases is of similar nature and has two noticeable peaks, one where most of the voidage lies and a small one depicting the wall region. As the superficial velocity increases, the frequency distribution curve for voidage slightly narrows and shifts towards right depicting higher voidage, which is quite different as compared to the distributions in the earlier case.

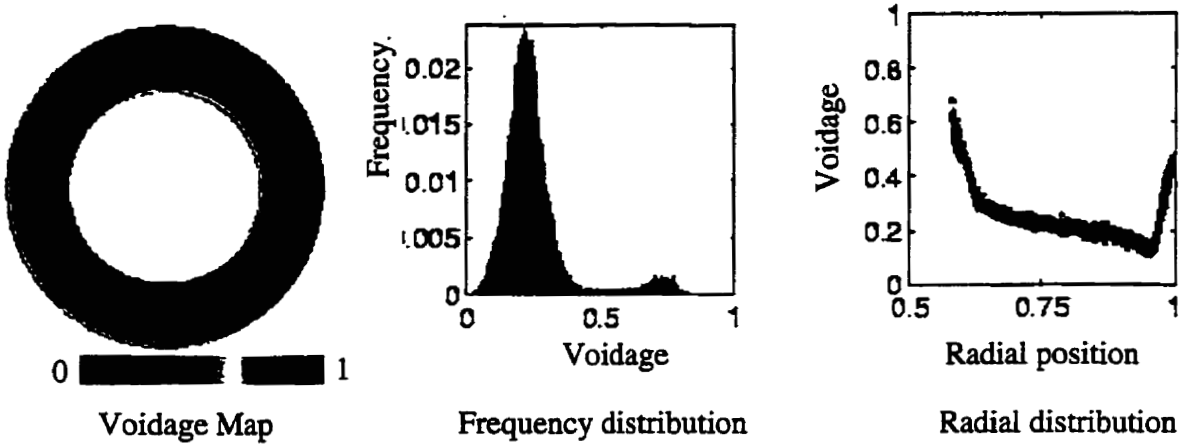

Figure 5.7 Settled bed at 10 cm. above distributor

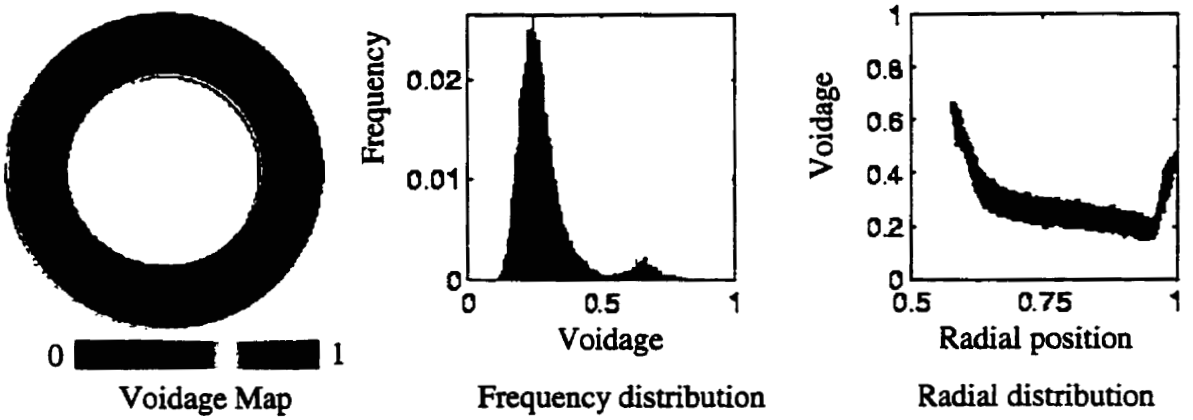

Figure 5.8 Near-fluidized bed (U_s=1.00 cm/s) in fully developed flow region

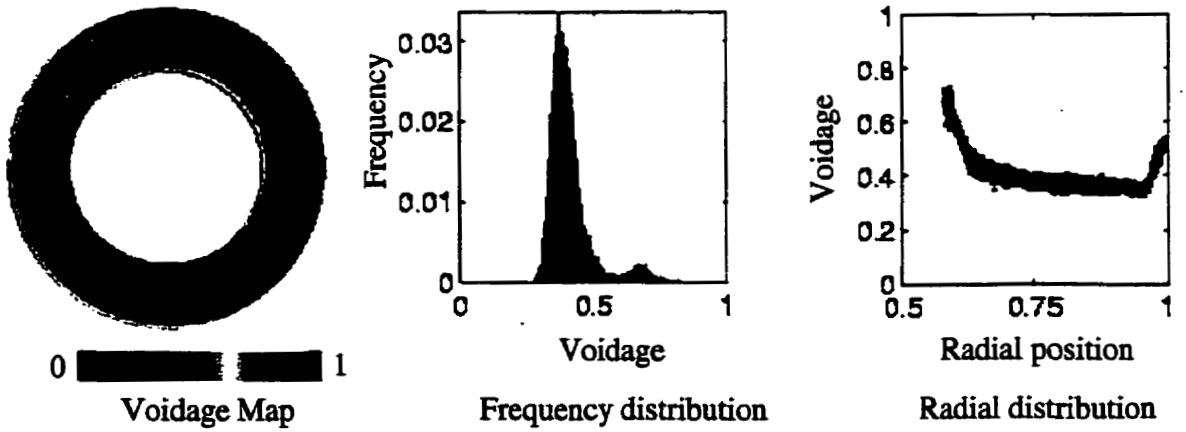

Figure 5.9 Fluidized bed (U_s=1.33 cm/s) in fully developed flow region

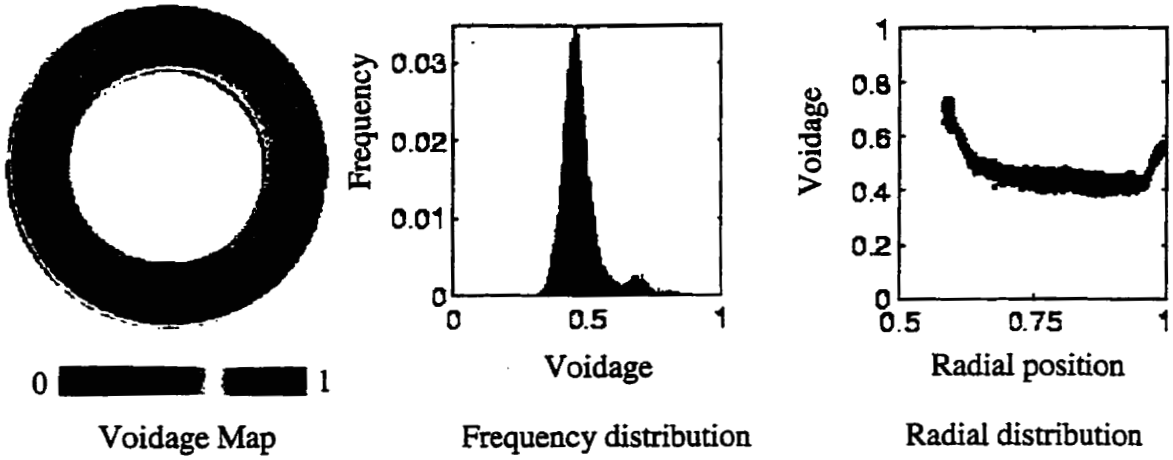

Figure 5.10 Fluidized bed (U_s=1.66 cm/s) in fully developed flow region

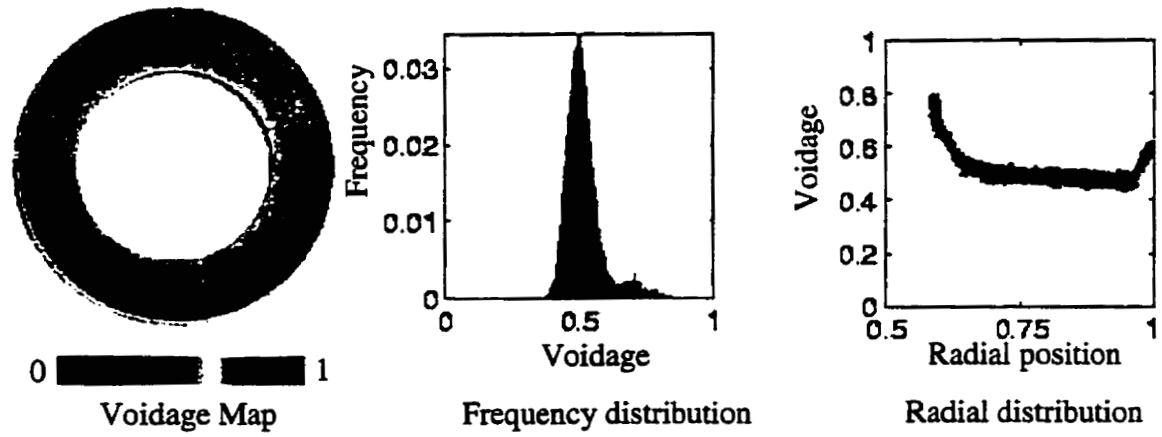

Figure 5.11 Fluidized bed (U_s=2.00 cm/s) in fully developed flow region

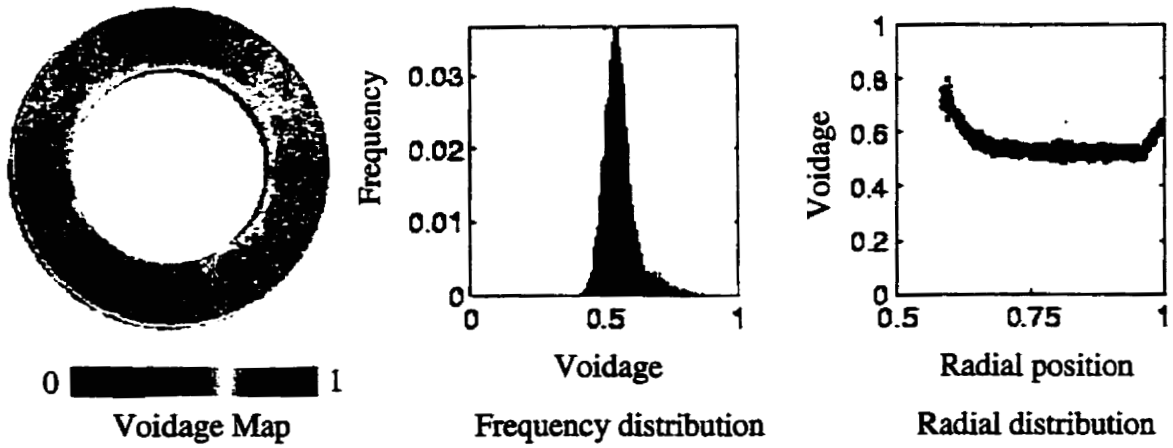

Figure 5.12 Fluidized bed (U_s=2.32 cm/s) in fully developed flow region

The acquired images were also analyzed to obtain mean and standard deviations of voidage at different superficial velocities along the column. Variations in mean bed voidage are depicted in Figure 5.13. The results obtained show a constant mean voidage in case of settled bed all along the column except a little variation near the distributor, which can be attributed to the fact that images acquired include a part of the perforated distributor. All the curves for various superficial velocities show three distinct regions. The lower region in distributor zone where a sudden drop in voidage is observed owing to water jets; the middle region where there is a gradual increase in voidage and smooth fluidization occurs; the upper region which is the freeboard region and there is a sharp increase in voidage. Mean voidage and fluidized bed height increases as the superficial velocities increase. Bakker and Heertjes (1960) also obtained very similar results when they studied porosity distributions for a bed of glass beads with smaller particle sizes (175-210 microns) and have identified three distinct zones in the center of a fluidized bed. The results obtained can be used in the hydrodynamic model to predict the voidage precisely in these three distinct zones when the conventional theory fails.

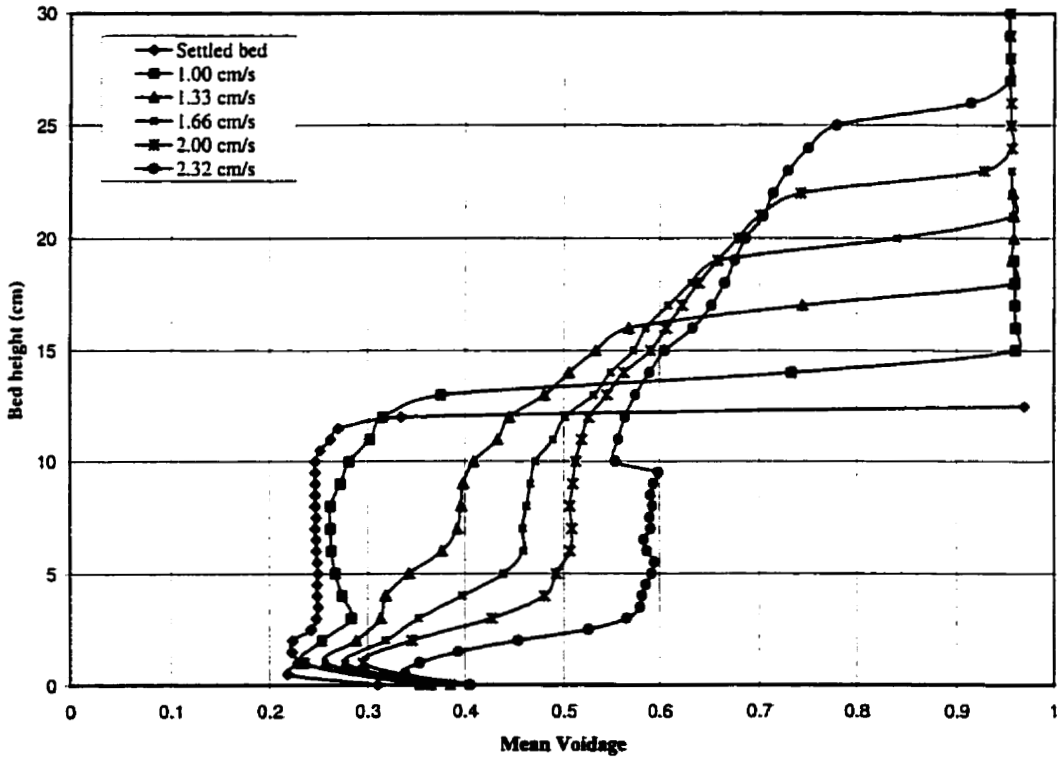

Figure 5.13 Mean voidage as a function of height in the fluidized bed at various superficial velocities

Standard deviations of voidage for various superficial velocities along the column are presented graphically in Figure 5.14. The greatest deviation is observed with settled bed and it decreases with increasing superficial velocities at the same bed heights. The maximum deviations are observed in distributor zone and drop drastically when we reach the fully developed flow region. In the fully developed flow region there is a gradual decrease in standard deviations and the transitions are more gradual at higher superficial velocities. In the freeboard region there is a noticeable change in deviations; it drops and then increases till it reaches a steady value.

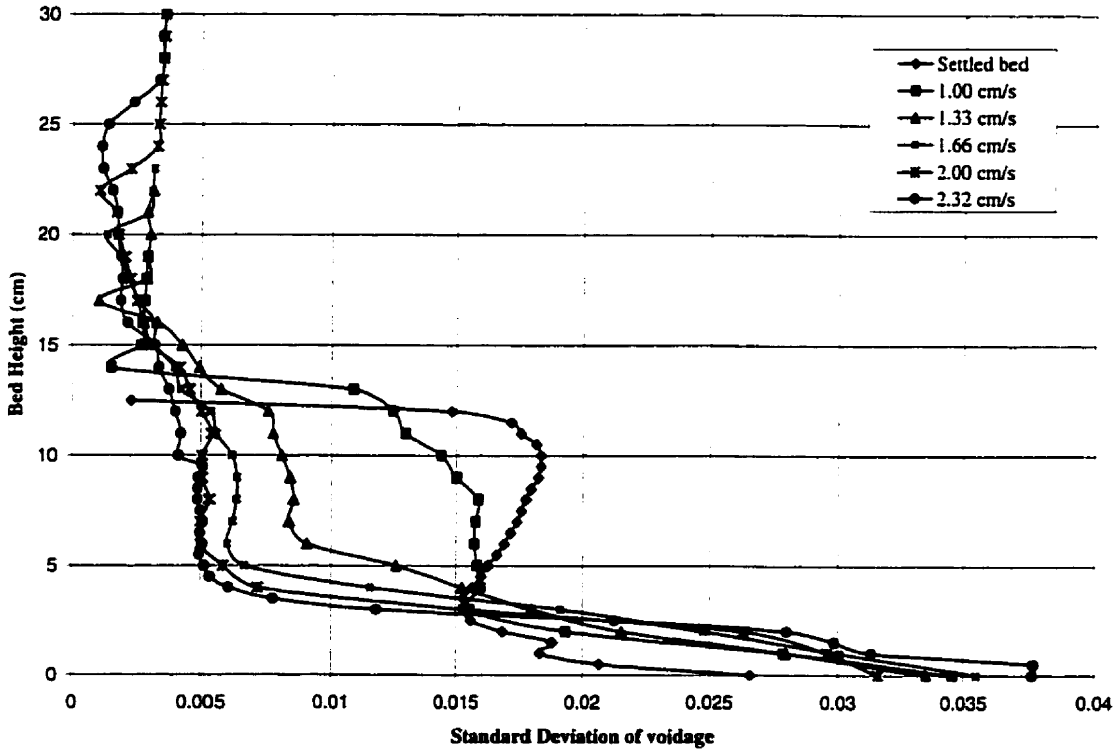

Figure 5.14 Standard deviation of voidage as a function of height in the fluidized bed at various superficial velocities

These results give an insight to the hydrodynamics of the fluidized bed and can be incorporated into a hydrodynamic model for the photocatalytic reactor to predict voidage in discrete elements in the region of interest based upon experimental data since conventional theory fails to predict the same accurately and reliably.

5.2 Radioactive Particle Tracking

The radioactive particle tracking experiments were conducted and produced a series of images which can be displayed in individual frames format, cine format or in 3 dimensions. Two-dimensional images were acquired for the first generation of catalyst, which have been presented elsewhere [Kantzas *et al.* (1999)] and are not being presented here. Three-dimensional images were acquired for the newest photocatalyst particles using two gamma cameras set-up at right angles to each other. Since, there were no means available to synchronize the image acquisition by the two cameras, both the cameras were started at the same time manually. The images were then synchronized by finding the time lag between two cameras using auto-correlation and adjusted accordingly. The images had to be clipped at the beginning and end of acquisition so as to have meaningful 3 dimensional data. All the images showed good contrast and were acquired at the rate of 5 Hz. Initial tests were done to determine the optimum frequency of acquisition. The particle had sufficient counts to penetrate surrounding media, water, glass and was easily distinguishable from the background radiation. A resolution of 3.2 mm has been obtained and a detailed analysis of the experiments has been conducted using programs developed in-house.

Figure 5.15 to Figure 5.20 show some typical results depicting particle positioning and movement obtained from radioactive particle tracking experiments conducted at various superficial velocities. Ten sets of images for each superficial velocity were acquired amounting to 10,000 frames, each frame lasting for a duration of 200 ms, which is about 20 minutes of real time data for each velocity. Since each of these 10 sets of data for a particular velocity were collected over two hours of experimental time, the results should represent the time averaged quantities in the bed and give a representative picture with an insight into the hydrodynamic behavior of the fluidized bed.

All the figures display particle positioning and particle trajectories in x, y and z directions. Figure 5.15 corresponds to images acquired at 0.66 cm/s superficial velocity, which is below the minimum fluidization velocity, and we observe localized movement

of the particle when it was caught up in the jets near the distributor. In this case, there was very poor mixing and particle movement was restricted to a small area.

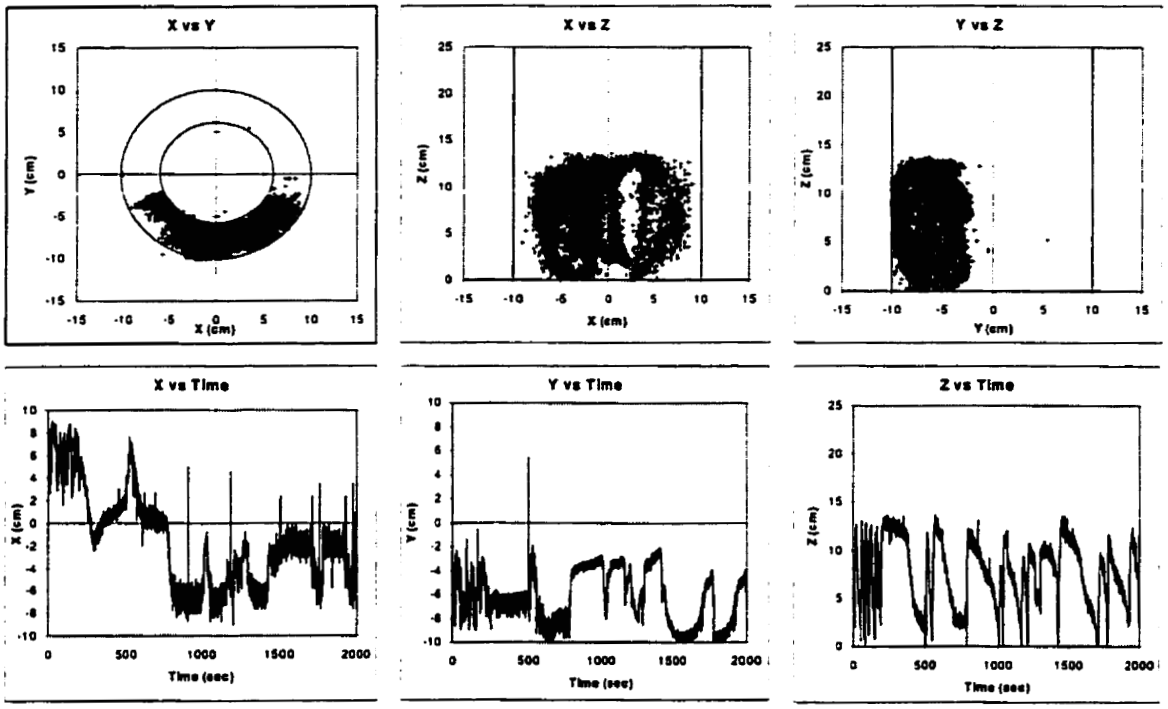

Figure 5.15 Particle positioning and particle trajectories for U_s=0.66 cm/s

Increasing the superficial velocity leads to better mixing, fewer dead zones, and particle visiting everywhere as is evident from Figures 5.16 to 5.20. However, it was observed that the particle spent more time in the freeboard region than in other parts of the bed. This may be attributed to the fact that the chosen particle was doped with radioactive material using glue and since glue is lighter than the material of photocatalyst, it might have resulted in a slightly lighter radioactive particle. Another reason for this behaviour could be that the specific particle chosen to be tracked would have been lighter or smaller than the rest of the photocatalyst particles.

The process of analyzing images obtained from two gamma cameras lead to the development of procedures and softwares for 3-dimensional particle tracking which could

have immense practical applications in studying hydrodynamic characteristics of fluidized beds.

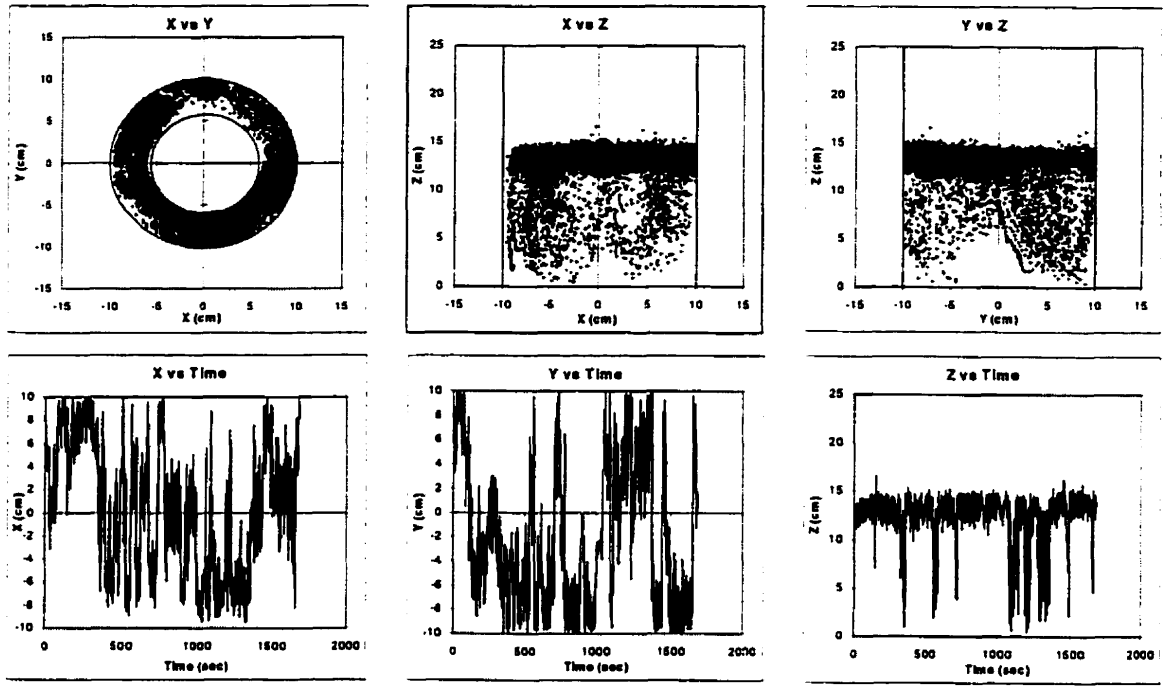

Figure 5.16 Particle positioning and particle trajectories for U_s=1.00 cm/s

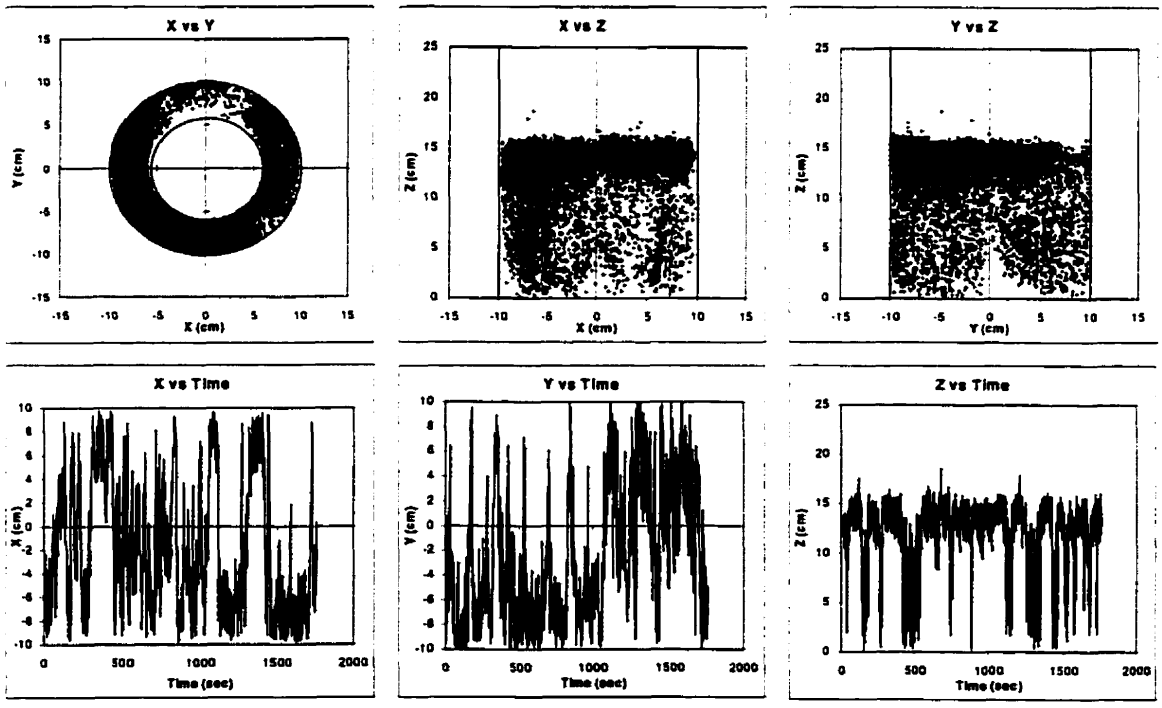

Figure 5.17 Particle positioning and particle trajectories for U_s=1.33 cm/s

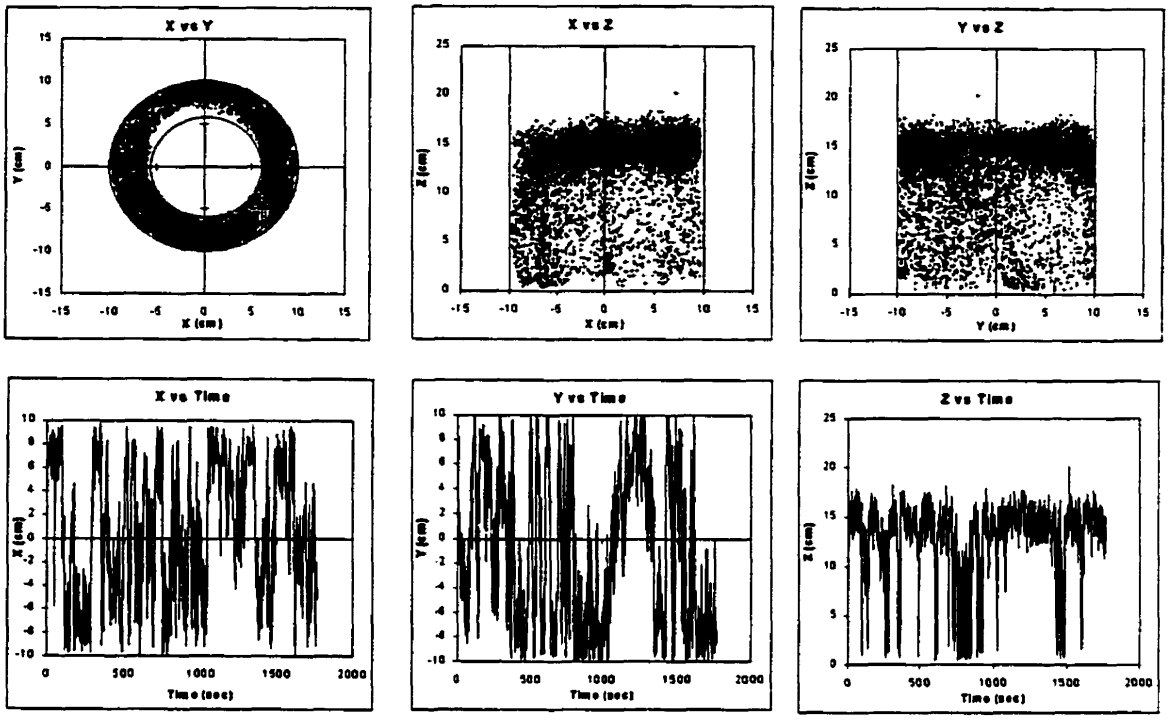

Figure 5.18 Particle positioning and particle trajectories for U_s=1.66 cm/s

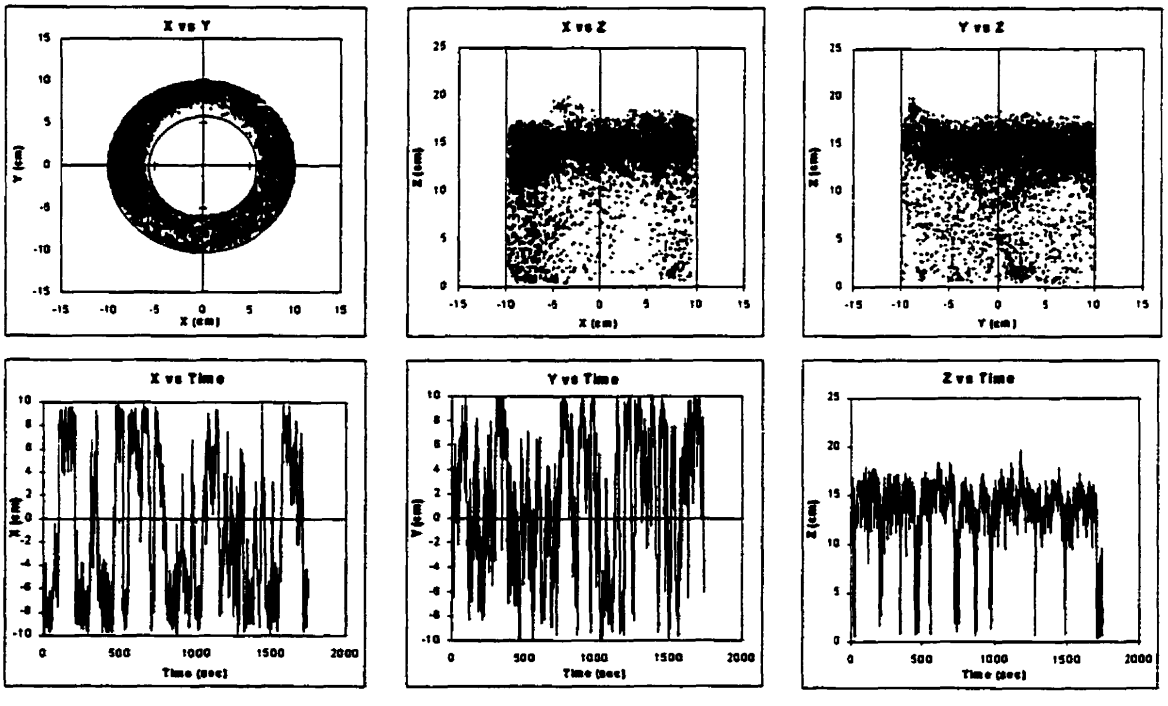

Figure 5.19 Particle positioning and particle trajectories for U_s=2.00 cm/s

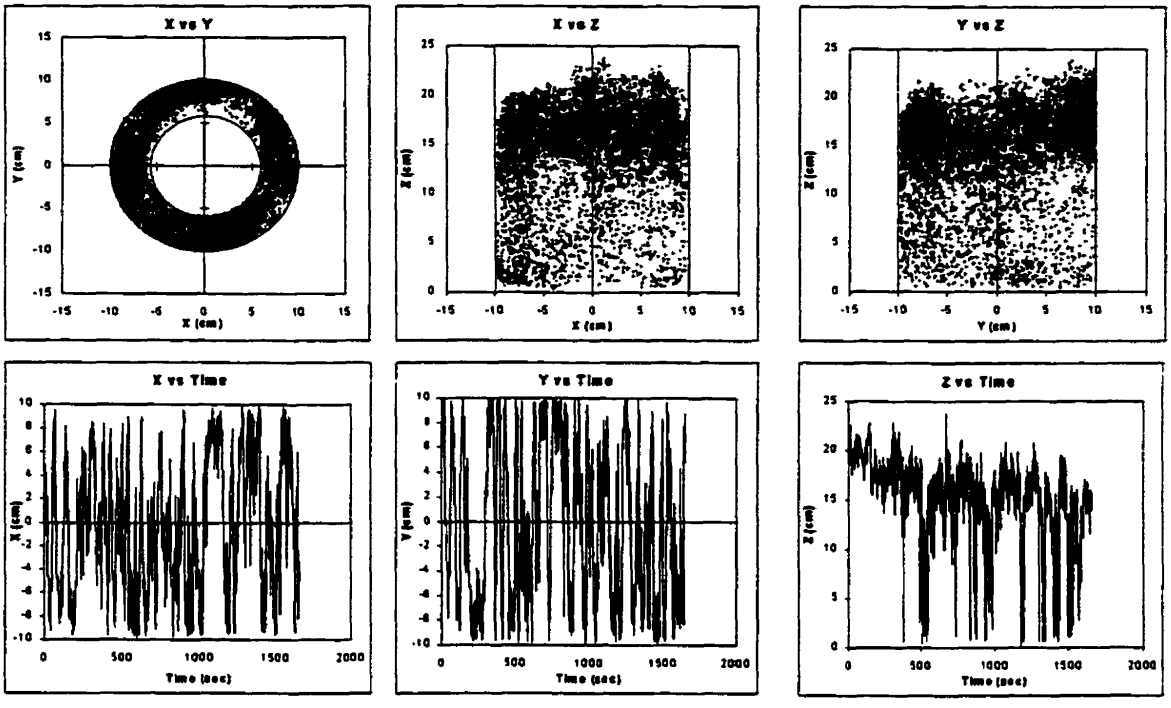

Figure 5.20 Particle positioning and particle trajectories for U_s=2.32 cm/s

Figures 5.21 and 5.22 show the probability distribution function (PDF) of particle occurrence in the bed at the same conditions as discussed above. These plots were obtained by dividing the bed into many compartments of known sizes and computing the number of particle occurrences (particle visiting times) in each compartment. It is evident that the particle visited everywhere in the bed. In the top part or freeboard region of the bed, the PDF of particle occurrence seems higher than the bottom part implying that the particle stayed longer in this part. All the curves are similar in nature beyond the minimum fluidization velocity. However, at superficial velocity of 0.66 cm/s, both figures show a drastically different natured curve which can be attributed to the fact that the superficial velocity is below the minimum fluidization velocity. From Figure 5.22, we can notice the wall effect, the PDF at various superficial velocities drops down very close to the outside and inside walls. As we go away from the inside wall, PDF increases steadily for all superficial velocities above minimum fluidization and then decreases when we reach the outer wall of the photocatalytic reactor.

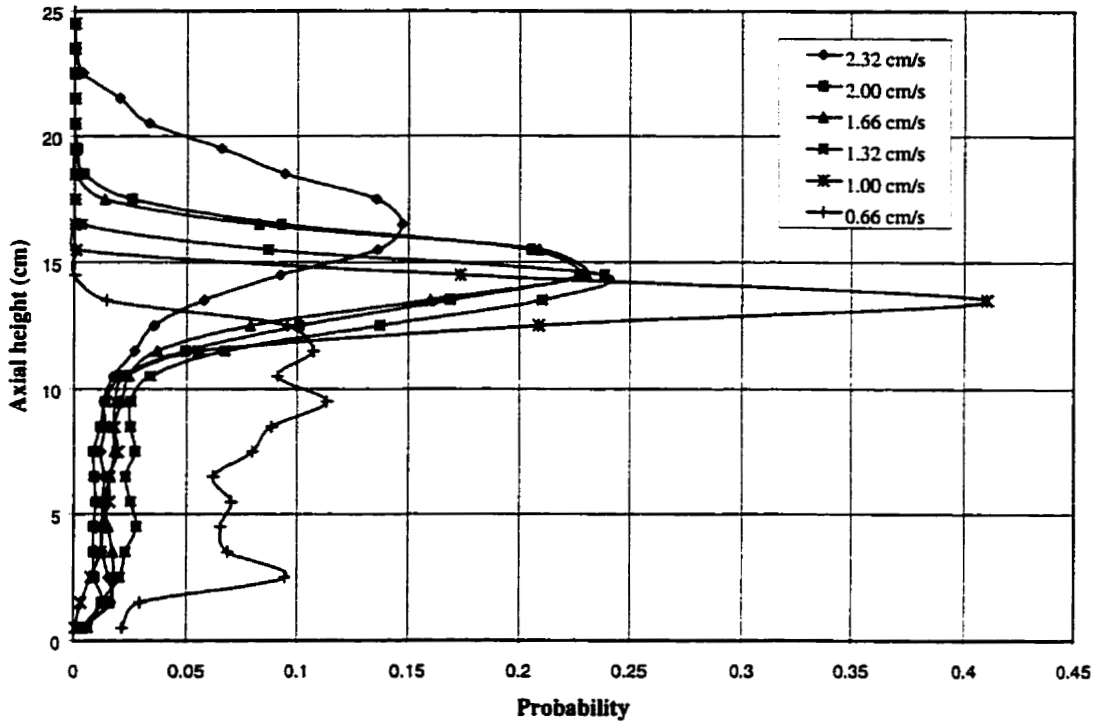

Figure 5.21 Probability distribution function (PDF) of particle occurrence in the bed with respect to bed height

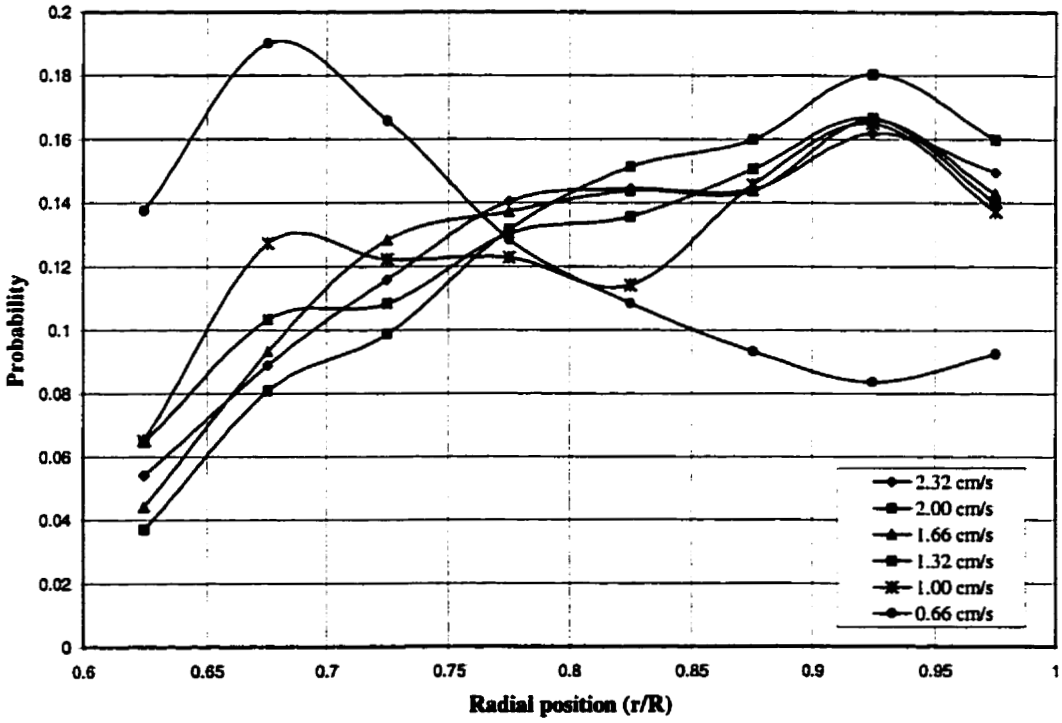

Figure 5.22 Probability distribution function (PDF) of particle occurrence in the bed with respect to radial position

Figure 5.23 and 5.24 show the axial velocity component of the particle as a function of axial and radial position, respectively. In the former, the radial velocity component is a mean of velocity component in all compartments at the same axial bed height and in the latter case, axial velocity component is a mean of velocity component in compartments equidistant from the centre. All the axial components of particle velocities range from −1.50 to 1.50 cm/s which is lesser than the superficial velocities indicating the presence of particle-particle interactions. It is hard to draw any conclusions from the two figures and the particle does not seem to fit into core-annulus model type behaviour. Figure 5.23 indicates that there is a higher oscillatory motion with higher velocities in the fully developed flow region of the bed. The axial component of particle velocity first increases as the bed height increases and then drops down to very low velocities in the freeboard region. The magnitude of velocities increases with the increasing superficial velocities, as one would expect. Figure 5.24 depicts the variation in axial velocity component along the radius of the reactor. In general, we can say that the particle rises in the core i.e. away from the walls and falls down near the inner and outer walls. The fact that particle does not show typical core-annulus type behaviour could be because of the geometry of the annular photoreactor.

Further analysis of radioactive particle tracking experiments provides with the radial component of particle velocities as a function of axial and radial position which are presented in Figures 5.25 and 5.26 respectively. In the former, the radial velocity component is a mean of velocity component in all compartments at the same axial bed height and in the latter case, axial velocity component is a mean of velocity component in compartments equidistant from the centre. Again, it is difficult to draw any conclusions but it appears that the particle exhibits oscillations in radial velocity in all directions. The magnitude of radial velocity components is lower than axial velocity components. This is understandable since the motion of solids in liquid fluidized beds is axially dominant.

Both axial and radial velocity components show no particular trends in axial or radial direction since the bed undergoes smooth fluidization. This has also been confirmed by

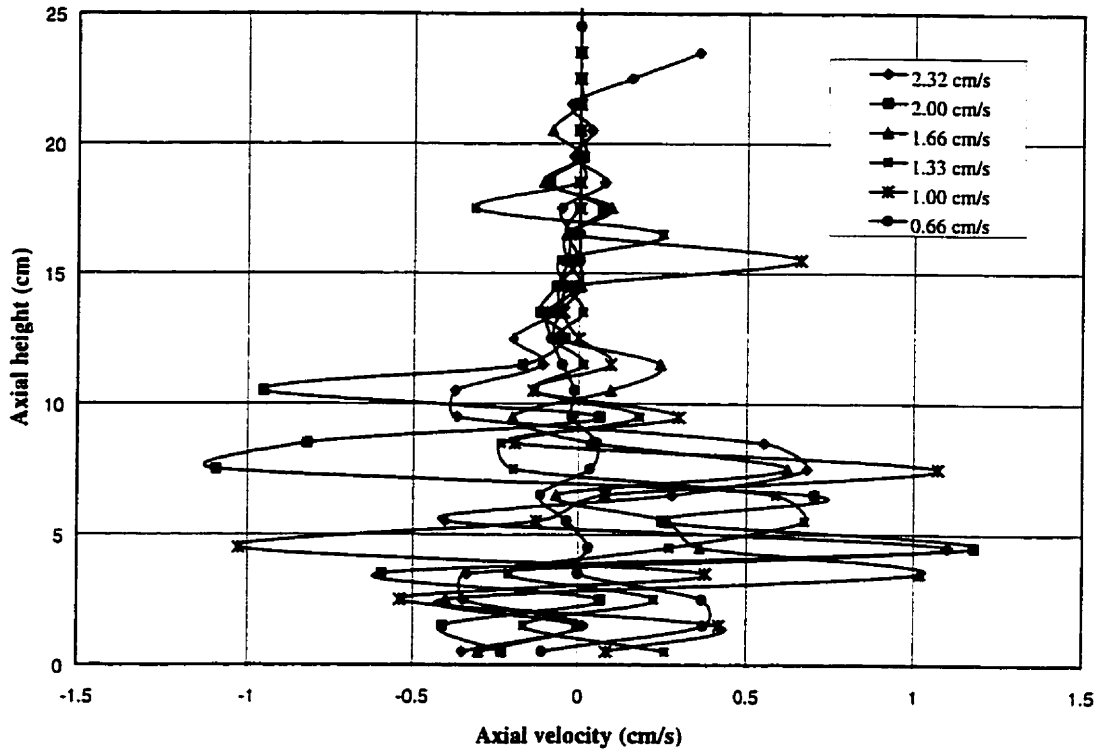

Figure 5.23 Axial component of particle velocity as a function of axial bed height

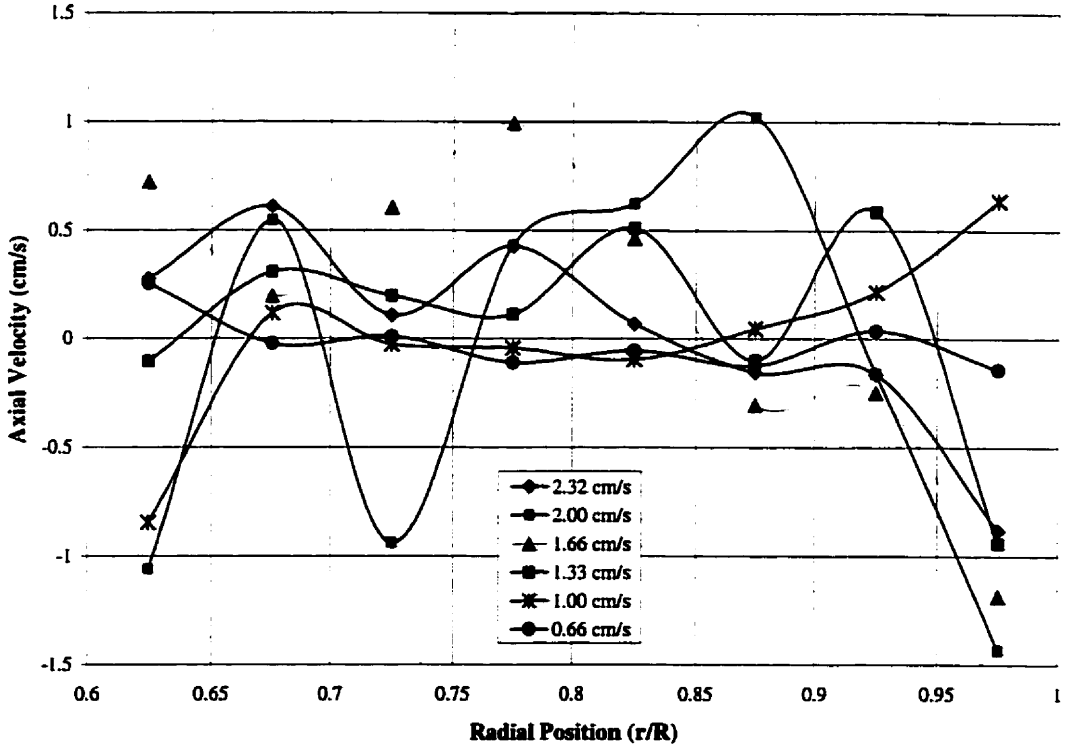

Figure 5.24 Axial component of particle velocity as a function of radial position

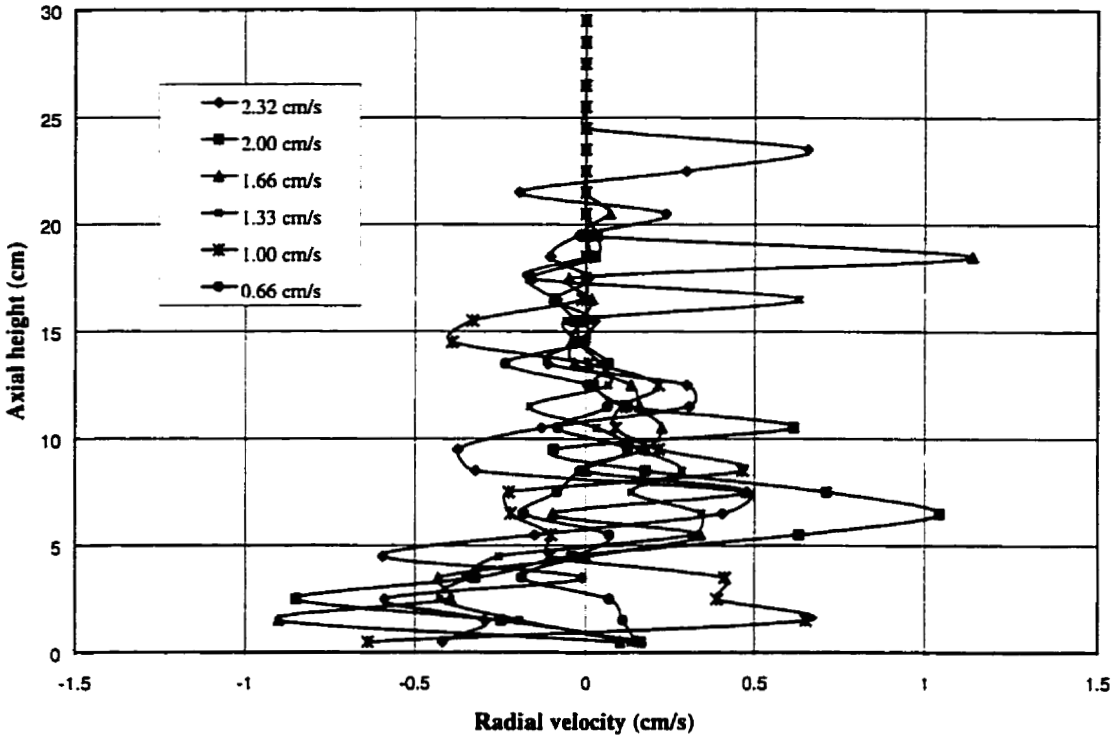

Figure 5.25 Radial component of particle velocity as a function of axial bed height

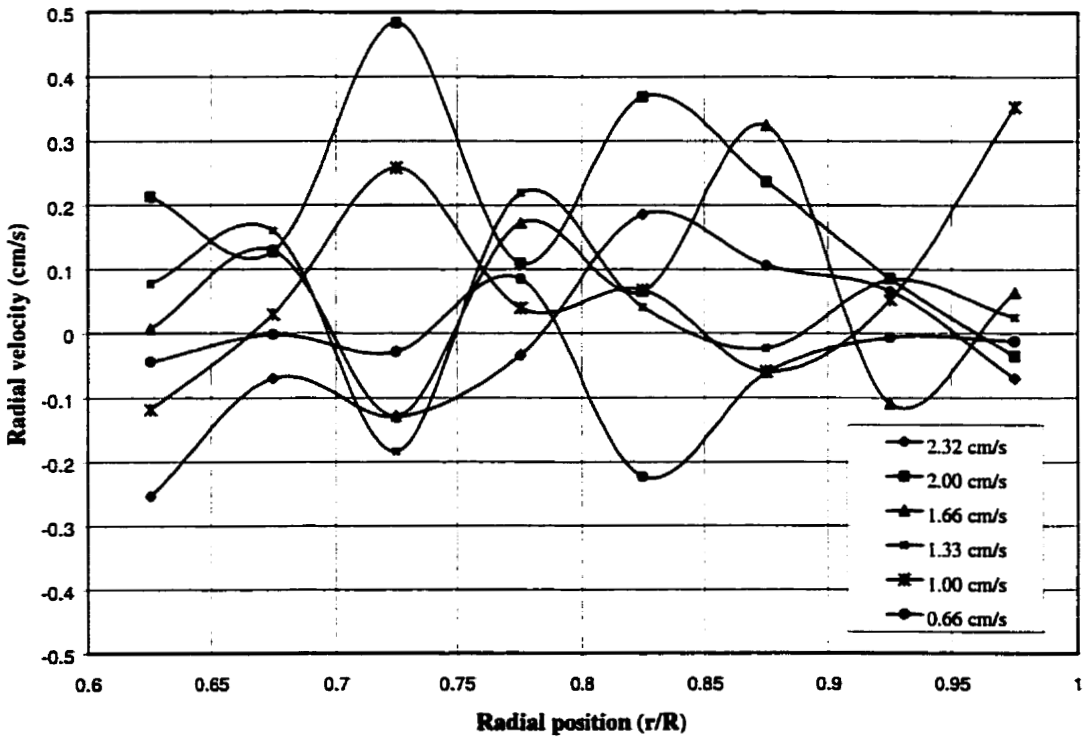

Figure 5.26 Radial component of particle velocity as a function of radial position

results obtained by CT Scanning. As we already observed from the PDF, the particle visits everywhere indicating good mixing characteristics in the photoreactor. This is quite desirable as the frequency of light hitting the photocatalyst particle increases if the particles move everywhere, so that every particle gets a chance to be irradiated resulting in better quantum yields and higher reaction rates.

Thus, a 3-dimensional radioactive particle tracking technique has been established and used to demonstrate its utility in study of hydrodynamic behaviour and modeling of fluidized beds. In the case of this study, the technique can be used to predict the probability and extent of a particle being in front of the lamp and receiving UV radiation, which is of extreme importance in formulation of a better and improved model of the photocatalytic process and reactor system.

5.3 Reaction Experiments

Three reaction experiments were conducted on the pilot-scale photocatalyic reactor to test the technology in principle. A number of experiments were conducted earlier in a bench-scale reactor to determine optimum photocatalyst requirements, effect of pH, light intensity, oxygen concentration and hydrogen peroxide concentration. Those results are not being discussed here since they were conducted in Department of Chemistry, University of Calgary.

The first experiment was conducted with a view to determine whether external replenishment of oxygen is required or the reaction rates can sustain with the initial amount of oxygen present in tap water. The reactor was filled with 1671 g (dry weight) of photocatalyst and 100 L of tap water at ambient temperature was filled in the recirculation tank. Phenol was added to water and mixed properly to result in a concentration of 36 ppm in the synthetic wastewater. Water was pumped through the reactor where dark adsorption was carried out and phenol concentration reduced to 22 ppm after 45 minutes of adsorption through the bed. Water samples were collected at the inlet and outlet every 10 min and since there was no further reduction in concentration of phenol, we can safely assume that the bed had reached its break-through. The UV lamp was turned on at this point and within a couple of minutes an appearance of pink colour

indicated that there was formation of dimers and higher polymeric compounds. This colour was accompanied by a noticeable rise in temperature due to the reaction and there was loss of water due to evaporation. After carrying out the reaction for 60 min, the temperature increased to 34 °C and evaporative loss of water amounted to 10 litres. At this time, lamp was turned off and HCl was added to decrease the pH to 5, diffused aeration was started in the recirculation tank. Illumination was started again and regular samples were collected every 10 min at the reactor inlet and outlet. However, there was no effect and the colour persisted. Another 60 minutes later, 5×10^{-3} M H_2O_2 was added but it did not aid in the disappearance of colour. Photocatalyst was extracted from the reactor and it had an orange tinge to it. Results from the analysis of water samples analyzed on HPLC indicate a decrease in phenol concentration with time, however as suspected from the appearance of pink colour, the phenol formed dimers and other polymeric compounds after ring opening. This was verified by conducting UV-Spectrometry, where the phenol peak broadened and decreased in height indicating presence of phenolic compounds in water samples collected (Appendix H). The same was cross-checked from the Total Organic Carbon (TOC) analysis, where TOC values did drop down due to adsorption from 38 ppm to 25 ppm but had virtually no reduction even after 1.5 hrs of illumination. Results of analysis of water samples obtained from the first experiment are summarizeded in Table 5.1.

Table 5.1 Phenol concentration and TOC of water samples for Experiment #1

Time (min)	**Phenol conc. (ppm)**	**TOC (ppm)**
0	36.6	38.2
45 (dark adsorption)	24.8	25.4
0 (illumination)	24.6	-
10	21.9	-
20	19.6	-
30	18.8	-
45	16.7	-
60	15.7	24.2
90	13.9	24.7

The second experiment was conducted to study the effect of adding hydrogen peroxide on reaction path. The recirculation tank was filled with 100 lts. of tap water and 5 gms. of phenol was added to achieve a concentration of 44 ppm in the synthetic wastewater. Initial pH was 6.8 and the water temperature was 21 °C. Water was pumped through the reactor for 45 min for dark adsorption to take place. Hydrogen peroxide ($5x10^{-3}$ M) was added alongwith HCl to bring down the pH to about 5. The UV lamp was turned on at this time and the same pink colour started to appear within the first 3 minutes of reaction, however it faded within the first 10 minutes of illumination. There was a slight increase in temperature (by 5 °C in 90 min) of water during the course of illumination but there was no noticeable loss of water due to evaporation. This increase in temperature is due to the reactions and not due to the lamp since the temperature of water exiting the cooling water jacket was always lower than the synthetic wastewater. A summary of analytical results of water samples is presented in Table 5.2.

Table 5.2 Phenol concentration and TOC of water samples for Experiment #2

Time (min)	**Phenol conc. (ppm)**	**TOC (ppm)**
0	43.6	-
45 (dark adsorption)	29.9	25.6
0 (illumination)	28.6	22.8
10	13.6	23.5
20	4.4	-
30	2.2	15.0
45	0.2	-
60	0	8.2
90	0	3.3

These results indicate a decrease in phenol concentration to undetectable levels in 45 min accompanied by decrease in TOC. A small sample of catalyst was extracted from the reactor after 45 minutes of dark adsorption and analyzed for phenol adsorbed on the photocatalyst. The photocatalyst adsorbed 7.6 mg of phenol per gram of wet catalyst. Another sample was extracted after 90 minutes of illumination and it indicated that phenol was undetectable on the photocatalyst. It is obvious from this experiment that photocatalysis proceeded towards mineralization. The UV-Visible spectra of water

samples also confirm the fact that phenol was mineralized to carbon dioxide and water rather than getting converted to dimers and other polymeric compounds (Appendix I). This may be attributed either to the formation of hydroxyl radicals due to irradiation of hydrogen peroxide or the lack of sufficient levels of oxygen in the first experiment to facilitate the formation of hydroxyl radicals by trapping electrons and preventing them from recombination with holes.

The third experiment was conducted to resolve if hydrogen peroxide was the beneficiary factor for the mineralization or the lack of oxygen hindered the photocatalysis process in the first experiment. All the experimental conditions for this experiment were the same as earlier except no hydrogen peroxide was added and that the dark adsorption was carried out for 1 hr and the regeneration was done using fresh tap water instead of the synthetic wastewater. The initial phenol concentration was 43.7 ppm which reduced to 27.6 ppm after 1 hr of adsorption and the corresponding TOC decreased from 36.7 to 24.9 ppm. As the illumination was started and the bed fluidized, phenol adsorbed onto the photocatalyst was desorbed into water as apparent from the analytical results of water samples presented in Table 5.3.

Table 5.3 Phenol concentration and TOC of water samples for Experiment #3

Time (min)	**Phenol conc. (ppm)**	**TOC (ppm)**
0	43.7	36.7
60 (dark adsorption)	27.6	24.9
0 (illumination)	0.2	1.3
15	2.9	2.9
20	2.8	-
30	2.5	6.2
45	2.3	7.7
60	1.8	-

The above results and UV-Visible spectra (Appendix J) indicate that phenol was desorbed into water but illumination did not facilitate mineralization and the presence of pink color in the solution accompanied by heat liberation suggested the formation of

dimers and polymeric phenolic compounds. The extract obtained from the photocatalyst after the experiment also showed the presence of phenol and phenolic compounds.

Thus, we can conclude that oxygen was not the crucial factor for the reaction path and there is a need for further detailed investigation to find out the reason for inactivity of the photocatalyst. The photocatalyst is either unable to produce enough hydroxyl radicals or there is some hinderence to the migration of these radicals from the site of generation to the adsorbed phenol molecules. There is a need to investigate in detail under bench top conditions keeping a track of TOC in samples in order to confirm that decrease in phenol concentration is due to its mineralization to carbon dioxide and water and not due to the conversion of phenol to even more complex molecules.

5.4 Model Predictions

The model simulation results discussed in Chapter 3 have insufficient basis of comparison to the actual results obtained from reaction experiments due to the following two major reasons:

i) The kinetic model was based upon the study conducted by Rideh *et al.* (1997) since we do not have any intrinsic kinetic data available for the photocatalytic reactor system.

ii) The reaction experiments conducted on the reactor in our lab did not proceed towards mineralization in the absence of hydrogen peroxide.

Thus, at this point we are unable to verify or validate the developed model due to lack of experimental data. However, it is a first step towards successful modeling of this complex photocatalytic reactor system and more understanding would pave the way for a much improved version of this model.

CHAPTER 6

Conclusions and Recommendations

6.1 Conclusions

i) A basic pseudo plug flow model and simulator was developed for single mode and dual mode photocatalysis process based on kinetic studies done by Rideh *et al.*, (1997). The effect of various parameters for single mode (batch annular photocatalytic fluidised bed reactor) were studied using the developed simulator and matched the trends in literature (qualitatively). The effect of various parameters on regeneration time requirement in dual mode process was investigated. The parameters that were studied using the model were oxygen partial pressure, light intensity of source, initial bed height and flow rate.

ii) A pilot-scale photocatalytic reactor was designed and constructed. An experimental apparatus with all the flow measuring, control and pressure measuring devices and pump for re-circulation has been set-up.

iii) Three-dimensional RPT experiments at six different flow rates (30 min. of real time data for each) have been conducted and this data has been analysed to provide particle occurrence profiles, radial and axial velocity profiles along radial and axial directions respectively. The above analysis has enabled us to establish a technique for 3-dimensional particle tracking using a non-intrusive method. Hardly any trends could be identified from this data suggesting that particle motion is quite random and particle visits everywhere in the bed.

iv) CT Scans for settled bed and five different superficial velocities all along the column length have been conducted to obtain voidage maps, histograms and radial profiles and variations of mean voidage and its standard deviations with superficial velocities. This experimental data could be used to predict voidage in

the discrete element of interest in the photocatalytic reactor where conventional theory fails to predict reliably and accurately.

v) Three reaction experiments (with and without hydrogen peroxide and without aeration) have been conducted to prove the technology in principle. It was found that photocatalysis does not lead to mineralization without the presence of hydrogen peroxide. In the absence of it, the reaction goes towards polymerisation instead of mineralization to carbon dioxide and water.

6.2 Recommendations

i) Reactor Design & Construction

Another photoreactor with the exact same dimensions (made of stainless steel and quartz tubes) has to be constructed for conducting reaction experiments while the existing prototype can be used for hydrodynamic studies. The need for this reactor is that when a lamp is inserted in our current prototype (made of Plexiglas) problems are encountered with containment of fluids.

ii) RPT and CT scanning experiments

Radioactive particle tracking and CT scanning experiments have to be conducted for different initial bed heights and different superficial velocities for a particular initial bed height. Three-dimensional RPT would provide a particle density function and axial & radial dispersion coefficient. The CT experiments would provide bed voidage distribution, voidage maps, histogram and radial profiles at different heights along the column. Effects of operational variables need to be investigated.

iii) Tracer and Mass transfer studies

Tracer studies need to be conducted in order to study the flow patterns and find out residence time in the reactor. Also, detailed mass transfer studies should be conducted using radioactive tracers to find out various mass-transfer parameters using the gamma camera system.

iv) Adsorption Isotherm

There is a need to obtain adsorption isotherms for various pollutants on photocatalyst and oxygen / hydrogen peroxide adsorption on photocatalyst surface. An adsorption-desorption cell could be built and used for this purpose.

v) Kinetics

The key reactions and the rate-determining step should be identified and rate kinetics for the reactor has to be obtained. Also, it is required to experimentally obtain optimum photocatalyst requirements and study the effect of flow rate, effect of oxygen / hydrogen peroxide concentration and effect of light intensity emitted by source on regeneration times.

vi) Modeling

The existing model has to be improved, to take into account the smaller size of lamp (improve on LSPP model or formulate another), to incorporate radial and axial dispersion and to discretize voidage and model extension to a number of adsorption and regeneration cycles. A model thus obtained integrating the hydrodynamics, mass-transfer and kinetics would finally need to be validated using the experimental data obtained from previous tasks.

vii) Scale -up of the reactor

Successful modeling and validation of the model by experimental data will facilitate the scale-up of the reactor as a modular unit with a number of such units arranged in a way to have a continuous treatment process i.e. some units would be operating while others are regenerating.

REFERENCES

Ahmed S. and Ollis D.F., "Solar Photoassisted Catalytic Decomposition of the Chlorinated Hydrocarbons Trichloroethylene and Trichloromethane", *Solar Energy*, **32**, 597-601, 1984.

Akmehmet, B.I. and Yuksel, I., "Photocatalytic degradation of organic contaminants in semiconductor suspensions with added H_2O_2", *Journal of Environmental Science and Health*, **A31**, 123-138, 1996.

Al-Sayyed, G., D'Oliveira, J.C. and Pichat, P., "Semiconductor-sensitized photodegradation of 4-chlorophenol in water", *Journal of Photochemistry and Photobiology, A :Chemistry*, **58**, 99-114, 1991.

Andre, J.C., Viriot, M.L., Midoux, N. and Roizard, C., "Why not Industrial Photochemistry?", *Industrial Photochemistry*, Virior, M.L., Andre, J.C. and Braun, A.M. Editors, CPIC-ENSIC, Nancy, **A**, 1, 1990.

Augugliaro, V., Loddo V., Schiavello M., "Heterogeneous Photocatalytic Reactors: An Assessment of Fundamental Engineering Aspects", *Heterogeneous Photocatalysis*, Edited by Schiavello, M., John Wiley & Sons Ltd., 169, 1997.

Barbeni, M., Morello, M., Pramauro, E., Pelizzetti, E., Vincenti, M., Borgarello, E., and Serpone, N., "Sunlight Photodegradation of 2,4,5-trichlorophenoxy-acetic acid and 2,4,5-trichlorophenol on TiO_2. Identification of Intermediates and Degradation Pathways", *Chemosphere*, **16**, 1165-1179, 1987.

Bard, A.J., "Design of Semiconductor Photoelectrochemical Systems for Solar Energy Conversion", *Journal of Physical Chemistry*, **86**, 172-177, 1982.

Bellobono, I. R., Carrara, A., Barni, B. and Gazzotti, A., "Laboratory- and pilot-plant-scale photodegradation of chloroaliphatics in aqueous solution by photocatalytic membranes immobilizing titanium dioxide", *Journal of Photochemistry and Photobiology. A :Chemistry*, **84**, 83-90, 1994.

Braun A.M., Jakob, L., Oliveros, E., "Up-scaling Photochemical Reactions", *Advances in Photochemistry*, **18**. 235-314, 1993.

Braun, A..M., "Photochemical Conversion and Storage of Solar Energy", In *Proceedings of the 8 th International Conference on Photochemical Conversion and Storage of Solar Energy*, Palermo, Italy, 551-560, 1991.

Braun, A.M., Jakob, L., Oliveros, E. and Nascimento, C., "Up-scaling Photochemical Reactions", *Advances in Photochemistry*, Volman, D., Hammond, G.S. and Neckers, D.C. Editors, John Wiley & Sons, **18**, 235-313, 1993.

Brezova, V., Jankovicova, M., Soldan, M., Blazkova, A., Rehakova, M., Surnina, I., Ceppan, M., Havlinova, B., "Photocatalytic degradation of p-toluenesulphonic acid in aqueous systems containing powdered and immobilized titanium dioxide", *Journal of Photochemistry and Photobiology. A :Chemistry*, **83**, 69, 1994.

Carey, J.H., Lawrence J., Tosine, H.M., "Photodechlorination of PCB's in the Presence of Titanium Dioxide in Aqueous Suspensions", *Bulletin of Environmental Contamination and Toxicology*, **16**, 697-701, 1976.

Castellana, F.S. and Duddley, B.A., "Imaging of Particle Motion in Fluid-Solid Systems Using a Gamma Camera", *Chemical Engineering Communications*, **29**, 113-123, 1984.

Chen, D. and Ray, A.K., "Photodegradation kinetics of 4-Nitrophenol in TiO_2 suspension", *Water Resources*, **32**, 3223-3234, 1998.

Childs, L.P., Ollis, D.F., "Is Photocatalysis Catalytic?", *Journal of Catalysis*, **66**, 383-390, 1980.

Crittenden J.C., Suri, R.P.S., Perram, D.L. and Hand D.W., "Decontamination of Water using Adsorption and Photocatalysis", *Water Resources*, **31**, 411-418, 1997.

Davis, M. E., "Zeolite Synthesis: Can It Be Designed?", *ACS Symposium Series*, **561**, 27-37, 1994.

D'Oliveira, J.C., Al-Sayyed, G. and Pichat, P., "Photodegradation of 2- and 3-chloropenol in TiO_2 aqueous suspensions", *Environmental Science & Technology*, **24**, 990-996, 1990.

Duran, N., Dezotti, M. and Roderiguez, J., "Biomass photochemistry. XV: Photobleaching and biobleaching of Kraft effluent", *Journal of Photochemistry and Photobiology. A :Chemistry*, **62**, 269, 1991.

Fox, M.A. and Dulay, M.T., "Heterogeneous Photocatalysis", *Chemical Reviews*, **93**, 341-357, 1993.

Haarstrick, A., Kut, O.M. and Heinzle, E., "TiO_2-Assisted Degradation of Environmentally Relevant Organic Coumpounds in Wastewater Using a Novel Fluidized Bed Photoreactor", *Environmental Science & Technology*, **30** (3), 817-824, 1996.

Hamilton, K., Wright, I., Zarabi, T. and Kantzas, A., "A Novel Method for Particle Tracking Using Single Photon Emission Computed Tomography and Radioactive Tracers", Provisional Application 1997.

Harris, P.R. and Dranoff, J.S., "A Study of Perfectly Mixed Photochemical Reactors", *AIChE Journal*, **11**, 497, 1965.

Herrmann, J.M., Guillard, C. and Pichat, P., "Heterogeneous photocatalysis: an emerging technology for water treatment", *Catalysis Today*, **17**, 7-20, 1993.

Hoffman, A.J., Carraway, E.R., Hoffmann, M.R., "Photocatalytic Production of H_2O_2 and Organic Peroxides on Quantum-Sized Semiconductor Colloids", *Environmental Science & Technology*, **28**, 776-785, 1994.

Hofstadler, K., Bauer, R., Novalic, S. and Heisler, G., "New reactor design for photocatalytic wastewater treatment with TiO2 immobilized on fused-silica glass fibers: photomineralization of 4-chlorophenol", *Environmental Science & Technology*, **28**, 670, 1994.

Hsiao, C.Y., Lee, C.L. and Ollis, D.F., "Heterogeneous Photocatalysis : Degradation of Dilute Solutions of Dichloromethane (CH_2Cl_2), Chloroform ($CHCl_3$), and Carbon Tetrachloride (CCl_4) with Illuminated TiO_2 Photocatalyst", *Journal of Catalysis*, **82**, 418-423, 1983.

Ibusuki, T, Kutsuna, S. and Takeuchi, K., "Removal of Low Concentration Air Pollutants through Photoassisted Heterogeneous Catalysis", In *Photocatalytic Purification and Treatment of Water and Air*, Ollis, D.F. and Al-Ekabi, H., Editors, Elsevier : Amsterdam, The Netherlands, 375, 1993.

Irazoqui, H.A., Cereda, J. and Cassano, A.E., "Radiation Profiles in an empty annular photoreactor with a source of finite spatial dimensions", *AIChE Journal*, **19**, 460-467, 1973.

Jacob, S.M. and Dranoff, J.S., "Light Intensity Profiles in a Perfectly Mixed Photoreactor", *AIChE Journal*, **16**, 359-363, 1970.

Kantzas, A., Hamilton, K., Zarabi, T., Bhargava, A., Wright, I., Brook, G. and Chen J.; "Application of Gamma Camera Imaging and SPECT Systems in Chemical Processes", 1st World Congress on Industrial Process Tomography, Buxton, Greater Manchester, UK, April 14-17, 1999, *Chemical Engineering Journal*, **77**(1,2), 2000.

Kantzas, A. and Kalogerakis, N., "Monitoring the Fluidization Characteristics of Polyolefin Resins Using X-Ray Computer Assisted Tomography Scanning", 14th International Symposium on Chemical Reactor Engineering (ISCRE 14), Brugge, Belgium May 5-8, *Chemical Engineering Science*, **51**(10), 1979-1990, 1996.

Kantzas, A., Wright, I. and Kalogerakis, N., "Quantification of Channeling in Polyethylene Resin Fluid Beds Using X-Ray Computer Assisted Tomography (CAT)", *Frontiers in Industrial Process Tomography*, San Luis Obispo, California, October 29 - November 3, 1995, *Chemical Engineering Science*, **52**(13), 2023-2035, 1997.

Kawaguchi, H., "Dependence of photocatalytic reaction rate on photocatalyst concentration in aqueous suspensions", In *Photocatalytic Purification and Treatment of Water and Air*, Ollis, D.F. and Al-Ekabi, H., Editors, Elsevier : Amsterdam, The Netherlands, 665-673, 1993.

Kormann, C., Bahnemann, D.W. and Hoffmann, M.R., "Photolysis of chloroform and other organic molecules in aqueous TiO_2 suspensions", *Environmental Science & Technology*, **25**, 494-500, 1991.

Koster, T.P.M., Assink, J.W., Van der Veen, C., "Photocatalytic oxidation of multi-component organochlorine mixtures in water", In *Photocatalytic Purification and Treatment of Water and Air*, Ollis, D.F. and Al-Ekabi, H., Editors, Elsevier : Amsterdam, The Netherlands, 613-618, 1993.

Legrini, O., Oliveros, E., and Braun, A.M., "Photochemical Processes for Water Treatment", *Chemical Reviews*, **93** (2), 671-698, 1993.

Leopore, G.P., "Primary Events Governing Photocatalytic Activity of Different Titanium Dioxide Archetypes", Ph.D. dissertation, University of Calgary, 1995.

Lu, M.C., Roam, G.D., Chen, J.N. and Huang, C.P., "Factors affecting the photocatalytic degradation of dichlorvos over titanium dioxide supported on glass", *Journal of Photochemistry and Photobiology: A. Chemistry*, **76**, 103-110, 1993.

Matsuura, T. and Smith, J.M., "Light Distribution in Cylindrical Photoreactors", *AIChE Journal*, **16**, 321-324, 1970.

Matthews, R. W., "Photooxidative Degradation of Coloured Organics in Water Using Supported Catalysis. TiO_2 on Sand", *Water Resources*, **25**, 1169-1176, 1991.

Matthews, R.W., "Photocatalysis in Water Purification: Possibilities, Problems and Prospects", In *Photocatalytic Purification and Treatment of Water and Air*, Ollis, D.F. and Al-Ekabi, H., Editors, Elsevier : Amsterdam, The Netherlands, 121, 1993.

Matthews, R.W., "Photooxidation of organic impurities in water using thin films of titanium oxide", Journal of Physical Chemistry, **91**, 3328-3333, 1987 a.

Matthews, R.W., "Photo-oxidation of Organic Material in Aqueous Suspensions of Titanium Dioxide", *Water Research*, **20**, 569-578, 1986.

Matthews, R.W., "Solar-electric water purification using photocatalytic oxidation with TiO_2 as a stationary phase", *Solar Energy*, **38**, 405-413, 1987 b.

Matthews, R.W., "Titanium dioxide and the solar purification of water", *Sunworld*, **9**, 3-5, 1985.

Matthews, R.W. and McEvoy, S.R., "Photocatalytic degradation of phenol in the presence of near-UV illuminated titanium dioxide", *Journal of Photochemistry and Photobiology. A: Chemistry*, **64**, 231-246, 1992.

Mazzarino, I. and Piccinini, P., "Photocatalytic Oxidation of Organic Acids in Aqueous Media by a Supported Catalyst", *Chemical Engineering Science*, **54**, 3107-3111, 1999.

Mengyne, Z., Shifn, C. and Yaown, T., "Photocatalytic degradation of organophosphorous pesticides using thin films of TiO_2", *Journal of Chemical Technology and Biotechnology*, **6**, 339-344, 1995.

Mills, A. and Davies, R., "The photomineralization of reactive black 5 sensitised by titanium dioxide: A study of the initial kinetics of dye photobleaching" In *Proceedings of The First International Conference on TiO_2 Photocatalytic Purification and Treatment of Water and Air*, London, Ontario, Nov. 8-13, 595-600, 1992.

Nguyen, T. and Ollis, D.F., "Complete Heterogeneously Photocatalyzed Transformation of 1,1- and 1,2-Dibromoethane to CO_2 and HBr", *Journal of Physical Chem*istry, **88**, 3386, 1984.

Ollis, D.F., "Photochemical Conversion and Storage of Solar Energy", Pelizzetti, E. and Schiavello, M. Editors, Kluwer Academic Publishers, Dordrecht, 593, 1991.

Ollis, D.F., Pelizzetti, E. and Serpone, N., "Destruction of water contaminants", *Environmental Science & Technology*, **25**, 1523-1529, 1991.

Ollis, D.F., Hsiao, C.Y., Budiman, L. and Lee, C.L., "Heterogeneous Photoassisted Catalysis: Conversions of Perchloroethylene, Dichloroethane, Chloroacetic Acids, and Chlorobenzenes", *Journal of Catalysis*, **88**, 89-96, 1984.

Peill, N.J. and Hoffmann, M.R., "Chemical and Physial Characterization of a TiO_2-Coated Fiber Optic Cable Reactor", *Environmental Science & Technology*, **30**, 2806, 1996.

Pelizzetti, E., Minero, C., Carlin, V. and Borgarello, E., "Photocatalytic soil decontamination", *Chemosphere*, **25**, 343-351, 1992.

Pelizzetti, E., Minero, C., Hidaka, H. and Serpone, N., "Photocatalytic Processes for Surfactant Degradation", In *Photocatalytic Purification and Treatment of Water and Air*, Ollis, D.F. and Al-Ekabi, H., Editors, Elsevier : Amsterdam, The Netherlands, 261-273, 1993.

Pelizzetti, E., Pramauro E., Minero, C. and Serpone, N., "Sunlight Photodegradation Degradation of Organic Pollutants in Aquatic Systems", *Waste Management*, **10**, 65, 1990.

Pelizzetti, E., Minero, C. and Peramauro, E., "Photocatalytic processes of organic water contaminants", In Chemical reactor Technology for Environmentally Safe Reactors and Products, deLasa, H.I. et al. Editors, Kluwer, The Netherlands, 577-607, 1993.

Pruden, A.L. and Ollis, D.F., "Degradation of Chloroform by Photoassisted Heterogeneous Catalysis in Dilute Aqueous Suspensions of Titanium Dioxide", *Environmental Science & Technology*, **17**, 628-631, 1983a.

Pruden, A.L. and Ollis, D.F., "Photoassisted Heterogeneous Catalysis : The Degradation of Trichloroethylene in Water", *Journal of Catalysis*, **82**, 404-417, 1983b.

Ray, A.K. and Beenackers, A. A., "Novel Swirl-Flow Reactor for Kinetic Studies of Semiconductor Photocatalysis", *AIChE Journal*, **43**, 2571-2578, 1997.

Rideh, L., Wehrer A., Ronze, D. and Zoulalian, A. , "Photocatalytic Degradation of 2-Chlorophenol in TiO_2 Aqueous Suspension : Modeling of Reaction Rate", *Industrial Engineering Chemistry Research*, **36**, 4712-4718, 1997.

Serpone, N., Borgarello, E., Harris, R., Cahill, P. Bogarello, M. and Pelizzetti, E., "Photocatalysis over TiO2 supported on a glass substrate", Solar Energy Material, **14**, 121-127, 1986.

Sierka, R.A. and Bryant, C.W., "Biological treatment of Kraft wastewater following pretreatment of the extraction waste stream by illuminating titanium dioxide and membranes" In *Proceedings of The First International Conference on TiO_2 Photocatalytic Purification and Treatment of Water and Air*, London, Ontario, Nov. 8-13, 275-290, 1992.

Sorenson, J.A. and Phelps, M.E., "Physics in Nuclear Medicine", 2nd Edition, p.300, W.B. Saunders Co., Philadelphia, PA 1987.

Tinucci, L., Borgarello, E., Minero, C. and Pelizzetti, E., "Treatment of Industrial Wastewaters by Photocatalytic Oxidation on TiO_2", In *Photocatalytic Purification and Treatment of Water and Air*, Ollis, D.F. and Al-Ekabi, H., Editors, Elsevier : Amsterdam, The Netherlands, 585, 1993.

Turchi, C.S. and Ollis, D.F., "Photocatalytic reactor Design: An Exampl of Mass-Transfer Limitations with an Immobilized Catalyst", *Journal of Physical Chemistry*, **92**, 6852, 1988.

Weichgrebe, D., Vogelpohl, A., Bockelmann, D. and Bahnemann, D., " Treatment of Landfill Leachates by Photocatalytic Oxidation using TiO_2: A Comparison with Alternative Photochemical Technologies", In *Photocatalytic Purification and Treatment of Water and Air*, Ollis, D.F. and Al-Ekabi, H., Editors, Elsevier : Amsterdam, The Netherlands, 579, 1993.

Zhang, P.C., Scrudato, R.J., Pagano, J.J. and Roberts, R.N., "Photocatalytic decomposition of PCBs in aqueous systems with solar light", In *Proceedings of The First International Conference on TiO_2 Photocatalytic Purification and Treatment of Water and Air*, London, Ontario, Nov. 8-13, 619-624, 1992.

APPENDIX A

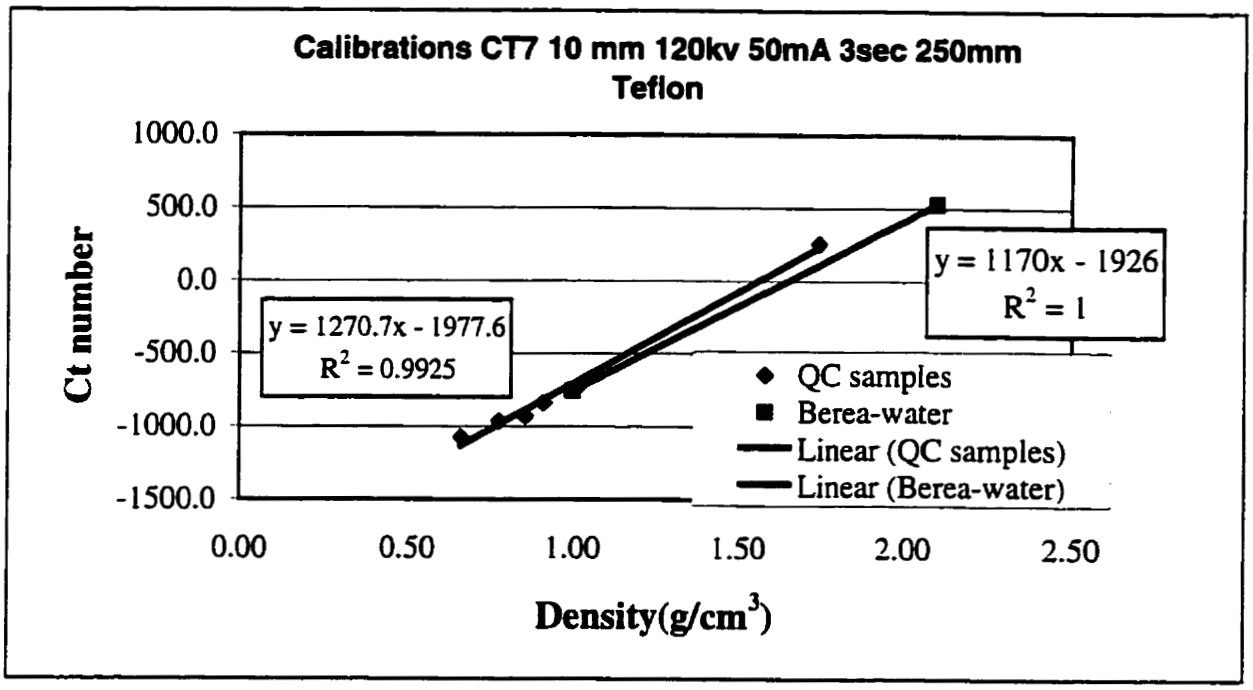

Fig. 1 Calibrations for CT Scanner (EMI 7070)

APPENDIX B

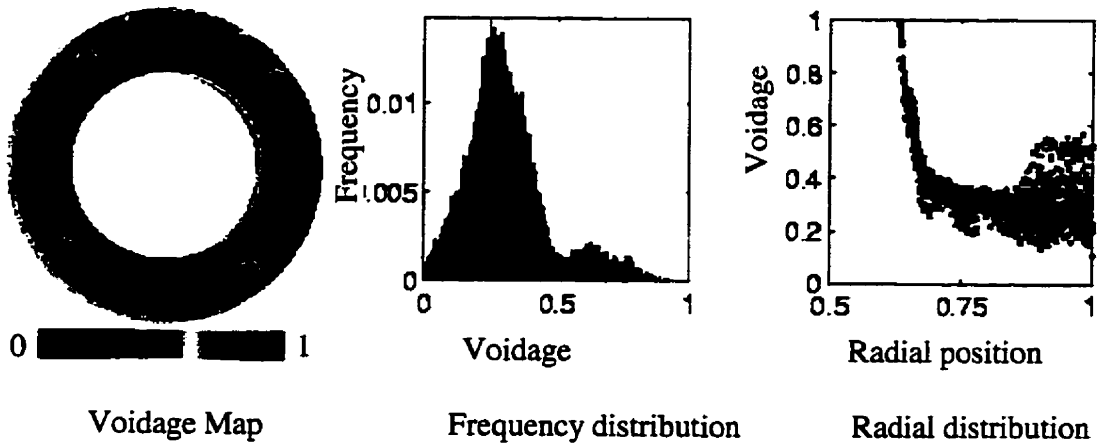

Fig. 1 Settled bed at distributor

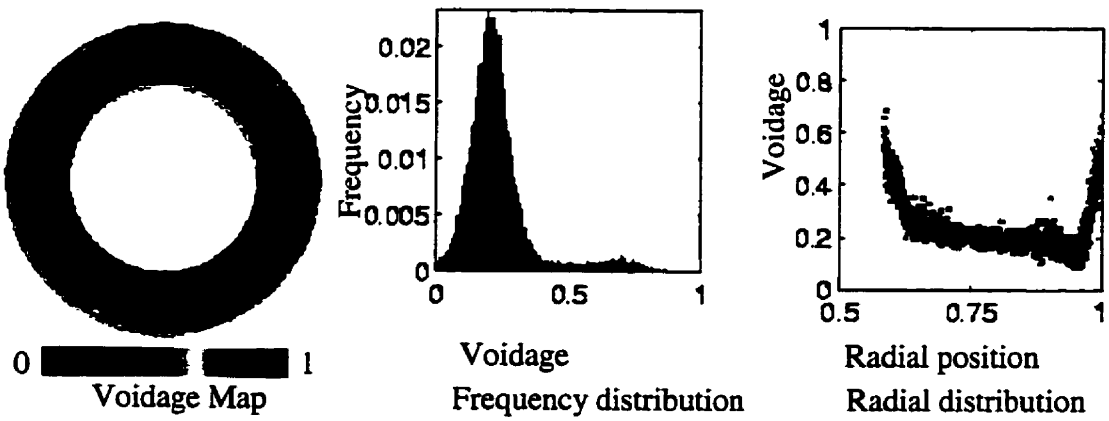

Fig. 2 Settled bed at 1 cm. above the distributor

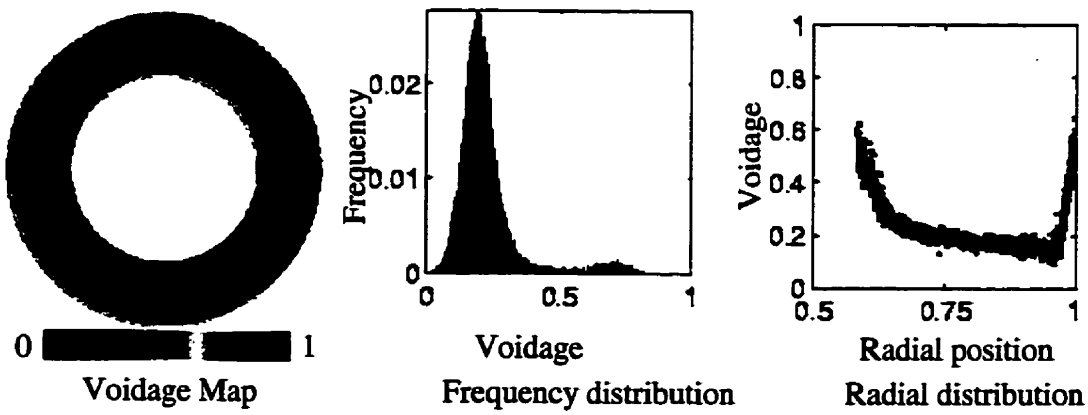

Fig. 3 Settled bed at 2 cm. above the distributor

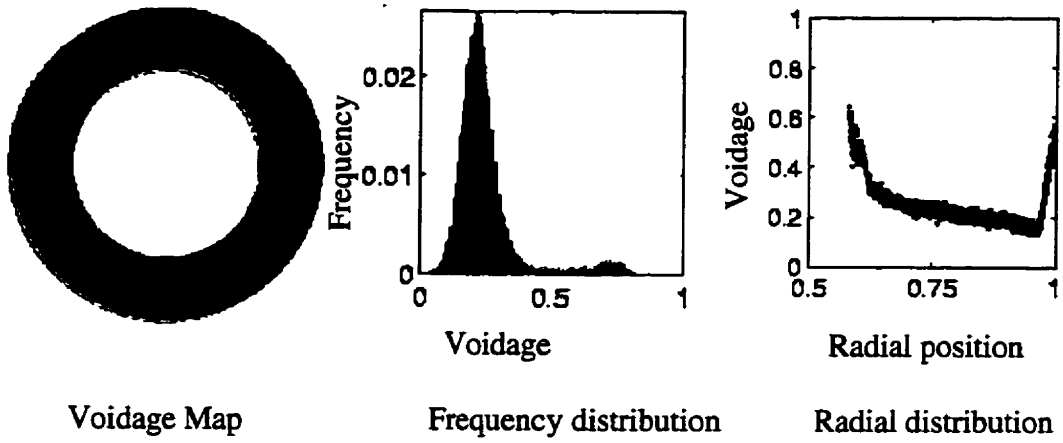

Fig. 4 Settled bed at 3 cm. above the distributor

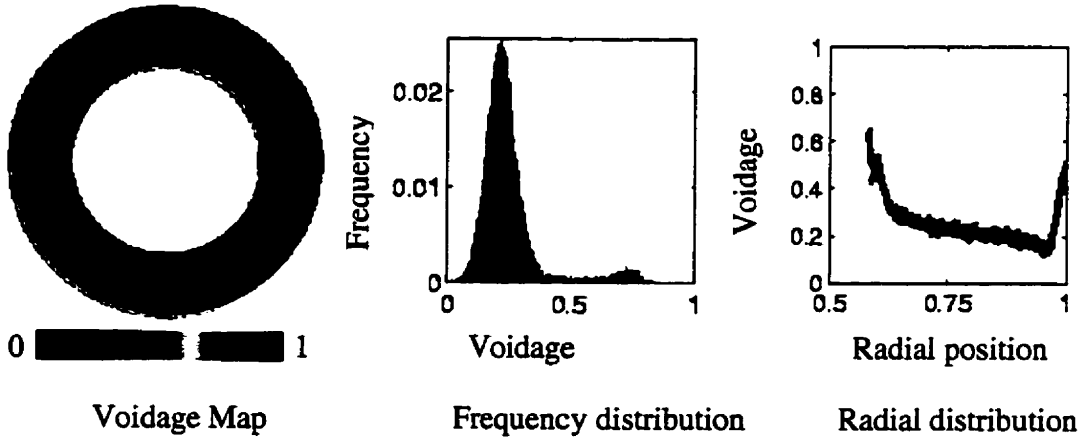

Fig. 5 Settled bed at 4 cm. above the distributor

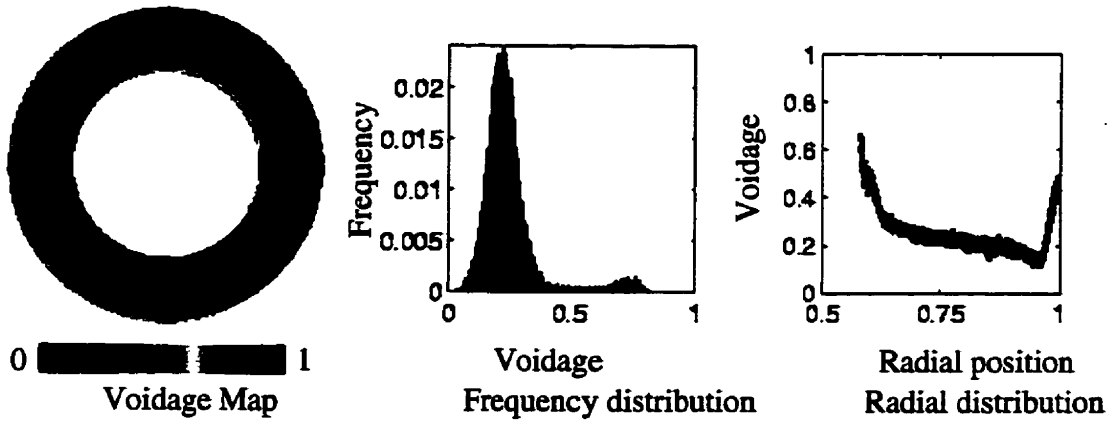

Fig. 6 Settled bed at 5 cm. above the distributor

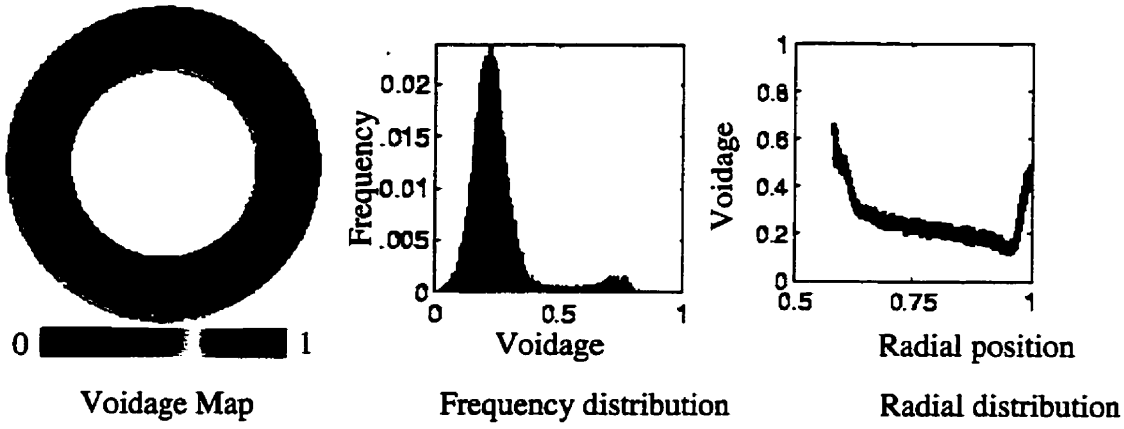

Fig. 7 Settled bed at 6 cm. above the distributor

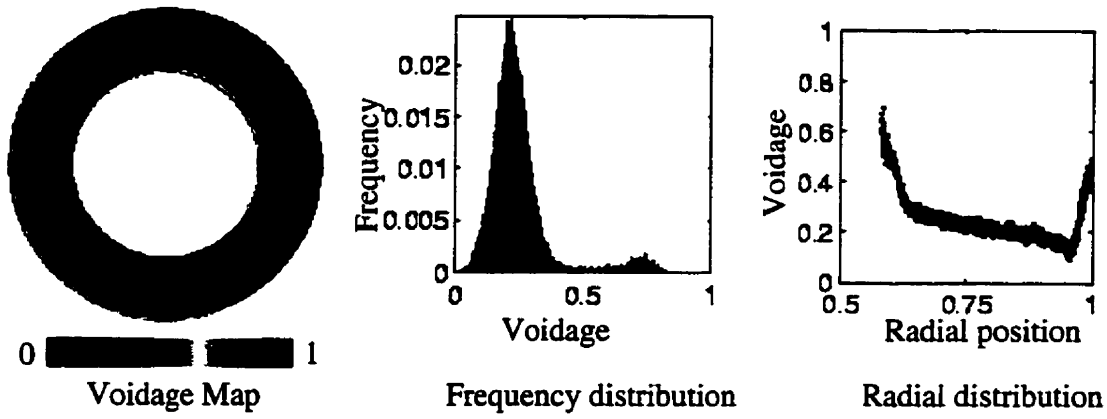

Fig. 8 Settled bed at 7 cm. above the distributor

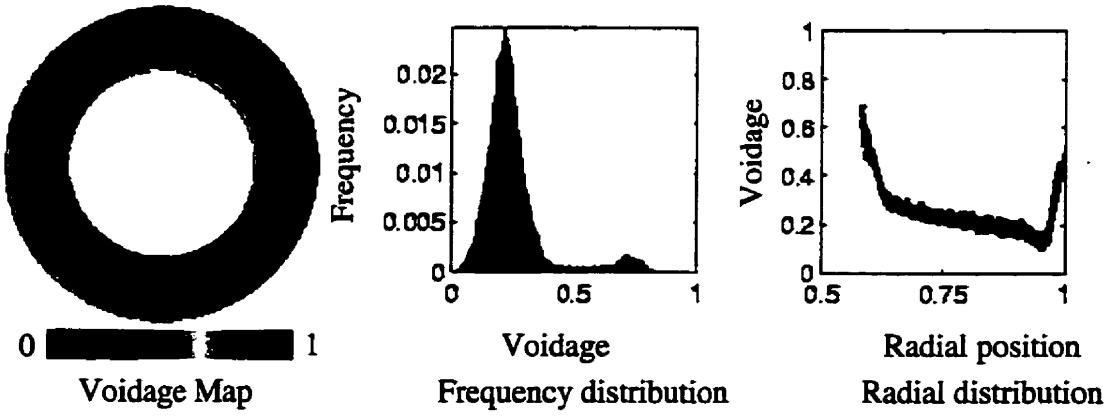

Fig. 9 Settled bed at 8 cm. above the distributor

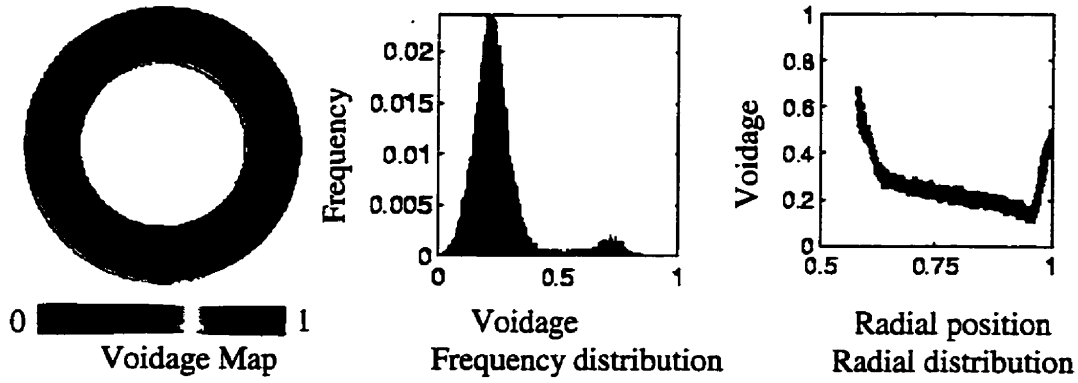

Fig. 10 Settled bed at 9 cm. above the distributor

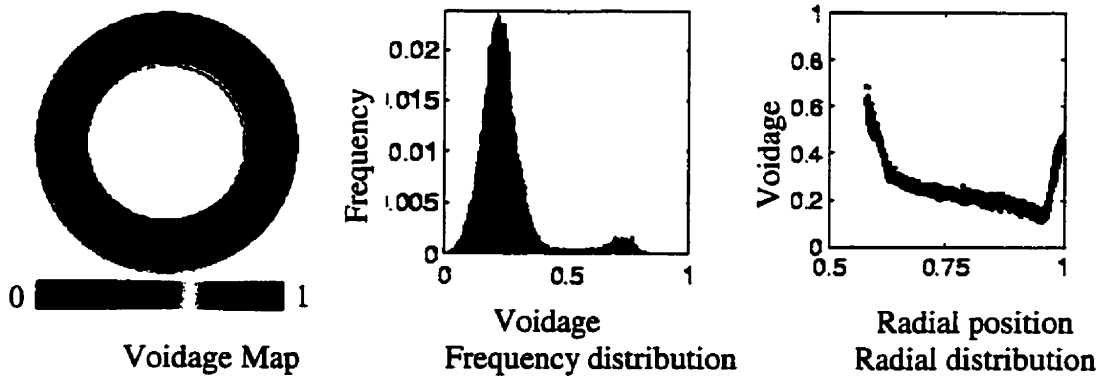

Fig. 11 Settled bed at 10 cm. above the distributor

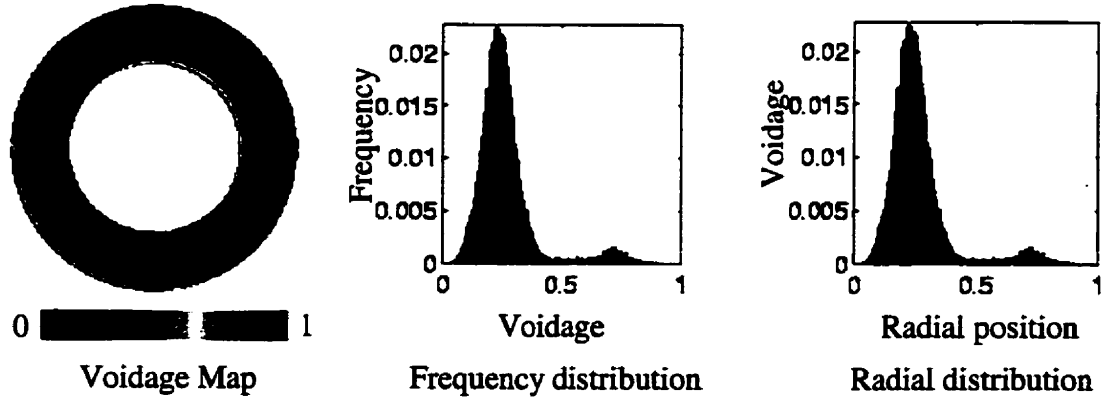

Fig. 12 Settled bed at 11 cm. above the distributor

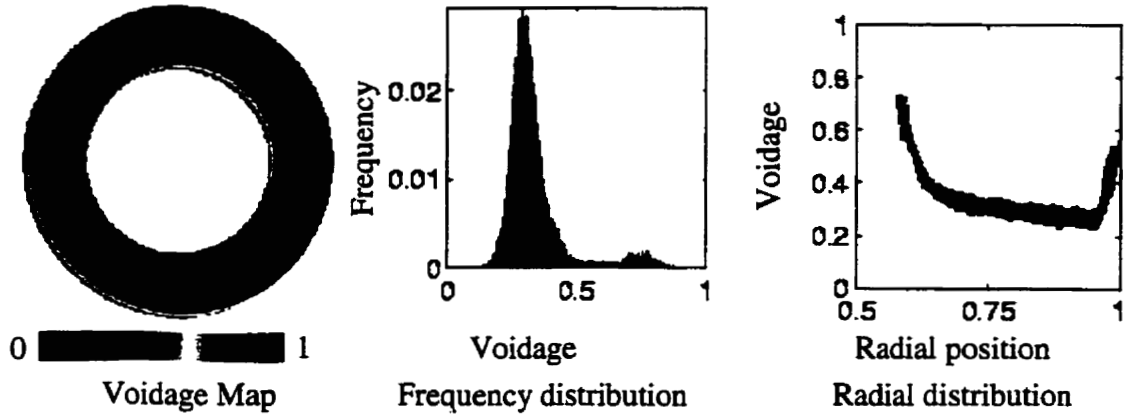

Fig. 13 Settled bed at 12 cm. above the distributor

APPENDIX C

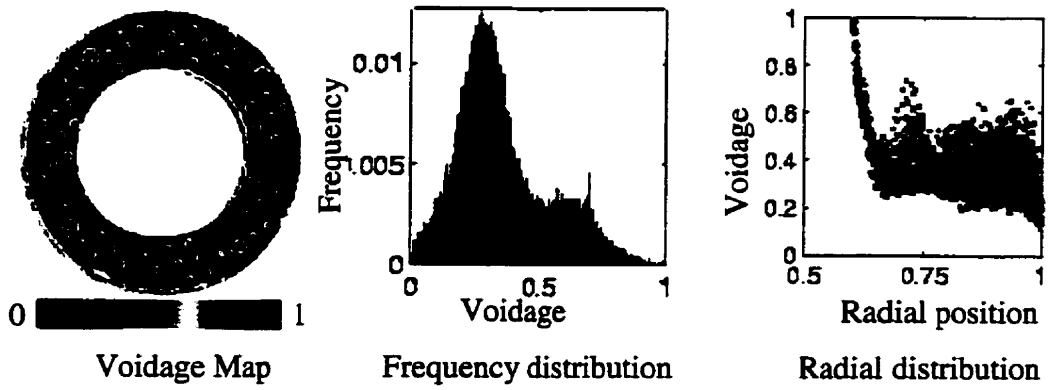

Fig. 1 Fluidized bed with U_s=1.00 cm/s at the distributor

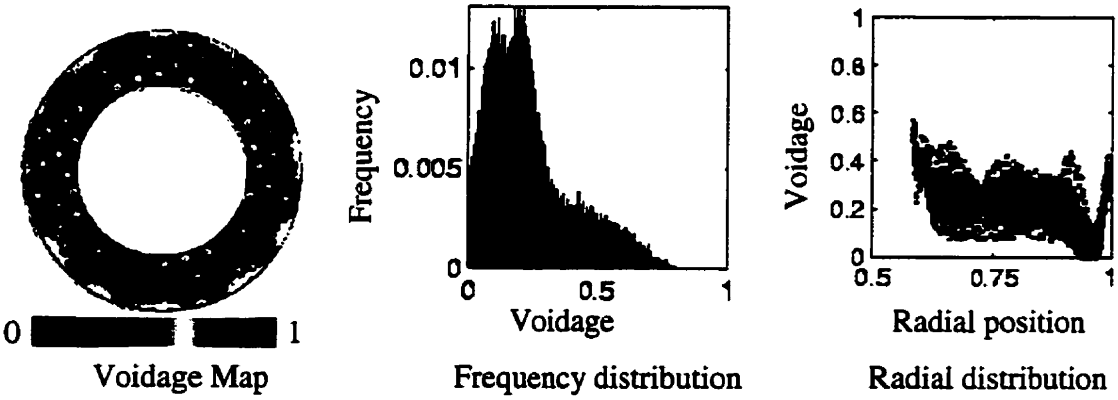

Fig. 2 Fluidized bed with U_s=1.00 cm/s at 1 cm. above the distributor

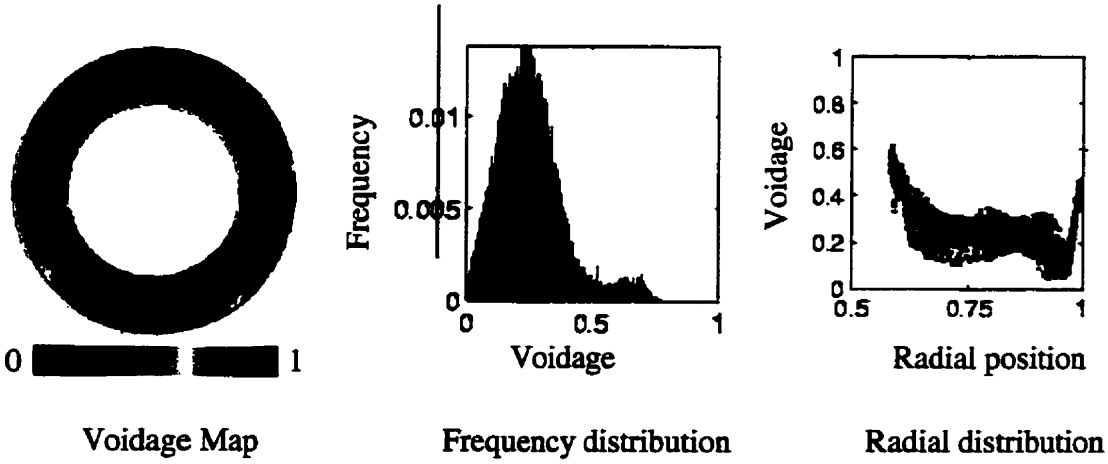

Fig. 3 Fluidized bed with U_s=1.00 cm/s at 2 cm. above the distributor

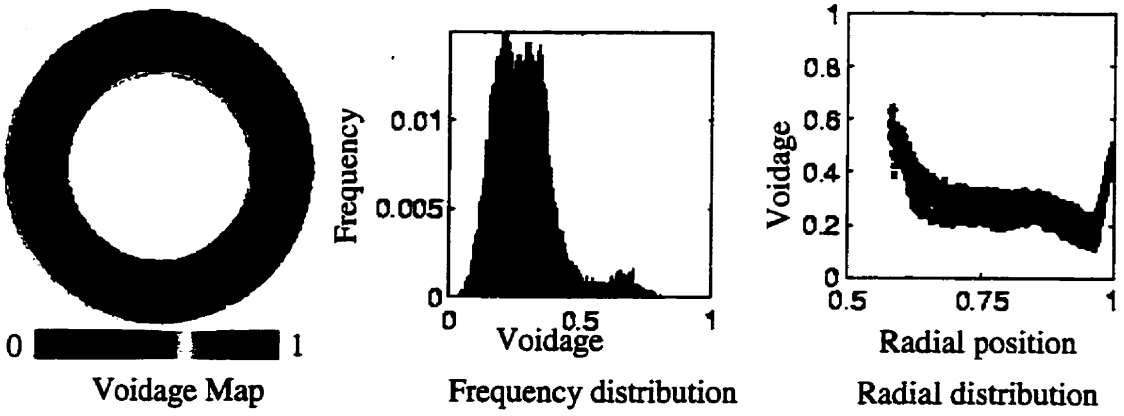

Fig. 4 Fluidized bed with U_s=1.00 cm/s at 3 cm. above the distributor

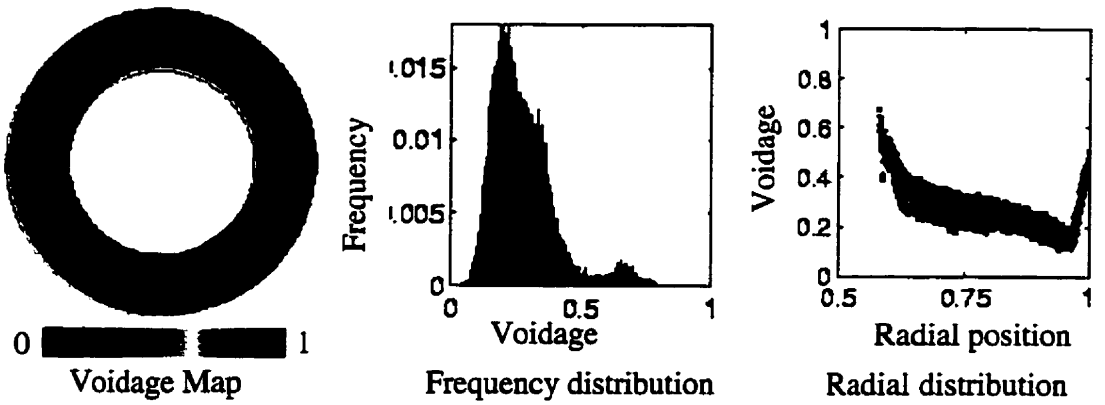

Fig. 5 Fluidized bed with U_s=1.00 cm/s at 4 cm. above the distributor

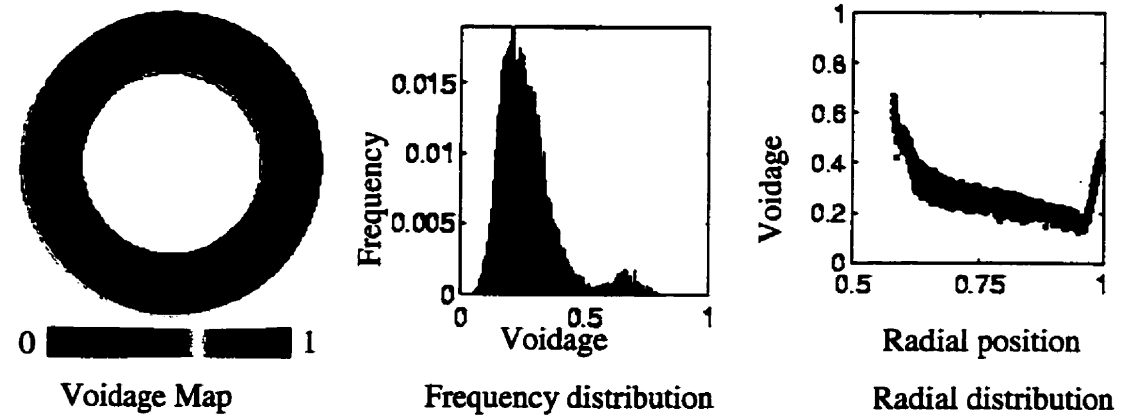

Fig. 6 Fluidized bed with U_s=1.00 cm/s at 5 cm. above the distributor

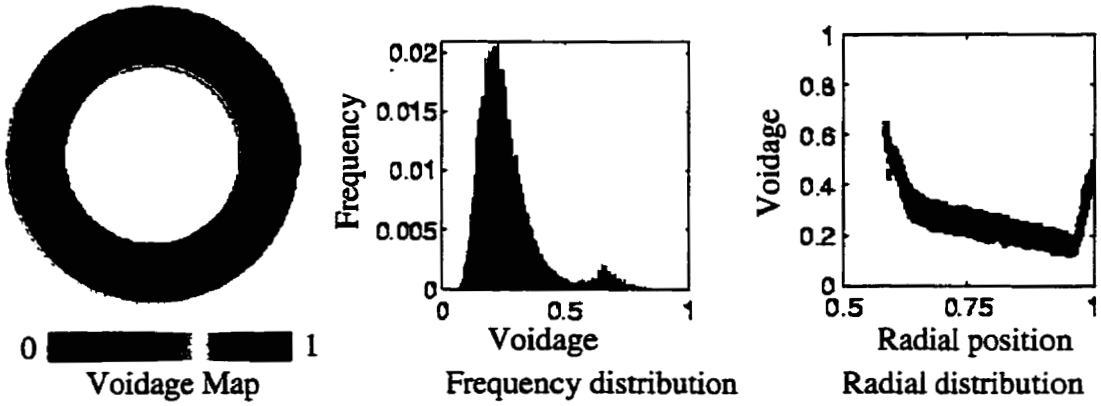

Fig. 7 Fluidized bed with U_s=1.00 cm/s at 6 cm. above the distributor

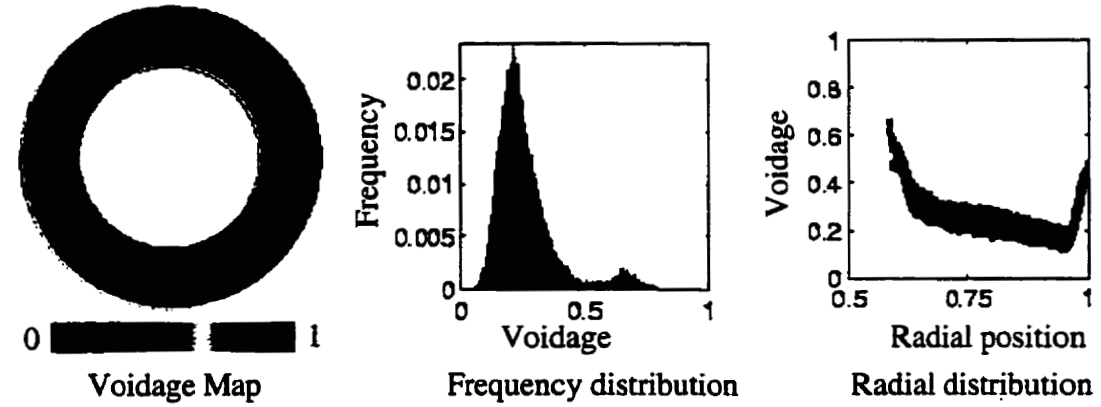

Fig. 8 Fluidized bed with U_s=1.00 cm/s at 7 cm. above the distributor

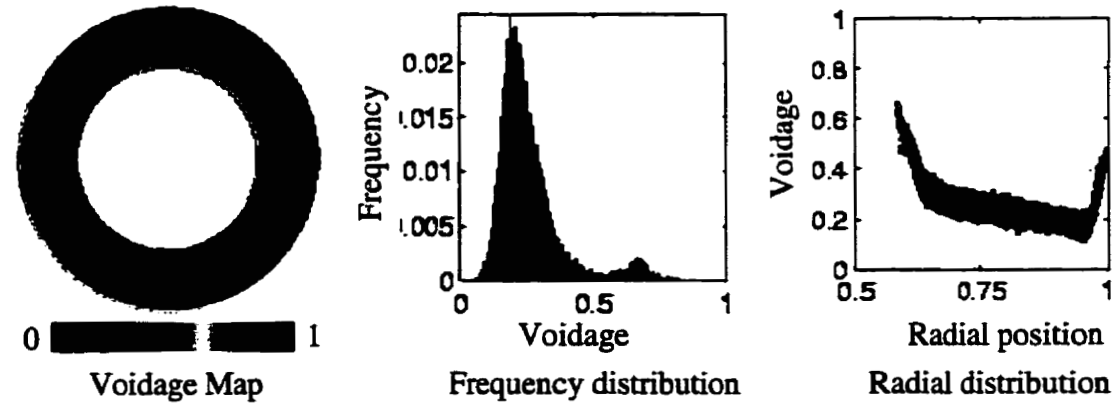

Fig. 9 Fluidized bed with U_s=1.00 cm/s at 8 cm. above the distributor

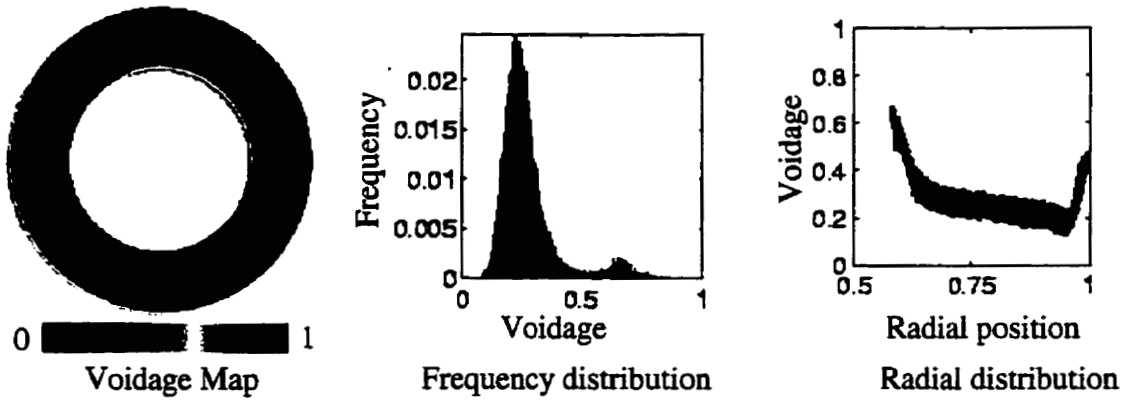

Fig. 10 Fluidized bed with U_s=1.00 cm/s at 9 cm. above the distributor

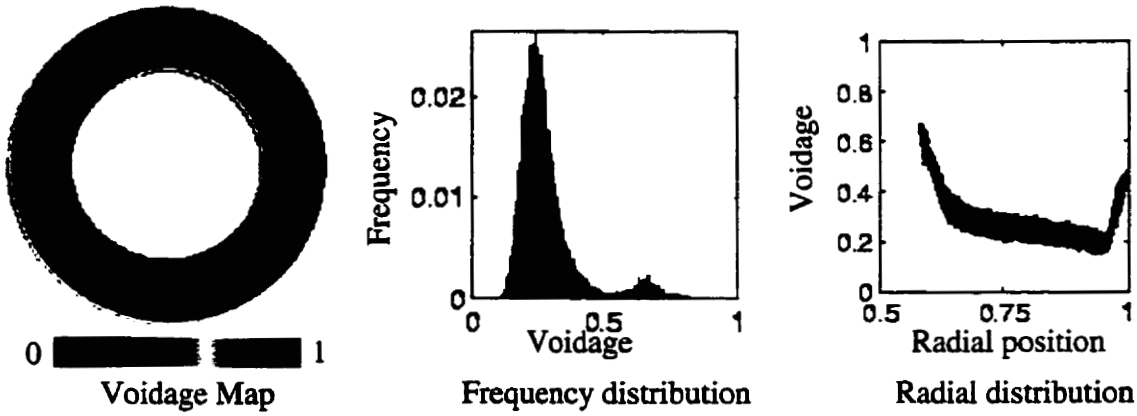

Fig. 11 Fluidized bed with U_s=1.00 cm/s at 10 cm. above the distributor

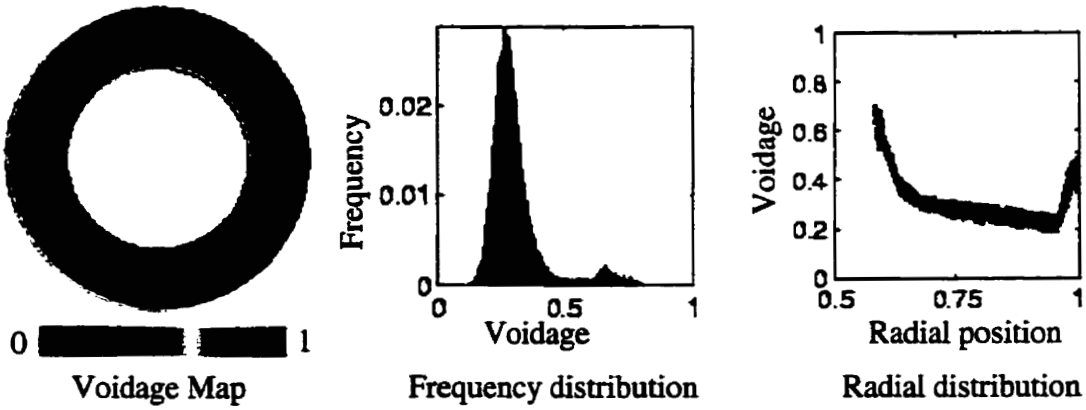

Fig. 12 Fluidized bed with U_s=1.00 cm/s at 11 cm. above the distributor

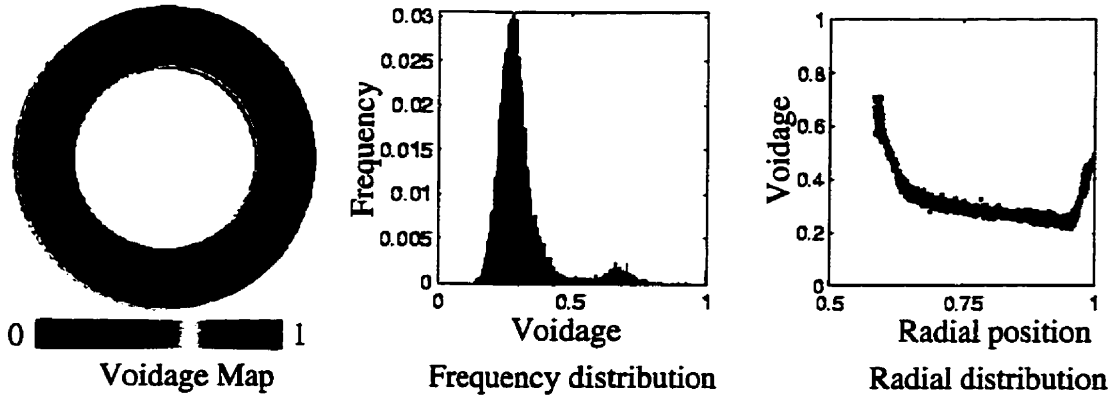

Fig. 13 Fluidized bed with U_s=1.00 cm/s at 12 cm. above the distributor

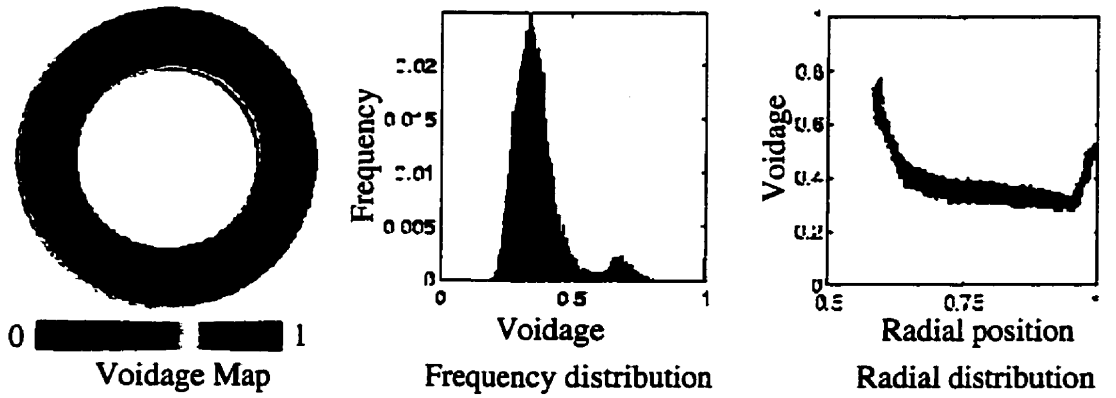

Fig. 14 Fluidized bed with U_s=1.00 cm/s at 13 cm. above the distributor

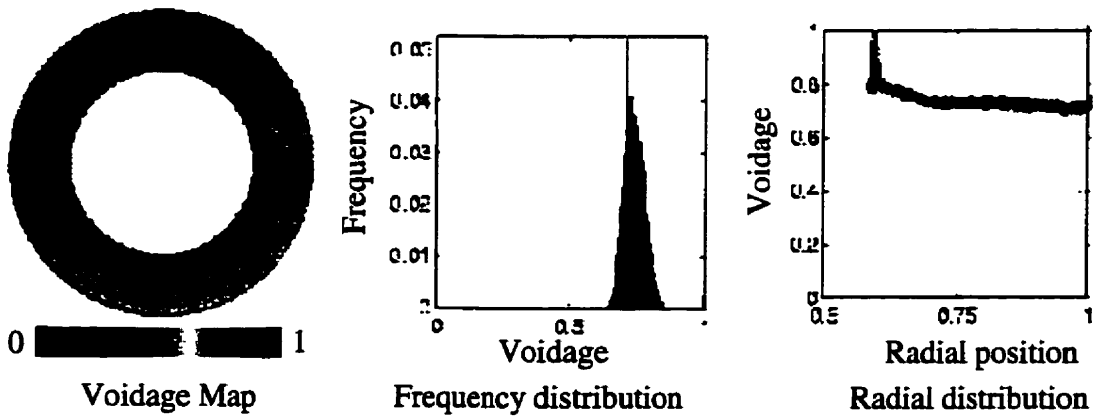

Fig. 15 Fluidized bed with U_s=1.00 cm/s at 14 cm. above the distributor

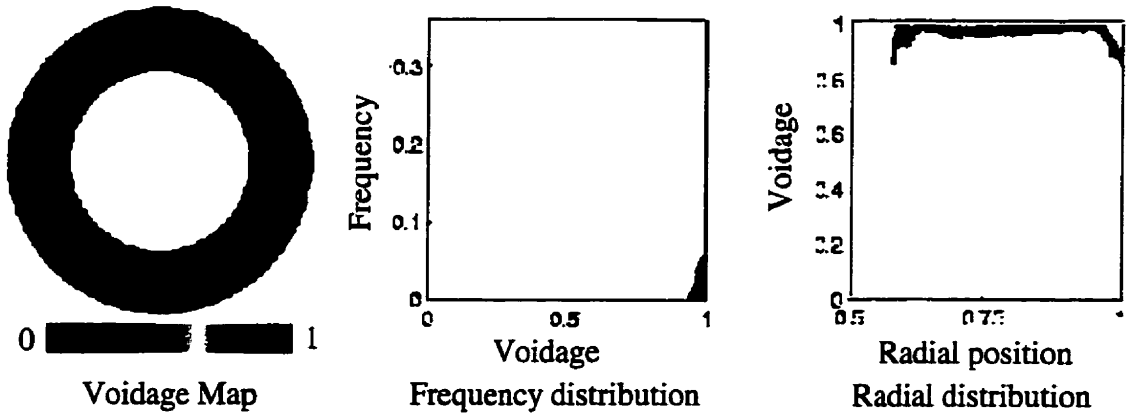

Fig. 16 Fluidized bed with U_s=1.00 cm/s at 15 cm. above the distributor

APPENDIX D

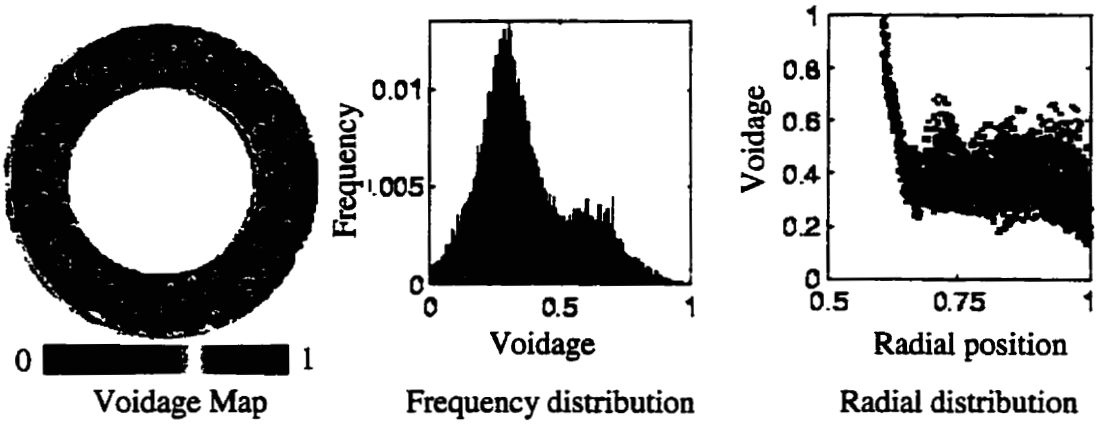

Fig. 1 Fluidized bed with U_s=1.33 cm/s at the distributor

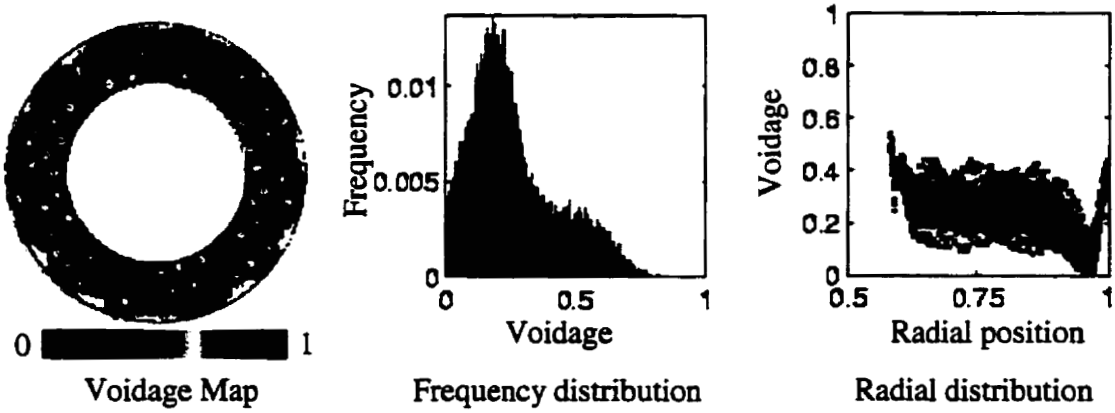

Fig. 2 Fluidized bed with U_s=1.33 cm/s at 1 cm. above the distributor

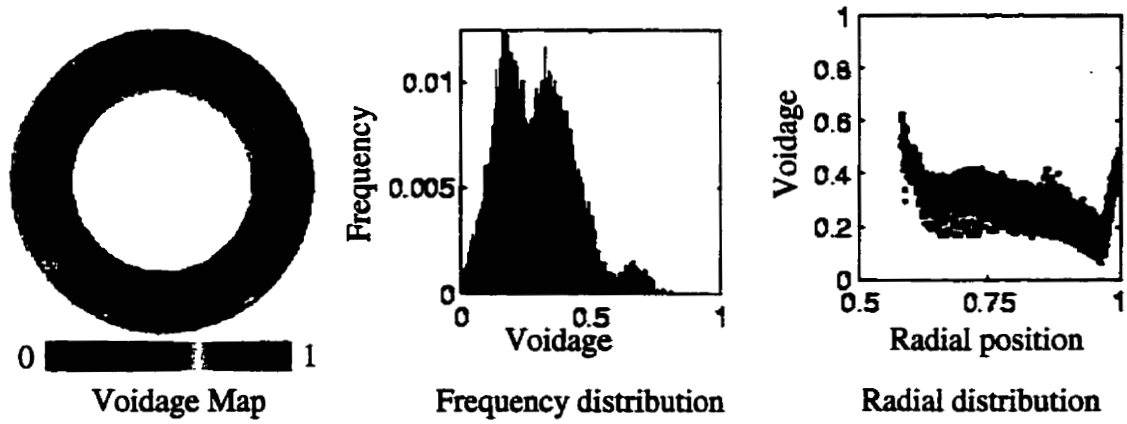

Fig. 3 Fluidized bed with U_s=1.33 cm/s at 2 cm. above the distributor

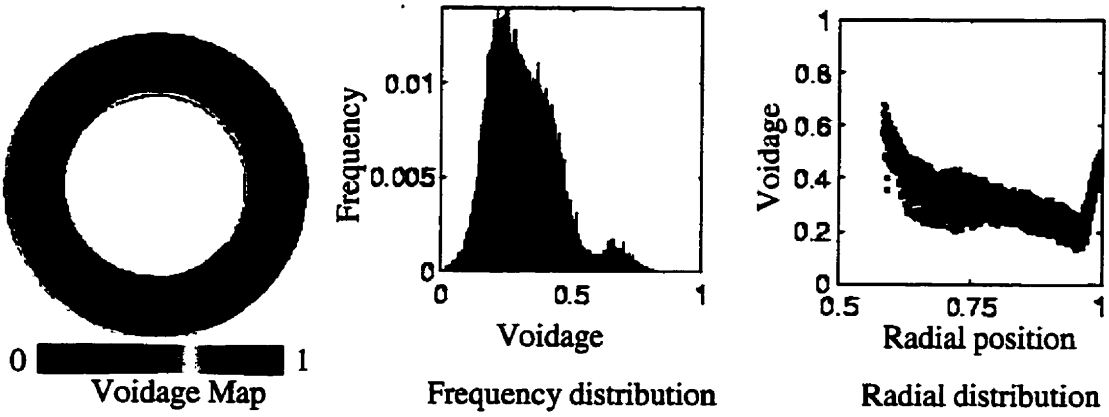

Fig. 4 Fluidized bed with U_s=1.33 cm/s at 3 cm. above the distributor

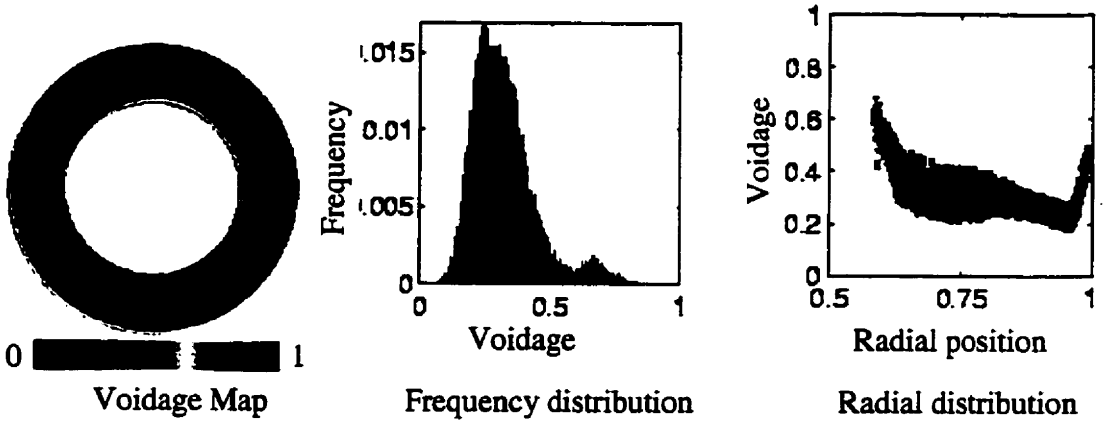

Fig. 5 Fluidized bed with U_s=1.33 cm/s at 4 cm. above the distributor

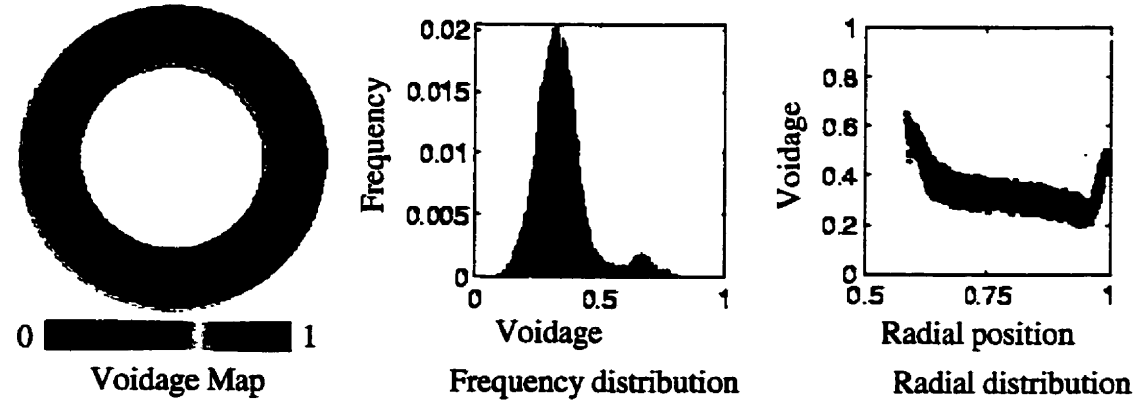

Fig. 6 Fluidized bed with U_s=1.33 cm/s at 5 cm. above the distributor

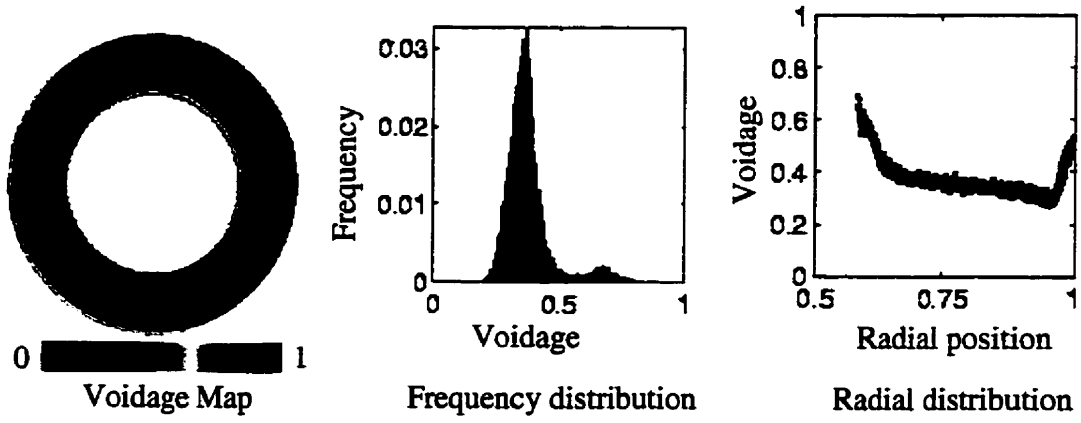

Fig. 7 Fluidized bed with U_s=1.33 cm/s at 6 cm. above the distributor

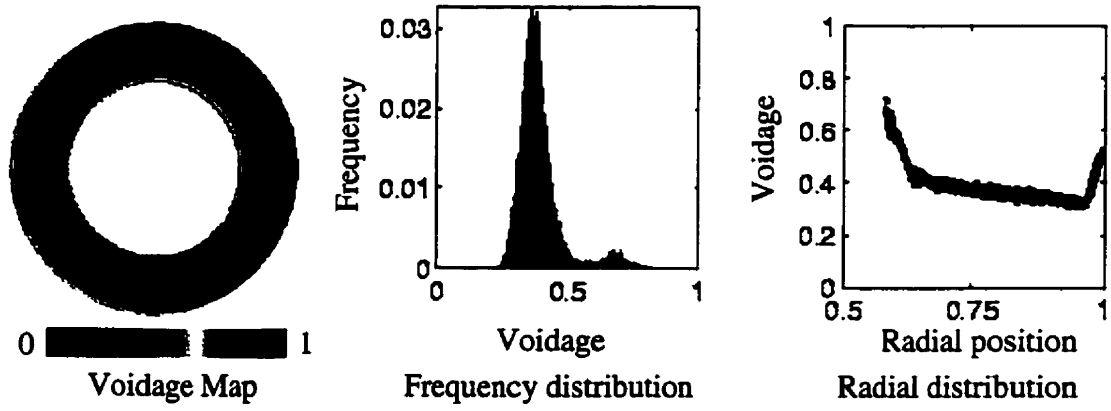

Fig. 8 Fluidized bed with U_s=1.33 cm/s at 7 cm. above the distributor

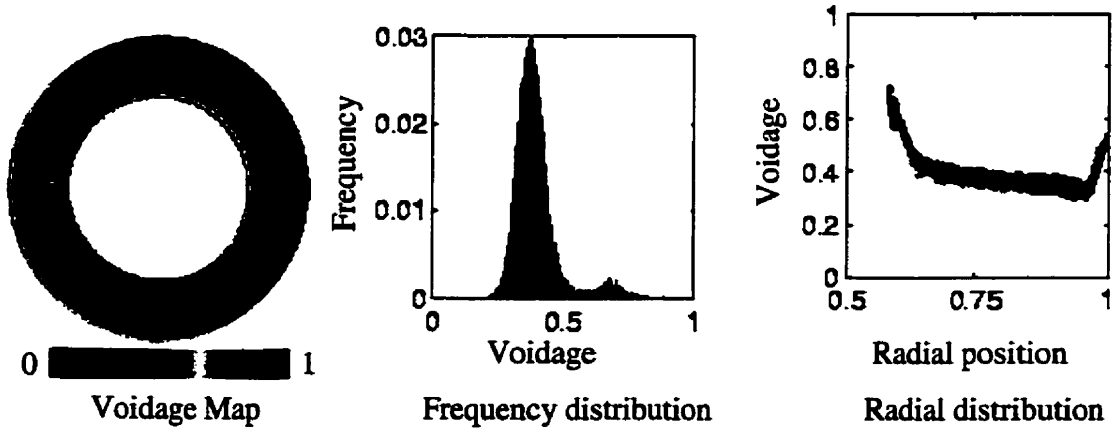

Fig. 9 Fluidized bed with U_s=1.33 cm/s at 8 cm. above the distributor

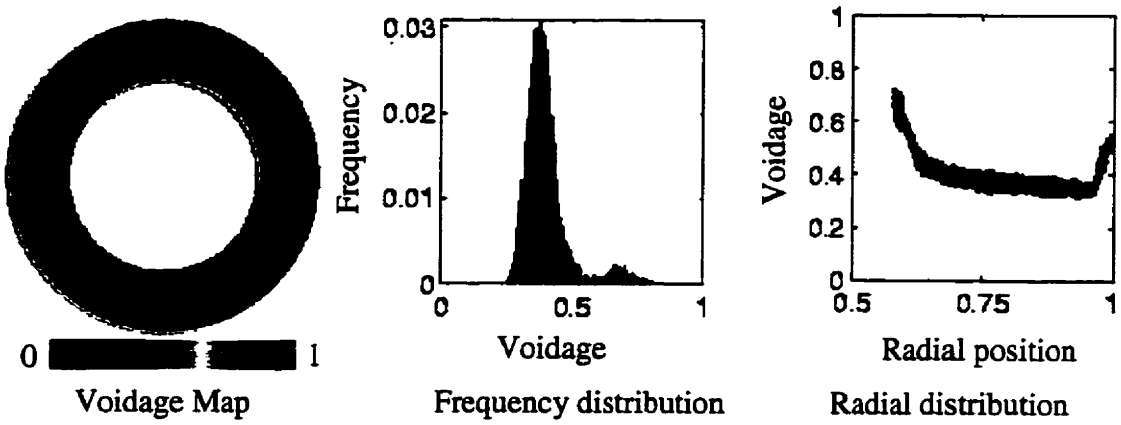

Fig. 10 Fluidized bed with U_s=1.33 cm/s at 9 cm. above the distributor

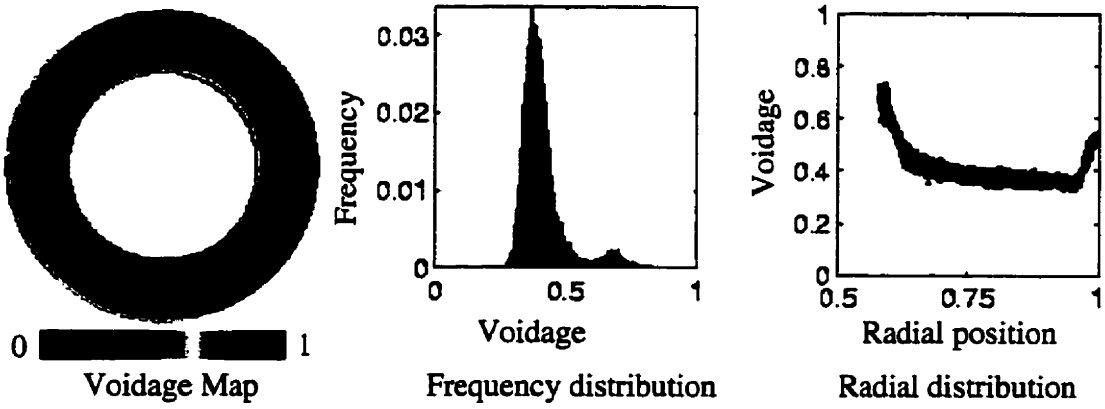

Fig. 11 Fluidized bed with U_s=1.33 cm/s at 10 cm. above the distributor

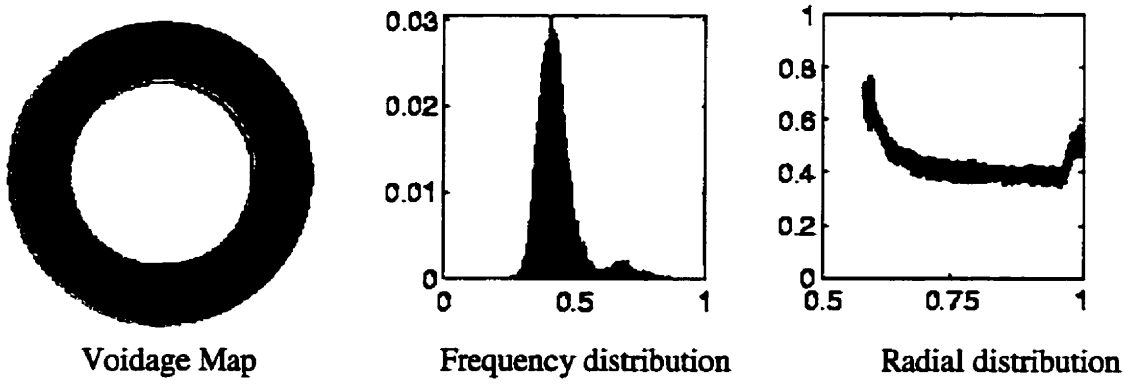

Fig. 12 Fluidized bed with U_s=1.33 cm/s at 11 cm. above the distributor

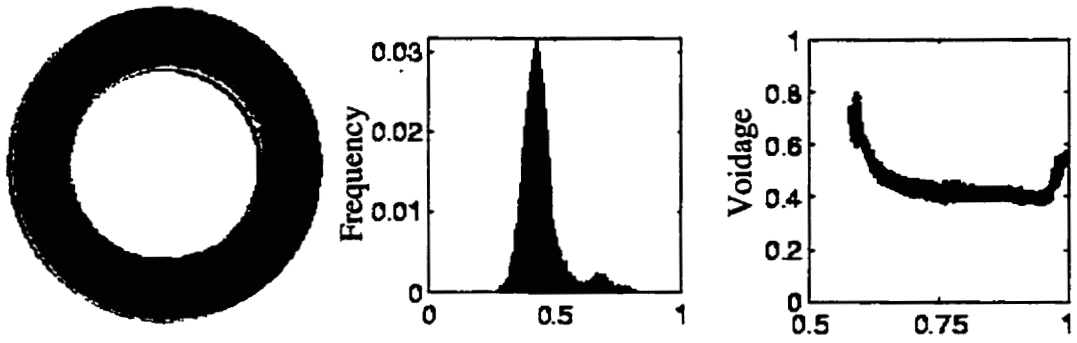

Voidage Map Frequency distribution Radial distribution

Fig. 13 Fluidized bed with U_s=1.33 cm/s at 12 cm. above the distributor

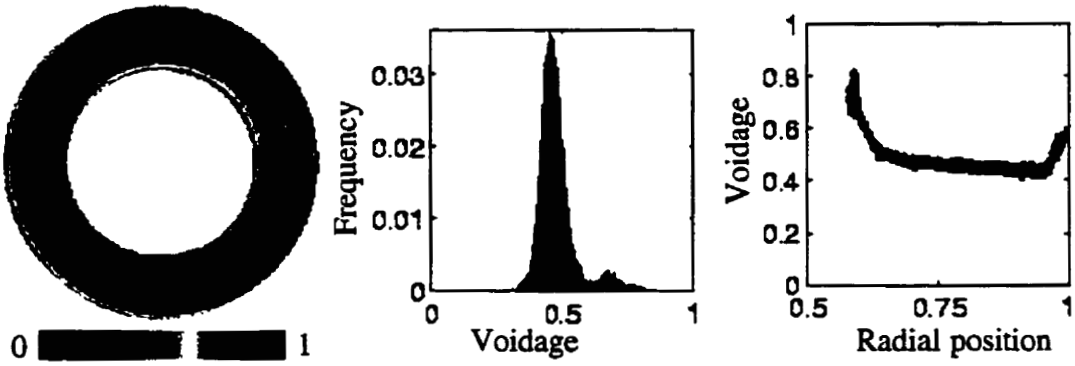

Voidage Map Frequency distribution Radial distribution

Fig. 14 Fluidized bed with U_s=1.33 cm/s at 13 cm. above the distributor

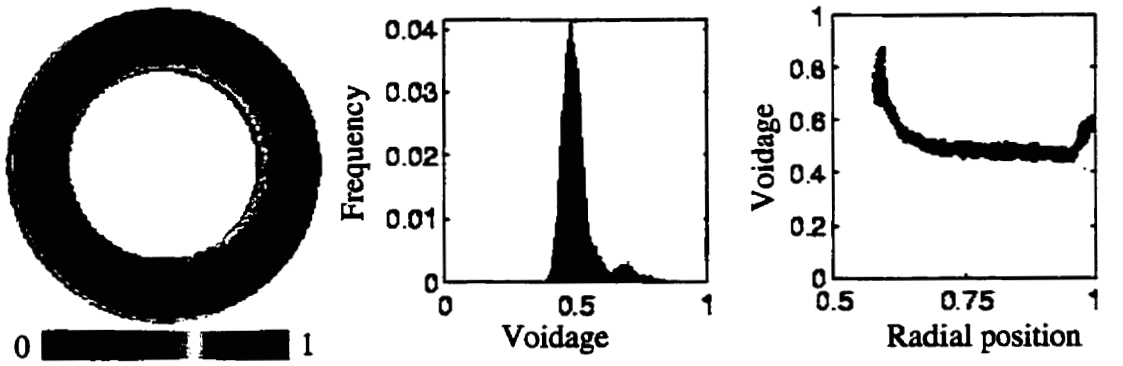

Voidage Map Frequency distribution Radial distribution

Fig. 15 Fluidized bed with U_s=1.33 cm/s at 14 cm. above the distributor

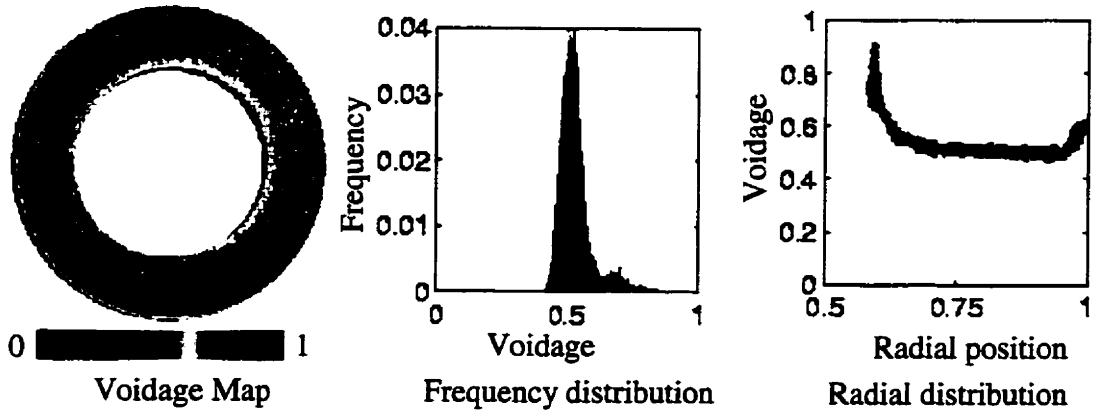

Fig. 16 Fluidized bed with U_s=1.33 cm/s at 15 cm. above the distributor

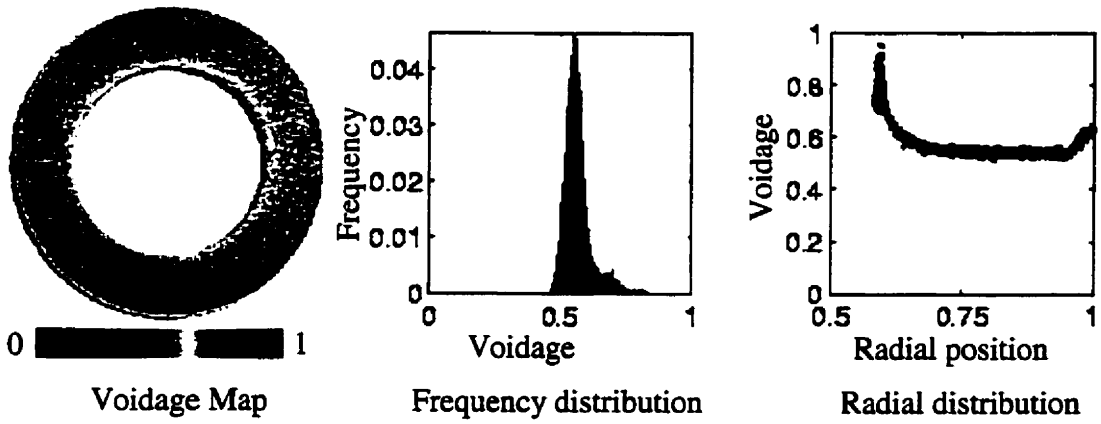

Fig. 17 Fluidized bed with U_s=1.33 cm/s at 16 cm. above the distributor

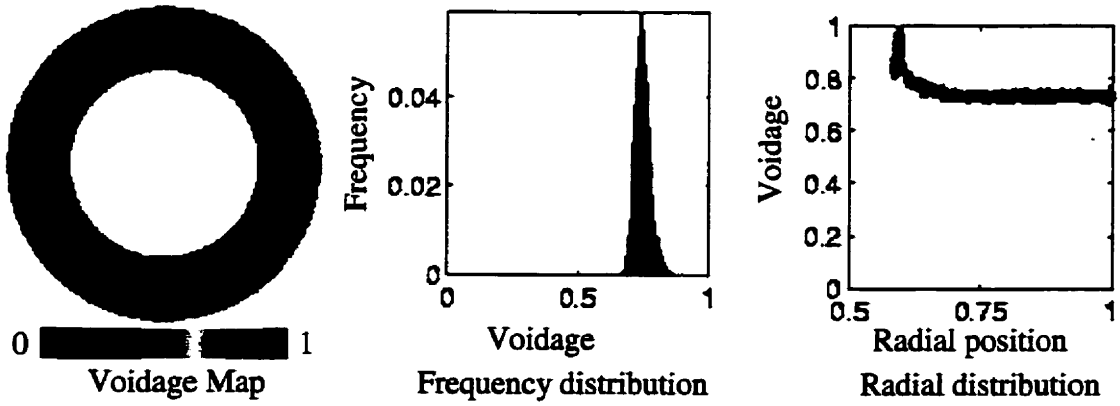

Fig. 18 Fluidized bed with U_s=1.33 cm/s at 17 cm. above the distributor

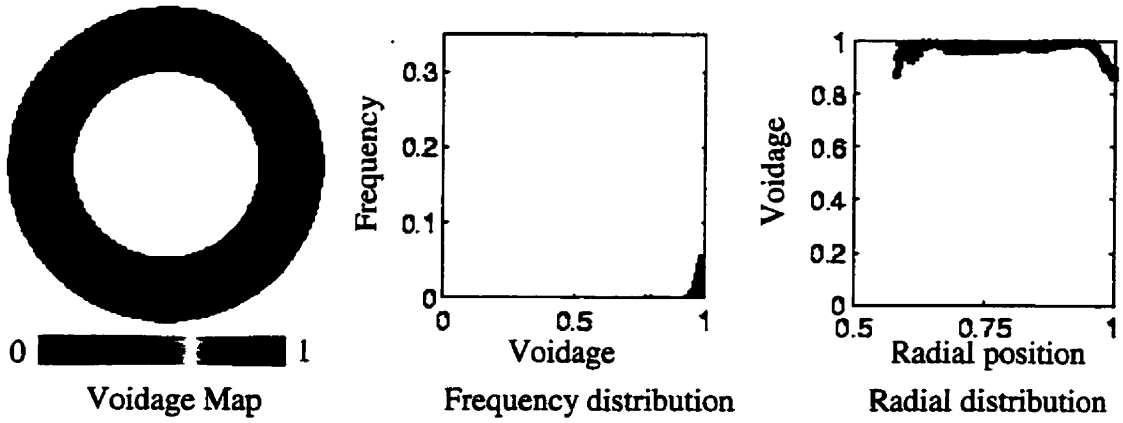

Fig. 19 Fluidized bed with U_s=1.33 cm/s at 18 cm. above the distributor

APPENDIX E

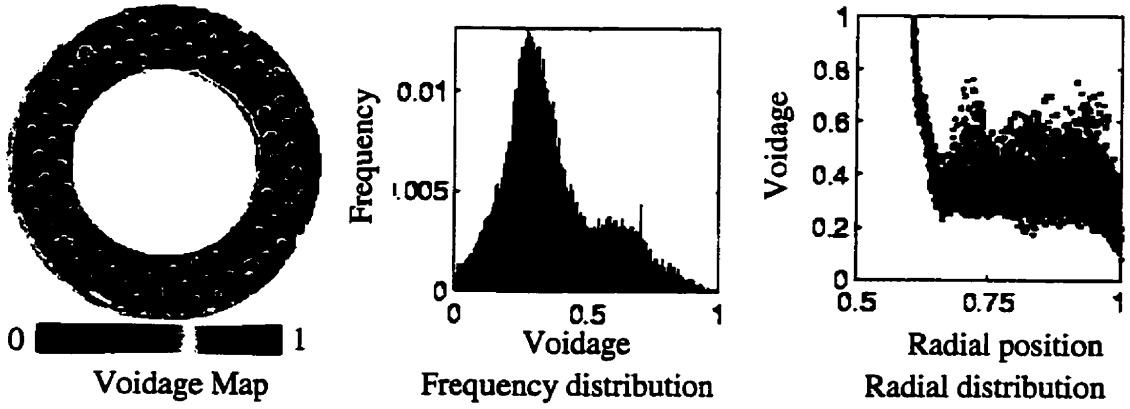

Fig. 1 Fluidized bed with U_s=1.66 cm/s at the distributor

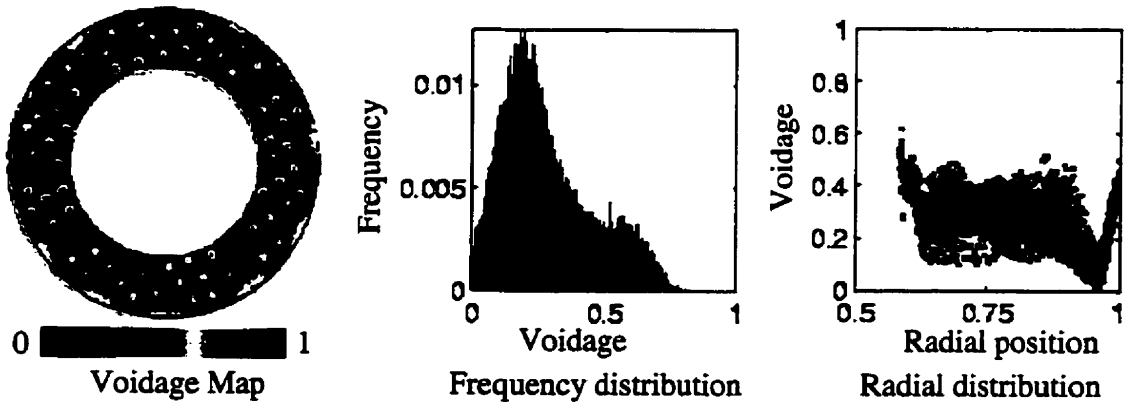

Fig. 2 Fluidized bed with U_s=1.66 cm/s at 1 cm. above the distributor

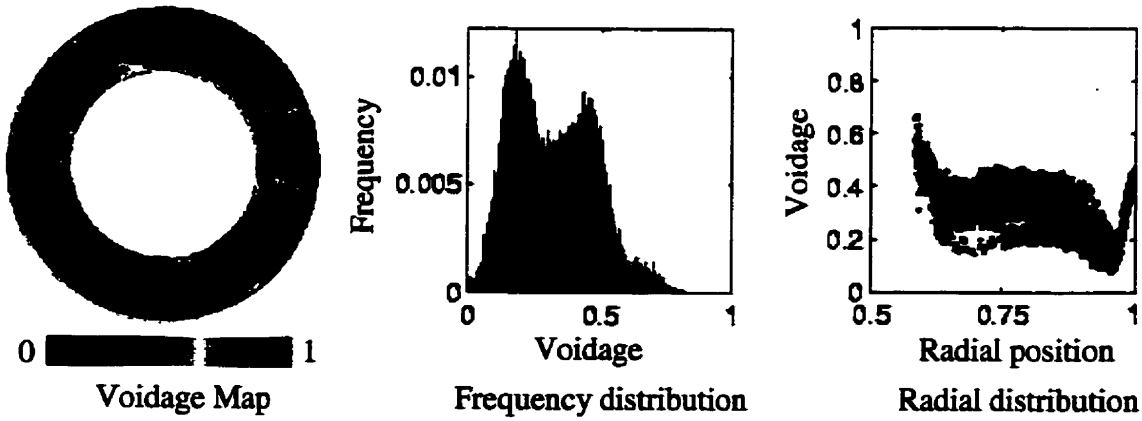

Fig. 3 Fluidized bed with U_s=1.66 cm/s at 2 cm. above the distributor

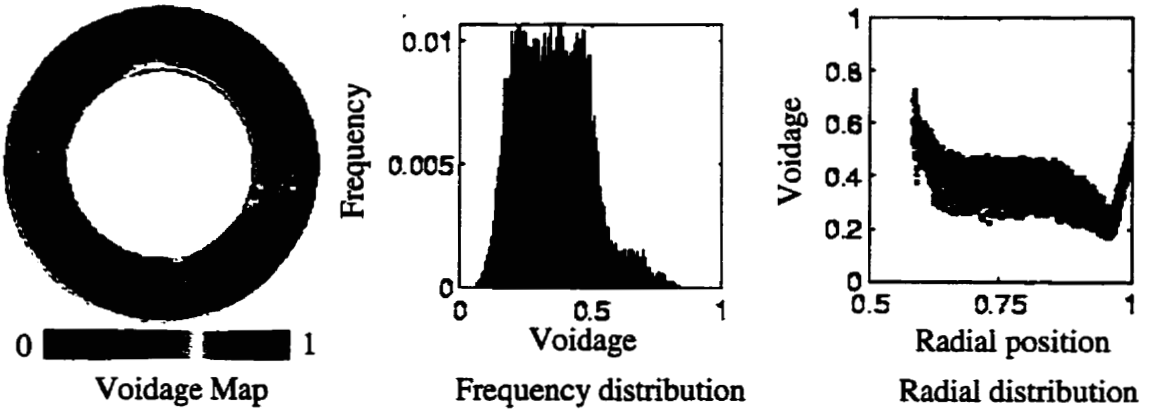

Fig. 4 Fluidized bed with U_s=1.66 cm/s at 3 cm. above the distributor

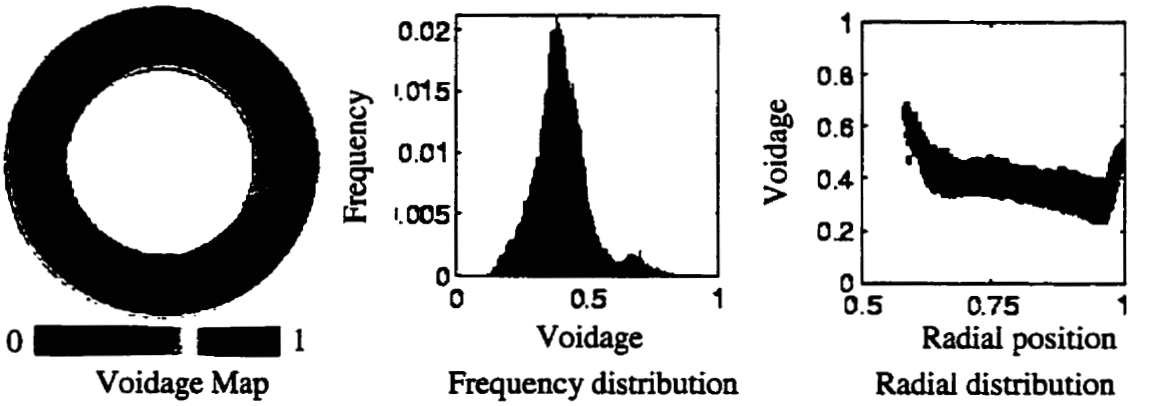

Fig. 5 Fluidized bed with U_s=1.66 cm/s at 4 cm. above the distributor

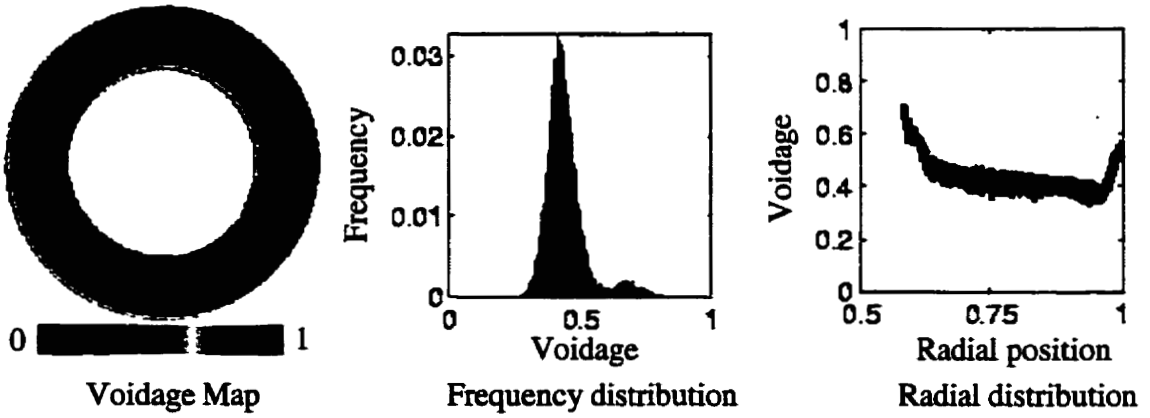

Fig. 6 Fluidized bed with U_s=1.66 cm/s at 5 cm. above the distributor

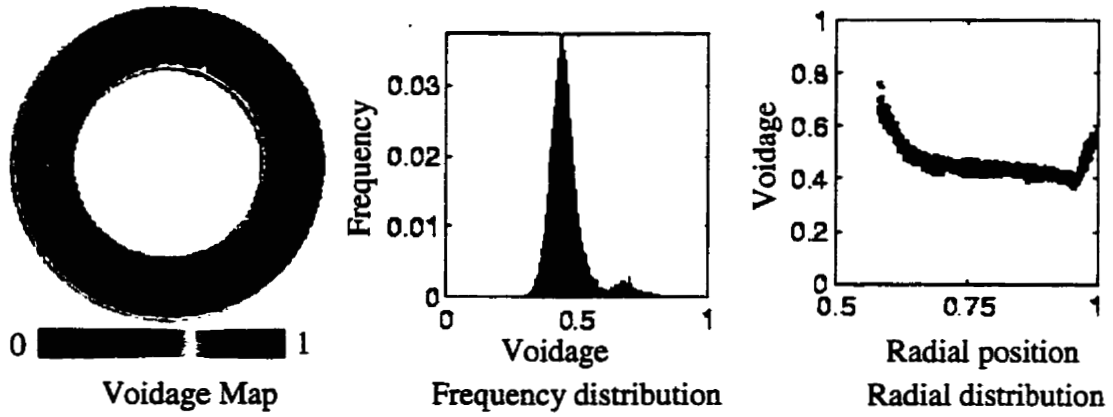

Fig. 7 Fluidized bed with U_s=1.66 cm/s at 6 cm. above the distributor

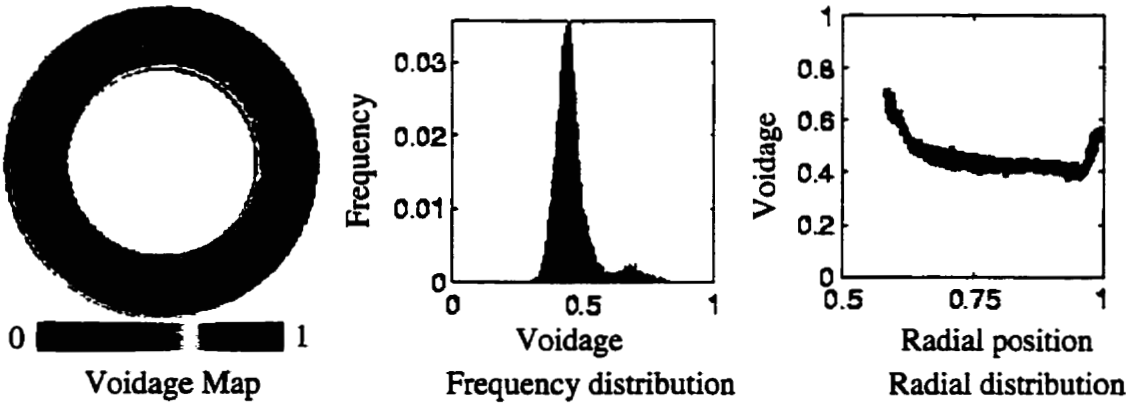

Fig. 8 Fluidized bed with U_s=1.66 cm/s at 7 cm. above the distributor

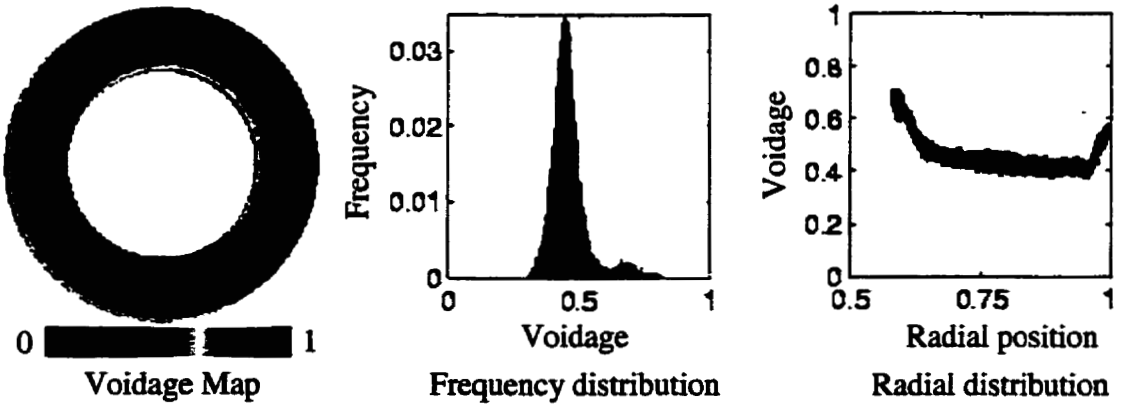

Fig. 9 Fluidized bed with U_s=1.66 cm/s at 8 cm. above the distributor

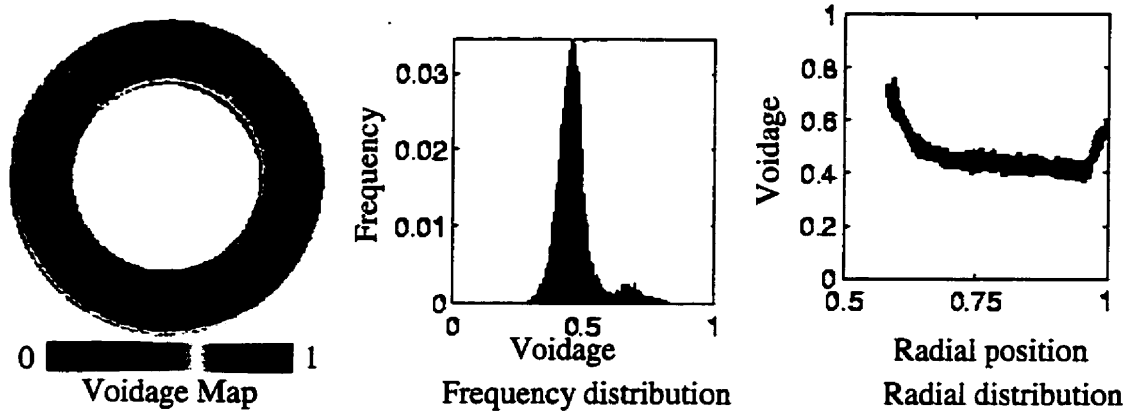

Fig. 10 Fluidized bed with U_s=1.66 cm/s at 9 cm. above the distributor

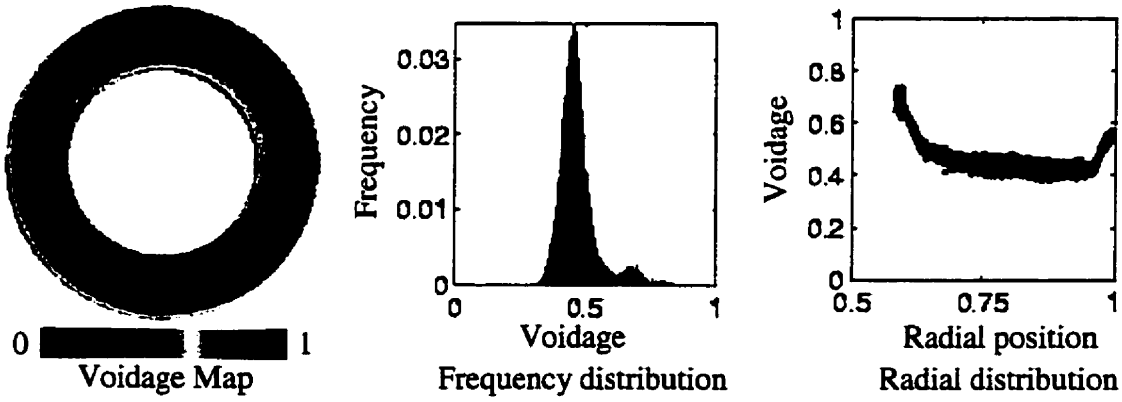

Fig. 11 Fluidized bed with U_s=1.66 cm/s at 10 cm. above the distributor

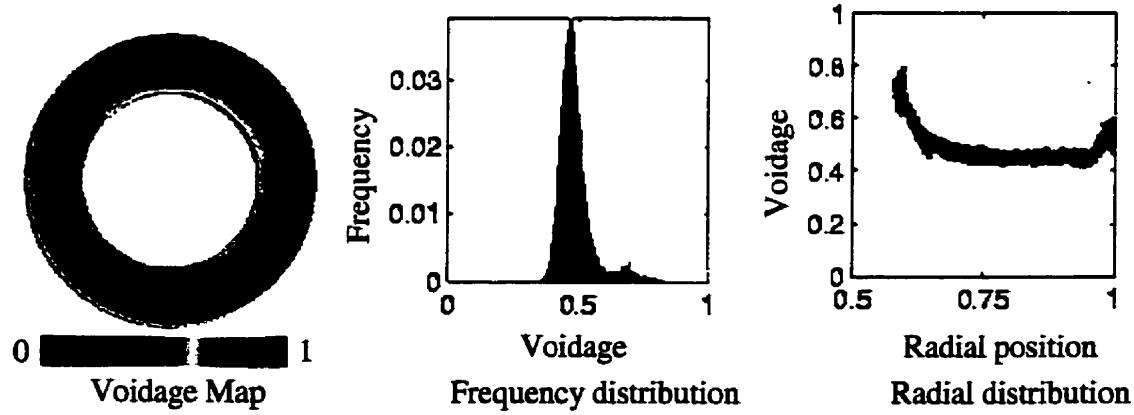

Fig. 12 Fluidized bed with U_s=1.66 cm/s at 11 cm. above the distributor

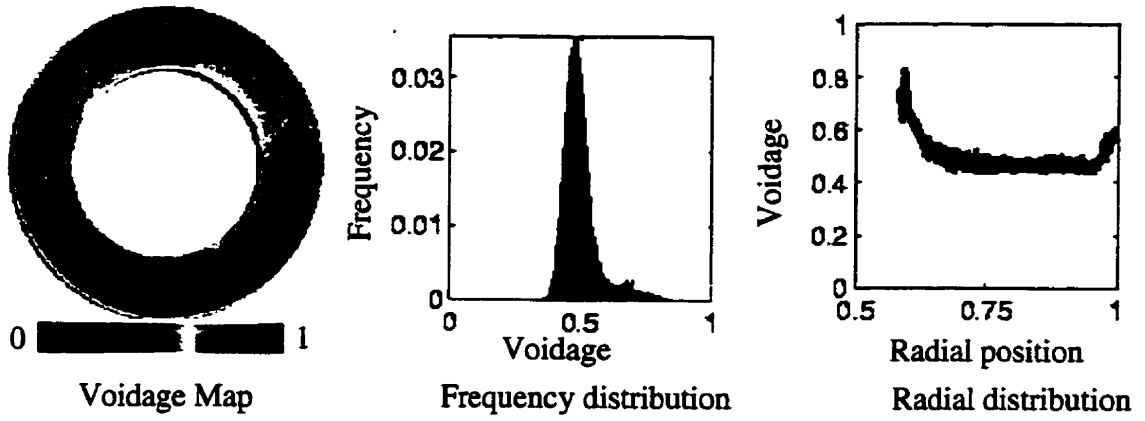

Fig. 13 Fluidized bed with U_s=1.66 cm/s at 12 cm. above the distributor

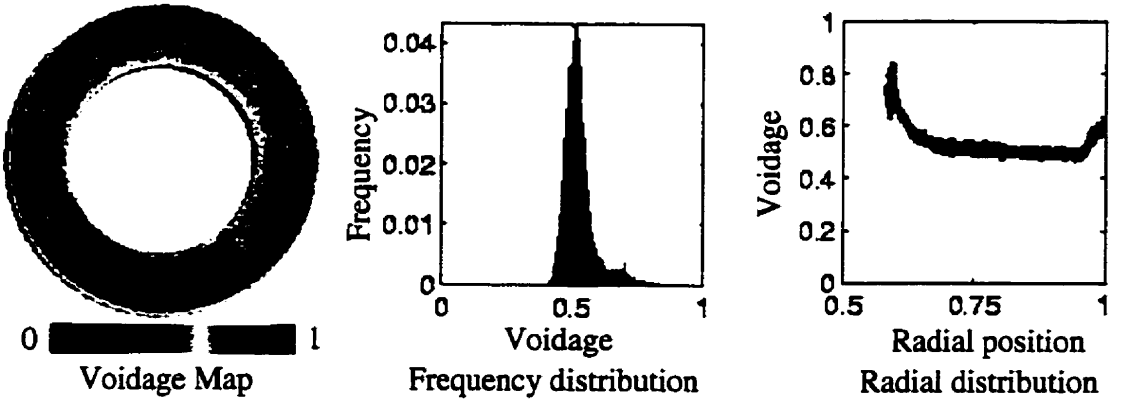

Fig. 14 Fluidized bed with U_s=1.66 cm/s at 13 cm. above the distributor

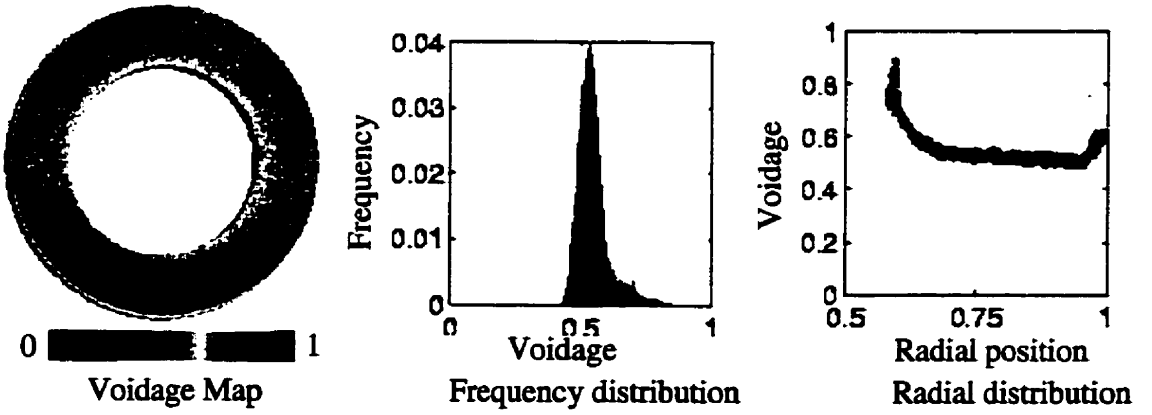

Fig. 15 Fluidized bed with U_s=1.66 cm/s at 14 cm. above the distributor

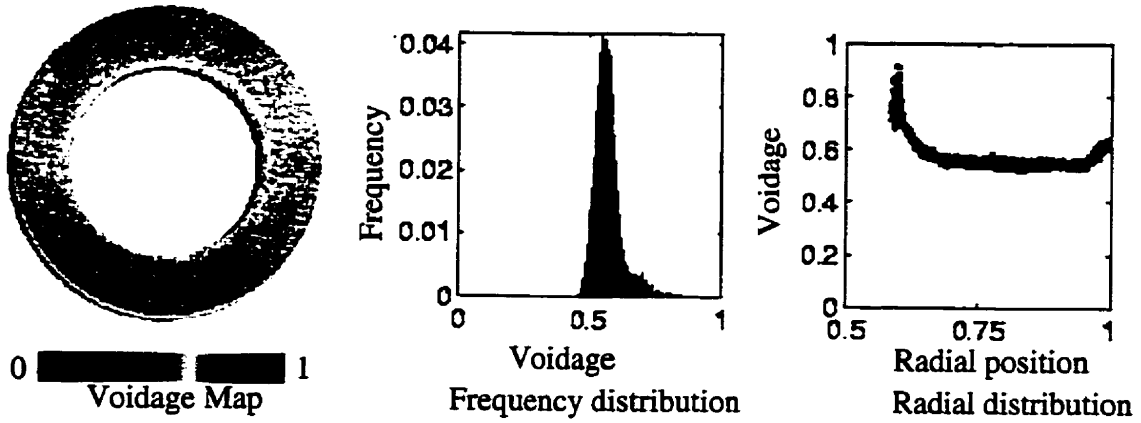

Fig. 16 Fluidized bed with U_s=1.66 cm/s at 15 cm. above the distributor

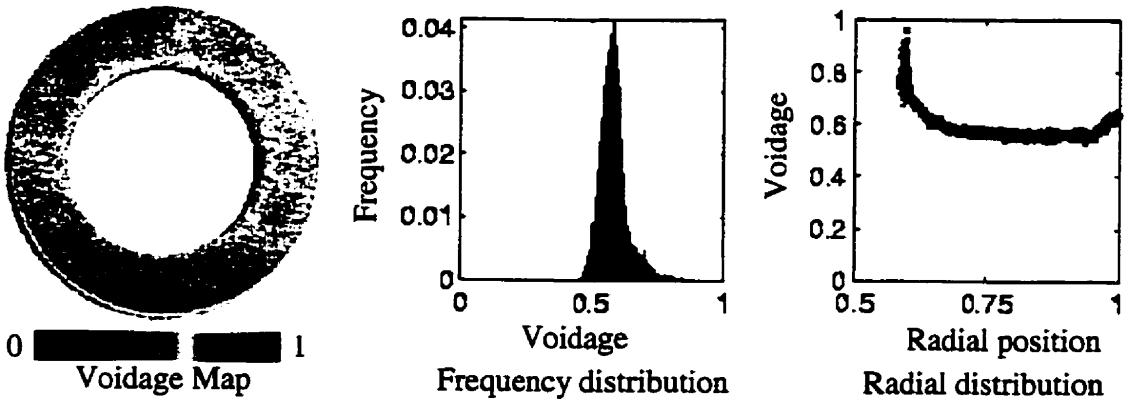

Fig. 17 Fluidized bed with U_s=1.66 cm/s at 16 cm. above the distributor

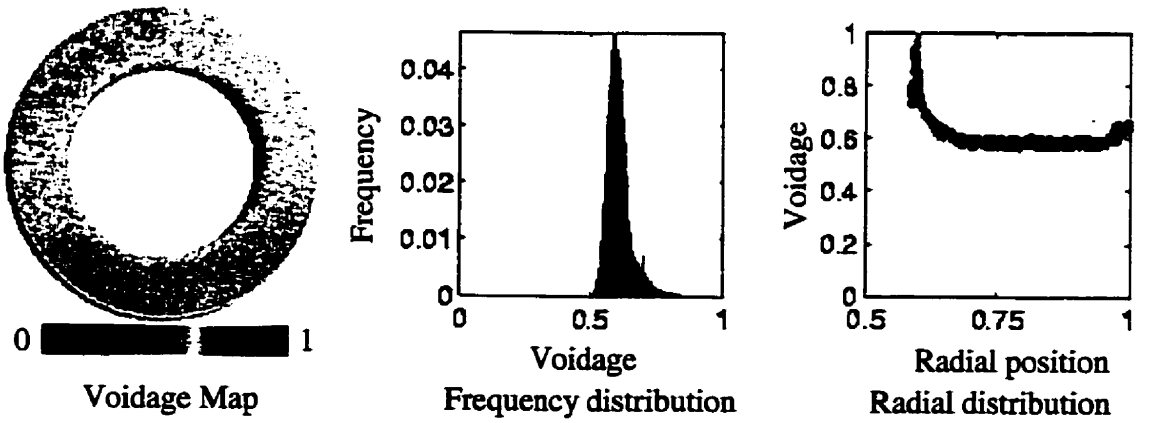

Fig. 18 Fluidized bed with U_s=1.66 cm/s at 17 cm. above the distributor

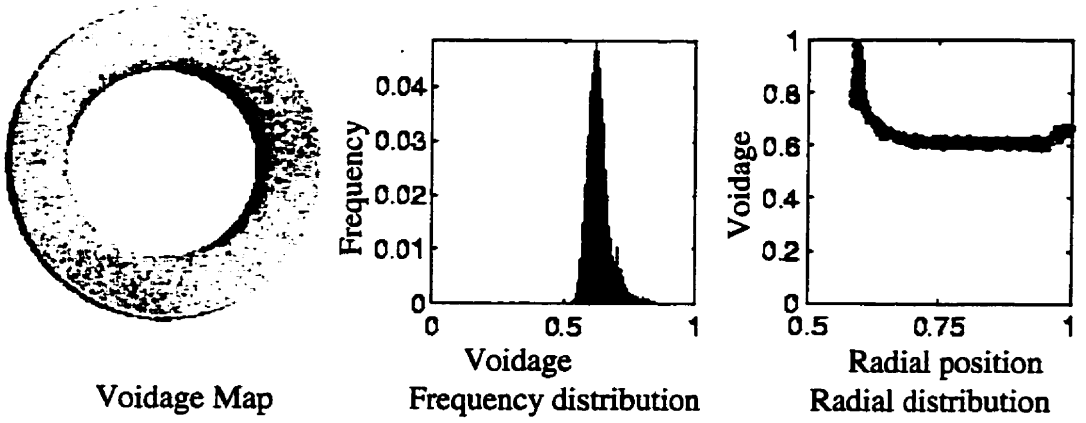

Fig. 19 Fluidized bed with U_s=1.66 cm/s at 18 cm. above the distributor

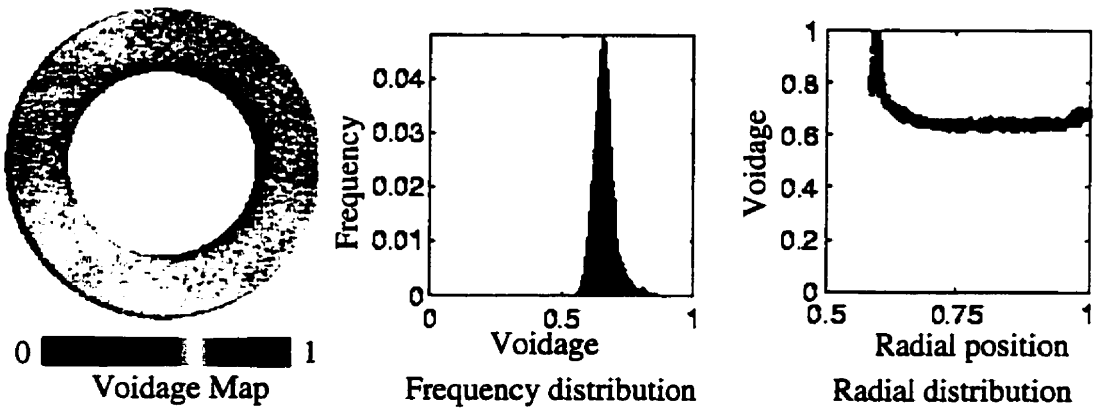

Fig. 20 Fluidized bed with U_s=1.66 cm/s at 19 cm. above the distributor

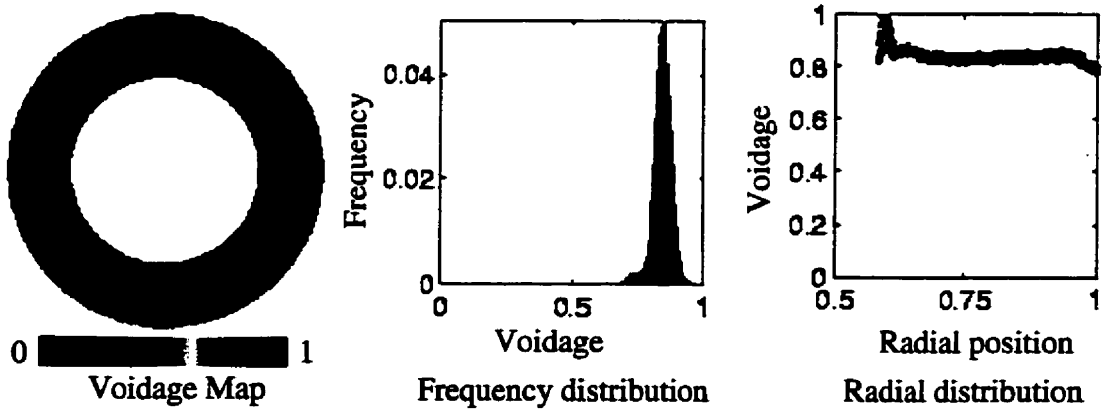

Fig. 21 Fluidized bed with U_s=1.66 cm/s at 20 cm. above the distributor

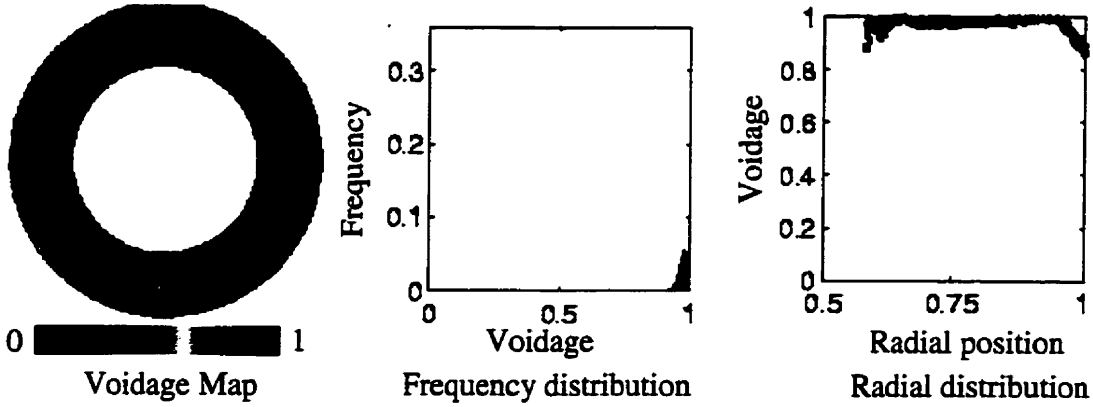

Fig. 22 Fluidized bed with U_s=1.66 cm/s at 21 cm. above the distributor

APPENDIX F

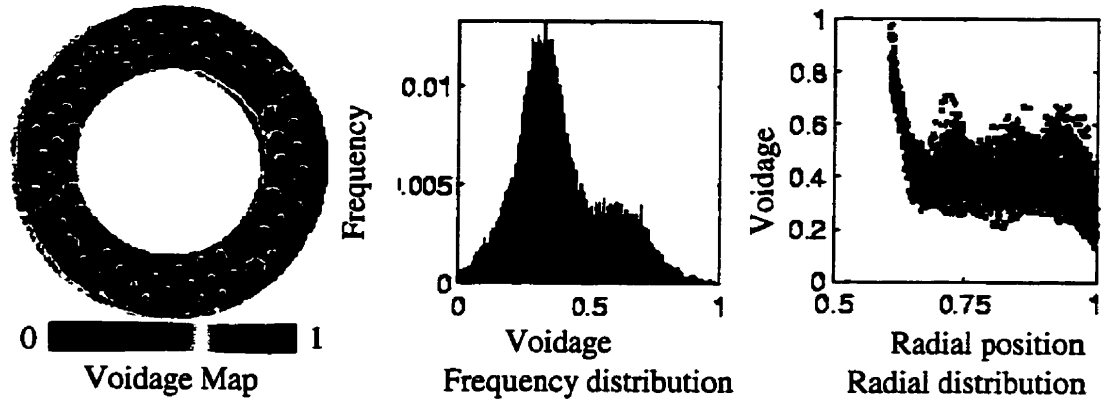

Fig. 1 Fluidized bed with U_s=2.00 cm/s at the distributor

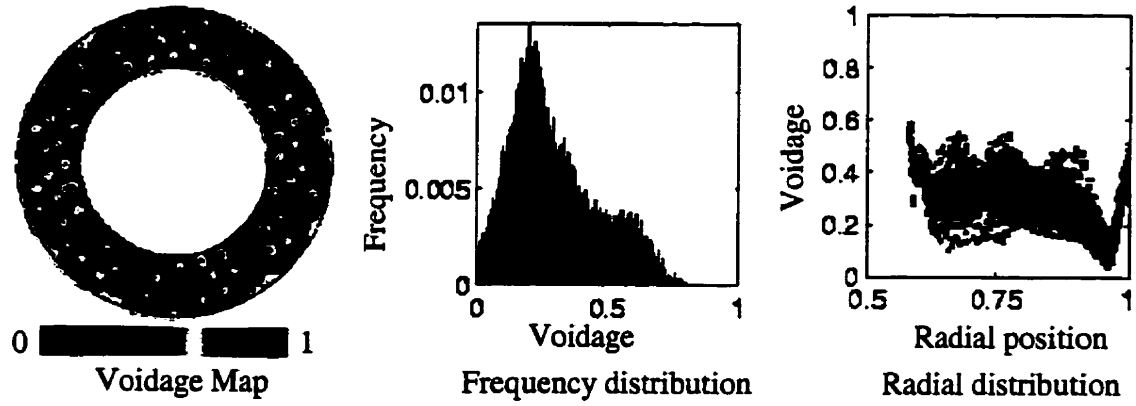

Fig. 2 Fluidized bed with U_s=2.00 cm/s at 1 cm. above the distributor

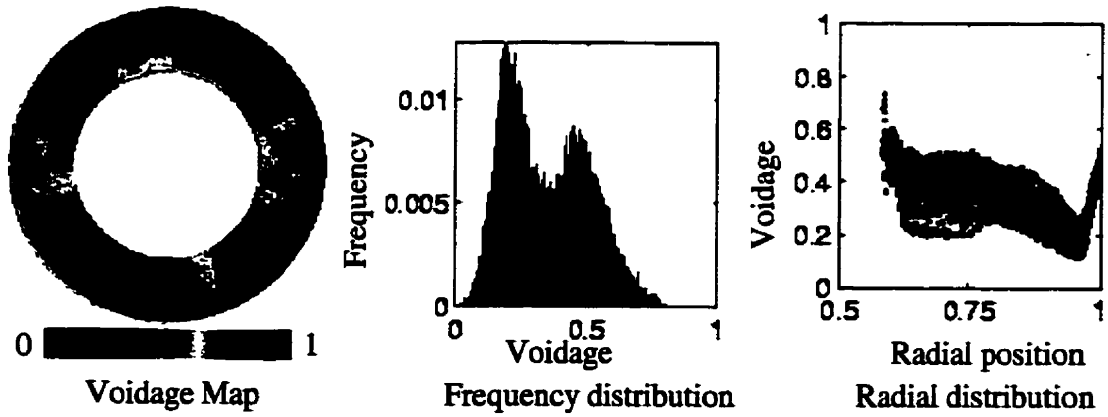

Fig. 3 Fluidized bed with U_s=2.00 cm/s at 2 cm. above the distributor

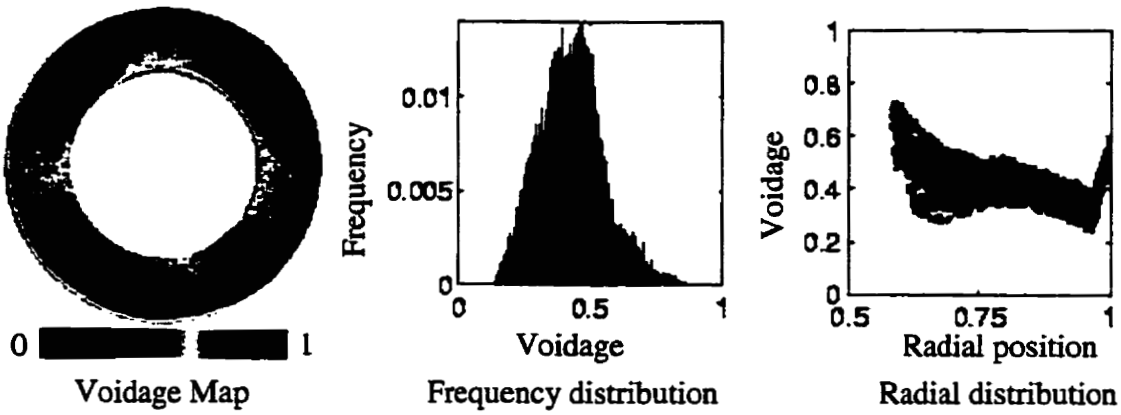

Fig. 4 Fluidized bed with U_s=2.00 cm/s at 3 cm. above the distributor

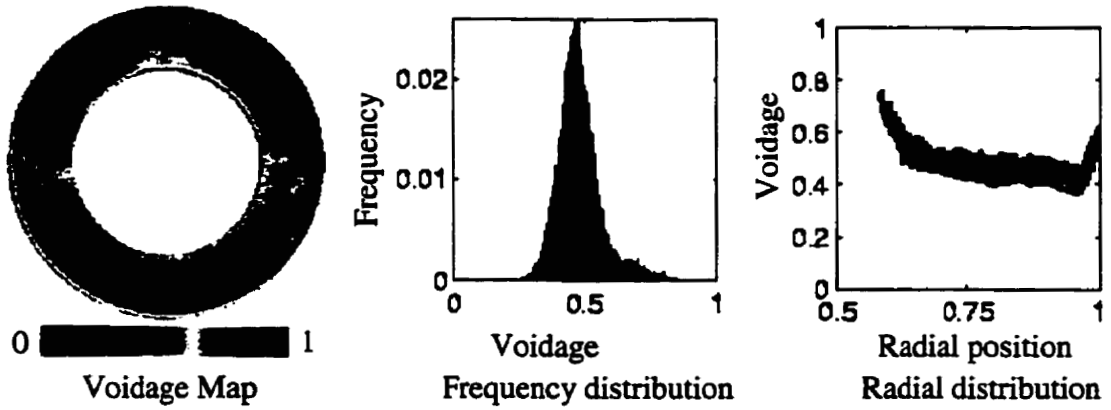

Fig. 5 Fluidized bed with U_s=2.00 cm/s at 4 cm. above the distributor

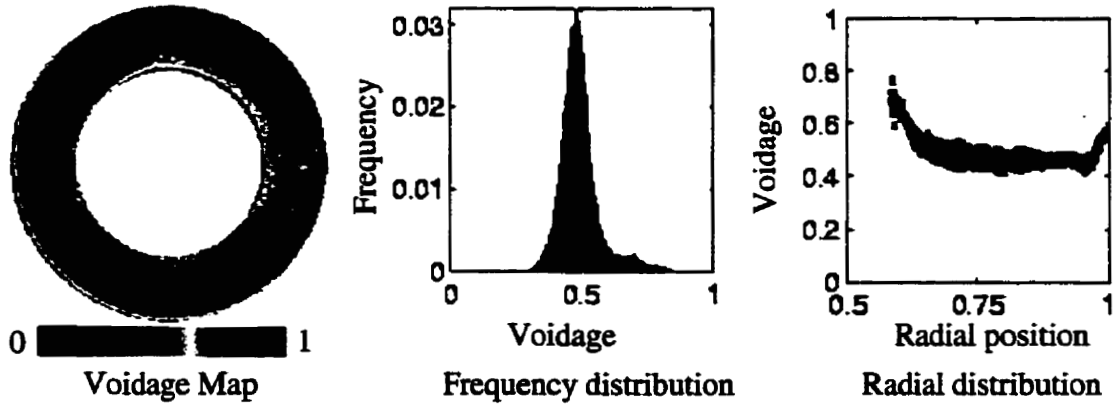

Fig. 6 Fluidized bed with U_s=2.00 cm/s at 5 cm. above the distributor

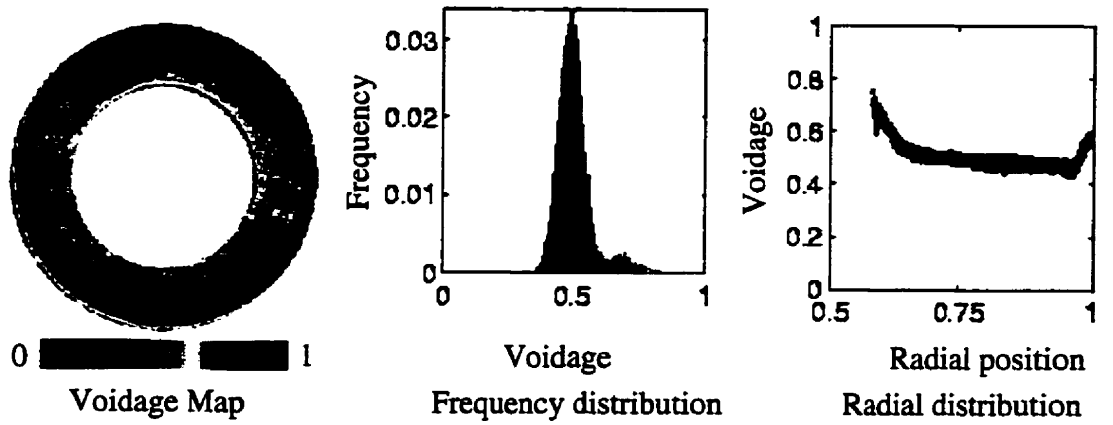

Fig. 7 Fluidized bed with U_s=2.00 cm/s at 6 cm. above the distributor

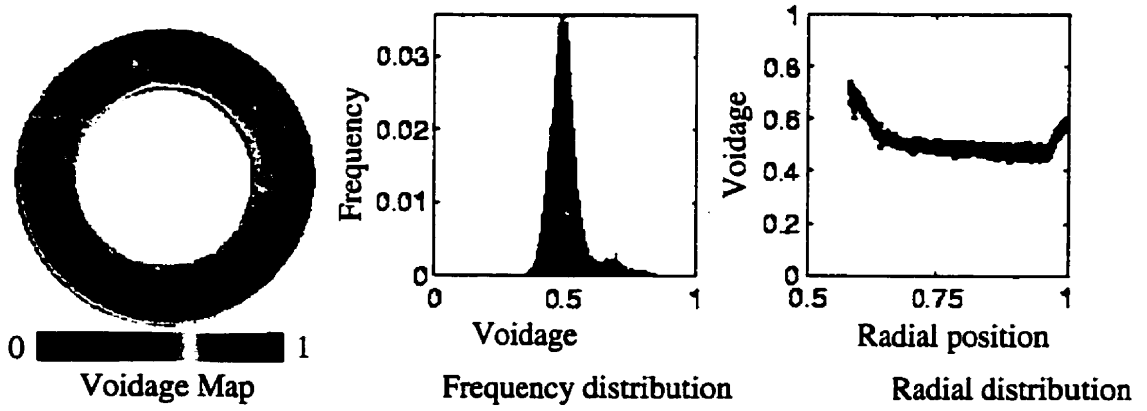

Fig. 8 Fluidized bed with U_s=2.00 cm/s at 7 cm. above the distributor

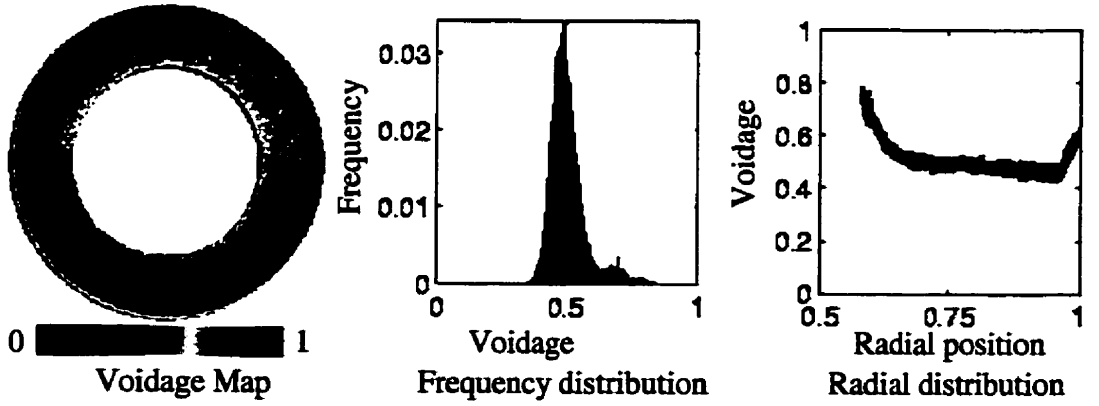

Fig. 9 Fluidized bed with U_s=2.00 cm/s at 8 cm. above the distributor

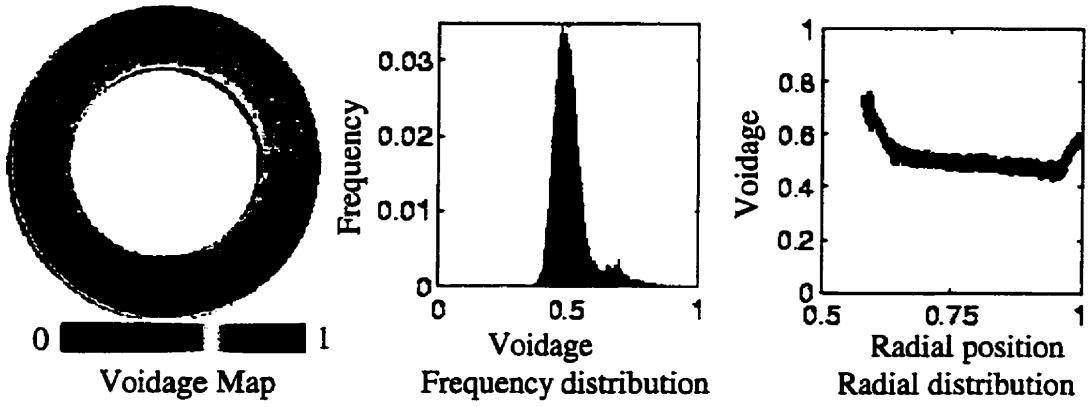

Fig. 10 Fluidized bed with U_s=2.00 cm/s at 9 cm. above the distributor

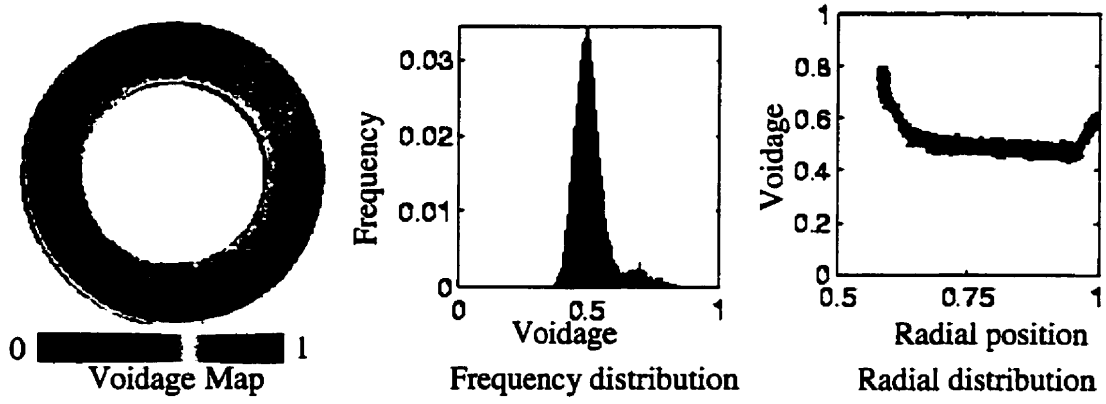

Fig. 11 Fluidized bed with U_s=2.00 cm/s at 10 cm. above the distributor

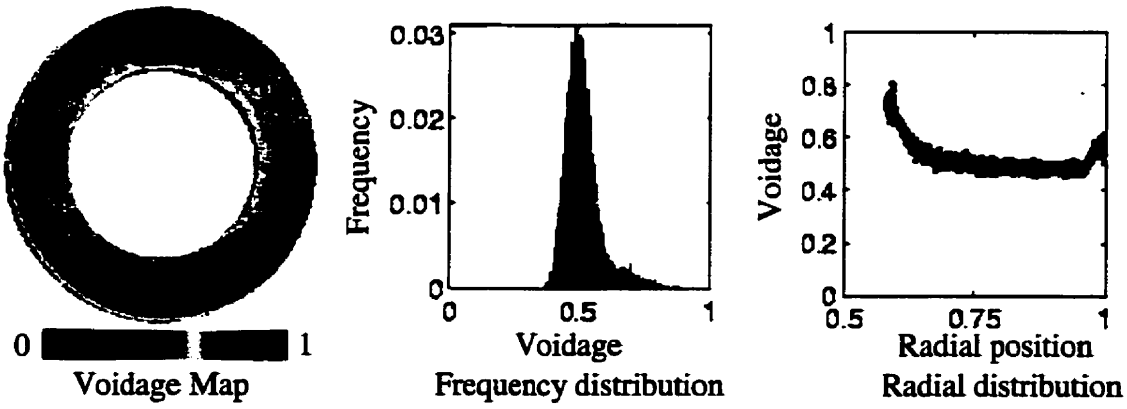

Fig. 12 Fluidized bed with U_s=2.00 cm/s at 11 cm. above the distributor

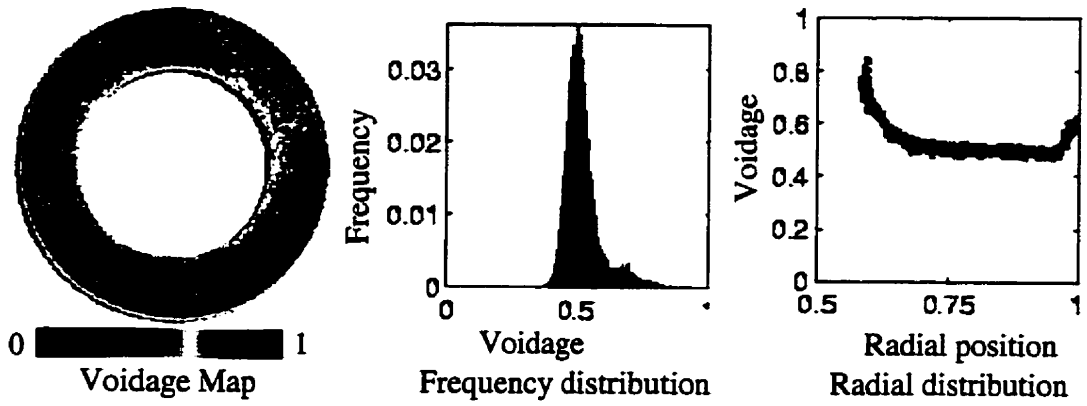

Fig. 13 Fluidized bed with U_s=2.00 cm/s at 12 cm. above the distributor

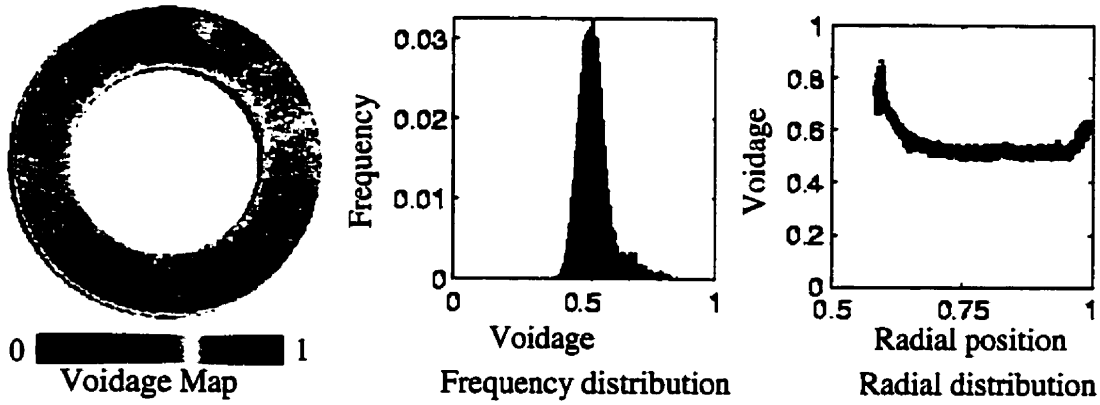

Fig. 14 Fluidized bed with U_s=2.00 cm/s at 13 cm. above the distributor

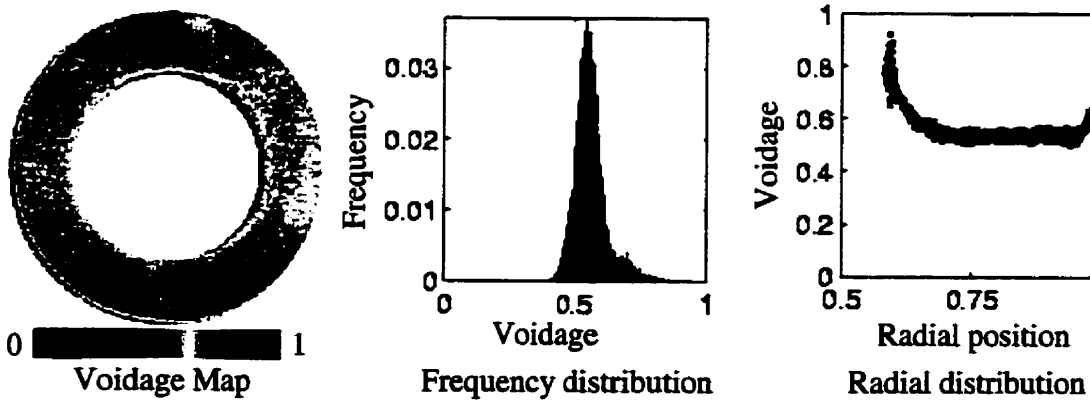

Fig. 15 Fluidized bed with U_s=2.00 cm/s at 14 cm. above the distributor

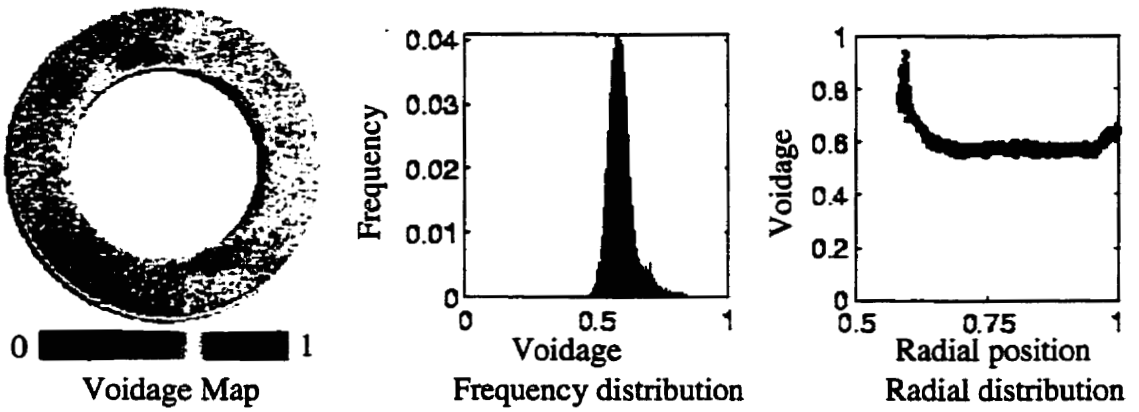

Fig. 16 Fluidized bed with U_s=2.00 cm/s at 15 cm. above the distributor

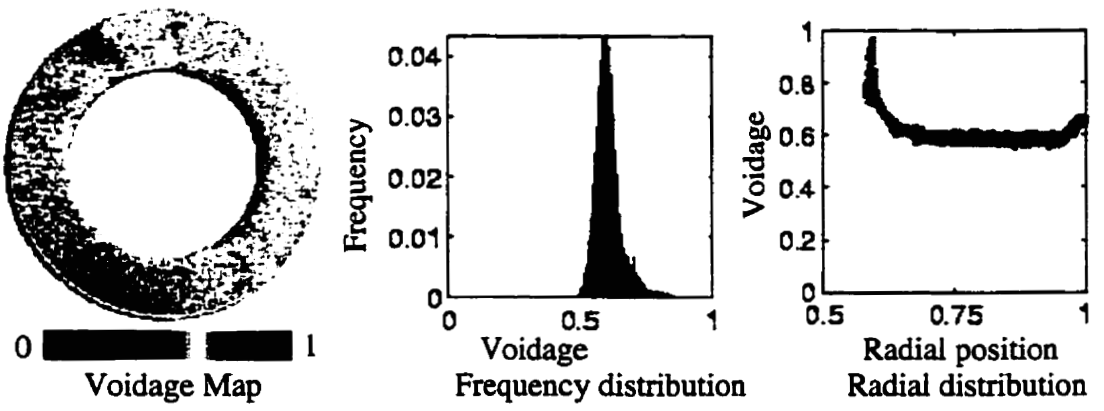

Fig. 17 Fluidized bed with U_s=2.00 cm/s at 16 cm. above the distributor

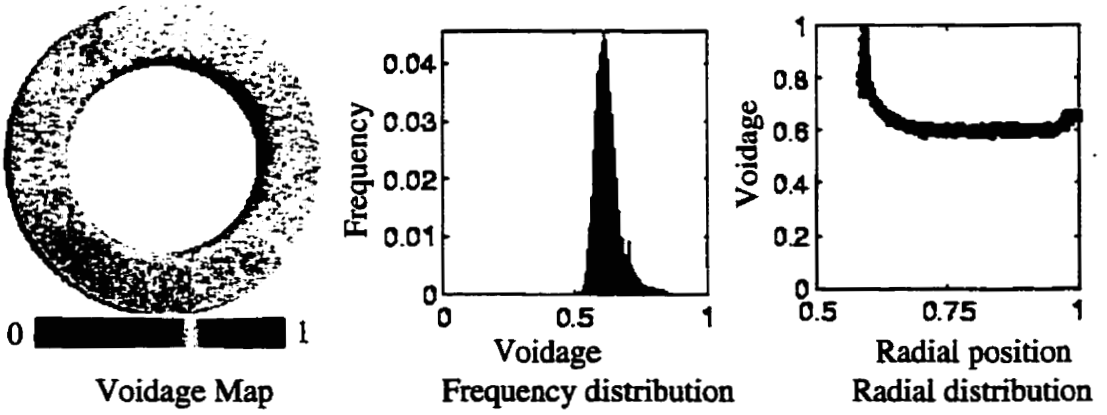

Fig. 18 Fluidized bed with U_s=2.00 cm/s at 17 cm. above the distributor

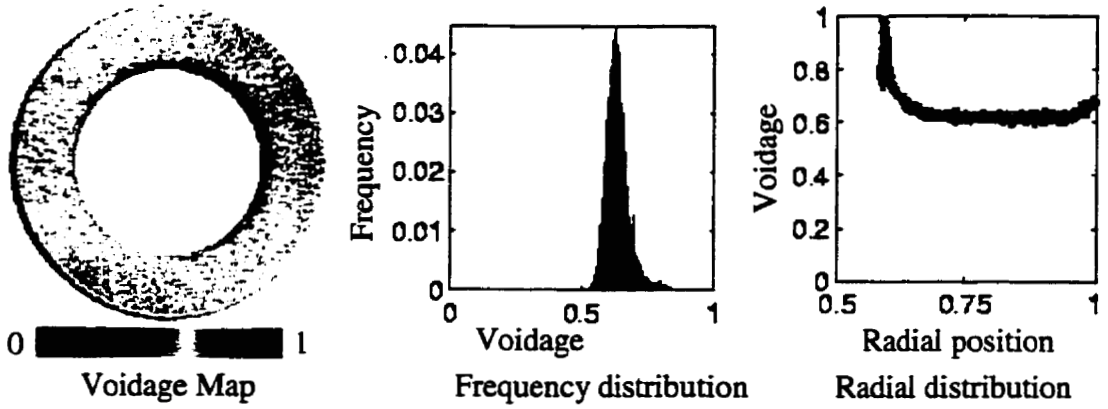

Fig. 19 Fluidized bed with U_s=2.00 cm/s at 18 cm. above the distributor

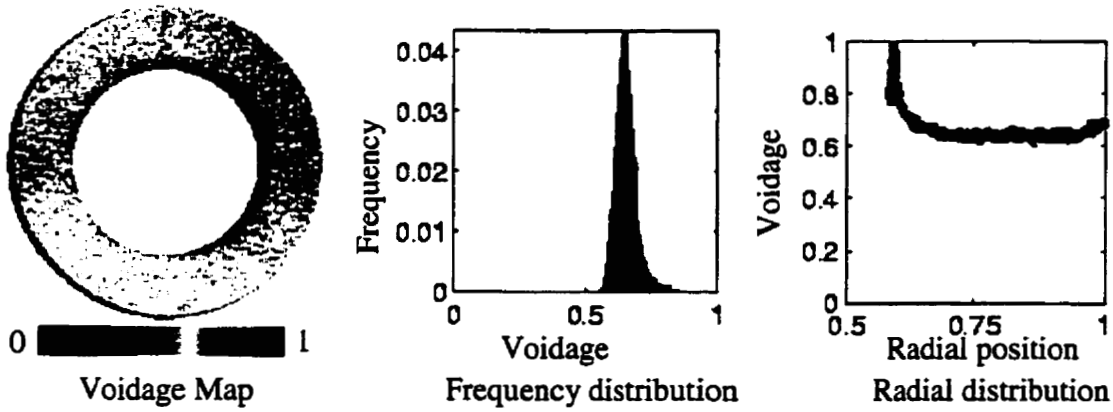

Fig. 20 Fluidized bed with U_s=2.00 cm/s at 19 cm. above the distributor

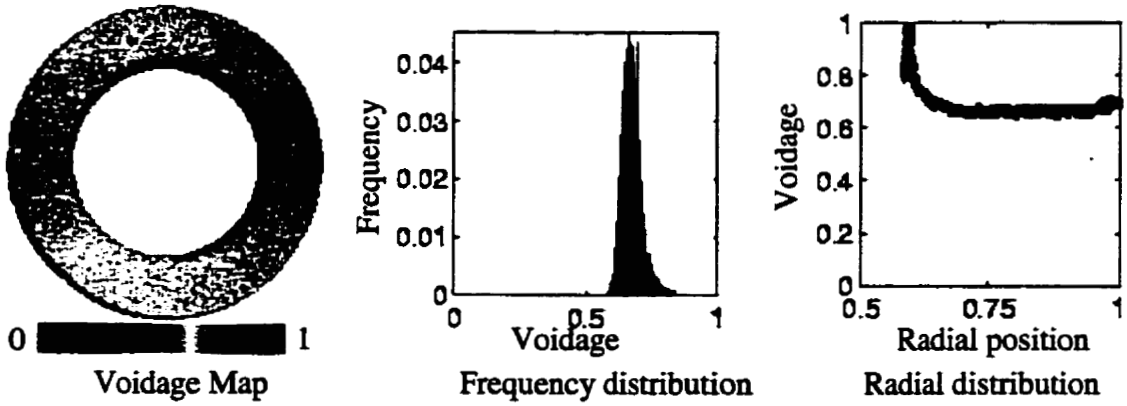

Fig. 21 Fluidized bed with U_s=2.00 cm/s at 20 cm. above the distributor

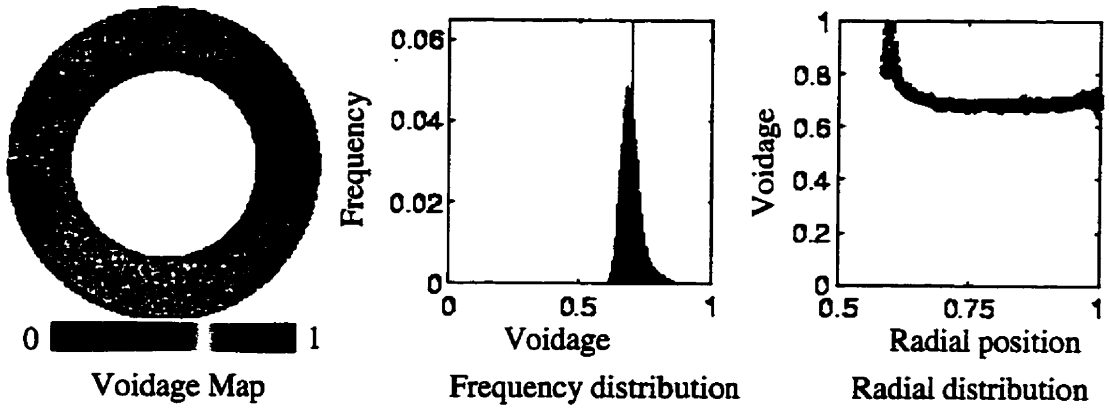

Fig. 22 Fluidized bed with U_s=2.00 cm/s at 21 cm. above the distributor

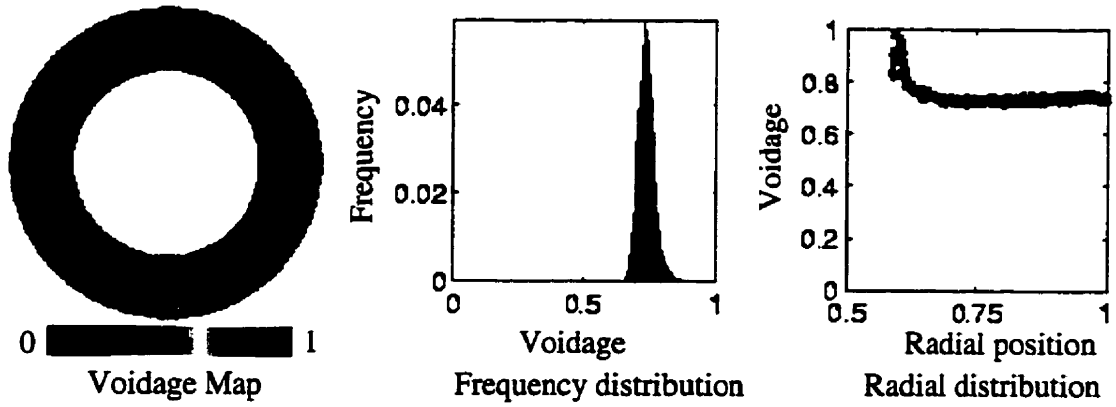

Fig. 23 Fluidized bed with U_s=2.00 cm/s at 22 cm. above the distributor

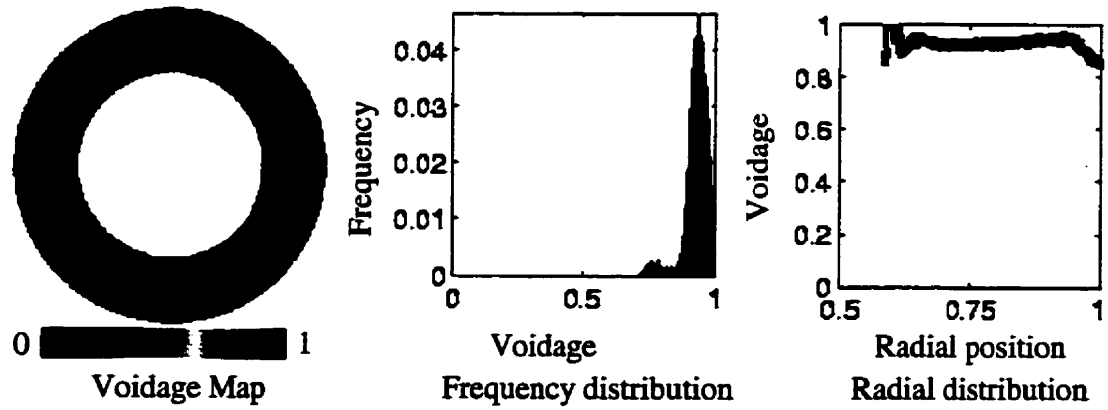

Fig. 24 Fluidized bed with U_s=2.00 cm/s at 23 cm. above the distributor

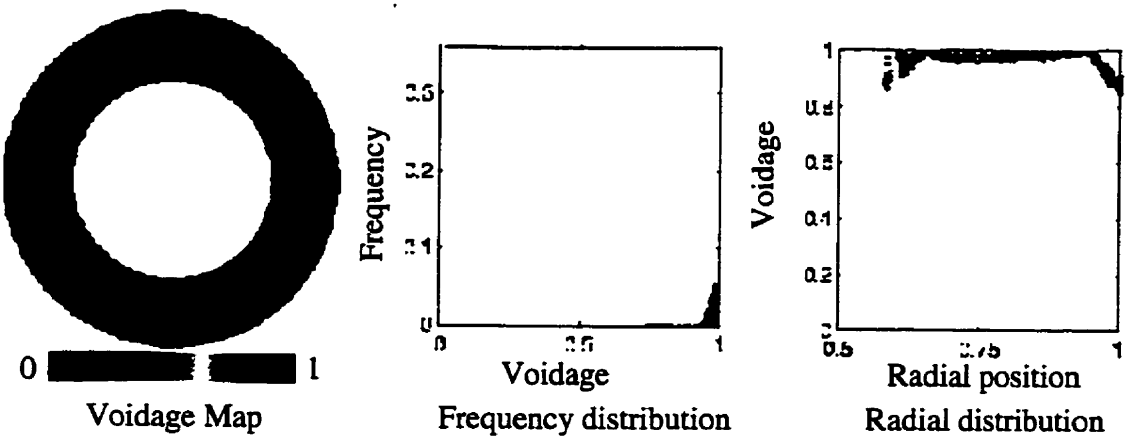

Fig. 25 Fluidized bed with U_s=2.00 cm/s at 24 cm. above the distributor

APPENDIX G

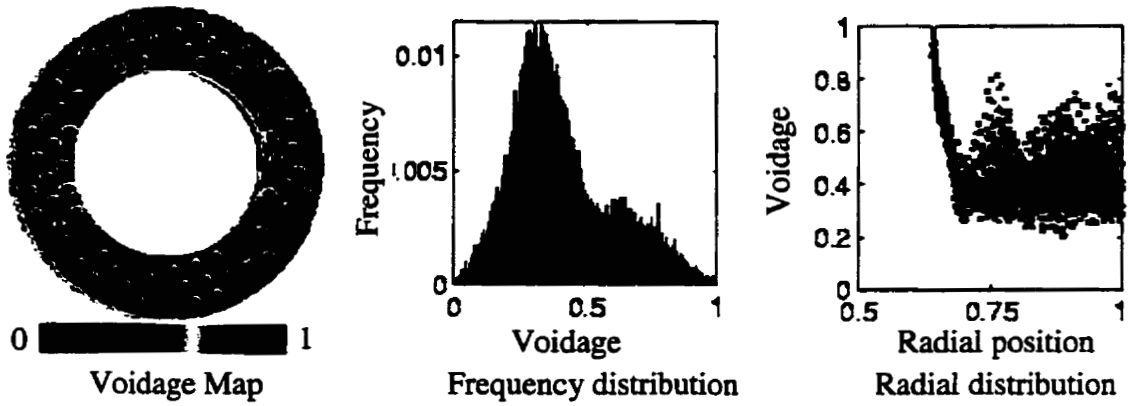

Fig. 1 Fluidized bed with U_s=2.32 cm/s at the distributor

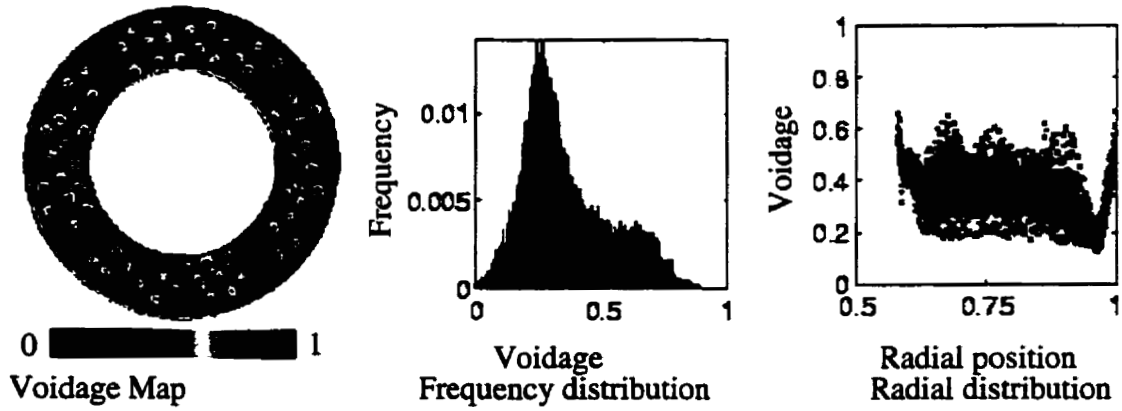

Fig. 2 Fluidized bed with U_s=2.32 cm/s at 1 cm. above the distributor

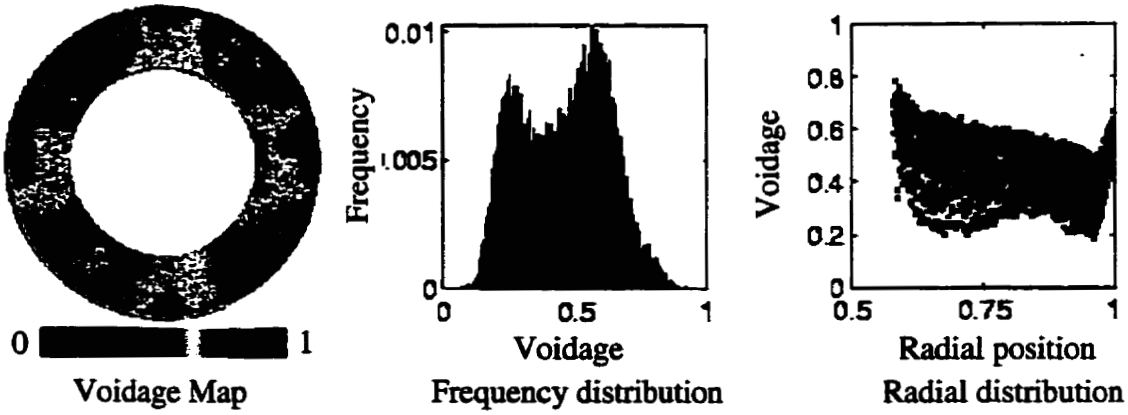

Fig. 3 Fluidized bed with U_s=2.32 cm/s at 2 cm. above the distributor

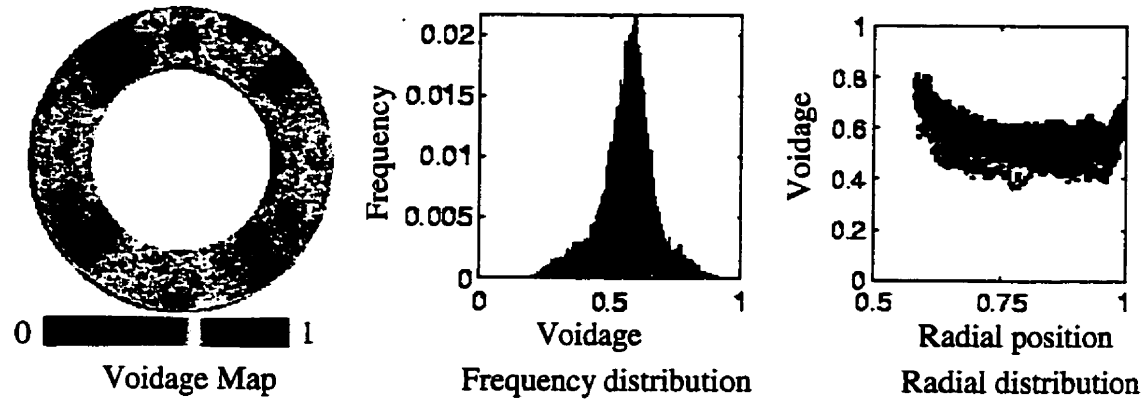

Fig. 4 Fluidized bed with U_s=2.32 cm/s at 3 cm. above the distributor

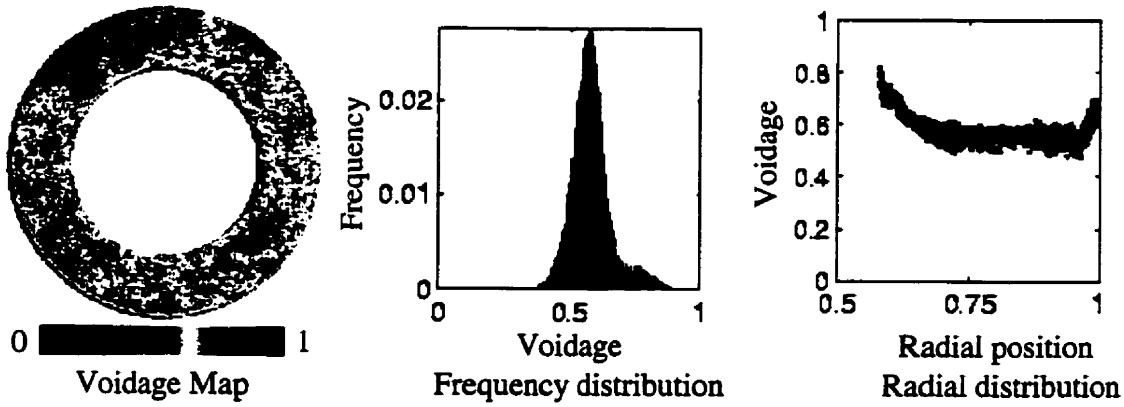

Fig. 5 Fluidized bed with U_s=2.32 cm/s at 4 cm. above the distributor

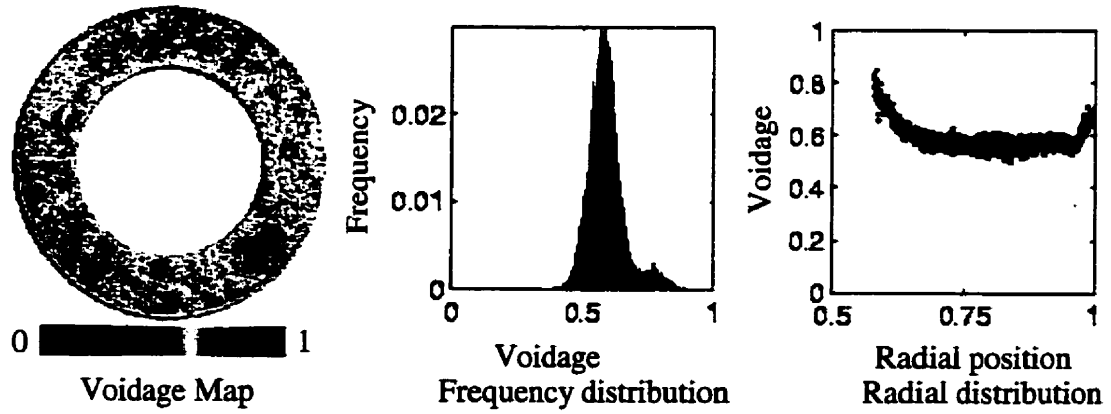

Fig. 6 Fluidized bed with U_s=2.32 cm/s at 5 cm. above the distributor

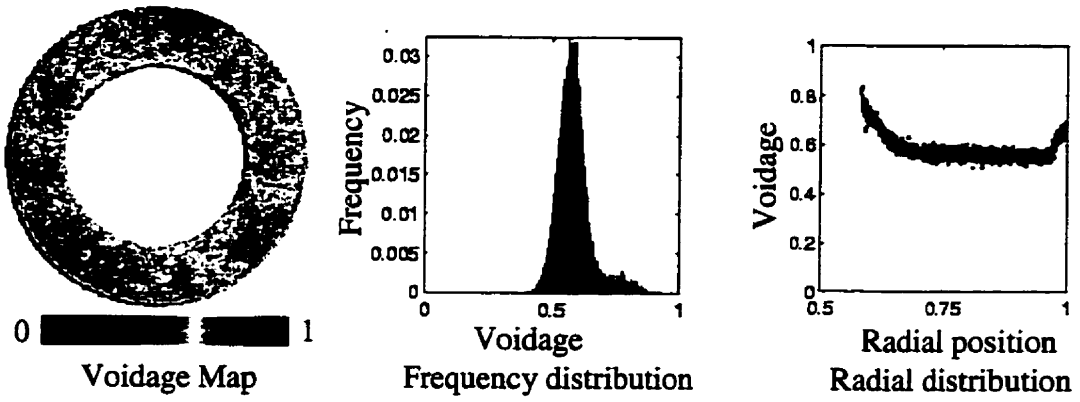

Fig. 7 Fluidized bed with U_s=2.32 cm/s at 6 cm. above the distributor

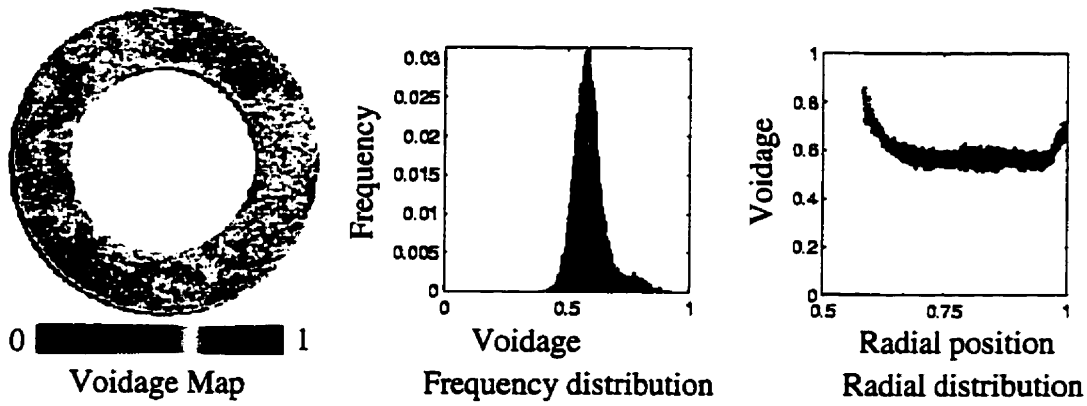

Fig. 8 Fluidized bed with U_s=2.32 cm/s at 7 cm. above the distributor

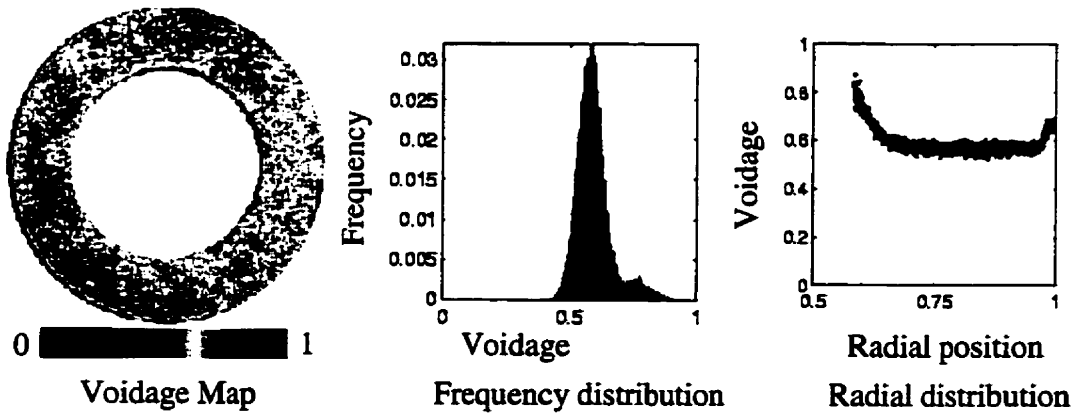

Fig. 9 Fluidized bed with U_s=2.32 cm/s at 8 cm. above the distributor

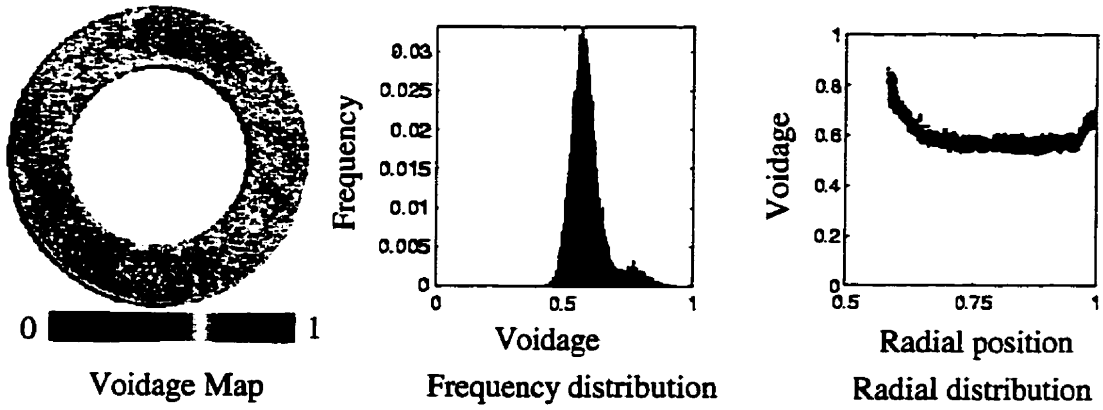

Fig. 10 Fluidized bed with U_s=2.32 cm/s at 9 cm. above the distributor

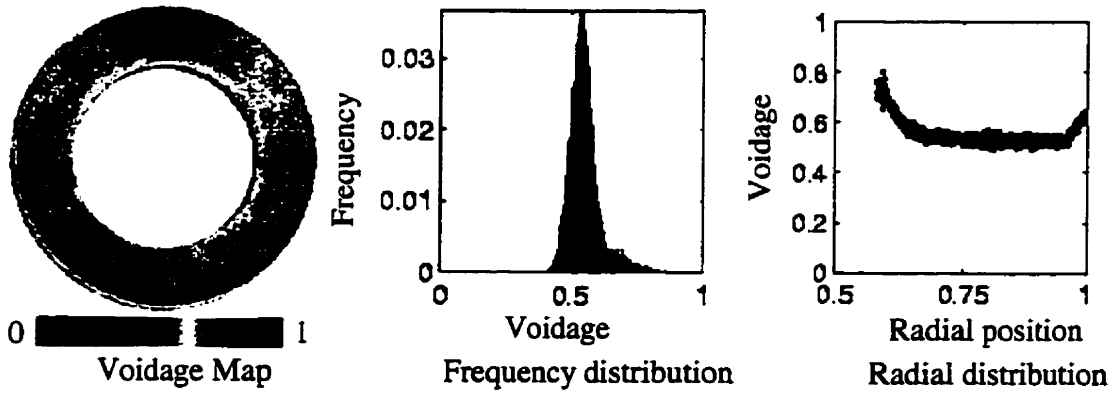

Fig. 11 Fluidized bed with U_s=2.32 cm/s at 10 cm. above the distributor

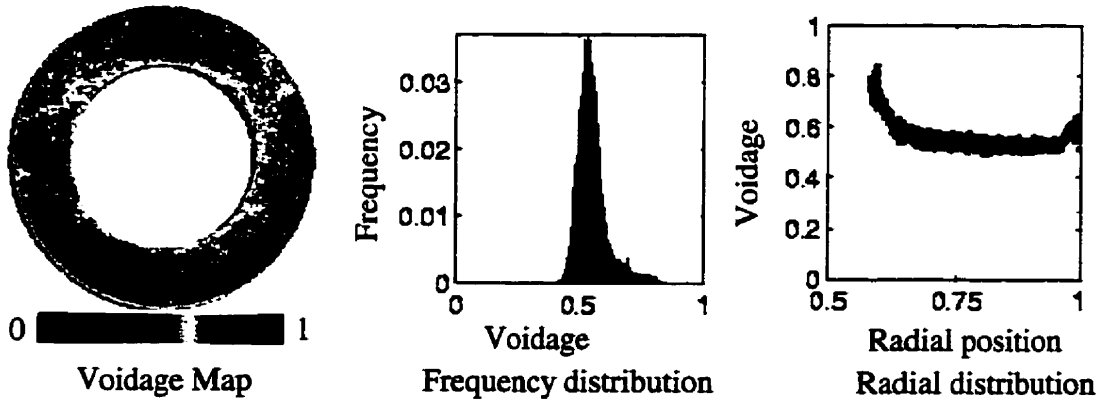

Fig. 12 Fluidized bed with U_s=2.32 cm/s at 11 cm. above the distributor

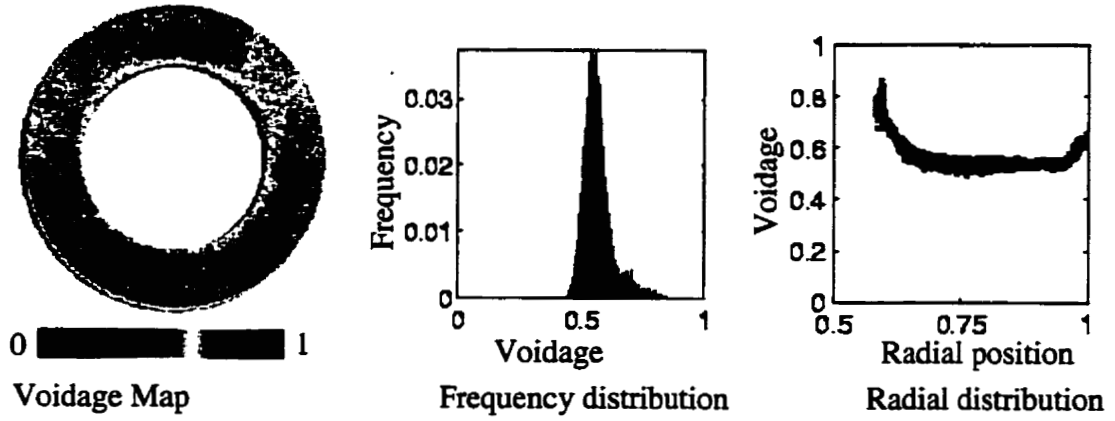

Fig. 13 Fluidized bed with U_s=2.32 cm/s at 12 cm. above the distributor

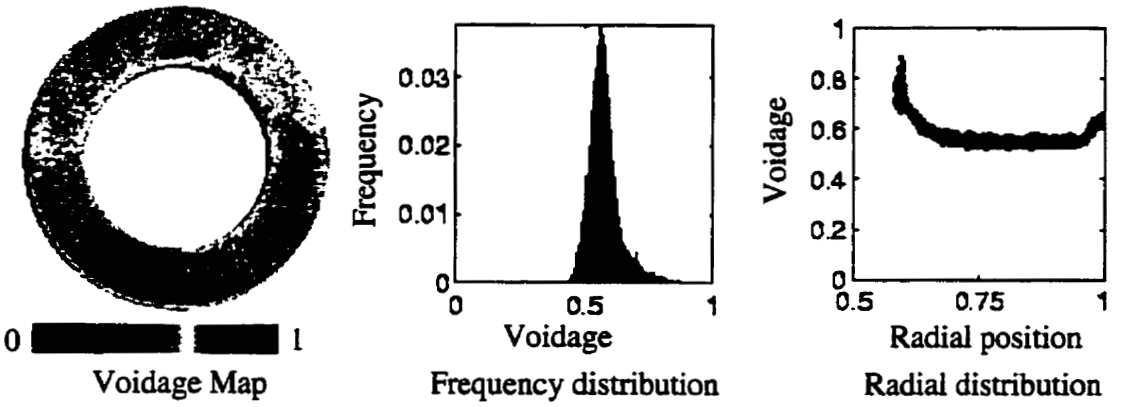

Fig. 14 Fluidized bed with U_s=2.32 cm/s at 13 cm. above the distributor

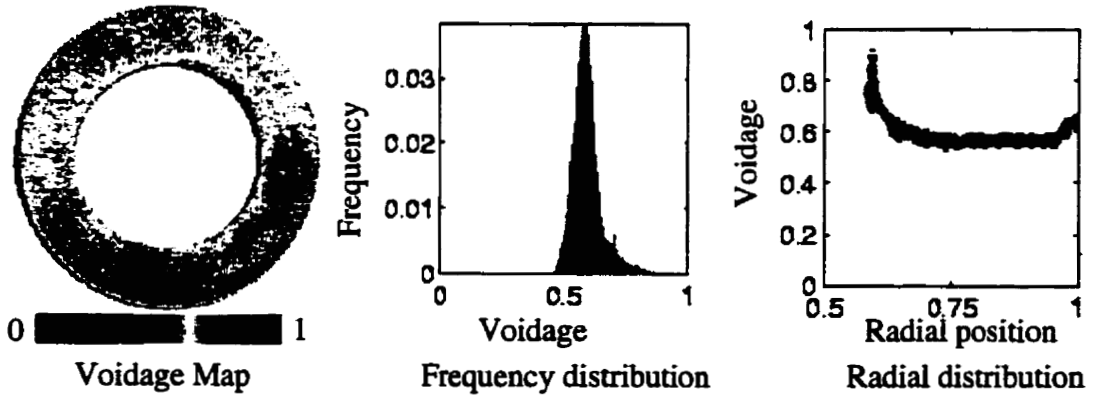

Fig. 15 Fluidized bed with U_s=2.32 cm/s at 14 cm. above the distributor

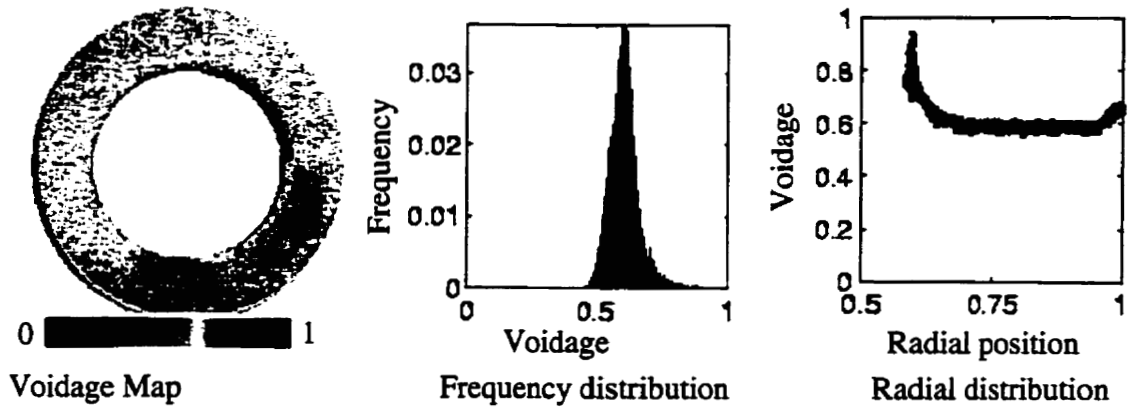

Fig. 16 Fluidized bed with U_s=2.32 cm/s at 15 cm. above the distributor

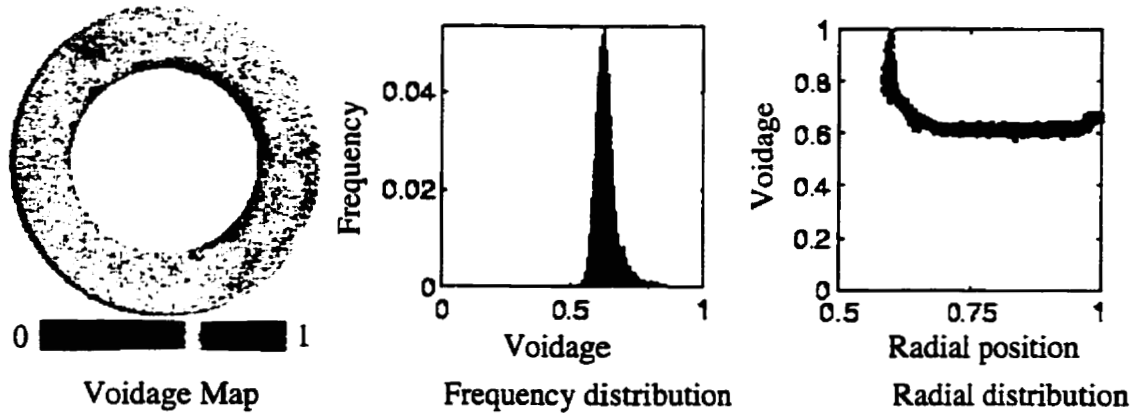

Fig. 17 Fluidized bed with U_s=2.32 cm/s at 16 cm. above the distributor

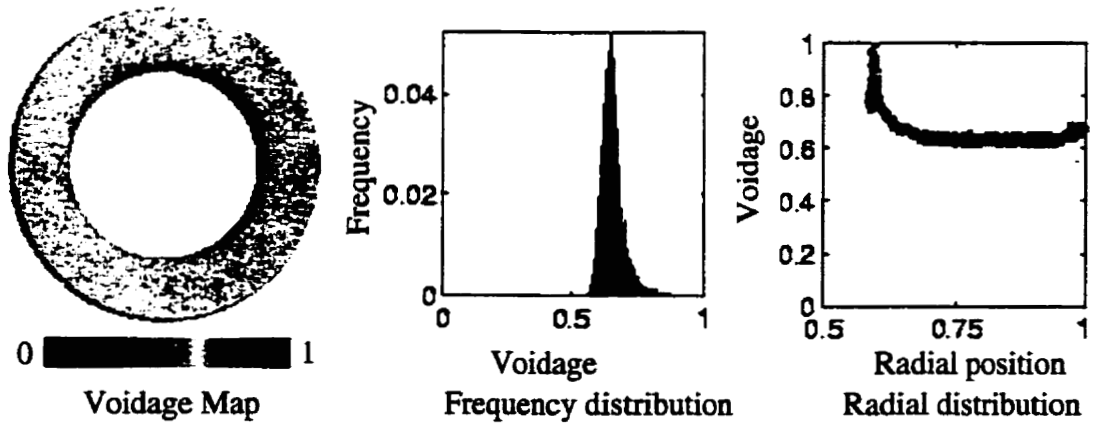

Fig. 18 Fluidized bed with U_s=2.32 cm/s at 17 cm. above the distributor

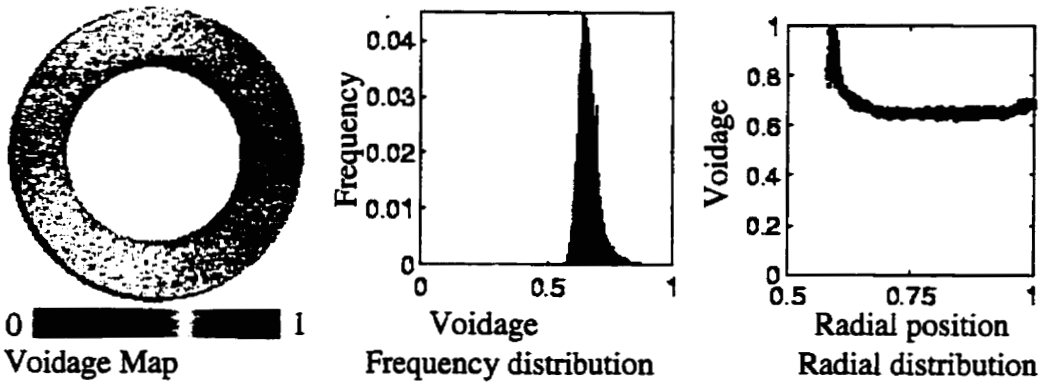

Fig. 19 Fluidized bed with U_s=2.32 cm/s at 18 cm. above the distributor

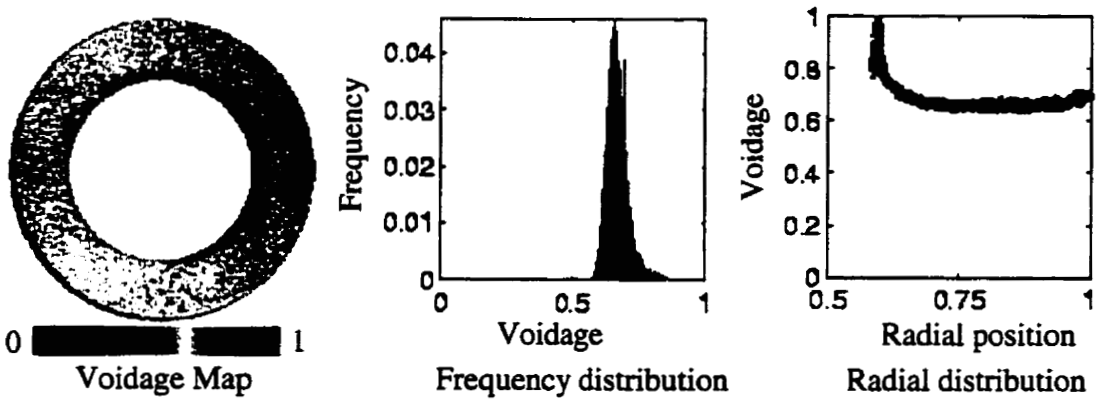

Fig. 20 Fluidized bed with U_s=2.32 cm/s at 19 cm. above the distributor

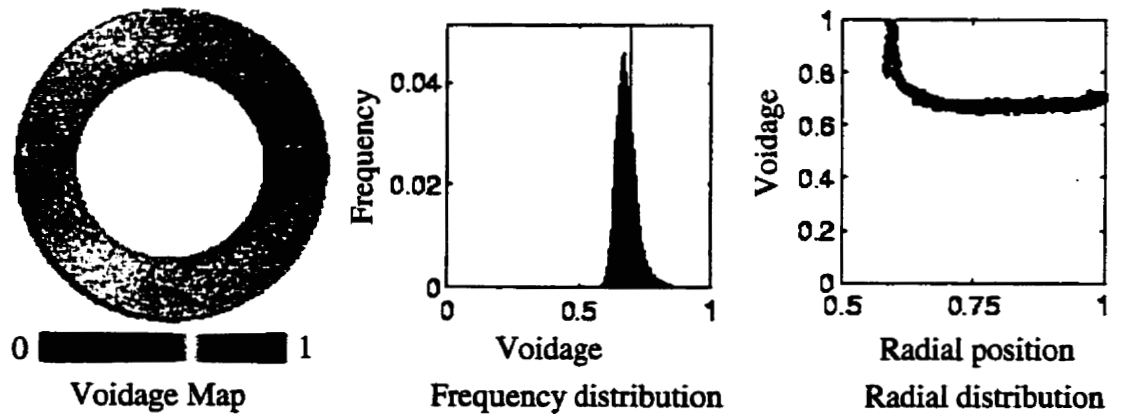

Fig. 21 Fluidized bed with U_s=2.32 cm/s at 20 cm. above the distributor

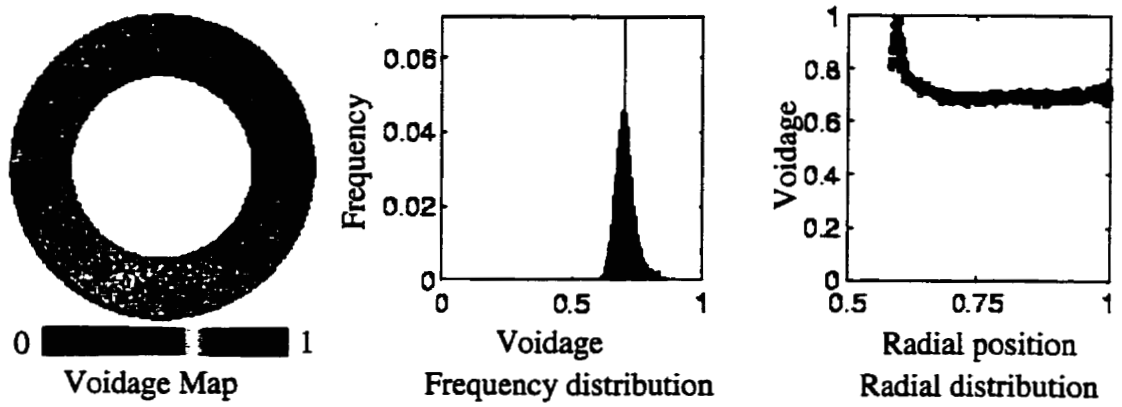

Fig. 22 Fluidized bed with U_s=2.32 cm/s at 21 cm. above the distributor

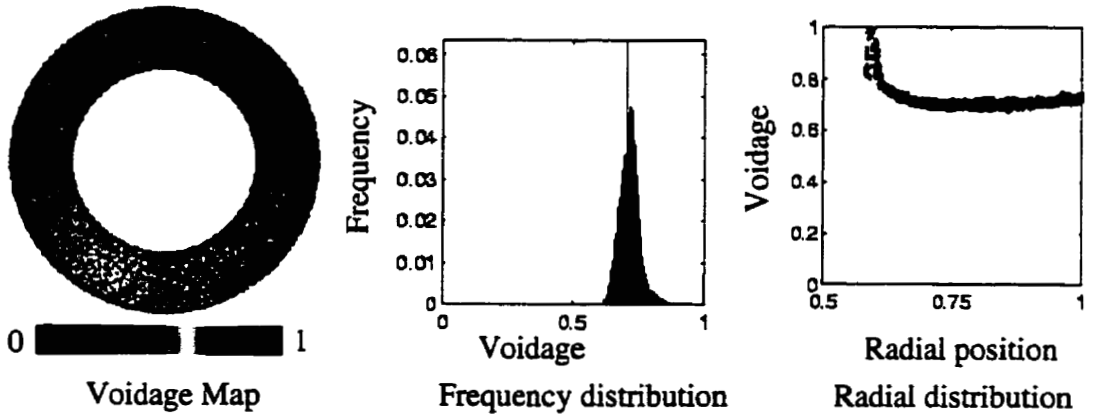

Fig. 23 Fluidized bed with U_s=2.32 cm/s at 21 cm. above the distributor

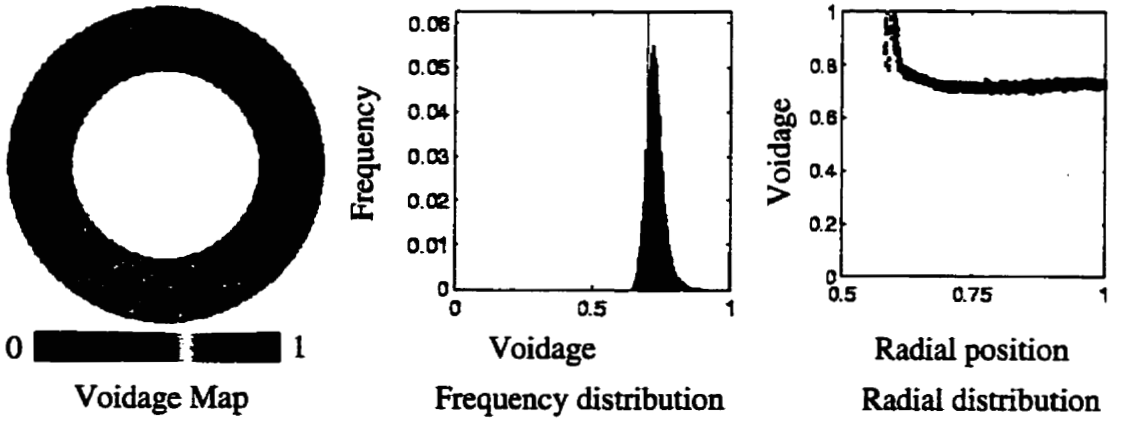

Fig. 24 Fluidized bed with U_s=2.32 cm/s at 23 cm. above the distributor

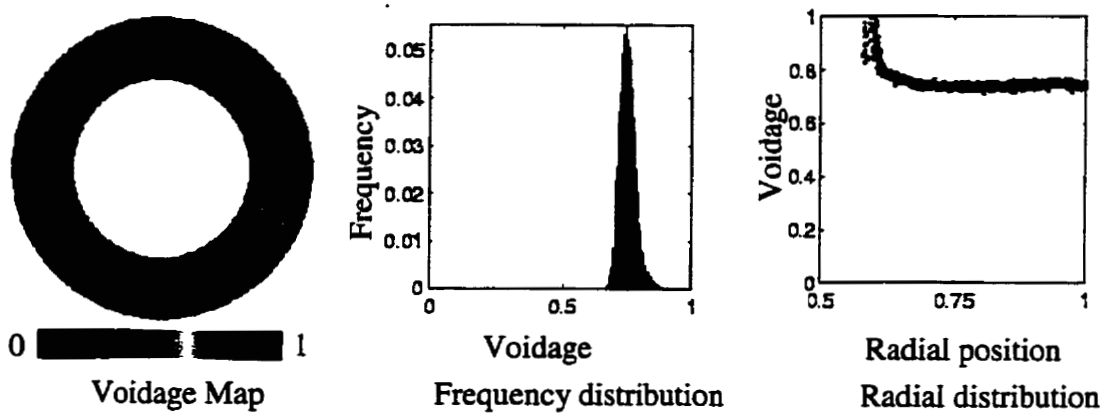

Fig. 25 Fluidized bed with U_s=2.32 cm/s at 24 cm. above the distributor

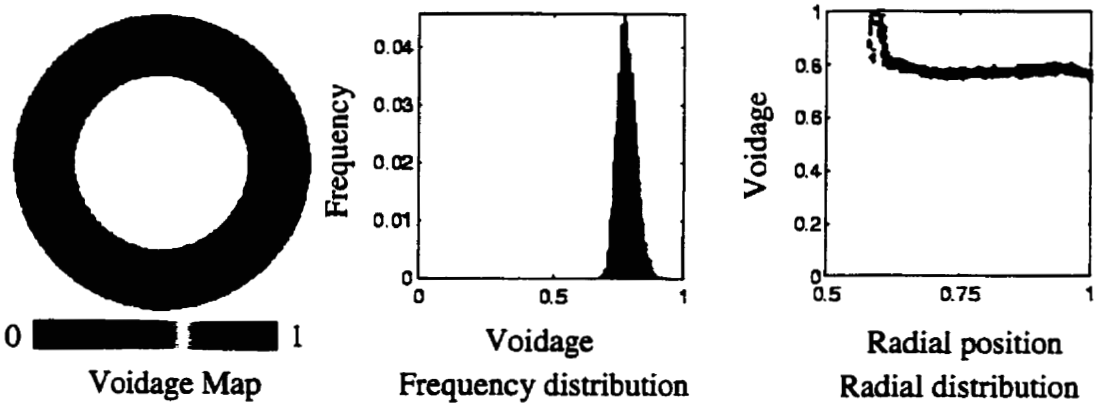

Fig. 26 Fluidized bed with U_s=2.32 cm/s at 25 cm. above the distributor

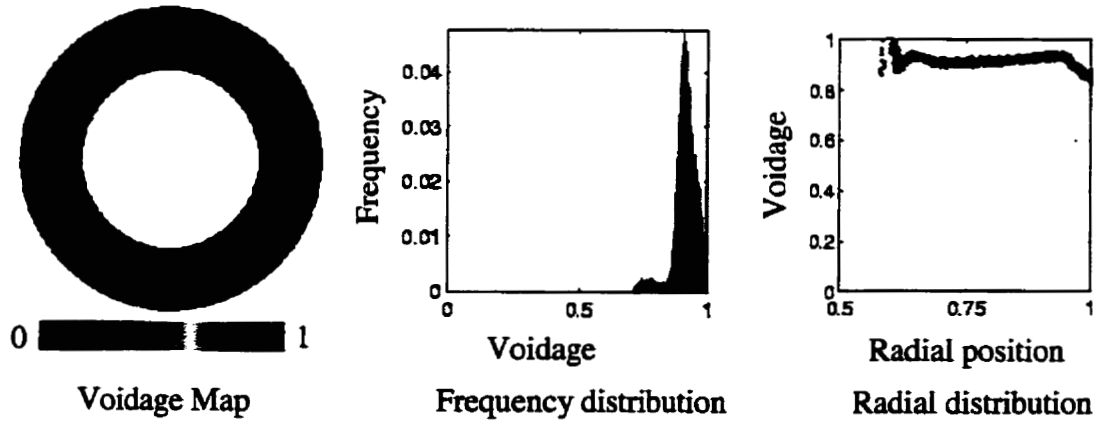

Fig. 27 Fluidized bed with U_s=2.32 cm/s at 26 cm. above the distributor

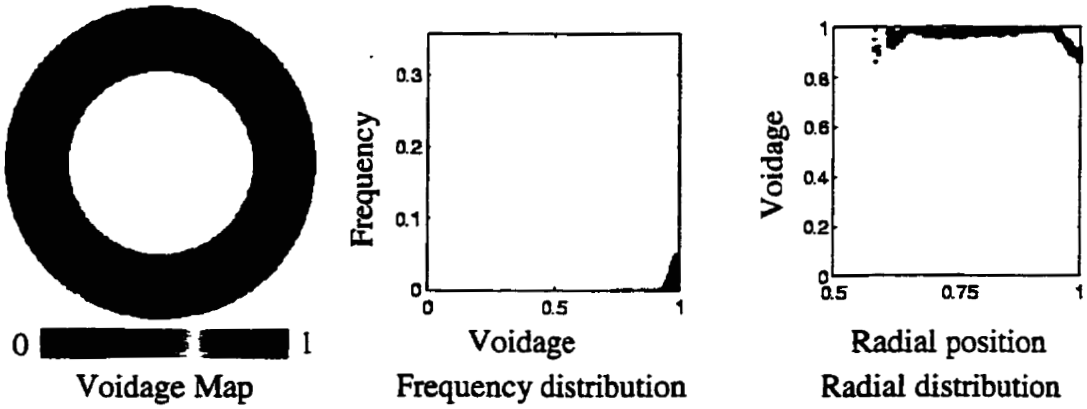

Fig. 29 Fluidized bed with U_s=2.32 cm/s at 28 cm. above the distributor

APPENDIX H

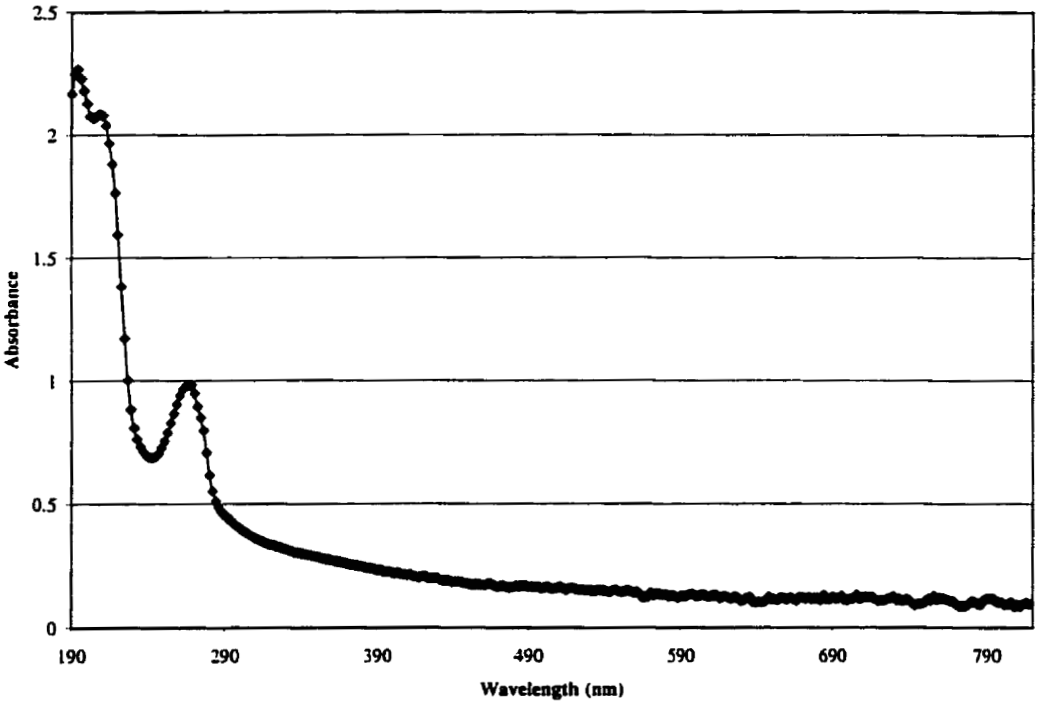

Fig. 1 Spectrogram of water sample after 1 hr. of dark adsorption

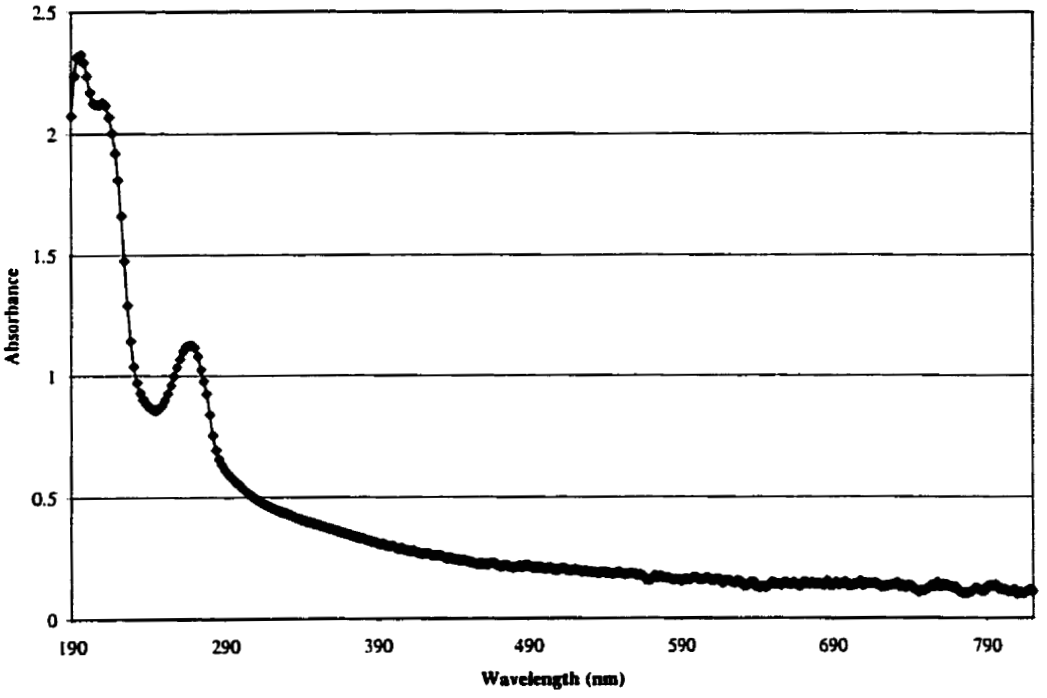

Fig. 2 Spectrogram of water sample after 1.5 hr. of illumination

APPENDIX I

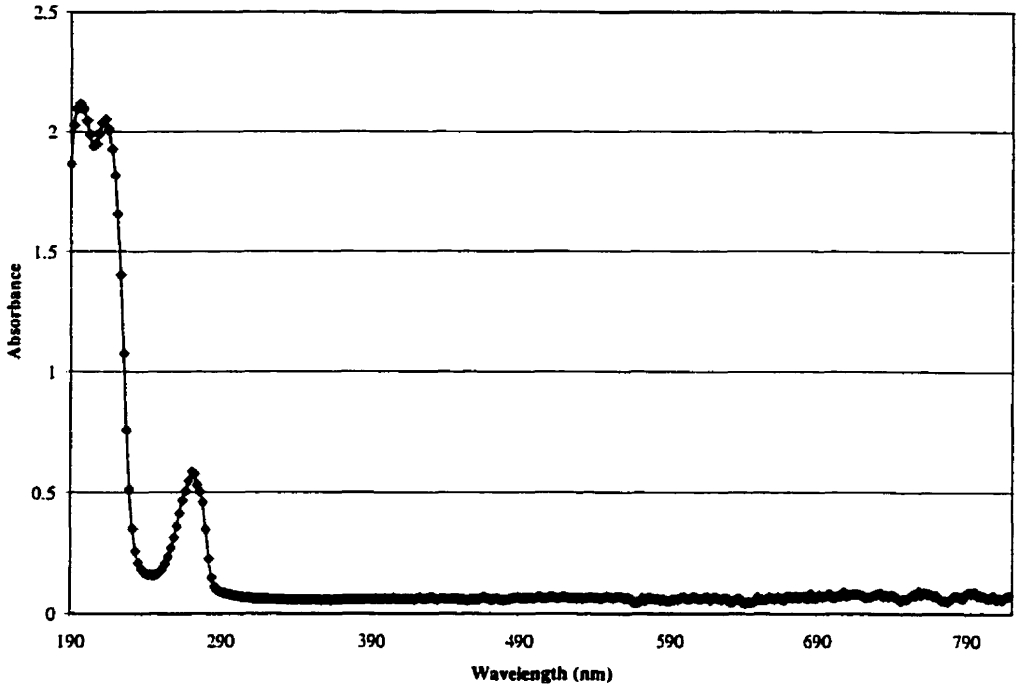

Fig. 1 Spectrogram of water sample after 45 min. of dark adsorption

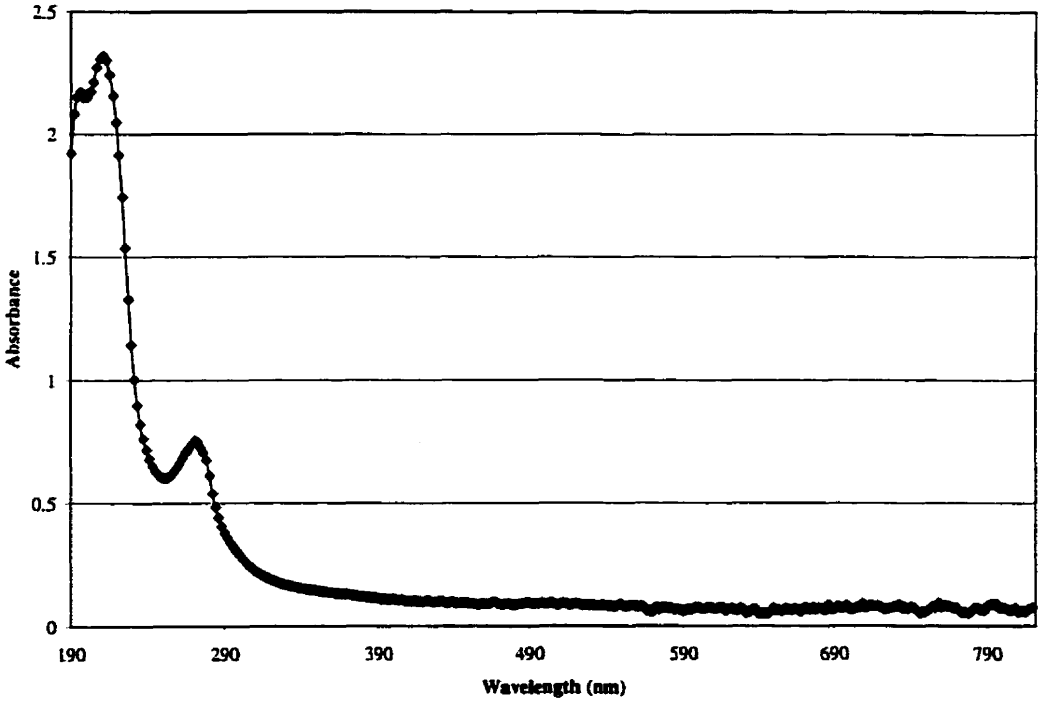

Fig. 2 Spectrogram of water sample after 10 min. of illumination

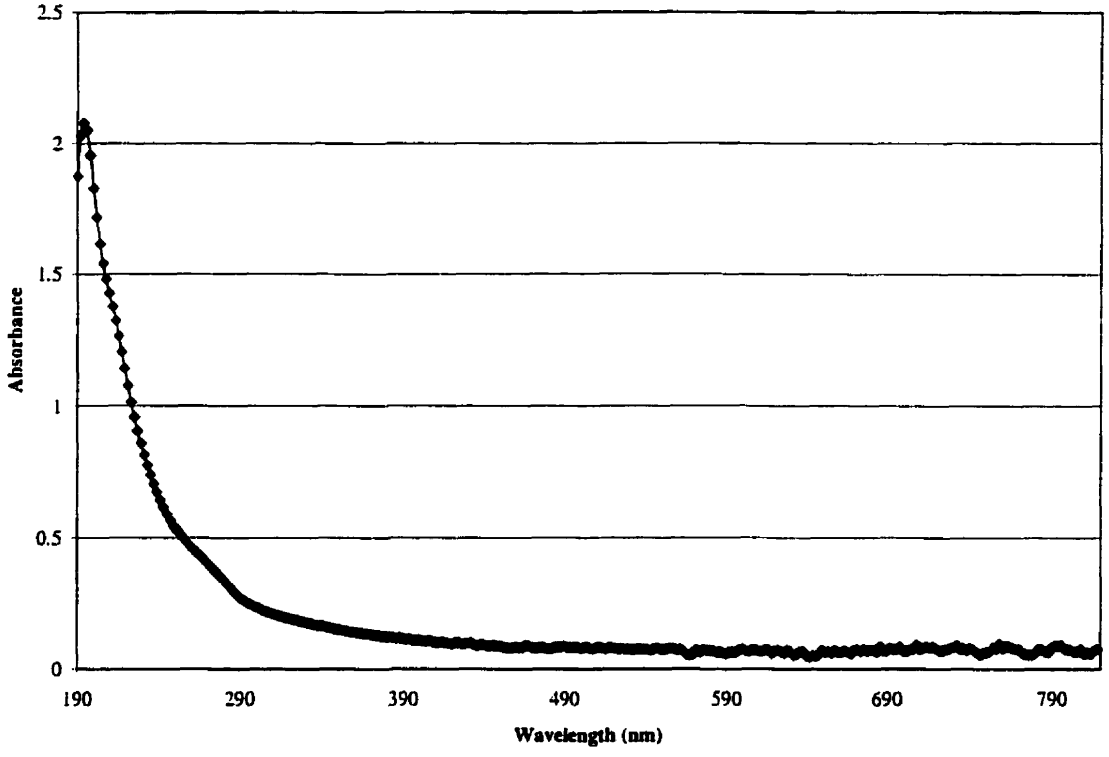

Fig. 3 Spectrogram of water sample after 30 min. of illumination

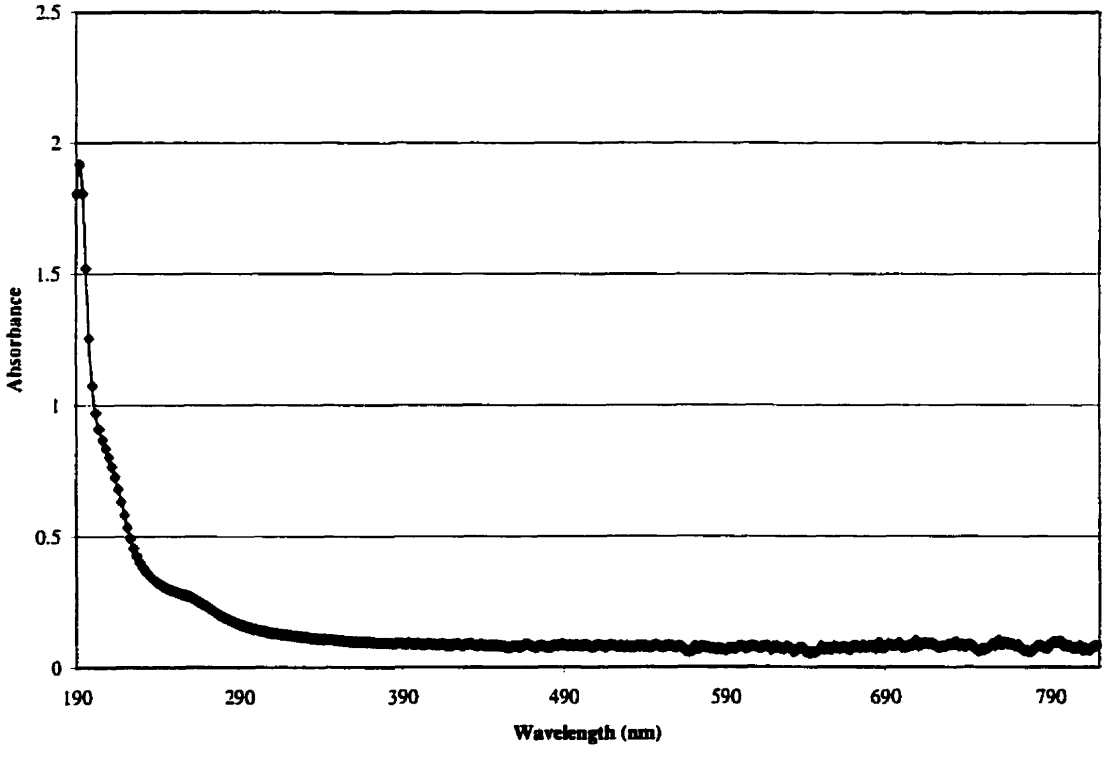

Fig. 4 Spectrogram of water sample after 1 hr. of illumination

APPENDIX J

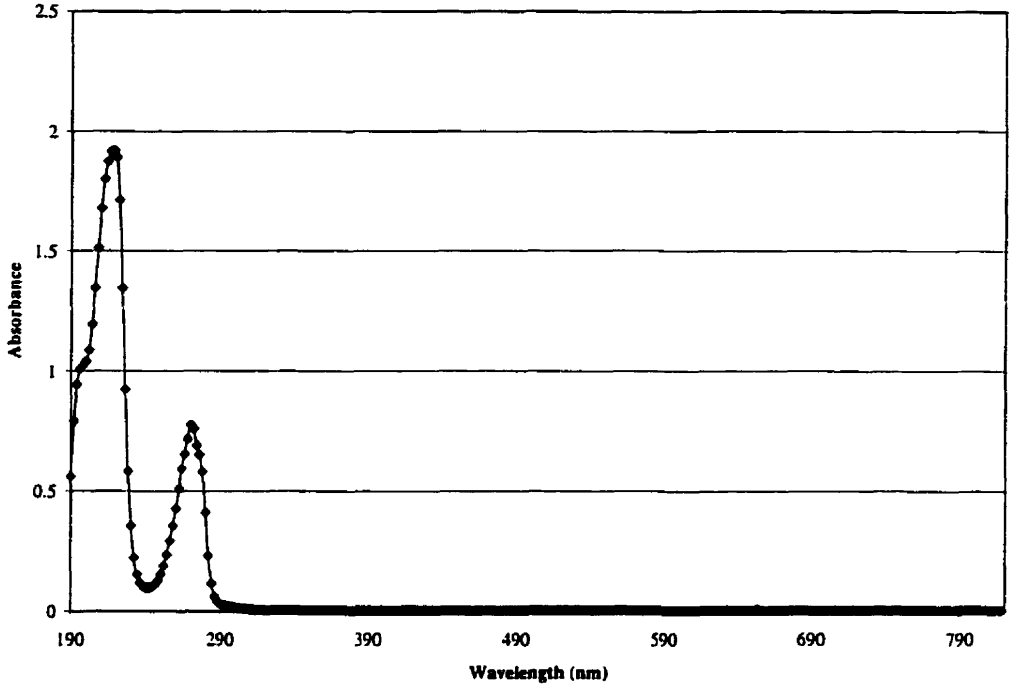

Fig. 1 Spectrogram of initial wastewater sample

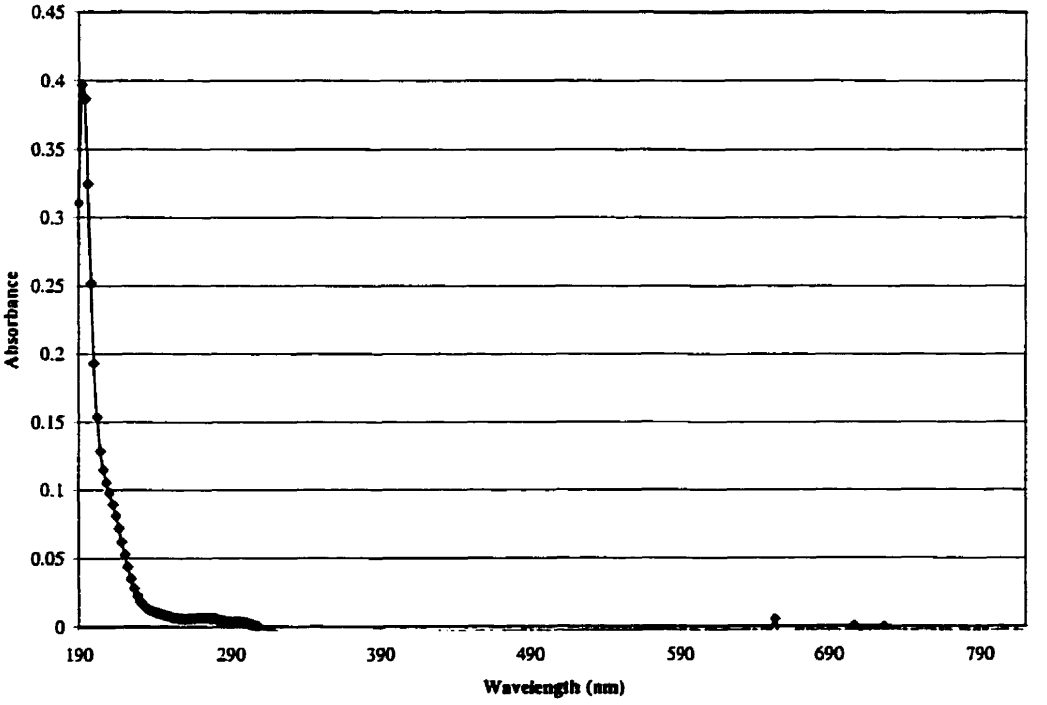

Fig. 2 Spectrogram of fresh water sample at the start of illumination

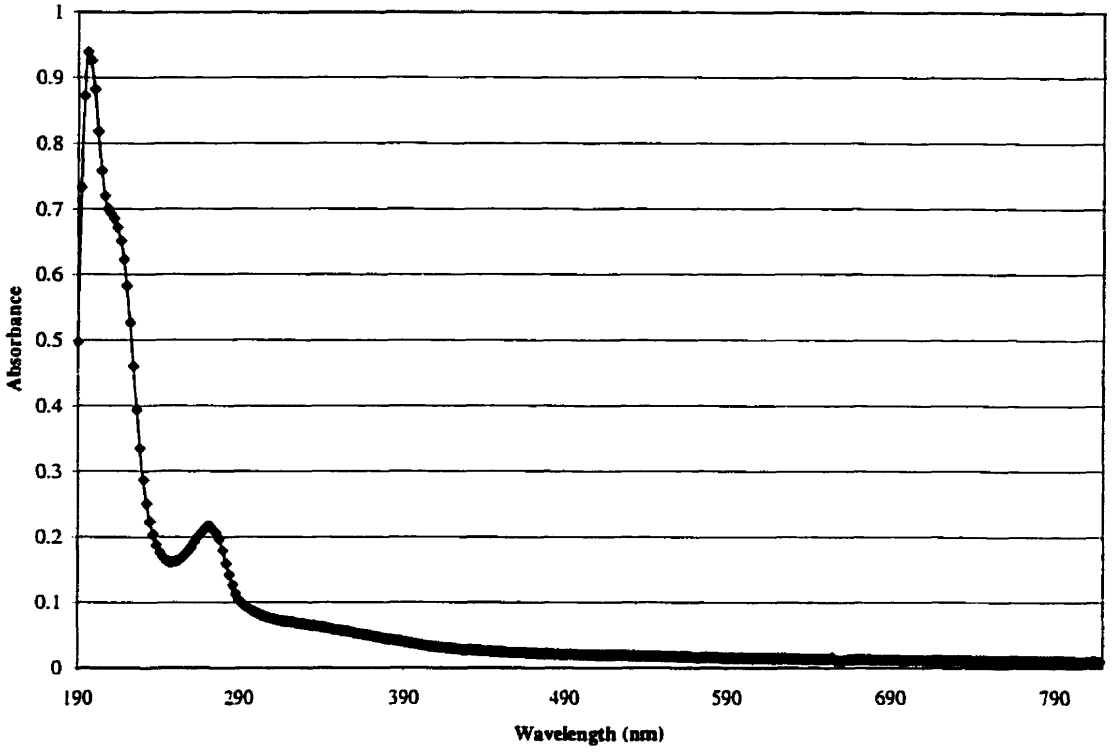

Fig. 3 Spectrogram of water sample after 30 min. of illumination

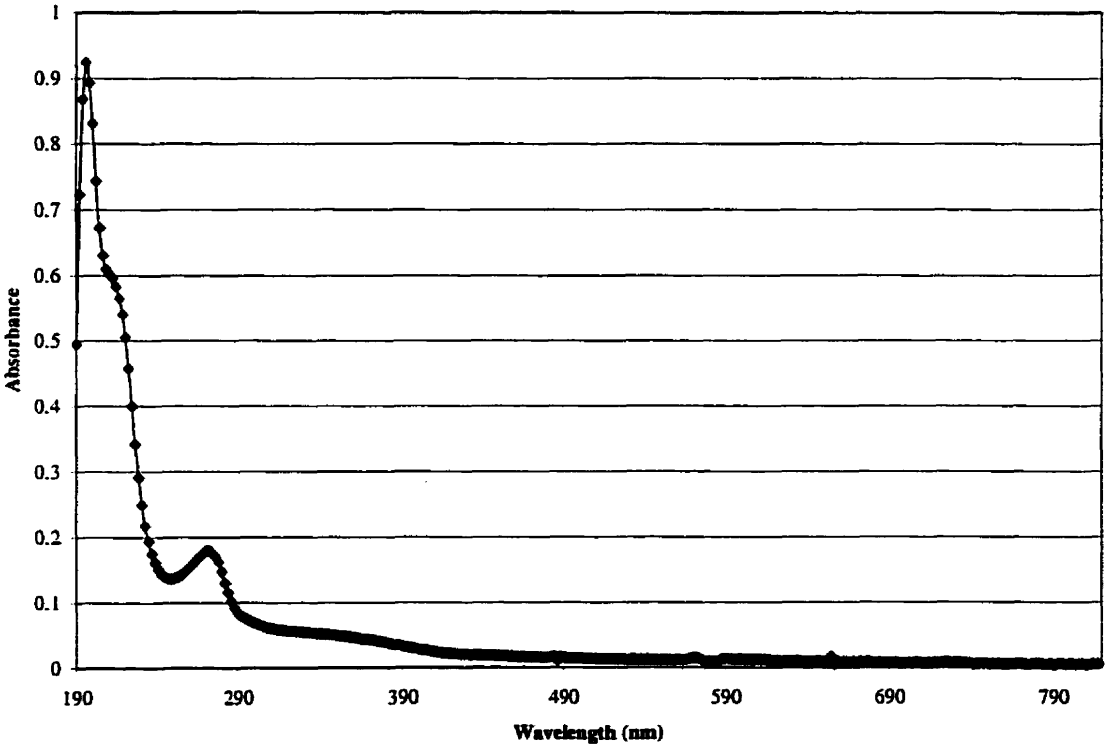

Fig. 4 Spectrogram of water sample after 1 hr. of illumination